COMPACT, LOW-THRESHOLD FEMTOSECOND LASERS

John-Mark Hopkins

A Thesis Submitted for the Degree of PhD
at the
University of St Andrews

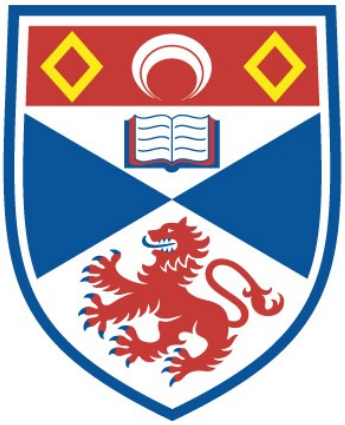

1999

Compact, Low-threshold Femtosecond Lasers

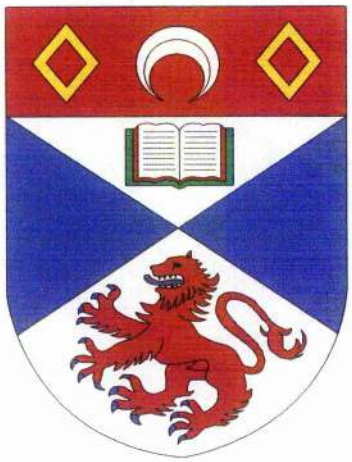

Thesis presented for the degree of

Doctor of Philosophy

To the University of St. Andrews

By

John-Mark Hopkins, Msci

The J. F. Allen Physics Research Laboratories
School of Physics and Astronomy
University of St. Andrews
North Haugh
St. Andrews
Scotland KY16 9SS

April, 1999

Declarations

I, John-Mark Hopkins, hereby certify that this thesis, which is approximately sixty thousand words in length, has been written by me, that it is the record of work carried out by me and that it has not been submitted in any previous application for a higher degree.

I was admitted as a research student and as a candidate for the degree of Doctor of Philosophy in October, 1995; the higher study for which this is a record was carried out at the University of St. Andrews between 1995 and 1998.

In submitting this thesis to the University of St. Andrews I understand that I am giving permission for it to be made available for use in accordance with the regulations of the University Library for the time being in force, subject to any copyright vested in the work not being affected thereby. I also understand that the title and abstract will be published, and that a copy of the work may be made and supplied to any *bona fide* library or research worker.

signature of candidate date 13/04/99

I hereby certify that the candidate has fulfilled the conditions of the Resolution and Regulations appropriate for the degree of Doctor of Philosophy in the University of St. Andrews and that the candidate is qualified to submit this thesis in application for that degree.

signature of supervisor date

For Bumper

and Pete

The Road goes ever on and on
Down from the door where it began.
Now far ahead the road has gone,
And I must follow, if I can,
Pursuing it with eager feet,
Until it joins some other way
Where many paths and errands meet.
And wither then? I cannot say.

J.R.R. Tolkien

Abstract

This thesis is concerned with the design and development of compact, all-solid-state femtosecond pulse lasers with low pump power requirements. A number of directly-diode-pumped laser systems based on the gain materials Cr^{3+}:$LiSrAlF_6$ (chromium-doped lithium strontium aluminium fluoride) and Cr^{3+}:$LiSrGaF_6$ (chromium-doped lithium strontium gallium fluoride) pumped with AlGaInP laser diodes are described.

The motivation behind this work was the development of portable, low-noise and lower cost ultrashort pulse lasers for a number of low-power applications such as the characterisation of electron-optical streak camera systems. The investigation into the modelocking of lasers with modest intracavity powers was also an important challenge. The achievement of a battery-powered, compact and efficient laser system represents an excellent outcome for this research programme.

Major consideration is given to the key factors that determine both the cw and modelocking thresholds of an ultrashort-pulse laser. In particular, the reduction of intracavity optical losses by designing the laser to operate with fewer cavity elements, the optimisation of second-order and higher-order dispersion for efficient modelocked operation and the inclusion of a semiconductor saturable absorber mirror for increased stability are discussed. This has enabled pump thresholds to be reduced to a level permitting, for the first time, the use of diffraction-limited, narrow-stripe laser diodes for efficient, low-power optical pumping. A number of laser oscillators with novel cavity designs and progressively lower pump thresholds are described. Pulses as short as 57 fs and average output powers as high as 9 mW for only 80 mW of incident pump power are reported for a battery powered femtosecond Cr:LiSAF laser. This represents an overall electrical-to-optical conversion efficiency of approximately 1% which is excellent for a femtosecond pulse laser system. In addition, the amplitude and phase noise performance is shown to be exceptionally good and is believed to be the best yet reported for this type of ultrashort pulse laser.

The design and demonstration of highly compact, ultrashort-pulse lasers incorporating novel resonator configurations and simplified dispersion compensation schemes are then described. These lasers produced sub-ps pulses at cavity frequencies as high as 450 MHz.

Synopsis

The format of this thesis is as follows.

In chapter 1, an introduction to the field of femtosecond optics is given; specifically the areas of pulse definition, propagation, and characterisation will be briefly outlined and then a summary of various pulse laser systems will be presented. In addition attention is paid to the properties and behaviour of the specific gain media Cr:LiSAF and Cr:LiSGaF chosen for this investigation. The aim of this first chapter is to give an overview of the wider field of ultrafast optics but issues that are important or specific to this work are also singled out and presented in more than casual detail.

In chapter 2, a more focussed approach is taken to some of the theoretical aspects pertaining to designing a short pulse laser with low-pump-power requirements. A discussion on the reduction of the cw and modelocking thresholds, and the stabilisation of pulses at low intracavity powers is presented. Two of the initial low-threshold laser systems are then described, including the pump laser used during their development and that of the laser systems described in the following chapter.

Chapter 3, concentrates solely on resonator designs with three cavity mirrors. These cavities have been shown to enable a more compact and efficient femtosecond laser to be achieved without degrading the modelocking performance over more traditional cavity designs. Two specific three-mirror cavities each with a marked threshold improvement over previous ultrashort pulse systems are detailed and selected results taken from each system are presented. The low-threshold of these systems permitted the use of an alternative highly compact pump scheme incorporating narrow stripe diffraction limited laser diodes[1]. The measurement of the phase and amplitude noise of a femtosecond laser is then discussed. The three-mirror lasers exhibited impressively low noise properties and were used in the characterisation of electron-optical streak camera tubes.

---

[1] G. J. Valentine, J-M. Hopkins, P. Loza-Alvarez, G. T. Kennedy, W. Sibbett, D. Burns and A. Valster, Opt. Lett. 22, 1639 (1997).

In Chapter 4, further improvements of the laser system involving a new resonator configuration and the inclusion of a semiconductor saturable absorber mirror (SESAM)[2] will be detailed. The combination of a novel resonator design and diffraction-limited pump source and intracavity saturable absorber led to the demonstration of an efficient sub-100 fs laser system which could be powered by six AA-type batteries for over 14 hours[3]. Using this laser cavity as a building block, intracavity doubling was carried out to demonstrate the further capabilities of the system. Using a 500 μm crystal of BBO placed between two curved mirrors femtosecond pulses with over 1.5 mW average power at 430 nm were generated.

Chapter 5 describes the development of more compact ultrashort pulse laser systems using standard optical components. By placing one of the dispersion compensating prisms on each side of the gain medium cavity frequencies as high as 400 MHz are achieved. An investigation into the origin of the dispersion contribution due to this prism configuration leads to the conclusion that only one prism is necessary. Subsequently, a more simple and easier to align laser system laser producing ultrashort pulses at cavity frequencies as high as 450 MHz is demonstrated.

In Chapter 6, the main achievements and general conclusions of the work are presented in a short summary. Consideration is then given on the future directions of compact and efficient femtosecond lasers with a view to obtaining higher average output powers.

---

[2] D. Kopf, A. Prasad, G. Zhang, M. Moser and U. Keller, *Opt. Lett.* 22, 621 (1997).

[3] J-M. Hopkins, G. J. Valentine, W. Sibbett, J. Aus der Au, F. Morier-Genoud, U. Keller and A. Valster, Opt. Commun, 154, 54 (1998).

Contents

Chapter 1:
Introduction and Background

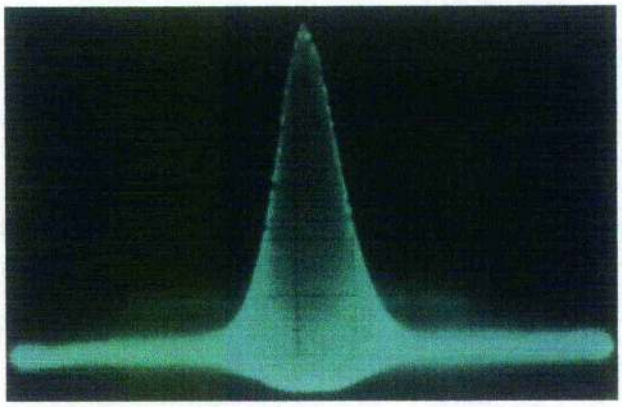

1.1 Dinner plates to Atom bombs

One 10^{15}th of a second, a femtosecond, is a short amount of time, really short, in fact it is so short that gaining a conceptual understanding of this timescale is nontrivial, to say the least. It is often helpful in our understanding of such mind-boggling concepts to somehow scale them into the more familiar universe we know. For instance, there are actually more femtoseconds in one second than there have been years since the beginning of the universe, although that said, we do not really have a fair idea of how long that is either. To try to gain a better understanding of scale we can transform ourselves from the dimension of time into a dimension of length. If we consider a typical ultrashort pulse laser which can routinely produce a hundred million pulses every second each with a duration of the order of 100 fs then each pulse has a length of about 30 μm and will be separated from the next pulse by 3 m. Scaling our 30 μm long pulse to the width of a typical dinner plate would mean that the next pulse would be over 5 km away!

The microscopic dimensions of a femtosecond laser pulse and some of its unique associated qualities have fuelled an increasing research effort into the design and operation of ultrashort-pulse (USP) sources. Many atomic and molecular events, which define the macroscopic universe, occur on timescales of the order of femtoseconds to

picoseconds (10^{-12} s). Using the USP laser as a tool, we have been able to observe some of these fundamental events for the first time. They have allowed us to gain a better understanding of how light interacts with matter and how this may be manipulated in new ways. To stop at this point would be justification enough for the growth in the number of ultrafast laser sources but femtosecond pulses also exhibit other unique and exploitable properties rather than just their physical dimensions. Ultrashort pulses have characteristically large bandwidths (~ THz) associated with them and in many instances can be thought of as a source of broadband 'white light' or continuum radiation. This has been exploited in the generation of terahertz pulses for electro-optic sampling[1], spectroscopy, imaging[2] and remote sensing for environmental monitoring applications. Femtosecond pulses have very short coherence lengths, which can be used for high-resolution medical and biological prompt imaging[3]. Two-photon absorption effects have been utilised in confocal microscopy[4] and florescence imaging[5] to investigate living tissue in three dimensions with increased resolution. Although femtosecond pulse lasers have average output powers similar to that of many cw lasers, the peak powers associated with the individual pulses are very high allowing the precision machining and ablation of a variety of materials[6]. Using these high powers other nonlinear and high intensity phenomena may be studied. In a scheme known as chirped-pulse amplification (CPA)[7], focussed pulse intensities of 10^{20} Wcm^{-2} have been produced resulting in electric fields strong enough to dissociate electrons from their atoms and higher intensities than if the entire solar flux incident on the earth were focussed on the head of a pin. These types of high power systems, both benchtop[8] and larger[9], have been used to generate high XUV and X-ray harmonics[10] from solid[11] and gas targets[12] with the possibility of attosecond (10^{-18} s) pulse durations. The National Ignition Facility[13] in California will be able to irradiate targets with 1.8 MJ pulses to investigate fast ignition in inertial confinement fusion experiments simulating nuclear weapon detonation!

The femtosecond laser in all its guises has proved itself to be an amazing tool but just like all tools (the personal computer for example) we are always looking for improvements over the one we had access to yesterday be it faster, smaller, cheaper or more simple. This thesis and the work presented herein represents the improvement of ultrashort pulse lasers in at least some of these categories.

In the following chapter, some of the fundamentals of ultrashort pulse propagation and generation will be presented and particular attention will be paid to areas more relevant to this work.

1.2 Pulses and pulse propagation

To begin a discussion on the design and optimisation of ultrashort pulse laser systems we must first understand something of the structure and behaviour of light pulses. In the following sections, the form and some of the fundamental propagation properties of such pulses will be introduced.

It is mathematically convenient to represent the temporally dependent electric field associated with an optical pulse with a complex field amplitude

$$E(t) = \mathcal{E}(t)e^{i\phi(t)}e^{i\omega_0 t}$$

Equation 1.1

where ω_0 is the optical carrier frequency, $\mathcal{E}(t)$ is the time varying electric field envelope and $\phi(t)$ represents the phase variation across the pulse. Equation 1.1 contains the slowly varying envelope approximation[14] that the pulse envelope is slowly varying with respect to the carrier frequency ω_0 i.e $\Delta\omega/\omega_0 << 1$. Primarily, the pulse envelopes referred to during the course of this thesis will have a temporal envelope $\mathcal{E}(t)$ characterised by a hyperbolic secant function and may be represented by the general form

$$\mathcal{E}(t) = \mathcal{E}_o \operatorname{sech}\left(t/\tau_S\right)$$

Equation 1.2

where $\mathcal{E}_o$ is the real electric field amplitude and τ_S is related to the FWHM pulse duration $\Delta\tau_p$ by

$$\tau_S = \Delta\tau_p / 1.763$$

Equation 1.3

This pulse shape is also referred to as a sech^2 pulse as the intensity $I(t)$ is of the form

$$I(t) \sim |\mathcal{E}(t)|^2 = \mathcal{E}_o{}^2 \operatorname{sech}^2\left(t/\tau_S\right)$$

Equation 1.4

The temporal and spectral characteristics of a pulse are Fourier transforms of one another, hence the bandwidth $\Delta\nu_p$ and pulse width $\Delta\tau_p$ cannot vary independently. Due to the bandwidth theorem there is a limit to the simultaneous spectral and temporal resolution achievable resulting in a finite duration-bandwidth product

$$\Delta\omega_p\Delta\tau_p = 2\pi\Delta\nu_p\Delta\tau_p \geq 2\pi C_B$$

Equation 1.5

where C_B is a numerical constant of the order of 1 depending on the particular pulse shape, ($C_B \approx 0.315$ for a sech^2 pulses). Pulses that are free from modulation or frequency 'chirp' and for which the above equality holds are said to be 'transform limited' or 'bandwidth limited'. These pulses exhibit the shortest possible durations for their particular spectral extent. The Fourier transform of a sech^2 pulse profile implies a spectral profile of the form

$$I(\omega) \propto \text{sech}^2(\pi\omega\tau_s/2)$$

Equation 1.6

with a transform-limited FWHM bandwidth of

$$\Delta\omega_s = 1.122/\tau_s$$

Equation 1.7

A pulse in the presence of frequency chirp, i.e. non-zero $\phi(t)$, will exhibit a larger spectral bandwidth than that necessary to support its duration and will have a duration-bandwidth product greater than C_B. Figure 1.1 below shows the pulse envelope $I(t) = |\mathcal{E}(t)|^2$ and transform-limited spectral profile or power spectrum $I(\lambda)$ for a 30 fs sech^2 pulse with central wavelength $\lambda_0 = 855$ nm.

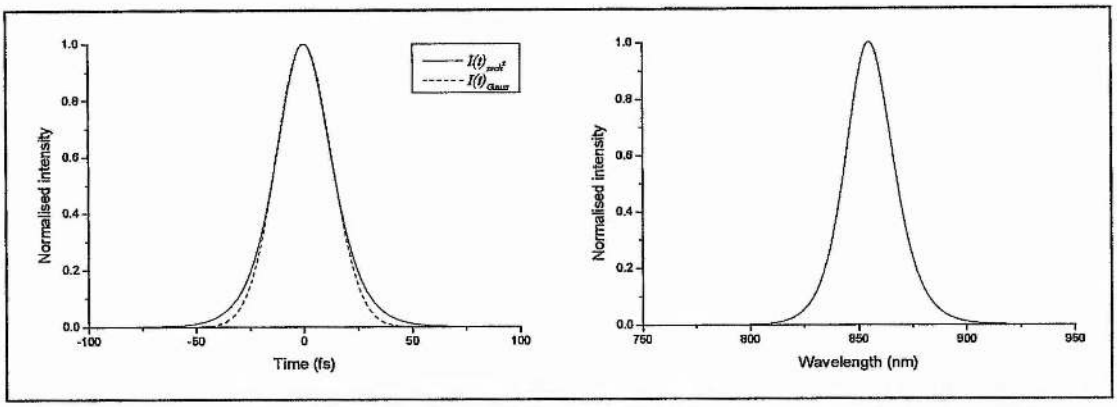

Figure 1.1 Temporal and spectral profile of a 30 fs sech² pulse with a central wavelength of 855 nm (a temporal profile of a Gaussian pulse with identical pulse duration is also shown for comparison).

Table 1-1 summarises the fundamental properties of sech^2 and Gaussian pulse shapes.

Field envelope	Intensity profile	$\Delta\tau_p$ (FWHM)	Spectral profile	$\Delta\omega_p$ (FWHM)	C_B
sech^2	$\text{sech}^2(t/\tau_S)$	$1.763\tau_S$	$\text{sech}^2(\pi\omega\tau_S/2)$	$1.122/\tau_S$	0.315
Gaussian	$e^{-2(t/\tau_G)^2}$	$1.177\,\tau_G$	$e^{-(\omega\tau_G)^2/2}$	$2.355/\tau_G$	0.441

Table 1-1 Summary of the terms and relations associated with the temporal and spectral profiles of sech² and Gaussian pulse shapes where τ_G is related to the FWHM Gaussian pulse duration $\Delta\tau_p$ by $\tau_G = \Delta\tau_p/\sqrt{2\ln 2}$.

Pulse propagation

The ultimate pulse duration achievable from a laser system is determined by the linear and nonlinear responses to the propagating pulse of the reflective and transmissive elements within the cavity.

The application of an electric field to a dielectric medium induces a polarisation response $p(E)$, which we may expand to a power series described by

$$p = p_L + p_{NL} = \varepsilon_0\chi_{(1)}E + \varepsilon_0\left(\chi_{(2)}E^2 + \chi_{(3)}E^3 + \ldots\right)$$

Equation 1.8

where ε_0 is the permitivity of free space, $\chi_{(1)}$ is the linear susceptibility which gives rise to the linear optical effects such as refraction, diffraction and dispersion and $\chi_{(j)}$ is

the jth order dielectric susceptibility representing weaker higher-order nonlinearities in the response of the medium. The $\chi_{(2)}$ intensity dependent term relates to nonlinear processes such as second harmonic, sum/difference-frequency generation and parametric amplification and is zero for typical 'centro-symmetric' laser gain media. The third-order susceptibility $\chi_{(3)}$ is however non-zero in most dielectric materials and results in the nonlinear propagation phenomena.

Pulse propagation in linear dielectric media

Firstly we will look at the consequences of the linear (low intensity) term in the above expansion on a pulse propagating through a length L of a given transparent material. The phase change at a frequency ω on propagation through a medium of length L is described by

$$\phi(\omega) = Lk(\omega) = L\frac{n_0(\omega)\omega}{c}$$

Equation 1.9

where $k(\omega)$ is the frequency-dependent propagation constant[15] for the material and the linear refractive index is related to its first-order susceptibility by

$$n_0(\lambda) = 1 + \frac{1}{2}\mathrm{Re}\left[\chi_{(1)}(\lambda)\right]$$

Equation 1.10

Away from optical resonances the linear refractive index of the material may be described by the empirical Sellmeier equation

$$n_0^{\,2}(\lambda) - 1 = \sum_{i=1}^{k}\frac{A_i\lambda^2}{\lambda^2 - B_i^{\,2}}$$

Equation 1.11

where B_i is the wavelength of the i_{th} optical resonance with strength represented by the constant A_i.

It is the frequency dependence of the first-order susceptibility in Equation 1.10 that gives rise to linear dispersive effects in dielectric media. When considering a pulse with

a finite bandwidth it is convenient to expand $\phi(\omega)$ in a Taylor series about the central frequency of the pulse ω_0

$$\phi(\omega)=\phi_0+\phi'\times[\omega-\omega_0]+\frac{1}{2!}\phi''\times[\omega-\omega_0]^2+\frac{1}{3!}\phi'''\times[\omega-\omega_0]^3+\ldots$$

Equation 1.12

where $\phi_0=\phi(\omega_0)$, ϕ' is the first-order derivative of $\phi(\omega)$ with respect to ω evaluated at $\omega=\omega_0$ and so on. The terms in the expansion determine the behaviour of a pulse propagating in a dispersive dielectric medium and may be interpreted in the following manner. The first term ϕ_0 is a phase delay of the optical carrier and is related to the phase velocity $v_\phi=L(\omega_0/\phi_0)$, the speed at which the central carrier frequency ω_0 propagates through the medium. The second term ϕ' is related to the group velocity $v_g=L(d\omega/d\phi)$ and represents the speed at which the pulse envelope propagates through the medium. The ϕ'' or 'quadratic spectral phase' term is related to the first derivative of the group velocity, which is termed the 'group velocity dispersion' (GVD). While the first two terms do not represent a distortion of the pulse shape, GVD leads to simple pulse broadening, as the spectral components of pulses with significant bandwidth will experience a distribution of group velocities. Although in the strictest sense quadratic phase and GVD are mathematically different and related by

$$GVD=\frac{dv_g}{d\omega}=\frac{\omega^2 v_g{}^2}{2\pi c}\frac{\phi''}{L}$$

Equation 1.13

the term GVD or second-order dispersion has come to refer to ϕ''. The GVD of most materials is positive at visible and near-infrared wavelengths resulting in simple broadening of unchirped or positively chirped pulses. Higher-order GVD such as the 'cubic phase' term ϕ''' (often referred to as third-order dispersion - TOD) and higher-order terms (ϕ'''' etc.) result in more complicated pulse distortions. Table 1-2 details the form and physical significance of the first four terms of the expansion in Equation 1.12.

Term in Taylor expansion	Physical parameter
$\phi_0 \equiv \phi(\omega_0) = \frac{L}{c} n(\omega_0)\omega_0 = Ln(\lambda)\frac{2\pi}{\lambda}$	Phase velocity $v_\phi = L\left(\frac{\omega_0}{\phi_0}\right)$
$\phi' \equiv \left.\frac{d\phi}{d\omega}\right\|_{\omega=\omega_0} = \frac{L}{c}\left(n(\omega_0) + \omega_0 \frac{dn}{d\omega}\right) = \frac{L}{c}\left(n - \lambda\frac{dn}{d\lambda}\right)$	Group velocity $v_g = L\left(\frac{d\omega}{d\phi}\right)$
$\phi'' \equiv \left.\frac{d^2\phi}{d\omega^2}\right\|_{\omega=\omega_0} = \frac{L}{c}\left(2\frac{dn}{d\omega} + \omega_0 \frac{d^2n}{d\omega^2}\right) = \left(\frac{\lambda_0}{2\pi c}\right)\frac{L}{c}\left(\lambda_0{}^2 \frac{d^2n}{d\lambda^2}\right)$	second-order or 'group velocity dispersion' (GVD)
$\phi''' \equiv \left.\frac{d^3\phi}{d\omega^3}\right\|_{\omega=\omega_0} = \frac{L}{c}\left(3\frac{d^2n}{d\omega^2} + \omega_0 \frac{d^3n}{d\omega^3}\right) = -\left(\frac{\lambda_0}{2\pi c}\right)^2 \frac{L}{c}\left(3\lambda_0{}^2 \frac{d^2n}{d\lambda^2} + \lambda_0{}^3 \frac{d^3n}{d\lambda^3}\right)$	third-order dispersion (TOD) $= \frac{dGVD}{d\omega}$

Table 1-2 Form and physical interpretation of the terms in the Taylor expansion of $\phi(\omega)$.

An initially unchirped Gaussian pulse with a FWHM pulsewidth $\Delta\tau_{p0}$ will increase in duration by a factor of $\sqrt{2}$ after a propagation distance L_D given by

$$L_D = \frac{\Delta\tau_{p0}{}^2}{[4\ln 2]k''(\omega_0)}$$

Equation 1.14

where k'' is the second-order derivative of the propagation constant $k(\omega)$ from Equation 1.9 with respect to ω evaluated at $\omega = \omega_0$, $\left.\frac{d^2k(\omega)}{d\omega^2}\right|_{\omega=\omega_0} = \frac{\phi''}{L}$.

Equation 1.14 implies that for a 100 ps pulse travelling through a typical dielectric medium this length will be roughly 10 km while for a pulse of 100 fs this distance becomes ~10 mm which is comparable to the length of the gain medium. A chirped pulse will undergo broadening or compression depending on the initial sign of the chirp and sign of k''.

A Gaussian pulse with linear frequency chirp may be represented by[16]

$$\mathcal{E}(t) = \mathcal{E}_o e^{-(1+ia)\left(t/\tau_G\right)^2}$$

Equation 1.15

where the chirp parameter a is negative for a positive 'up' chirp (a frequency shift from low to high through the pulse) and positive for a 'down' chirp as

$$\frac{d\phi}{dt} = \frac{-2at}{\tau_G{}^2}$$

Equation 1.16

Figure 1.2 below shows the electric field $E(t)$ for a heavily 'up-chirped' 30 fs pulse with $a = -10$ and a central wavelength of 855 nm.

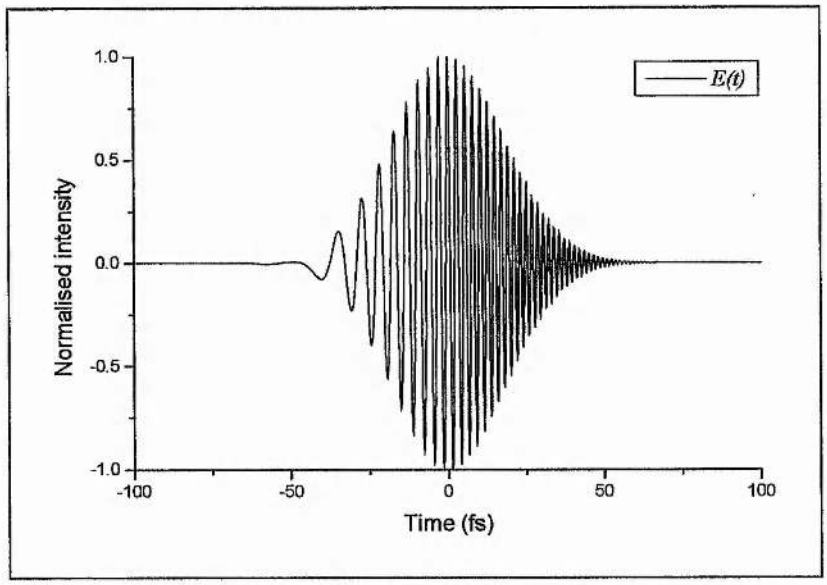

Figure 1.2 Electric field $E(t)$ and power spectrum $I(\lambda)$ for a heavily up chirped 30 fs Gaussian pulse with central wavelength of 850 nm and chirp parameter $a = -10$.

Figure 1.3 below describes the pulse width behaviour of a positively chirped, a negatively chirped and an unchirped pulse on propagation through a length of Cr:LiSAF crystal (k'' positive).

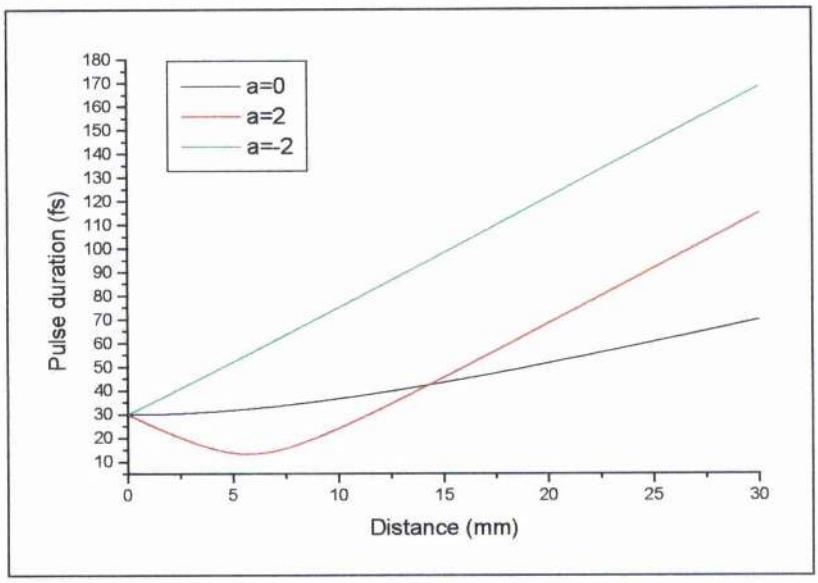

Figure 1.3 Behaviour of a positively chirped (a=2), negatively chirped (a=-2) and an unchirped (a=0) Gaussian pulse with an initial pulse duration $\Delta\tau_p$ of 30 fs on propagation through a crystal of Cr:LiSAF ($k'' = 22.7\ fs^2 mm^{-1}$).

The values of ϕ'' and ϕ''' for some relevant prism and gain materials are given in Table 1-3 on the following page. For most materials ϕ'' and ϕ''' are calculated by differentiating the standard Sellmeier expression for $n(\lambda)$ and using the relations in Table 1-2. In the case of Cr:LiSAF however, the widely used Sellmeier equations[17]

$$n_c(\lambda) = \sqrt{1.98448 + \frac{0.00235}{\lambda^2 - 0.10936} - 0.01057\lambda^2}$$

$$n_a(\lambda) = \sqrt{1.97673 + \frac{0.00309}{\lambda^2 - 0.00935} - 0.00828\lambda^2}$$

Equation 1.17

where $n_c(\lambda)$ and $n_a(\lambda)$ are the refractive indices for light polarised parallel and perpendicular to the crystal c axis respectively, have been found to produce large errors in the quadratic and cubic phase curves[18] (see Figure 1.4). Uemura directly measured the quadratic and cubic phase in Cr:LiSAF with an optical dispersion analyser[19]. The behaviour of ϕ' in Cr:LiSAF in the plane parallel to the c-axis is approximated well by the expression

$$\phi'(\lambda) = \frac{L}{10}\left[c_0 + 86.7495\left(\frac{c}{\lambda}\right) - 632.87\left(\frac{c}{\lambda}\right)^2 + 4785.1\left(\frac{c}{\lambda}\right)^3\right]$$

Equation 1.18

where ϕ' is in fsmm^{-1}, L is the length of the crystal in mm, c_0 is a constant, and λ is in μm. Differentiation of Equation 1.18 yields the correct experimental quadratic and cubic phase curves over the wavelength range 700 nm to 1000 nm[20]. Using these corrected dispersion curves and by carefully considering the higher-order dispersive effects pulses as short as 12 fs have recently been produced from a Cr:LiSAF laser[21]. It is these values that are quoted in the remainder of this thesis.

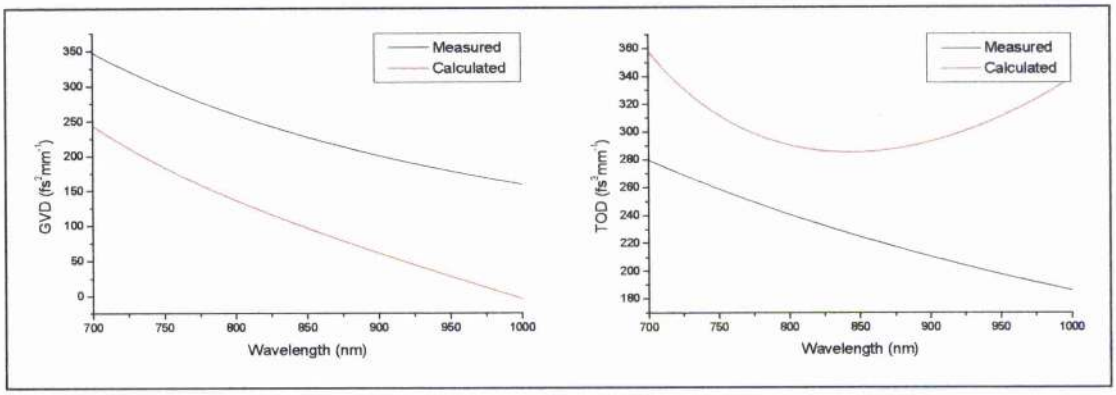

Figure 1.4 Quadratic and cubic phase curves for Cr:LiSAF parallel to the crystal c-axis, directly measured[18] and calculated from equation 1.17.

Material	ϕ'' (fs^{2}mm^{-1})	ϕ''' (fs^{3}mm^{-1})
Cr:LiSAF	9.7	28.6
Ti:sapphire	52.0	44.7
Fused silica	32.2	29.4
BK7	40.0	33.9
LaKL21	53.4	45.2
LAK31	63.4	50.8
F2	95.9	65.3
LaFN10	96.8	70.4
SF10	145.5	98.0
SF14	162.7	110.2

Table 1-3 Calculated material quadratic and cubic phase for various gain media and prism materials calculated at $\lambda_0 = 850$ nm.

Dispersion compensation

In order for the shortest pulses to propagate within a laser cavity it is necessary to include some form of compensation to balance the dispersive effects of the intracavity elements. To this end various geometric optical systems that provide a net negative dispersion have been used to control or compress the pulses produced from laser

systems. These include diffraction gratings[22], Gires-Tournois interferometers (GTIs)[23], systems of prisms[24] and chirped mirrors[25].

Prism Pairs

The standard method for achieving sensitive intracavity dispersion compensation is to use a system of Brewster-angled prisms[24]. The angular dispersion associated with a prism, while much smaller than a grating, is more than adequate for the compensation required in most ultrashort pulse lasers. The insertion losses associated with Brewster prisms are also typically much lower than gratings or GTIs making this system more attractive for a low threshold femtosecond laser systems and for this reason were used exclusively throughout this project. A typical 4-prism sequence used to compensate for quadratic phase is shown below in Figure 1.5. The individual, temporally dispersed, frequency components associated with a chirped incoming pulse may be made to experience sufficiently different optical path lengths to recompress the temporal envelope of the pulse. The prisms allow the quadratic phase to be carefully adjusted by translating more or less prism glass into the path of the beam while the output of the system is undeviated and undispersed with respect to the input.

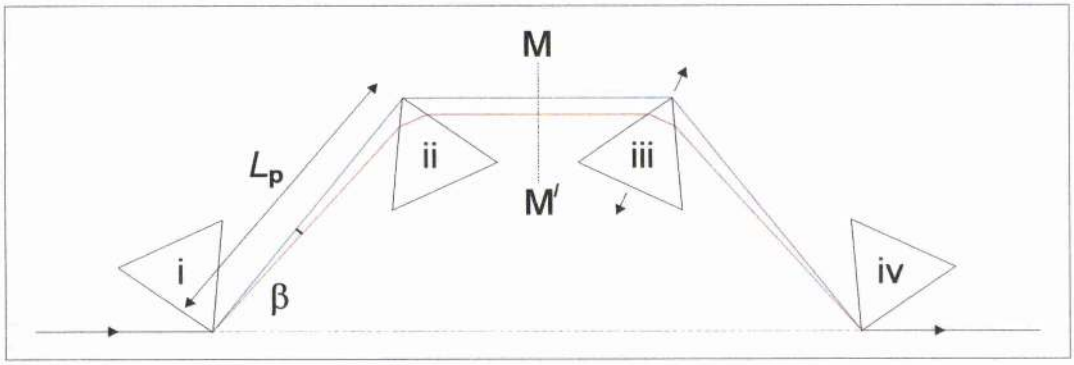

Figure 1.5 Symmetric 4-prism sequence with negative dispersion used to compensate for material dispersion arising from intracavity elements.

The plane MM' in Figure 1.5 indicates a point at which a slit may be placed to permit tuning of the laser or, in a linear cavity, a mirror may be placed producing a spatially dispersed output beam.

Fork *et al*[26] showed that the quadratic phase contribution or GVD of a prism system could be written as

$$\frac{d^2\phi_p}{d\omega^2} = \frac{\lambda_0^{\,3}}{2\pi c^2}\left(\frac{d^2P}{d\lambda^2} + L_m\frac{d^2n_p}{d\lambda^2}\right)$$

Equation 1.19

where L_m is the length of the beam path in the prisms, $d^2n_p/d\lambda^2$ is the material contribution to the dispersion due to this intraprism path and $d^2P/d\lambda^2$ is the geometrical contribution given by

$$\frac{d^2P}{d\lambda^2} = 4\left[\frac{d^2n_p}{d\lambda^2} + \left(2n_p - \frac{1}{n_p^{\,3}}\right)\left(\frac{dn_p}{d\lambda}\right)^2\right]L_p\sin\beta - 8\left(\frac{dn_p}{d\lambda}\right)^2 L_p\cos\beta$$

Equation 1.20

With the correct choice of prism separation and insertion the prism pair may be used to zero the quadratic phase at the desired operating wavelength (see Figure 1.6 and Figure 1.7).

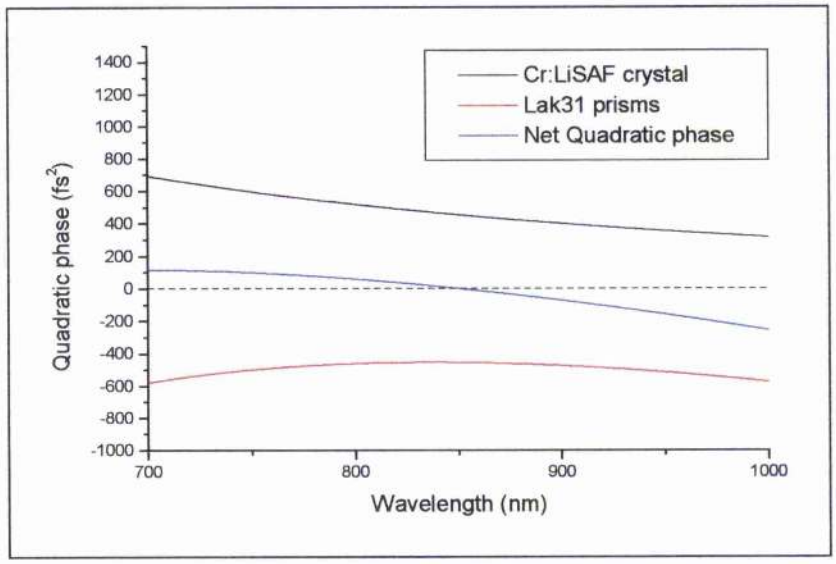

Figure 1.6 The round-trip quadratic phase contributions of a 10 mm Cr:LiSAF crystal (black) and LaK31 prism system with 4 mm total insertion set at a separation for zero quadratic phase at 850 nm (red) and the net round-trip quadratic phase of the combined crystal and prisms (blue).

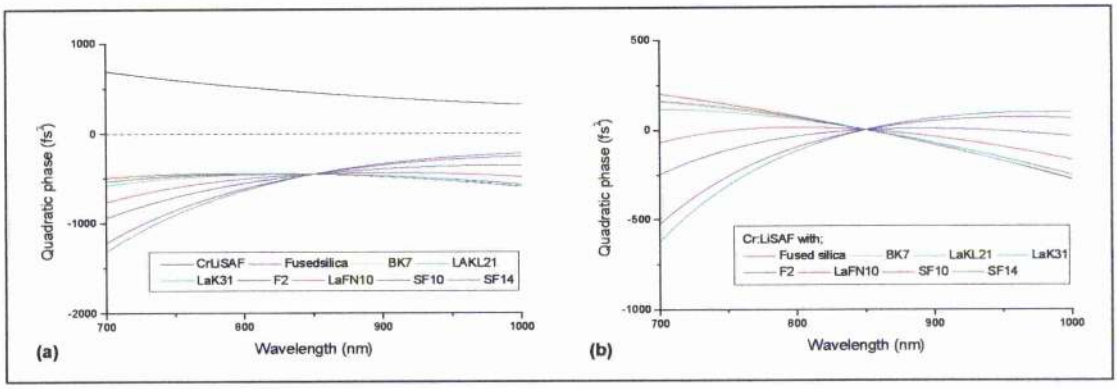

Figure 1.7 (a) The individual contributions of a 10 mm crystal of Cr:LiSAF and various prism pairs again set for zero quadratic phase at 850 nm with 4 mm insertion, (b) the net round-trip quadratic phase in each case.

More recently, advances in semiconductor growth techniques have permitted the fabrication of Bragg mirror structures with near angstrom (Å) precision. These advances have led to mirrors capable of introducing negative dispersion into a laser cavity[25]. These 'chirped' mirrors reflect different wavelengths at different depths in the mirror by increasing the thickness of the Bragg layers deeper into the structure[27]. Chirped mirrors offer more exact control over the intracavity dispersion and 'impedance matched' double chirped mirrors (DCM) have been shown to permit compensation of higher-order cubic phase allowing a smoother compensation across the lasing bandwidth[28]. DCMs have been used in conjunction with a prism pair to produce the shortest pulses from a Ti:sapphire laser with a measured pulse duration of 6.5 fs[29,30]. Provided the insertion losses associated with chirped mirror structures (usually arising from the requirement of multiple reflections) can be reduced, then for reasons highlighted later, they will offer the most simple and compact method of dispersion compensation for low-threshold femtosecond lasers.

Nonlinear pulse propagation in dielectric media

In centro-symmetric crystals where χ_2 is zero the nonlinear polarisation response is dominated by the χ_3 term[31] in Equation 1.8. This term is responsible for non-resonant, nonlinear effects such as the Kerr effect, third harmonic generation, Raman and Brillouin scattering and resonant nonlinear effects where the applied field frequency lies close to a material absorption. The strength of this term depends greatly on the strength

of the applied field and in the case of lasers often only becomes significant for the intensities experienced at the peak of an ultrashort pulse.

The Kerr effect

With a significantly strong DC electrical field $\mathcal{E}(t)$ applied to a transparent dielectric medium the χ_3 nonlinearity will give rise to a refractive index change related to the field by

$$n = n_0 + n_{2E}|\mathcal{E}(t)|^2$$

Equation 1.21

where n_0 is the linear part of the refractive index and n_{2E} is the nonlinear index coefficient, quoted in m^2V^{-2}

$$n_{2E} = \frac{3\chi_3}{8n_0}$$

Equation 1.22

Usually the field strengths required to provide a significant refractive index change are very high (100's $kVcm^{-1}$) but the electric field associated with an intense optical pulse can be sufficiently large for a notable refractive index change. This is referred to as the 'optical Kerr effect' where

$$n = n_0 + n_{2I}I(t)$$

Equation 1.23

where n_{2I} is quoted in m^2W^{-1} in S.I. units and is related to n_{2E} by

$$n_{2I} = \frac{2n_{2E}}{\varepsilon_0 c n_0}$$

Equation 1.24

In most materials where n_{2I} is positive, an increasing intracavity intensity results in an increase in refractive index as

$$I(t) \sim cn|\mathcal{E}(t)|^2$$

Equation 1.25

The optical Kerr effect gives rise to some important temporal, spatial and spectral behaviour in ultrashort pulse lasers that will be discussed briefly in the following sections.

Self phase modulation

Assuming the Kerr effect is instantaneous the refractive index change will follow the incident pulse profile reaching a maximum at the peak or centre of the pulse. For materials with a positive n_{2I} this will correspond to an increase in n. The resulting phase shift due to this refractive index change is given by[32]

$$\Delta\phi(t) = \frac{2\pi L n_{2I} I(t)}{\lambda}$$

Equation 1.26

where $I(t)$ represents the intensity profile of the pulse, and L is the propagation length in the material. During the leading edge of the pulse the material effectively becomes longer delaying the arrival of the optical cycles and hence red shifts the frequency components at the front of the pulse. Conversely the trailing edge of the pulse is blue-shifted by the reduction in the optical path length. Neglecting dispersion in the medium a smoothly varying input pulse will acquire an instantaneous frequency profile in time shown in Figure 1.8 below given by

$$-\left(\frac{d\phi(t)}{dt}\right) = -\frac{2\pi L n_{2I}}{\lambda}\left(\frac{dI(t)}{dt}\right)$$

Equation 1.27

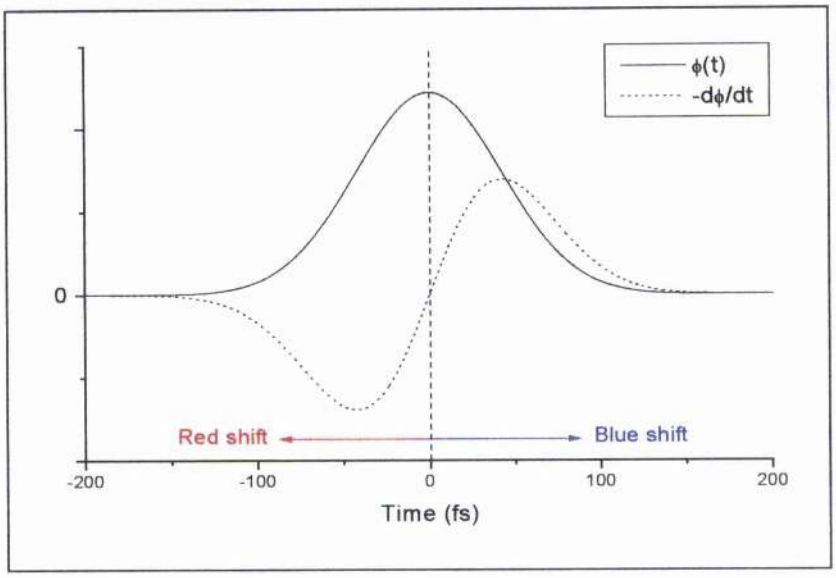

Figure 1.8 The phase (black) and instantaneous frequency (red) shift in a Cr:LiSAF crystal (equal in length to the confocal parameter of the focussed Gaussian beam) for a 100 fs pulse centred at 850 nm.

The result is a spectrally broadened pulse with a linear frequency chirp across the central portion of the temporal envelope. This chirp is positive (low to high) for positive n_{2I} and negative for negative values of n_{2I}. This spectral effect although approximately equivalent to propagation through a dispersive medium occurs independently of pulsewidth and instead results in a broadening of the spectral bandwidth. The spectrum broadens by a factor of $\sqrt{2}$ on propagation through a material length given by[33]

$$L = \frac{\lambda}{2\pi n_{2I} I_0}$$

Equation 1.28

where I_0 is the peak intensity. This is referred to as self-phase-modulation (SPM). To allow the shortest pulses to propagate in a laser system where the pulse peak intensity is sufficient to produce significant phase shifts the SPM must be compensated for. To allow an approximate compensation SPM may be crudely viewed as a dispersive effect, which may be balanced with appropriate quadratic phase, introduced into a cavity. The dispersive contribution from SPM in a laser system may be approximated by differentiating the power spectrum $I(\omega)$.

$$-\frac{d^2\phi(\omega)}{d\omega^2} = -\frac{d^2}{d\omega^2}\left(\frac{Ln_{2I}\omega I(\omega)}{c}\right) = -\frac{Ln_{2I}}{c}\left[2\frac{dI(\omega)}{d\omega} + \omega\frac{d^2I(\omega)}{d\omega^2}\right]$$

Equation 1.29

Evaluating Equation 1.29 at the central frequency ω_0 gives a value for SPM in fs^2 that may be compensated for by appropriate quadratic phase compensation. In crystals with negative material dispersion a balance may be achieved between the SPM and the quadratic phase without the need for additional geometrically dispersive elements.

Solitonic pulse shaping

It is the interplay between the quadratic phase and SPM in an ultrashort pulse laser cavity comprising discrete optical elements that permits soliton-like pulse formation to occur. As in the case of optical fibres the broadening of the spectral bandwidth due to SPM will permit the propagation of shorter and shorter pulses (Equation 1.5). The dispersion may then be used to remove the group delay between different frequency components and recompress the temporal envelope of the pulse. Once the pulse reaches a minimum duration and starts to broaden again, SPM acts to remove the now opposite frequency chirp. If correctly balanced short, unchirped pulses may propagate within a laser over many round-trips that act somewhat like a fundamental soliton[34,35]. This solitonic modelling predicts $sech^2$ pulse-shapes with durations limited by higher-order nonlinear and dispersive effects.

Self-Focusing

The intensity-dependent optical Kerr effect which produces SPM can also result in self-focusing, which is a very important effect in modern ultrashort pulse lasers. The optical field inside a laser resonator will have an approximately Gaussian cross-section with a higher intensity on axis than off axis. In a material with a positive Kerr coefficient the phase fronts in the centre of the beam will experience a larger phase shift and become retarded with respect to those at the edge (see *Figure 1.9*). This results in the formation of an intensity-dependent 'Kerr-lens' within the laser resonator that acts in much the same way as a graded index lens. It is this lensing action which is exploited in the revolutionary self-modelocked lasers described later.

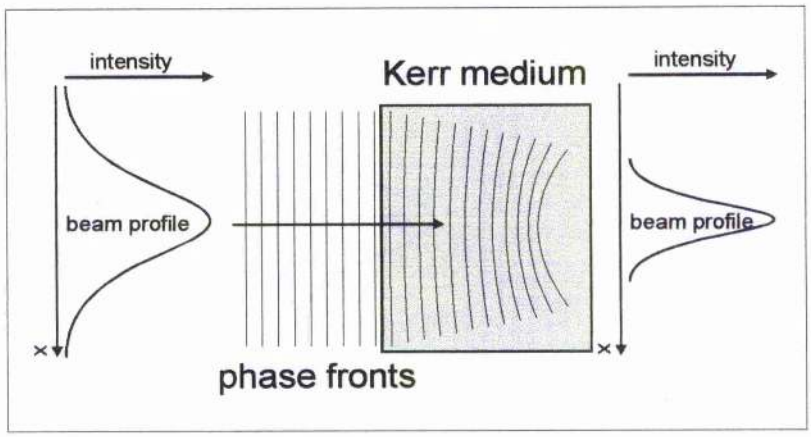

Figure 1.9 *The intensity dependent self-focussing experienced by a Gaussian spatial field distribution in a nonlinear Kerr medium.*

1.3 Pulse characterisation

Before the major methods of producing pulses from laser cavities are examined it is useful to briefly investigate some of the fundamentals of pulse measurement. It is widely understood that in order to measure an event that occurs with a given time duration, a faster event is required, for example, the camera shutter speed to capture a fast moving object or event. So how then do we measure the fastest man-made event – the ultrashort pulse? Using a photodiode and oscilloscope can give us useful information about the pulse train and pulse-to-pulse effects but given that the fastest photodetectors operate at ~ 50 GHz we are still restricted by their response times (10's ps)[36]. The electron-optical streak camera[37,38] which will be described later, provides direct linear measurements of optical pulses at a resolution close to 1 ps (or ~0.5 ps in a single-shot mode[39]). The measurement of an ultrashort pulse with duration significantly shorter than 1 ps is a challenging problem. Until recently the measurement of pulses of the order of ~100 fs duration and below required less direct and more ambiguous measurement techniques.

SHG autocorrelation

One widely used technique and the method used throughout this thesis is that of second harmonic (SHG) autocorrelation[40,41,42]. The SHG autocorrelator uses a copy of the pulse in the measurement process, which cannot by definition be a faster event than the pulse

to be measured. This results in ambiguity and the unfortunate necessity of assuming something about the pulseshape before the measurement is made. Acquiring spectral data alongside an autocorrelation helps to corroborate the assumed pulse shape although only a qualitative assessment of any chirp present in the pulse may be made.

The incoming train of pulses is divided into two trains of equal intensity in a Michelson-type delay line arrangement (see Figure 1.10). The pulse trains are recombined and made to interfere in an SHG (non-zero χ_2) crystal. The nonlinear response of the SHG crystal provides a signal that is proportional to the degree of overlap of the pulses in the interferometer. By varying the delay between arrival of the pulses from each train, a temporal measurement is transformed into a spatial (delay) measurement. Significant distortion of the pulses due to the measurement process may be eliminated[43,44] provided the group velocity mismatch (GVM)[45] in the SHG crystal is minimised by using suitably thin crystal combined with tight focussing for efficient second harmonic generation.

We may define the electric field corresponding to the two overlapping pulses as

$$E(t)+E(t-\tau)$$

Equation 1.30

where τ is the delay of the second pulse with respect to the first and $E(t)=\mathcal{E}(t)\cos(\omega_0 t+\phi(t))$. The recorded second harmonic signal is given by

$$G(\tau)=\int_{-\infty}^{\infty}\left|[E(t)+E(t-\tau)]^2\right|^2 dt=$$

$$\int_{-\infty}^{\infty}\left|[\mathcal{E}(t)\cos(\omega_0 t+\phi(t))+\mathcal{E}(t-\tau)\cos(\omega_0(t-\tau)+\phi(t-\tau))]^2\right|^2 dt$$

Equation 1.31

For the pulse measurements made during the course of this project the SHG autocorrelator shown in Figure 1.10 was used. The SHG crystal was a 200 μm thick KDP crystal cut for Type-I phase matching and the variable delay in one arm of the interferometer was provided by a loudspeaker driven at $10-20$ Hz. The SHG signal, after appropriate filtering was detected with a sensitive photomultiplier (PM) tube and recorded on a storage oscilloscope. Calibration of the autocorrelator could be made by altering the delay in the second arm by means of a translation stage to which the corner cube reflector was mounted. The colinear Type-I phase matching used in the autocorrelator results in a background level as an SHG signal is produced even when

one arm of the interferometer is blocked. Background-free autocorrelation may be achieved using opposite polarisations (Type-II)[41,42] or by non-colinear propagation of the pulses[40].

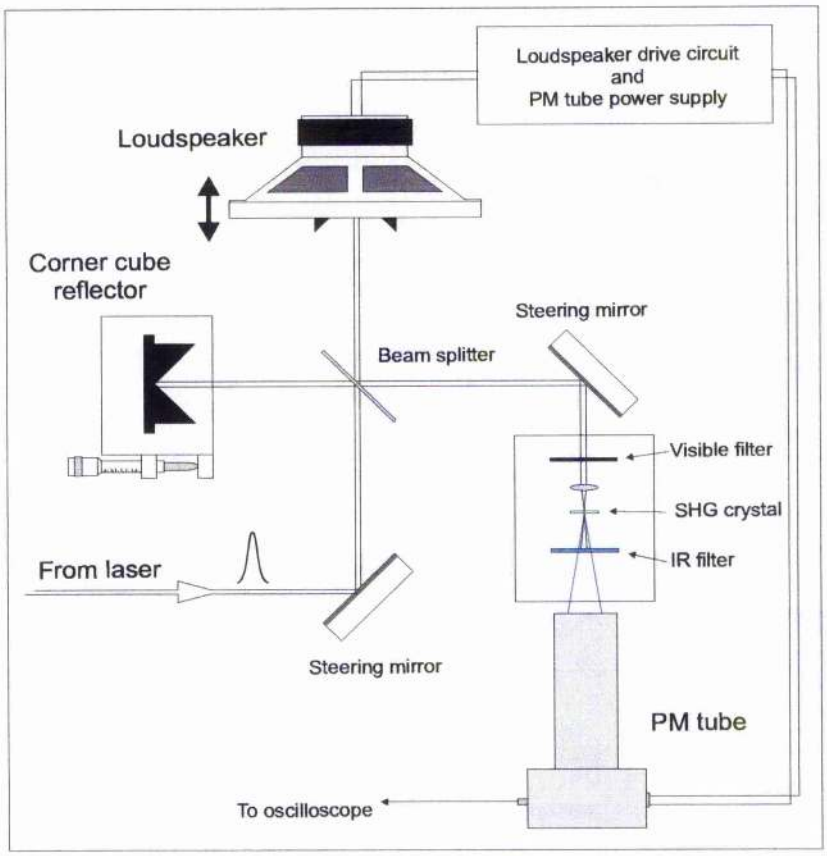

Figure 1.10 Schematic of the SHG autocorrelator used to measure pulse durations

In the case of a slow frequency response of the detection system (oscilloscope and PM tube) the rapidly varying terms in Equation 1.31 may be ignored. The autocorrelator will record the time-averaged intensity autocorrelation described by

$$G_i(\tau) = 1 + 2g(\tau)$$

Equation 1.32

where $g(\tau)$ is the background-free autocorrelation function defined by

$$g(\tau) = \frac{\int_{-\infty}^{\infty} I(t)I(t-\tau)dt}{\int_{-\infty}^{\infty} I^2(t)dt}$$

Equation 1.33

As the above expressions are purely functions of intensity, it follows that the intensity autocorrelation is unaffected by the presence of frequency chirp in the pulse. Care must be taken when measuring an autocorrelation trace as it has been shown[46] that only slight deviation from a perfect contrast ratio (2.92:1) results in a large decrease in the percentage of the intracavity power contained within the pulse.

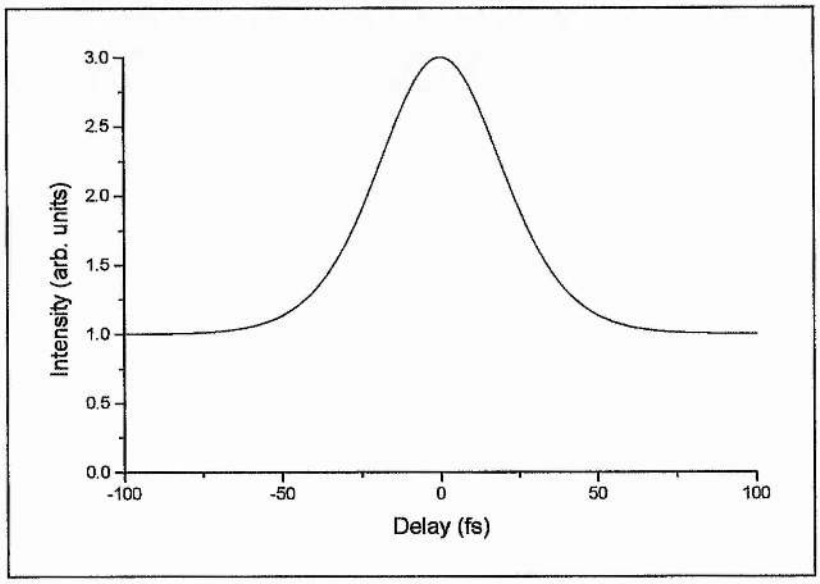

Figure 1.11 Intensity autocorrelation trace of a 30 fs duration pulse at 850 nm

As indicated earlier, a pulse-shape must first be assumed in order to arrive at a pulse duration from an autocorrelation. The relationship between the measured intensity autocorrelation width Δt_i and the FWHM pulse duration $\Delta\tau_p$ is given by

$$\Delta\tau_p = \frac{\Delta t_i}{k_i}$$

Equation 1.34

where k_i is a constant depending on the pulse shape. As the autocorrelation is symmetric about $\tau = 0$ and therefore gives no useful indication of the pulse shape it is necessary to measure the pulse spectral profile and use the duration bandwidth products outlined in

Table 1-4 to make a more informed guess of the pulse temporal profile. It has been shown that if the pulse duration is prone to fluctuation then the autocorrelation will underestimate the pulse width. Provided a correct assumption of the profile and absence of noise can be assured an intensity autocorrelation will give a definitive pulse duration.

A fringe-resolved autocorrelation can be obtained by improving the response time of the measurement system. This was achieved by impedance matching the oscilloscope and the PM tube with a suitable termination resistor. This is known as an interferometric autocorrelation and is described by

$$G_f(\tau)=\frac{\int_{-\infty}^{\infty}\left|\left[\mathcal{E}(t)\cos(\omega_0 t+\phi(t))+\mathcal{E}(t-\tau)\cos(\omega_0(t-\tau)+\phi(t-\tau))\right]^2\right|^2 dt}{2\int_{-\infty}^{\infty}\mathcal{E}^4(t)dt}$$

Equation 1.35

where $G_f(\tau)$ corresponds to $G(\tau)$ normalised to give a unitary background. For unchirped pulses the addition and subtraction of the electric field amplitudes of the pulses correspond to the envelopes that define the upper and lower bounds of the fringes described by

$$G_{fu}(\tau)=\frac{\int_{-\infty}^{\infty}\left|\mathcal{E}(t)+\mathcal{E}(t-\tau)\right|^4 dt}{2\int_{-\infty}^{\infty}\mathcal{E}^4(t)dt} \text{ and } G_{fl}(\tau)=\frac{\int_{-\infty}^{\infty}\left|\mathcal{E}(t)-\mathcal{E}(t-\tau)\right|^4 dt}{2\int_{-\infty}^{\infty}\mathcal{E}^4(t)dt}$$

Equation 1.36

As $G_f(\tau=0)=8$ for an unchirped pulse the contrast ratio of an interferometric pulse is 8:1 compared to the contrast ratio of 3:1 for an intensity autocorrelation. This higher contrast ratio and the fact that the phase information is not averaged out result in a measurement that is more sensitive to pulseshape and chirp as the interference between individual fringes can be resolved. For this reason extreme care must be taken when interpreting an interferometric autocorrelation. Due to the faster response time of the measurement, pulse-to-pulse stability will also have more influence on the trace. Figure 1.12 below shows a fringe resolved interferometric autocorrelation of a 30 fs sech^2 pulse at a wavelength of 850 nm.

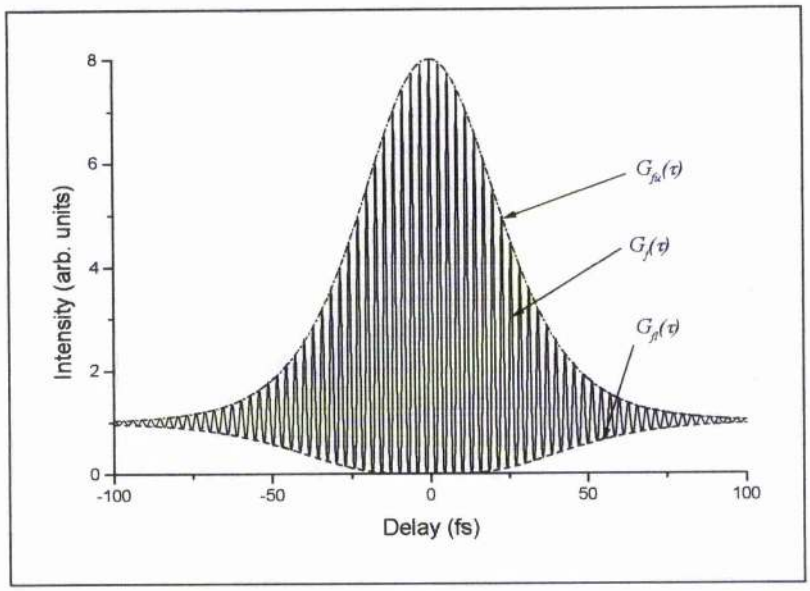

Figure 1.12 SHG interferometric autocorrelation of a 30 fs sech2 pulse at a central wavelength of 850 nm

The duration of the measured interferometric autocorrelation width Δt_f is related to the FWHM pulse duration $\Delta\tau_p$ by

$$\Delta\tau_p = \frac{\Delta t_f}{k_f}$$

Equation 1.37

where k_f depends on the pulse shape and chirp. The interferometric autocorrelation is a more powerful measurement technique but also more prone to error and for this reason, iterative pulse fitting schemes which involve both the intensity and interferometric autocorrelation and pulse spectrum have been developed[47,48,49].

Table 1-4 below summarises the values of k_i and k_f for some more common pulse shapes.

Pulse profile	Duration bandwidth product $\Delta\tau_p\Delta\nu$	k_i	k_f
Gaussian	0.441	$\sqrt{2}$	1.697
$sech^2$	0.315	1.543	1.897

Table 1-4 Intensity and interferometric correction factors for unchirped incident pulses

Other pulse characterisation schemes

More recently novel pulse characterisation schemes have been demonstrated that remove some or all of the ambiguities associated with autocorrelation[50-53]. One of the most seminal of these was work carried out by Trebino *et al.* into frequency resolved optical gating (FROG)[54-65] and derivatives, TREEFROG[66], TADPOLE[67] and POLYWOG[68]. These methods employ intensive but unambiguous computational recovery of amplitude and phase of the ultrashort pulse.

Trebino[54] realised that if a pulse were chirped in the frequency domain then a measurement of the power spectrum of the SHG correlation signal would give added information about the chirp and subsequent pulse shape. By then using mathematical modelling and in an iterative comparison with the measured signal (spectrogram), a single solution entirely describing the pulse shape and phase could be 'retrieved'.

1.4 Ultrashort pulse lasers

Various methods exist to force or persuade a laser into releasing its stored energy in a periodic manner, that is, in a steady stream of pulses. These methods, which will be briefly outlined in the following sections generally, involve some form of cavity modulation that is either externally applied (active) or induced by the laser field itself (passive). Active methods that induce a periodic cw laser field to be produced by effectively switching on and off the laser in some way include Q-switching[69], gain switching[70] and cavity dumping[71].

Modelocking

To produce the shortest pulses (sub picosecond) from a laser it is necessary to ensure that the intracavity field is continuous, taking the form of an oscillating pulse that produces an output pulse at each cavity reflector. The method of creating this specialised intracavity field is called modelocking.

As previously mentioned, for a laser to emit temporally short pulses of the order of femtoseconds, it must support a large oscillating bandwidth, $\Delta\nu$, in the frequency domain (~ THz). The shorter the pulse, the larger the range of frequencies that is

required. The frequency spectrum emitted by a laser system depends on the spectral components permitted to oscillate, the cavity configuration and on the gain bandwidth of the active medium[72,73]. For a particular frequency (or wavelength) to be supported by a laser cavity, the field must interfere constructively with itself after every round-trip. Hence a linear standing-wave cavity will only allow a number of discrete 'longitudinal cavity modes' to oscillate. The frequency separation $\Delta\nu$ of these allowed modes is related to the cavity round-trip optical path length P by

$$\Delta\nu = \frac{c}{P}$$

Equation 1.38

Several of these longitudinal cavity modes will fall under the gain bandwidth of the laser medium and be permitted to oscillate within the cavity. Once oscillating the modes will normally exhibit a random phase relationship resulting in a noise-like output. If however, the modes are forced (or encouraged) to develop a fixed phase relationship with one another i.e. 'locked' together then their amplitudes will add constructively at one point in time to produce a short pulse. This 'modelocking', also called 'phaselocking', is accomplished by introducing some form of modulation into the laser at the cavity frequency. The modulation can either be introduced to the laser actively by an external source, so called 'active modelocking', or introduced passively, 'passive modelocking', This latter method is achieved by utilising the laser's fluctuating intracavity intensity to modulate itself in some way and is know as 'self-amplitude modulation' (SAM)[74-77].

Active modelocking

Active modelocking involves a modulation of the gain or loss of a laser cavity at a frequency equal to the reciprocal of the cavity round-trip time (or a multiple thereof). The resulting mode relationship ensures that they add constructively forming an intracavity pulse, able to pass through the modelocking element when its loss is lowest. Another way of looking at this is as an addition to the cavity of a frequency ν_m equal to the frequency separation of the longitudinal modes $\Delta\nu$. Each mode will therefore acquire modulation sidebands that coincide in frequency with the adjacent modes. These modes, in turn, have sidebands that overlap with their adjacent modes and so on. In this way, power is transferred coherently from the central mode to its neighbours, and

on to their neighbours. This has the effect of fixing the amplitude and phase relationships of the modes, which results in a periodic stream of discrete pulses. Active modelocking is typically achieved by modulating the amplitude or phase[78] of a laser either by incorporating an active loss modulator such as an acousto-optic[79] or electro-optic[80] modulator or by gain modulation[81], synchronous pumping[82] and hybrid modelocking[83]. These latter three methods involve modulating the gain in the cavity to lock the longitudinal modes together.

Passive modelocking

In passive modelocking, a nonlinear intracavity element, which exhibits an intensity dependent loss, is included to allow the circulating radiation to modulate and subsequently modelock itself. This is because the phases of the modes in a laser will self-adjust to produce a field that experiences the least loss as it travels through the cavity. This phenomenon is called the maximum emission principle[84] and ensures, given the correct circumstances that a pulsed laser field will build up from ever-present amplitude noise. The pulse durations obtainable with passive modelocking techniques are typically shorter than those from actively modelocked systems, as the pulse shortening mechanisms are driven by the laser itself. In picosecond passively modelocked lasers SAM is the dominant pulse shaping mechanism but for shorter pulse generation the dispersive processes and soliton like pulse shaping described earlier begin to dominate. In these systems SAM serves only to initiate and/or stabilise the modelocking process.

The femtosecond lasers presented in the following chapters all rely on passive modelocking techniques to produce ultrashort pulses.

Regenerative modelocking and regenerative initiation

In regenerative modelocking, a loss modulator, commonly an acousto-optic (AO) modulator, is employed to provide mode coupling in the laser. Regeneratively modelocked lasers therefore have more in common with actively modelocked lasers than with other forms of passive modelocking. When using an AO modulator in a purely actively modelocked cavity, a sinusoidal current is applied to the transducer producing a standing wave within the modulator that depends on the driving signal.

This standing wave alters the refractive index of the quartz and produces an intermittent optical diffraction grating, acting as a periodic loss within the cavity. If the modulating frequency matches the cavity round-trip frequency then after a number of round-trips an intracavity pulse will form.

The major difference of a laser operating in a regeneratively modelocking regime over an actively modelocked laser is that the driving RF signal for the modulator is derived directly from longitudinal mode beating in the cavity output. In this way the system may track any small changes in the cavity dimensions which result in a shift of frequency mode spacing and re-apply the corresponding amplified signal back into the laser[85]. The ability to track minute cavity length changes permits pulse durations of the order of 50-100ps to be produced using this method.

Although this method of modelocking cannot produce ultrashort pulses directly it may be used in conjunction with other modelocking methods to either provide an initiation mechanism or an added degree of stabilisation. This is especially useful for the nonlinear passive modelocking methods employed in cavities with moderate intracavity powers described in chapters 2 and 3. The specific details of the particular regenerative schemes used will be described later.

Slow saturable absorbers

The use of saturable absorption to produce pulses in a laser cavity is a field almost as old as the laser itself[86,87,88]. A saturable absorber adds a selective passive loss into a laser that suppresses low intensity cw laser operation while a more intense intracavity field saturates or 'bleaches' the absorber experiencing less loss. If the recovery time of the absorber is long compared to the pulse-duration, the front of the pulse will be attenuated but the pulse tail will be allowed to pass freely through. This effect is called 'slow saturable absorption'. Early solid-state lasers modelocked with saturable absorbers tended to produce Q-switched modelocking as the upper state lifetime of the gain medium was long compared to the recovery time of the absorber.

The first CW ultrashort (fs) pulse lasers in the mid 1970's, used organic dye solutions as gain media and slow saturable absorbers (SSAs). The slow saturable absorption was used in conjunction with the pulses ability to deplete the gain in the dye 'jet' attenuating the tail of the pulse which resulted in a short net gain window and a pulse shortening mechanism[89,90] (see Figure 1.13). These dye-lasers emitted ~300fs pulses with average

output powers ~10mW[91,92]. In the 1980's, pulse durations were improved below 100 fs using a technique dubbed 'colliding pulse modelocking' (CPM)[93] and in 1988 pulses were shortened to less than 20 fs by the inclusion of intracavity dispersion compensation in the form of a sequence of prisms[94-96].

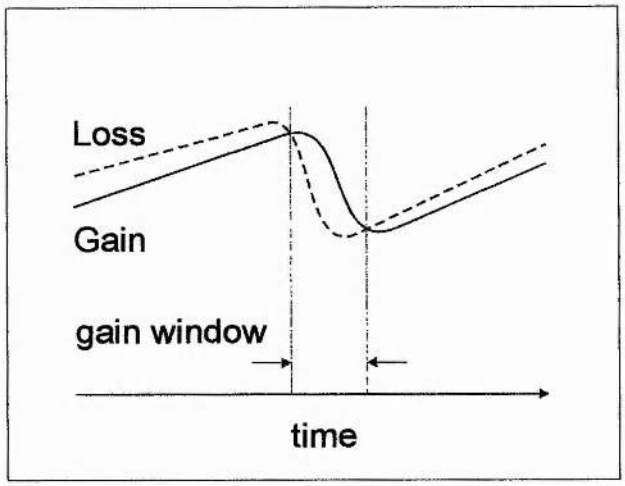

Figure 1.13 Schematic of the saturable absorption and dynamic gain saturation which give rise to a short net gain window in a CPM dye laser

These lasers were used extensively in the study of ultrafast phenomena during the 1980's[97]. However, due to their low energy storage densities (~1mJ/cm-1), necessary for gain depletion and pulse shortening, these lasers were limited in tunability and output power. In addition dye-lasers used hazardous chemicals and were fairly complex to operate, requiring constant attention.

Fast saturable absorbers and synthetic fast saturable absorbers

For solid-state materials with characteristically smaller gain cross-sections σ_g and therefore little or no dynamic gain saturation, it is necessary for the saturable absorber alone to produce the short net gain window. This results in the need for an absorber with a fast recovery time[98,99] (see Figure 1.14).

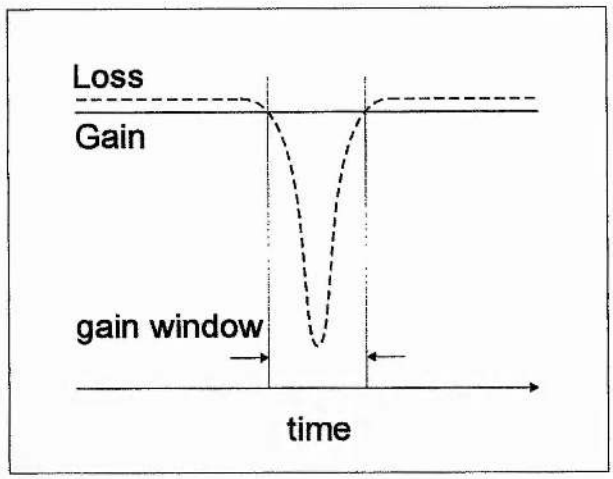

Figure 1.14 Schematic of fast saturable absorption which give rise to a short gain window in a laser system.

With the advent of new broadband solid-state gain media[100] such as Ti:sapphire ($Ti:Al_2O_3$)[101] modelocking schemes based on reactive non-resonant nonlinear effects were increasingly used to produce short pulses from modelocked lasers. Utilising an almost instantaneous nonlinear effect to induce amplitude modulation resulted in a synthetic fast saturable absorber action and very short pulses. The following sections detail some of the most common methods used.

Coupled-cavity modelocking

The first successful cavity configuration to produce synthetic fast saturable absorber modelocking relied on SPM to shift the phase of a noise feature or 'spike' from the cw background. By placing a nonlinear element in a second interferometrically coupled cavity, the intensity of the noise feature in the first cavity could be magnified by constructively interfering the centre of the feature while destructively interfering any wings. This results after a number of round-trips in a modelocked pulse train. This coupled-cavity modelocking (CCM) or additive-pulse modelocking (APM)[102] was demonstrated for the first time in 1984 in a synchronously modelocked $KCl:Tl^{(0)}$ colour-centre laser[103] producing pulses as short as 60 fs[104]. Using this type of modelocking the wavelength regions directly accessible to ultrashort pulse lasers were extended into the IR (~ 1.5 μm). CCM/APM systems offered numerous advantages over the CPM dye laser including higher powers, greater stability and wider tunability. The drawback of these CCM lasers was the requirement of precise alignment of the two cavity lengths, which often required active stabilisation.

Self-modelocking – "the first ultrashort pulse revolution"

It was during an optimisation experiment on a CCM Ti:sapphire laser that the field of ultrashort pulse lasers was revolutionised. Spence *et al* [105,106] observed short (~ 2 ps) pulses with excess bandwidth from the laser while the coupled-cavity with nonlinear fibre was blocked. With appropriate dispersion compensation included in the cavity this pulse duration was shortened to the bandwidth limit of 60 fs, the laser was producing ultrashort pulses without a visible modelocking element! Initially the nonlinear mechanism in the Ti:sapphire crystal behind this aptly dubbed 'self-modelocking' (SML) behaviour was unclear. It was soon realised however, that the optical Kerr effect, specifically self-focussing, was the major contributor of the SAM that initialised and sustained modelocking[107,108]. A spatial modulation of the transverse beam profile within the cavity due to the induced Kerr lens in the gain medium could be made to favour the higher intensity pulses over the cw background. Research effort across the world was focussed on this new modelocking mechanism which could produce output powers from a Ti:sapphire laser equivalent to the intracavity powers of many of the CPM dye lasers. As a result large commercial laser manufacturers quickly adopted the attractive simplicity of this modelocking phenomenon[109,110,111]. Although this modelocking process has come to be known as Kerr Lens Modelocking (KLM)[112] due to the influential nonlinear process in the gain medium, the term self-modelocking better incorporates the self-focussing, self-amplitude modulation and the self-phase modulation all necessary to generate the shortest pulses. Two main types of self-modelocking have been identified[113], hard-aperture[114,115] and soft-aperture[113]. A third process called gain guiding[116] has also been identified as being influential in both of these processes.

Hard-aperture self-modelocking occurs when a physical aperture is placed within a laser cavity at a point where an increase in laser intensity inside the gain medium will cause a reduction in the cavity mode size (in one or both transverse planes)[117,118]. The loss inside the laser will therefore reduce preferring the higher intensities associated with an intracavity pulse (see Figure 1.16). A number of useful models have been suggested by Magni and co-workers for the design of practical hard-aperture systems[119-123] and these will be described in more detail in chapter 2. Figure 1.15 below shows a typical Ti:sapphire laser cavity designed for hard-aperture self-modelocking[124]. The two curved 'folding' mirrors, M2 and M3, focus the cavity mode tightly inside the gain medium to

ensure as high an intensity as possible for the most efficient Kerr lens.

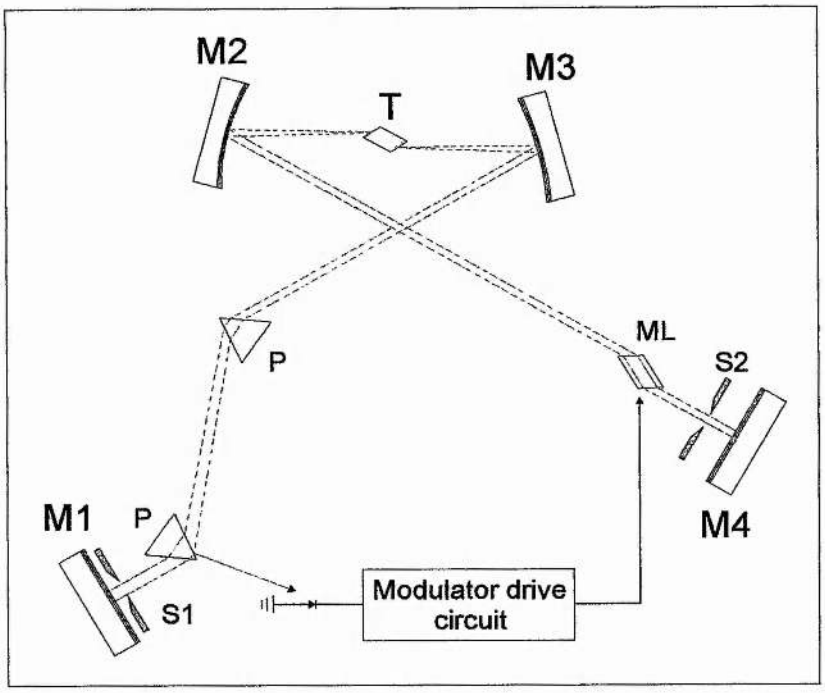

Figure 1.15 *A dispersion compensated, regeneratively initiated self-modelocked Ti:sapphire laser. T – Brewster-angled Ti:sapphire crystal, P - intracavity dispersion compensating prisms, ML - modelocker (quartz acousto-optic modulator), S1 - tuning slit, S2 - hard-aperture self-modelocking slit.*

Soft-aperture, self-modelocking allows pulsed operation to be achieved without a physical aperture in the cavity[125]. This modelocking method uses the pumped volume of the gain medium as a virtual aperture and relies on the self-focussing in the gain medium to improve the extraction of gain in the inverted region by the laser field. This results a power dependent gain, which again favours a pulsed mode of operation over CW lasing. The pump mode volume in the gain medium may be viewed as a virtual or 'soft' aperture and the ability of a particular laser system to work in a soft-aperture regime implies a good (near-diffraction-limited) quality of pump laser beam. Soft aperture self-modelocking is employed in the low-threshold laser systems presented later in chapters 2 and 3.

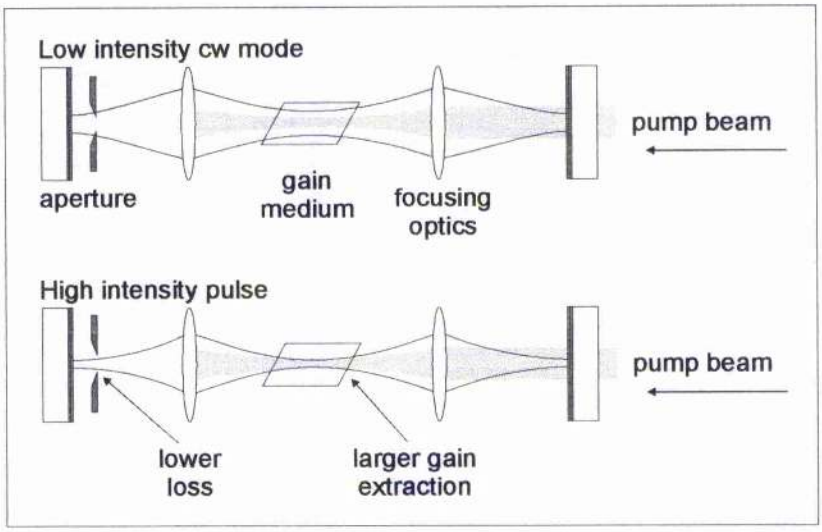

Figure 1.16 Graphical representation of the mechanisms of both hard and soft-aperture self-modelocking in an ultrashort pulse laser cavity.

Gain guiding[116] is more complicated and is present in both hard and soft-aperture modelocked lasers. The spatial gain profile created by the pump beam may be thought of as a Gaussian aperture that does not produce loss but causes a transverse redistribution of the radiation in the cavity mode. This mode redistribution alters the spatial and stability properties of the resonator and hence can favour one temporal mode over another.

Although purely self-starting, self-modelocking is possible[122] more commonly some form of mechanism is employed to provide enough perturbation or noise (typically with picosecond structure) to invoke femtosecond pulse build up, even if it is just the tapping of an end mirror[106]. A variety of methods have been used to initialise self-modelocking including the use of resonant effects such as saturable absorption[114,126-128], mode beating[105,129], regenerative modelocking (described earlier)[85] and even synchronous pumping[130] although this can interfere with the self-modelocking once initiated. Self-modelocking has been demonstrated in a wide variety of other materials and cavities some of which include: Cr^{3+}:colquiriites[131,132,133,134], Nd:YAG[135], Nd:YLF[136,137], Nd:glass[138], Cr^{4+}forsterite[139,140], Cr^{4+}:YAG[141], NaCl:OH^-[130], and a Rh6G dye laser[142].

The relative ease of use of self-modelocked lasers over earlier femtosecond sources has prompted an impressive growth in the research of ultrafast phenomena. The wavelength range now available to researchers has been widely extended using harmonic[143] and parametric[144] generation. Using Ti:sapphire lasers as a source, wavelengths shorter than 200 nm[145] and longer than 5 μm[146] have been reported. Careful consideration of higher-order dispersion[147] and improvement in Ti:sapphire crystal growth technology has

permitted the routine generation of sub-20 fs pulses from self-modelocked lasers[148,149] with peak powers measured in megawatts[150]. Self-modelocking is presently responsible for the shortest pulse duration of 6.5 fs directly from a laser[151]. The limitation to the achieved pulse duration is still thought to be dispersion[152,153] as the gain bandwidth of Ti:sapphire can theoretically support pulses as short as 3 fs! Work in this field is also being directed towards using these short pulses to generate wavelengths at which the pulse duration corresponds to a single optical cycle, or less![154]

Other synthetic fast saturable absorbing schemes

A number of alternative methods of achieving fast saturable absorber action have also been demonstrated. Ti:sapphire lasers have been successfully modelocked by taking advantage of Kerr induced polarisation rotation to provide saturable loss[155,156]. Stankov *et al*[157] used a second harmonic generation (SHG) crystal in a Nd:YAG laser to provide intensity selectivity. By placing the crystal in front of a dichroic mirror (low reflectivity at the fundamental at 1064 nm and high reflectivity at the second harmonic) and ensuring correct phase matching between the reflected fundamental and the harmonic signal for efficient back conversion via three-wave mixing, ~10 ps pulses were observed. This impressive technique has since been demonstrated in a Nd:YLF system[158]. In a similar arrangement where the dichroic mirror was replaced with one highly reflecting at both wavelengths and a slit mask placed between the crystal and this mirror short pulse operation has also be achieved[158,159].

These latter two methods are very useful for decoupling the gain and modelocking mechanism or for laser systems with low peak intensities.

Soliton Modelocking

The models suggested to describe the soliton like pulse shaping in CPM dye lasers[160,161,162] and synthetic fast saturable absorber modelocked systems[98,99] specifically self-modelocked Ti:sapphire lasers[163,164,165] do not incorporate a shortening mechanism. A stable solution of these models always requires the presence of a gain window whose duration is of the order of the pulse duration. Keller and colleagues[166,167,168] have suggested a third type of passive modelocking based solely on soliton formation and propagation with compensated dispersion and SPM. In this model they call 'soliton

modelocking', based on soliton perturbation theory[162], such short gain windows are not necessary and the soliton formation itself is thought to be the dominant pulse shortening mechanism. This permits the saturable absorber to have a recovery time significantly longer than the final pulse duration (see Figure 1.17).

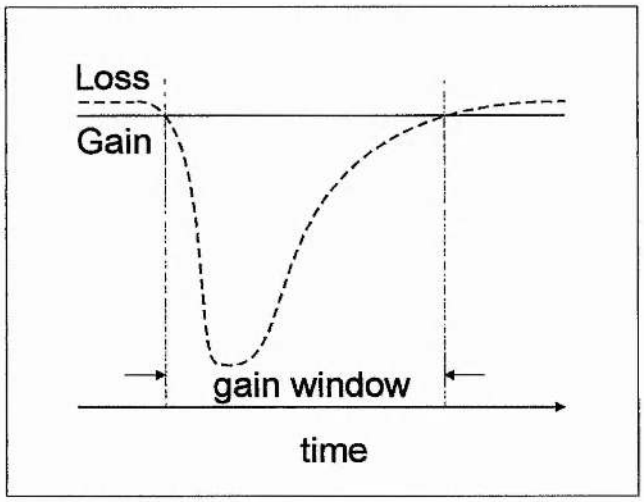

Figure 1.17 Schematic of slow saturable absorption in a laser incorporating a gain medium with a long upper state lifetime giving rise to a longer gain window.

In the soliton modelocking model[166-168] the presence of a saturable absorber in the cavity (treated as a perturbation term) acts only to initialise the formation of a soliton from background noise bursts and to stabilise the soliton once formed. As a confirmation of this new modelocking theory Keller and co-workers claim that pulses as short as 300 fs in cavities where self-focussing was deemed not to be assisting the modelocking and the loss modulation was provided by an AO modulator[169,170]. The modulator provided a gain window of up to ten times the pulse duration. Soliton modelocking has been demonstrated in a number of systems incorporating semiconductor saturable absorber structures[166,168] that will be discussed in the following sections.

Semiconductor saturable absorbers

An interesting and innovative branch of ultrafast laser physics that has grow up alongside that of self-modelocking is the field of semiconductor saturable absorbers and related structures.

Saturable absorbers based on semiconductor materials were first used in 1974 with CO_2 lasers[171] followed by the modelocking of semiconductor lasers in the early 80's[172,173]. The recovery times of these absorbers could be engineered to an extent by introducing damage processes during fabrication. The reliability of the saturable absorbers was improved by the ability to use nonlinear excitonic absorption in multiple quantum well (MQW) structures[174,175]. The first non-diode solid-state lasers to benefit from semiconductor saturable absorbers were passively modelocked colour-centre lasers[176]. Although, as in the case of the diode lasers, the final pulse duration was determined jointly by the absorber and dynamic gain saturation.

The increasing push of the electronics and optoelectronics industry lead to remarkable improvements in semiconductor fabrication technology. The arrival of techniques such as molecular beam epitaxy (MBE) and metal-organic chemical vapour deposition (MOCVD) allowed the production of saturable absorbers with greater sophistication which could be exactly tailored for specific laser systems by precisely controlling the growth process. One of the most notable advances was the ability to incorporate the saturable absorber directly into a high quality mirror structure thereby providing a compact saturable loss mechanism that could be easily incorporated into a laser cavity. These semiconductor saturable absorber structures (SESAMs)[177,178,179] were initially used with long upper state lifetime materials such as Ti:sapphire[180] and Nd:YLF[181] in a coupled-cavity configuration called resonant passive modelocking (RPM) to produce picosecond pulses. Femtosecond pulses were achieved when RPM was used as a starting mechanism for self-modelocking[182,183]. RPM however was quickly superseded by advances in fabrication that allowed intracavity incorporation of the SESAMs and the production of stable, Q switch free cw modelocking from Nd:YAG and Nd:YLF lasers[184].

The ability of the semiconductor saturable absorbers to initialise self-modelocking addressed some of its remaining disadvantages. Although self-modelocking solved many of the problems of ultrashort pulse propagation and revolutionised laser cavities in terms of simplicity and availability, "real world" laser requirements are tougher still. As will be discussed in chapter 2, often a self-modelocked cavity requires precise alignment to provide pure self-starting operation and self starting of a laser with pulse durations less than 50 fs has not been demonstrated due to the very large distinction between cw and modelocked operating conditions. SESAMs offer a robust and cheap method of self-starting and hence improving the performance of such systems. It is the

marriage of SESAM initiation and self-modelocking that has produced the shortest ever modelocked pulses from a Ti:sapphire laser with a measured duration of 6.5 fs[151]. SESAMs have also helped to develop 'turn-key', more 'hands off' laser systems in the picosecond regime using purely passive saturable absorber modelocking and in the femtosecond regime by initialising and sustaining soliton modelocking and also the initiation of self-modelocking. A summary of SESAM structures and laser systems will be given in chapter 4 where a laser system based on Cr:LiSAF will be presented for which the inclusion of a SESAM dramatically improved both the operation and noise properties.

1.5 All-solid-state ultrashort pulse lasers

The transition in recent years from hazardous dyes, large discharge tubes and cryogenically cooled systems back to room temperature solid-state and all-solid-state operation can almost be described as the second revolution of ultrashort pulse laser systems. This renaissance has been made possible firstly by the development of solid-state gain media with broad emission spectra covering wavelengths from the visible well into the near-IR (~3 μm) and by the development of high power, long lifetime semiconductor diode pump lasers. The demonstration of efficient and more compact 'all-solid-state' ultrashort pulse lasers has increased the potential market and applications of this type of laser.

One of the most recent and major breakthroughs in this particular field has been the emergence of all-solid-state pump sources for the ultrafast material Ti:sapphire. Until recently the advantages and simplicity of a self-modelocked Ti:sapphire laser were overshadowed somewhat by the necessary mainframe argon ion (Ar^+) laser to produce cw pump powers (~10-15 W) in the blue-green (420-580 nm) region of the visible spectrum. These bulky lasers use large, highly inefficient, water-cooled, gas discharge tubes producing ~20 W of light for about 50-60 kW of electrical power (the amount consumed by roughly 100 average households). With high annual running/maintenance costs and large initial outlay Ar^+ lasers represent quite an unattractive pump source for many potential users. Due to a massive academic and commercial research drive[185-194], efficient diode pumped solid-state laser (DPSSL) pump sources for Ti:sapphire and other broadband solid-state gain media[195] have emerged that outclass the previous pump sources on almost every front. Air-cooled DPSSL and frequency doubled DPSSL giving

over 10 W output at 1064 and 532 nm for pumping Cr^{4+}:YAG and Ti:sapphire respectively are now commercially available[196]. These lasers occupy a footprint less than a tenth of that for large frame pump sources and can be run from a wall-plug supply incurring much lower running costs. DPSSL are generally quieter[197] (<0.05% rms. noise to 2MHz) with greatly improved beam quality and beam pointing stability.

Directly diode pumped femtosecond lasers

Although these DPSSL systems are a giant leap forward towards more compact and efficient pump sources, the ultimate in potential simplicity, efficiency and compactness is offered by the ability to directly pump an ultrashort pulse laser with the output from a semiconductor diode laser. Excluding fibre lasers this has been achieved in broadband neodymium[198] and ytterbium[199] doped glass and in the chromium (Cr^{3+}) doped host materials $LiSrAlF_6$ (Cr:LiSAF)[200] and $LiSrGaF_6$ (Cr:LiSGaF)[201] which are based around the colquiriite[202] structure of Cr^{3+} doped lithium calcium aluminium fluoride, Cr^{3+}:$LiCaAlF_6$ (Cr:LiCAF)[203]. CW operation of a directly diode pumped Cr^{4+}:YAG laser has also recently been demonstrated[204]. Ti:sapphire is unsuited to direct pumping with diode lasers because its absorption region is centred in the blue/green area of the visible spectrum where, as yet, the operation of diode lasers with any sort of feasible reliability and output power have not yet been reported. Ti:sapphire is also unsuitable because its emission-cross-section (σ) upper-state-lifetime (τ) product is relatively small, resulting in higher CW thresholds and making the direct diode pumping of Ti:sapphire in the near future highly improbable.

As will be shown in the remainder of this chapter and thesis the Cr^{3+} doped colquiriite vibronic gain media are ideal materials for the production of a directly diode pumped alternative to Ti:sapphire[205]. They are also well suited as the basis for a study of low-threshold femtosecond lasers with modest pump power requirements for a number of specific short pulse applications.

The Cr^{3+} doped vibronic gain media

In a transition metal vibronic laser gain media[206], the relative positions and broadening of the electronic energy levels of the active dopant ion are determined by their

interactions with the crystal lattice vibration. Depending on the strength of the crystal field at the ion site, in particular host materials these interactions can produce large gain bandwidths and long upper state lifetimes. The lasing action and precise relationship between the energy levels of the chromium ions varies from host to host but is of a similar general form for broadband laser gain media.

For broadband vibronic gain media containing Cr^{3+} ions there are two principal pump absorptions corresponding to the $^4A_2 \rightarrow {}^4T_1$ and $^4A_2 \rightarrow {}^4T_2$ energy level transitions. Due to a displacement of the $^4T_2$ energy level with respect to the $^4A_2$ ground state electrons are excited into high vibrational energy states of the $^4T_1$ and $^4T_2$ levels. These electrons will rapidly relax through non-radiative phonon processes into the lowest energy states of the $^4T_2$ upper laser level. The electrons then drop back to an excited lattice state of the $^4A_2$ ground state emitting photons. This excited lattice rapidly relaxes by phonon emission to return the system to its overall electronic and vibrational ground state. Due to the fact that the energy gap between the two laser transition levels varies across the vibrational distributions a comparatively large distribution of photon energies is produced representing a vibrationally broadened 4-level laser system.

Although the first laser gain media was comprised of Cr^{3+} in a sapphire host (ruby) this was a narrow linewidth gain medium with minimal tunability[207]. The principal difference between ruby and broadband vibronic gain media doped with Cr^{3+} is the size of the crystal field at the laser ion sites. The high lattice field strength present in ruby results in the $^4T_2$ level lying above the ^2E level which becomes the upper laser level. This level originates from a spin-orbit interaction among the Cr^{3+} ions electrons and is centred on the same vibrational potential as the ground state. During lasing electrons excited from the $^4A_2$ ground state to the $^4T_2$ level quickly decay down to the ^2E level and lasing occurs on the $^2E \rightarrow {}^4A_2$ transition. The wavelength of the emitted light is constant regardless of the vibrational state of the host lattice and the transition is essentially independent of the sapphire host[208].

The lasing of Cr^{3+} transition metal ions has been demonstrated in over 20 vibronic oxide and fluoride host materials including the aforementioned colquiriites. The reason for the successful broadband lasing of Cr^{3+} in so many crystal hosts compared with many other transition metal ions can be attributed to[209] 1) its broad absorption and emission bands, 2) its resistance to both oxidation and reduction due to the trivalency of its oxidation state, 3) The flexibility of the available host materials in acceptance[210], structure and growth, 4) the resistance of the $^4T_2$ level to non radiative decay and 5) the ability for the

Cr^{3+} ions to exclusively occupy octahedral sites in a host giving rise to long upper state lifetimes[211].

In some specific host materials, Cr^{3+} ions provide a crystal structure with increased suitability for laser gain materials. They have been shown to provide virtually colour-centre free materials with unpopulated high lying terminal laser levels implying a low threshold. They exhibit resistance to ESA, and other non-radiative decay processes (at least at room temperature) and are virtually free from ground state and other anomalous absorption within the lasing band as they have minimal emission and absorption band overlap (sometimes a problem in Ti:sapphire). Also, in some host materials it is possible to easily achieve very high doping levels of Cr^{3+} approaching the stoichiometric limit (100%) without degrading the optical quality of the crystal. This is highly advantageous for close coupled diode laser pumping as large absorptions can be achieved in a short crystal length increasing coupling efficiency for non-diffraction-limited beams while minimising scattering losses aiding a low threshold. The Cr^{3+} hosts, can however, often suffer from poor fracture toughness, which results in an increased likelihood of mechanical failure at higher pump powers, but are suited to the relatively lower powers available from diode lasers.

The most promising host material for Cr^{3+} to date seems to be $Be_3Al_2(SiO_3)_6$ (Emerald)[212,213,214] because its fluorescence efficiency remains high at high temperatures it has a high fracture toughness and it has a large pump conversion (slope) efficiency > 60 %. Unfortunately, laser grade emerald has proved exceedingly difficult to grow. The next two promising materials are Cr:LiCAF and $BeAl_2O_4$ (Alexandrite) these materials both exhibit high slope efficiencies (>50%) and low ESA[215,216] although the ^2E level lies below the $^4T_2$ level in alexandrite which requires heating to overcome. The oxide hosts also tend to have larger refractive indexes and hence lower $\sigma\tau$ products than the fluoride hosts.

The work detailed in this thesis concentrates on two of the most promising Cr^{3+} laser gain media Cr:LiSAF and Cr:LiSGaF. Although these materials exhibit lower slope efficiencies than emerald, Alexandrite and Cr:LiCAF indicating some ESA is present. They come into their own because the principle absorption of the chromium ion is shifted in the plane parallel to the crystal c-axis from the $^4A_2 \rightarrow {}^4T_1$ transition at ~ 350-480 nm to the $^4A_2 \rightarrow {}^4T_2$ transition ~ 580-720 nm. This absorption band in the red region of the visible spectrum is directly accessible to GaInP/AlGaInP laser diodes and thus makes these colquiriites attractive materials for direct diode pumping. The

absorption and emission spectra for Cr:LiSGaF are almost identical to those of Cr:LiSAF which are shown in Figure 1.18 and Figure 1.19 respectively. Both materials exhibit large fluorescence/emission bandwidths (~200 nm). Both materials exhibit strong absorption in the red region of the visible spectrum leading to their characteristic greenish appearance and absorption is strongest in the plane parallel to the crystal c-axis (π or p-pol.). The sharp absorption features are due to the ^2E and $^2T_1$ levels and typical of most Cr^{3+} doped materials[217].

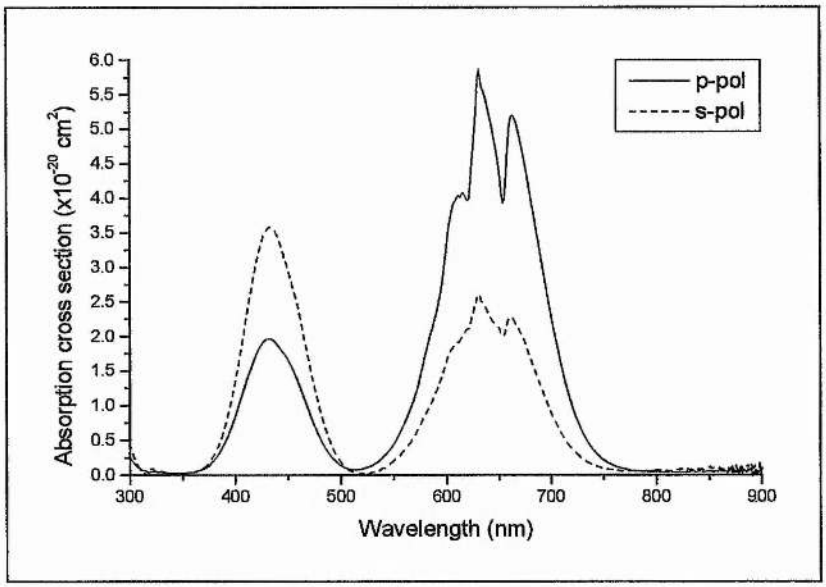

Figure 1.18 Absorption spectra for Cr:LiSAF of p-polarised light (solid line) and s-polarised light (dashed line).

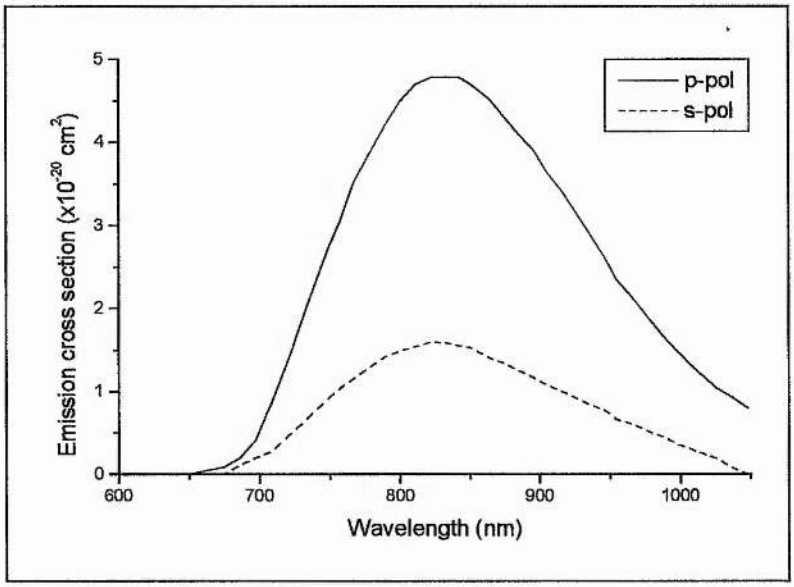

Figure 1.19 Emission spectra of p-polarised light (solid line) and s-polarised light (dashed line) for Cr:LiSAF.

The coefficients of expansion for the directions parallel to the crystal c-axis and a-axis are more isotropic for Cr:LiSGaF than Cr:LiSAF and hence it is less prone to thermal damage and the introduction of scattering losses during growth, the thermal conductivity is also slightly higher making this material more suited to higher power applications. The attractiveness of these particular colquiriites has meant that the growth processes have been refined to a point where scattering losses less than 0.1% cm^{-1} for Cr:LiSAF and less than 0.05% cm^{-1} for Cr:LiSGaF have been reported. Cr:LiSAF has a marginally higher $\sigma\tau$ product making it a good gain-medium candidate for a laser system having a low cw threshold and modest pump power requirements. In Table 1-5 the material and laser properties of some of the chromium-doped colquiriites are summarised.

Properties	Cr:LiCAF	Cr:LiSAF	Cr:LiSGaF
Emission peak (nm)	763	846	835
Lifetime at room temp. (μs)	170	63	88
Emission cross-section ($\times 10^{-20}$ cm^2)	1.3	4.8	3.3
Intrinsic efficiency (%)	67	53	52
Quantum intrinsic efficiency (%)	82	67	66
Nonlinear refractive index ($\times 10^{-14}$ esu)	—	2.9 ± 0.9	4.3 ± 0.9
Upconversion microparameter C_{DA} ($\times 10^{-37} cm^6/s$)	—	1.1	1.1
Melting point (°C)	810	766	716
Expansion coefficient (10^{-6}/°C)	$\alpha_c = 3.6$ $\alpha_a = 22$	$\alpha_c = -10$ $\alpha_a = 25$	$\alpha_c = 0$ $\alpha_a = 12$
Thermal conductivity (W/m°C)	$\kappa_c = 4.58$ $\kappa_a = 5.14$	$\kappa_c = 3.0$ $\kappa_a = 3.3$	$\kappa_c = 3.4$ $\kappa_a = 3.6$
Cr^{3+} segregation coefficient	—	$k = 0.94$	$k = 1.3$

Table 1-5 Optical and laser properties of some colquiriite crystals[201].

The first colquiriite lasers to produce femtosecond pulses were pumped with pumped with krypton ion (Kr^+)[218,219] at 647 nm and Nd:YLF DPSSL (hybrid modelocking)[220] at 659 nm on the $^4A_2 \rightarrow {}^4T_2$ absorption or with Ar^+ lasers at 488 nm on the $^4A_2 \rightarrow {}^4T_1$ absorption [221,222]. Although the cw first demonstration of diode pumped Cr:LiCAF[223], Cr:LiSAF[224] and Cr:LiSGaF[225] preceded the first modelocking results the output powers of commercially available laser diodes were low (~ 10 mW @ 670 nm diffraction limited and ~100 mW cw multimode[226]) and were not sufficient to allow femtosecond pulse production. The first femtosecond directly diode pumped Cr:LiSAF laser was demonstrated in 1994 by Mellish *et al*[227]. This laser used an intracavity multiple

quantum well absorber as a passive modelocker to produce 220 fs pulses. The first directly diode pumped self-modelocked Cr:LiSAF laser was demonstrated soon afterwards by Dymott and Ferguson[228] in a regeneratively modelocked X-fold cavity. The laser produced 97 fs pulses at an average output power of ~ 3 mW with a single 250 mW pump laser diode and exhibited a modelocking threshold of ~ 160 mW. This initial result was quickly improved to 34 fs pulses at an average output power of 42 mW (although not in a single output beam) by the same group[229] using two 400 mW pump diodes and extracavity dispersion compensation.

The major drawback of moderate and high power, single emitter laser diodes (at any wavelength) is the poor quality of the output beams. As the output intensity of a diode is limited by either thermal loading or optical damage of the output facet it is necessary to increase the emitter area. The depth of the facet is fairly fixed by the structure of the laser so the only dimension of freedom is along the length of the facet, parallel to the waveguide layer. Expansion of the facet along this axis results in a broad emitter area capable of producing higher powers but in a multi-spatial-mode and poor quality beam. In the plane perpendicular to the active region however, the beam is highly divergent but can be very nearly diffraction-limited. In other words, the divergence angle may be characterised by a plane wave incident on an aperture of the same dimension as the emitter facet. The output beam in the plane parallel to the active region, while not as divergent, exhibits a divergence angle many times (as much as 2000 times) the diffraction limit for the larger aperture in this plane. This is due to the oscillation of many spatial modes within the laser in this plane. The non-diffraction-limited nature of the beam from a broad area diode implies that tight focusing over any reasonable distance will be impossible as brightness can only ever be conserved in any lossless system of lenses. Laser systems that incorporate broad area pump diodes often require complex and extended coupling optics to provide some sort of acceptable pump and cavity mode overlap. The modelocking thresholds of these systems, however, remain relatively high, resulting in the requirement of higher power pump beams and cooling of the gain medium due to the onset of thermal quenching of the upper state lifetime (~ T > 50°C in Cr:LiSAF)[230].

A second problem particular to diode pumped colquiriite lasers is that thermal and optical damage issues are exacerbated in GaInP/AlGaInP devices over and above other laser diodes by absorption effects at the emitter facets. This has hampered the development of higher power diodes with improved beam properties. In uncompensated

laser diode structures the bandgap decreases at the facets leading to increased absorption and heating. The thermal and electrical resistivity is higher in AlGaInP[231] leading to so-called catastrophic optical mirror damage (COMD) at lower intensities (1-5 $MWcm^{-2}$)[232].

Despite these problems, the advantages of diode lasers over mainframe ion lasers in cost and performance and the fact that not all ultrashort pulses applications require high powers (the dye lasers mentioned earlier typically produced only ~10's mW), have fuelled much work in this area. Improvements in non-absorbing mirror structures have increased performance of laser diodes from that of 0.5 W from a 250 μm active stripe width[233] to over 0.5 W from a 50 μm stripe[234] the brightest high power AlGaInP laser diodes demonstrated so far. Sub-100fs pulses from diode pumped colquiriite lasers have been demonstrated for a wide variety of cavity and pump diode configurations in different modelocking regimes with average output powers ranging from 10-100mW[235,236-241].

As will be shown in chapter 2, the inability to focus the pump mode tightly over an appreciable distance has serious implications for the cw and self-modelocking threshold and efficiency of a laser. Ideally diffraction limited sources provide the most efficient means of pumping an ultrashort pulse laser but unfortunately due to the reasons stated above the output powers from narrow emitter facet or stripe diode lasers are still severely limited (< 50 mW).

One method of achieving higher powers (~ 0.5 W) from semiconductor devices in a diffraction-limited beam, and thereby avoiding many of the problems associated with broad area diode lasers, is either to use a master oscillator power amplifier (MOPA) or a tapered diode laser (TDL) in an extended cavity. These methods use a tapered stripe amplifier either in its own cavity or pumped by a low power diode laser with a narrow stripe width (< 5 μm) and diffraction-limited beam in both planes. Successful and efficient operation of ultrashort pulse colquiriite lasers has been demonstrated with both of these sources[242,243] however, these extended pump systems themselves are either experimental at this stage or prohibitively expensive.

An alternative method is to produce a femtosecond laser with a sufficiently low cw and modelocking threshold that it may be pumped directly by the diffraction-limited narrow stripe diode lasers. As these lasers may be purchased relatively cheaply and require no additional coupling optics other than a simple tightly focussing lens, this type of laser represents the most potentially compact and low cost femtosecond pulse source.

1.6 Conclusions

In this chapter a review of some of the applications, behaviour, generation and characterisation of ultrashort pulses has been presented. In particular, attention was paid to the techniques of self-modelocking and other fast saturable absorber mechanisms for modelocking. The broadband Cr^{3+}:doped colquiriites were then presented as an attractive, directly diode pumpable, alternative to Ti-doped sapphire for all-solid-state ultrashort pulse generation in the near-infrared. The work described in the remainder of this thesis will concentrate on these materials and related laser oscillators with a view to the development of robust and compact femtosecond lasers with low pump power requirements. These lasers will also be shown to have extremely good stability/noise properties for a number of specific applications. In Chapter 2 a more in-depth consideration is given to improving the efficiency and threshold properties of directly diode-pumped colquiriite lasers, notably Cr:LiSAF and Cr:LiSGaF.

Endnotes

1 M. Y. Frankel, J.F. Whitaker and G. A. Mourou, *IEEE J. Quantum Electron.* **28**, 2313 (1992).

2 B. B. Hu and M. C. Nuss, *Opt. Lett.* **20**, 1716 (1995).

3 B. Bouma, G. J. Tearney, S. A. Boppart, M. R. Hee, M. E. Brezinski and J. G. Fujimoto, *Opt. Lett.* **20**, 1486 (1995).

4 G. Robertson, D. Armstrong, M. J. P. Dymott, A. I. Ferguson and G. L. Hogg, *Appl. Optics*, **36**, 2481 (1997).

5 D. W. Piston, D. R. and W. W. Webb, J. R. Lakowicz editor, *Proc. SPIE*, **1640**, 379 (1992).

6 S. Nolte, C. Momma, G. Kamlage, B. N. Chickov, A. Tünnermann, F. von Alvensleben and H. Welling, *in Technical Digest of Conference on Lasers and Electro-optics (Optical Society of America, Washington D. C., 1998), paper* CFD3.

7 D. Strickland, and G. Mourou, Opt. Commun. 55, 447 (1985).

8 S. Szatmari, G. Almasi, M. Feuerhake and P. Simon, *Appl. Phys.* **B 63**, 463 (1996).

9 M. D. Perry, D. Pennington, B. C. Stuart, G. Tietbohl, J. A.Britten, C. Brown, S. Herman, B. Golick, M. Kartz, J. Miller, H. T. Powell, M. Vergino and V. Yanovsky, *Opt. Lett.* **24**, 160 (1999).

10 J. S. Wark, M. Bakarezos, K. Burnett, D. M. Chambers, A. E. Dangor, L. Dwivedi, A. Dyson, P. Fews, M. Holden, P. B. Holden, M. H. Key, P. Lee, C. L. S. Lewis, P. Loukakos, A. G. MacPhee, S. Moustaizis, D. Neely, P. A. Norreys, G. J. Pert, J. A. Ploues, S. G. Preston, A. Sanpera, C. G. Smith, G. J. Tallents, J. B. Watson, M. Zepf and J. Zhang, in *Atomic Physics 15*, (World Scientific Publishing, 1997), pp. 82-96.

11 D. M. Chambers, P. A. Norreys, A. E. Dangor, R. S. Marjoribanks, S. Moustaizhs, D. Neely, S. G. Preston, J. S. Wark, I. Watts and M. Zepf, *Opt. Commun*, **148**, 289 (1998).

12 P. Salieres, T. Ditmire, K. S. Budil, M. D. Perry and A. L'Huillier, *J. Phys.* **B 27**, L217 (1994).

13 J. D. Kilkenny, E. M. Campbell, J. D. Lindl, G. B. Logan, W. R. Meier, L. J. Perkins, J. A. Paisner, M. H. Key, H. T. Powell, R. L. McCroy and W. Seka, *Phil. Trans. Roy. Soc. Lond.* **357**, 533 (1999).

14 A. E. Siegman, *in Lasers (University Science Books, Sausalito, California 1986)*, chapter 5.

15 A. E. Siegman, *in Lasers (University Science Books, Sausalito, California 1986)*, chapter 10.

16 J-C. Diels and W. Rudolph, *in Ultrashort Laser Pulse Phenomena* (Academic Press, U.S.A. 1996) chapter 1.

17 M. D. Perry, S. A. Payne, T. Ditmire, R. Beach, G. J. Quarles, W. Ignatuk, R. Olson and J. Weston, *Laser Focus World*, **29**, No.9, 85 (1993) et. Seq.

18 S. Uemura, *Jpn. J. Appl. Phys.* **37**, 133, (1998).

19 K. Naganuma, K. Mogi and H. Yamada, *Opt. Lett.* **15** (1990).

20 Personal communication with Sadao Uemura. Optoelectronics Division, Electrotechnical Laboratory, 1-1-4 Umezono, Tsukuba, Ibaraki, 305, Japan.

21 S. Uemura and K. Torizuka, *Opt. Lett.* To be published (1999).

22 R. L. Fork, C. H. Brito Cruz, P. C. Becker and C. V. Shank, *Opt. Lett.* **12**, 483 (1987).

23 F. Gires and P. Tournois, *C. R. Acad. Sci.* **258**, 6112 (1964).

24 R. L. Fork, O. E. Martinez and J. P. Gordon, *Opt. Lett.* **9**, 150 (1984).

25 R. Szipöcs, K. Ferencz, C. Spielmann and F. Krausz, *Opt. Lett.* **19**, 201 (1994).

26 R. L. Fork, C. H. Brito Cruz, P. C. Becker and C. V. Shank, *Opt. Lett.* **12**, 483 (1987).

27 R. Szipöcs and A. Köházi-Kis, *Appl. Phys.* **B 65**, 115 (1997).

28 F. X. Kärtner, N. Matuschek, T. Schibli and U. Keller, *Opt. Lett.* **22**, 831 (1997).

29 I. D. Jung, F. X. Kärtner, N. Matuschek, D. H. Sutter, F. Morier-Genoud, G. Zhang, U. Keller, V. Scheuer, M. Tilsch and T. Tschudi, *Opt. Lett.* **22**, 1009 (1997).

30 D. H. Sutter, I. D. Jung, F. X. Kärtner, N. Matuschek, F. Morier-Genoud, V. Scheuer, M. Tilsch, T. Tschudi and U. Keller, *IEEE J. Sel. Topics Quantum Electron*, **4**, 169 (1998).

31 G. P. Agrawal, in Nonlinear Fibre Optics (Academic Press, London, 1995).

32 A. E. Siegman, *in Lasers (University Science Books, Sausalito, California 1986)*, chapter 10.

33 A. E. Siegman, *in Lasers (University Science Books, Sausalito, California 1986)*, chapter 10.

34 G. P. Agrawal, in *Nonlinear Fiber Optics (Academic Press London 1995)*.

35 O. E. Martinez, R. L. Fork and J. P. Gordon, *Opt. Lett.* **9**, 156 (1984).

36 D. G. Parker, P. G. Say, A. M. Hansom and W. Sibbett, *Electron. Lett.* **23**, 527 (1987).

37 E. K. Zavoiskii and S. D. Franchenko, *Sov. Phys. Doklady* **1**, 285 (1956).

38 D. J. Bradley, B. Liddy and W. E. Sleat, *Opt. Commun.* **2**, 391 (1971).

39 A. Finch, Y. Liu, H. Niu, W. Sibbett, W. E. Sleat, D. R. Walker, Q. L Yang and H. Zhang *in ultrafast phenomena VI (Springer-Verlag, New York, 1988)* p159-161.

40 M. Maier, W. Kaiser and J. A. Giordmaine, *Phys. Rev. Lett.* **17**, 1275 (1966).

41 J. A. Armstrong, *Appl. Phys. Lett.* **10**, 16 (1967).

42 H. P. Weber, *J. Appl. Phys.* **38**, 2231 (1967).

43 A. M. Wiener, *IEEE J. Quant. Electron.* **QE-19**, 1276 (1983).

44 A. M. Weiner, J. G. Fujimoto and E. P. Ippen, *Opt. Lett.* **10**, 71 (1985).

45 R. C. Miller, Phys. Lett. **26-A**, 177 (1968).

46 D. von der Linde, *IEEE J. Quant. Electron.* **QE-8**, 328 (1972).

47 J. C. Diels , W. Dietel, J. J. Fontaine, W. Rudolph and B. Wilhelmi, *J. Opt. Soc. Am.* **B 2**, 680 (1985).

48 J. C. Diels , J. J. Fontaine, I. C. McMichael and F. Simoni, *Appl. Opt.* **24**, 1270 (1985).

49 E. J. O. Williams, in *Optimisation of a Colliding Pulse Modelocked Dye Laser,* PhD thesis, University of St.Andrews, (1997), p53.

50 J. C. Diels, J. J. Fontaine, N. Jamasbi, M. Lai and J. Mackey, *in Technical Digest of Conference on Lasers and Electro-optics (Optical Society of America, Washington D. C., 1987), paper* MD3.

51 J. C. Diels, J. J. Fontaine and W. Rudolph, *Rev. Phys. Appl.* **22**, 1605 (1987).

52 C. Yan and J. C. Diels, *J. Opt. Soc. Am.* **B 8**, 1259 (1991).

53 J. L. A. Chilla and O. E. Martinez, *Opt. Lett.* **16**, 39 (1991).

54 R. Trebino and D. J. Kane, *J. Opt. Soc. Am.***A 10**, 1101 (1993).

55 D. J. Kane and R. Trebino, *IEEE J. Quant. Electron.* **QE-29**, 571 (1993).

56 D. J. Kane and R. Trebino, *Opt. Lett.* **18**, 823 (1993).

57 K. W. DeLong, R. Trebino and D. J. Kane, *J. Opt. Soc. Am.* **B 11**, 1595 (1994).

58 K. W. DeLong, R. Trebino J. Hunter and W. E. White, *J. Opt. Soc. Am.* **B 11**, 2206 (1994).

59 K. W. DeLong, D. N. Fittinghoff, R. Trebino B. Kohler and K. Wilson, *Opt. Lett.* **19**, 2152 (1994).

60 M. A. Krumbügel, C. L. Ladera, K. W. DeLong, D. N. Fittinghoff, J. N. Sweetser and R. Trebino, *Opt. Lett.* **21**, 143 (1996).

61 G. Taft, A. Rundquist, M. M. Murnane, H. C. Kapteyn, K. W. DeLong, R. Trebino and I. P. Christov, *Opt. Lett.* 20, 743 (1995).

62 G. Taft, A. Rundquist, M. M. Murnane, I. P. Christov, H. C. Kapteyn, K. W. DeLong, D. N. Fittinghoff, M. A. Krumbügel, J. N. Sweetser and R. Trebino, *IEEE J. Sel. Topics Quant. Electron.* **2**, 575 (1996).

63 K. W. DeLong, D. N. Fittinghoff and R. Trebino, *IEEE J. Quant. Electron.* **QE-32**, 1253 (1996).

64 T. Tsang, M. A. Krumbügel, K. W. DeLong, D. N. Fittinghoff and R. Trebino, *Opt. Lett.* **21**, 1381 (1996).

65 K. W. DeLong, M. A. Krumbügel, D. N. Fittinghoff, J. N. Sweetser, R. Trebino, G. Taft, A. Rundquist, E. Zeek, M. M. Murnane and H. C. Kapteyn, in *Technical Digest of Conference on Lasers and Electro-optics* (Optical Society of America, Washington D. C. 1997) paper CthU4.

66 K. W. DeLong, R. Trebino and W. E. White, *J. Opt. Soc. Am.* **B 12**, 2463 (1995).

67 D. N. Fittinghoff, J. L. Bowie, J. N. Sweetser, R. T. Jennings, M. A. Krumbügel, K. W. DeLong, R. Trebino and I. A. Walmsley, *Opt. Lett.* **21**, 884 (1996).

68 R. Trebino, in *Technical Digest of Conference on Lasers and Electro-optics* (Optical Society of America, Washington D. C. 1997) paper CWL1 (tutorial).

69 A. E. Siegman, *in Lasers (University Science Books, Sausalito, California 1986)*, Chapter 26.

70 A. E. Siegman, *in Lasers (University Science Books, Sausalito, California 1986)*, Chapter 25.

71 A. E. Siegman, *in Lasers (University Science Books, Sausalito, California 1986)*, Chapter 25.

72 A. Yariv, *in Quantum electronics, John Wiley & Sons Inc., New York, N.Y. 1989.*

73 A. E. Siegman, *in Lasers (University Science Books, Sausalito, California 1986).*

74 M. DiDomenico, J. E. Geusic, H. M. Marcos and R. G. Smith., *Appl. Phys Lett* **8**, 180 (1966).

75 D. J. Kuizenga and A. E. Siegman, *IEEE J. Quantum. Electron.* **QE-6**, 709 (1970).

76 H. W. Mocker and R. J. Collins, *Appl. Phys. Lett.* 7, 270 (1965).

77 A. J. DeMaria, D. A. Stetser and H. Heynau, *Appl. Phys. Lett.* **8**, 174 (1966).

78 J. B. Schlager, Y. Yamabayashi, D. L. Franzer and R. I. Juneau, *IEEE Phot. Tech. Lett.* **1**, 264 (1989).

79 A. Yariv, in *Quantum Electronics*, 3rd Edn. (Wiley, New York, 1989) p327.

80 A. E. Siegman, *in Lasers (University Science Books, Sausalito, California 1986)*, p980.

81 L. A. Glasser, *Electron. Lett.* **14**, 725 (1978).

82 Ch. Spielmann, F. Krausz, T. Brabec, E. Wintner and A. J. Schmidt, Opt. Lett. 16, 1180 (1991).

83 J. Q. Bi, W. Hodel, P. Beaud, J. Schutz, H. P. Weber, M. Proctor, M. A. Dupertuis, D. Martin, F. Morier-Genoud and F. K. Reinhart, *Opt. Commun.* **89**, 245 (1992).

84 H. Statz and C. L. Tang, *J. Appl. Phys.* **36**, 3923 (1965).

85 D. E. Spence, J. M. Evans, W. E. Sleat and W. Sibbett, *Opt. Lett.* **17**, 1762 (1991).

86 H. W. Mocker and R. J. Collins, *Appl. Phys. Lett.* 7, 270 (1965).

87 A. J. DeMaria, D. A. Stetser, and H. Heynau, *Appl. Phys. Lett.* **8**, 174 (1966).

88 P. W. Smith, *Proc. IEEE* **58**, 1342 (1970).

89 G. C. H. New, *Opt. Commun.* **6**, 188 (1974).

90 H. A. Haus, *IEEE J. Quantum Electron.* **12**, 169 (1975).

91 C. V. Shank and E. P. Ippen, *Appl. Phys. Lett.* **24**, 373 (1974).

92 I. S. Ruddock and D. J. Bradley, *Appl. Phys. Lett.* **38**, 1981, 671-672.

93 R. L. Fork, B. I. Greene and C. V. Shank, *Appl. Phys. Lett.* **38**, 671 (1981).

94 R. L. Fork, O. E. Martinez and J. P. Gordon, *Opt. Lett.* **9**, 150 (1984).

95 A. Finch, G. Chen, W. E. Sleat and W. Sibbett, *J. Mod. Opt.* **35** 345 (1988).

96 A. Finch, in *Linear and Nonlinear Optical Pulse Characterisation,* PhD Thesis, University of St Andrews, (1989).

97 J. L. Martin, A. Migus, G. A. Mourou and A. H. Zewail eds. in *"Ultrafast Phenomena VIII," Springer Series in Chemical Physics 55, Springer-Verlag Berlin, 1993.*

98 H. A. Haus, *J. Appl. Phys.* **46**, 3049 (1975).

99 H. A. Haus, J. G. Fujimoto and E. P. Ippen, *J. Opt. Soc. Am.* **B 8**, 2068 (1991).

100 P. F. Moulton, *Proc. IEEE* **80**, 340 (1992).

101 P. F. Moulton, *J. Opt. Soc. Am.* **B 3**, 125 (1986).

102 E. P. Ippen, H. A. Haus and L. Y. Liu, *J. Opt. Soc. Am.* **B 6**, 1736 (1989).

103 L. F. Mollenauer and R. H. Stolen, *Opt. Lett.* **9**, 13 (1984).

104 F. M. Mitschke and L. F. Mollenauer *Opt. Lett.* **12**, 407 (1987).

105 D. E. Spence, P. N. Kean and W. Sibbett, in *Technical Digest of Conference on Lasers and Electro-optics* (Optical Society of America, Washington D. C. 1990) paper PDP10.

106 D. E. Spence, P. N. Kean and W. Sibbett, *Opt. Lett.* **16**, 42 (1991).

107 F. Salin, J. Squire, G. Mourou, M. Piche and N. McCarthy, *in OSA Proceedings In Advanced Solid State Lasers,* Vol. **10**, (Optical Society of America, Washington D.C. 1991), pp.125-129.

108 M. Piché, *Opt. Comm.* **86**, 156 (1991).

109 D. K. Negus, L. Spinelli, N. Goldblatt, G. Feugnet, *in OSA Proceedings In Advanced Solid State Lasers,* Vol. 10, (Optical Society of America, Washington D.C. 1991), pp. 120-124.

110 The Mira laser from Coherent Inc. Santa Clara, CA, U.S.A.

111 The Tsunami laser from Spectra Physics, Mountain View, CA, U.S.A.

112 U. Keller, W. H. Knox and H. Roskos, *Opt. Lett.* **15**, 1377 (1990).

113 J. Herrmann, *J. Opt. Soc. Am.* **B 11**, 498 (1994).

114 U. Keller, G. W. t' Hooft, W. H. Knox and J. E. Cunningham, *Opt. Lett.* **16**, 1022 (1991).

115 F. Salin. J. Squier and M. Piché, *Opt. Lett.* **16**, 1674 (1991).

116 F. Salin and J. Squire, *Opt. Lett.* **17**, 1352 (1992).

117 T. Brabec, P. F. Curley, C. Spielmann, E. Wintner and A. J. Schmidt, *J. Opt. Soc. Am.* **B 10**, 1029 (1993)

118 V. L. Lashnikov, V. P. Kalosha, V. P. Mikhailov and I. G. Poloyko, *J. Opt. Soc. Am.* **B 12**, 462 (1995)

119 V. Magni, G. Cerullo and S. De Silvestri, *Opt. Commun.* **96**, 348 (1993).

120 V. Magni, G. Cerullo and S. De Silvestri, *Opt. Commun.* **101**, 365 (1993).

121 G. Cerullo, S. De Silvestri, V. Magni, and L. Pallaro, *Opt. Lett.* **19**, 807 (1994).

122 G. Cerullo, S. De Silvestri and V. Magni, *Opt. Lett.* **19**, 1040 (1994).

123 V. Magni, G. Cerullo, S. De Silvestri and A. Monguzzi, *J. Opt. Soc. Am.* **B 12**, 476 (1995).

124 J. M. Evans, *in Ultrashort Pulse Generation and Synchronisation in Self-Modelocked Vibronic Lasers*, PhD thesis, University of St.Andrews (1989), Chapter 3.

125 M. Piché and F. Salin, *Opt. Lett.* **18**, 1041 (1993)

126 G. W. t'Hooft, U. Keller, W. H. Knox and J. E. Cunningham. in *Technical Digest of Conference on Lasers and Electro-optics* (Optical Society of America, Washington D. C. 1991) paper JMA6.

127 N. Sarukura, Y. Ishida, T. Yanagawa and N. Nakano, *Appl. Phys. Lett.* **57**, 229 (1990).

128 I. D. Jung, F. X. Kärtener, N. Matuschek, D. H. Sutter, F. Morier-Genoud, Z. Shi, V. Scheuer, M. Tisch, T. Tschudi and U. Keller, *Appl. Phys. Phys.* **B 65**, 137 (1997).

129 J. D. Kafka and T. Baer, in *Technical Digest of Conference on Lasers and Electro-optics* (Optical Society of America, Washington D. C. 1991), paper JMA2.

130 G. T. Kennedy, R. S. Grant and W. Sibbett, *Opt. Lett*, **18**, 1736 (1993).

131 A. Miller, P. Li Kam Wa, B. H. T. Chai and E. W. Van Stryland, *Opt. Lett.* 17, 195 (1992).

132 I. T. Sorokina, E. Sorokin, E. Wintner, A. Cassanho and H. P. Jenssen, in *Technical Digest of Conference on Lasers and Electro-optics Europe* (Optical Society of America, Washington D. C. 1994), paper CThN3.

133 P. LiKamWa, B. H. T. Chai and A. Miller, *Opt. Lett.* **17**, 1438 (1992).

134 V. P. Yanovsky, F. W. Wise, A. Cassanho and H. P. Jensenn, *Opt. Lett.* **20**, 1304 (1995).

135 K. X. Liu, C. J. Flood, D. R. Walker and H. M. van Driel, *Opt. Lett.* **17**, 1361 (1992).

136 G. P. A. Malcolm and A. I. Fergusson, *Opt. Lett.* **16**, 1967 (1991).

137 M. Ramaswammy, A. S. Gouveianeto, D. K. Negus, J. A. Izatt and J. G. Fujimoto, *Opt. Lett.* **18**, 1361 (1993).

138 U. Keller, T. H. Chui and J. F. Ferguson, *Opt. Lett.* **18**, 1077 (1993).

139 A. Seas, Vetricevic and R. R. Alfano, *Opt. Lett.* **17**, 937 (1992).

140 V. P. Yanovsky, et al., *Opt. Lett.* **18**, 1541 (1993).

141 A. Sennaroglu, C. R. Pollock and H. Nathel, *Opt. Lett.* **19**, 390 (1994).

142 Y.-F. Chou, K.-L. Deng and J. Wang, *Opt. Lett.* **18**, 1247 (1993).

143 S. Backus, M. T. Asaki, C. Shi, H. C. Kapteyn and M. M. Murnane, *Opt. Lett.* **19**, 399 (1994).

144 D. T. Reid, G. T. Kennedy, A. Miller, W. Sibbett and M. Ebrahimzadeh, *IEEE J. Sel. Topics Quantum Electron.* **4**, 238 (1998).

145 J. Ringling, O. Kittlemann, F. Noack, G. Korn andJ. Squier, *Opt. Lett.* **18**, 2035 (1993).

146 K. C. Burr, C. L. Tang, M. A. Arbore and M. M. Fejer, *Opt. Lett.* **22**, 1458 (1997).

147 B. E. Lemoff and C. P. J. Barty, *Opt. Lett.* **18**, 57 (1993).

148 M. T.Asaki, C. P. Huang, D. Garvey, J. P. Zhou, H. C. Kapteyn and M. M. Murnane, *Opt. Lett.* **18**, 977 (1993).

149 P. Curley, C. Spielmann, T. Brabec, F. Krausz, E. Wintner and A. J. Schmidt, Opt. Lett. **18**, 54 (1993).

150 T. Bedard, W. Sibbett, D. T. Reid, J. GardunoMejia, N. Jamasbi and M. Mohebi, Opt. Lett. **24**, 163 (1999).

151 I. D. Jung, F. X. Kärtner, N. Matuschek, D. H. Sutter, F. Morier-Genoud, G. Zhang, U. Keller, V. Scheuer, M. Tilsch and T. Tschudi, *Opt. Lett.* **22**, 1009 (1997).

152 J. P. Zhou et al., *in Technical Digest of OSA Annual meeting* (Optical Society of America, Washington D. C. 1993), paper WD1.

153 J. P. Zhou G. Taft, C. P. Huang, M. M. Murnane, H. C. Kapteyn and I. P. Christov, *Opt. Lett.* **19**, 1149 (1994).

154 M. Nisoli, S. Stagira, S. De Silvestri, O. Svelto, G Valiulis and A. Varanavicius, *Opt. Lett.* **23**, 630 (1998).

155 G. Gabetta, D. Huang, J. Jacobson, M. Ramaswammy, H. A. Haus, E. P. Ippen and J. Fujimoto, *in Technical Digest of Conference on Lasers and Electro-optics* (Optical Society of America, Washington D.C. 1991), paper CPDP8.

156 M. H. Ober, M. Hofer, U. Keller and T. H. Chiu, *Opt. Lett.* **18**, 1532 (1993).

157 K. A. Stankov and J. Jethwa, *Opt. Commun.* **66**, 41 (1988).

158 M. B. Danailov, G. Cerullo, V. Magni, D. Segala and S. De Silvestri, *Opt. Lett.* **19**, 792 (1994).

159 R. DeSalvo, D. J. Hagan, M. Sheik-Bahae, G. Stegeman and E. W. Van Stryland, *Opt. Lett.* **17**, 28 (1992).

160 F. Salin, P. Grangier, G. Roger and A. Brun, *Phys. Rev. Lett.* **56**, 1132 (1986).

161 F. Salin, P. Grangier, G. Roger and A. Brun, *Phys. Rev. Lett.* **60**, 569 (1988).

162 D. J. Kaup, *Phys. Rev.* **A 42**, 5689 (1990).

163 T. Brabec, C. Spielmann and F. Krauz, *Opt. Lett.* **16**, 1961 (1991).

164 T. Brabec, C. Spielmann and F. Krauz, *Opt. Lett.* **17**, 748 (1992).

165 C.Spielmann, P.F.Curley, T.Brabec and F.Krausz, *IEEE J. Quantum Electron.* **30**, 1100 (1994).

166 F. X. Kärtner and U. Keller, *Opt. Lett.* **20**, 16 (1995).

167 I. D. Jung, F. X. Kärtner, L. R. Brovelli, M. Kamp and U. Keller, *Opt. Lett.* **20**, 1892 (1995).

168 F. X. Kärtner, I. D. Jung and U. Keller, *IEEE J. Sel. Topics Quantum. Electron.* **2**, 540 (1996).

169 F. X. Kärtner, D. Kopf and U. Keller, *J. Opt. Soc. Am.* **B 12**, 486 (1995).

170 D. Kopf, F. X. Kärtner, K. J. Wiengarten and U. Keller, *Opt. Lett.* **19**, 2146 (1994).

171 A. F. Gibson, M. F. Kimmitt and B. Norris, *Appl. Phys. Lett.* **24**, 306 (1974).

172 E. P. Ippen, D. J. Eichenberger and R. W. Dixon, *Appl. Phys. Lett.* **37**, 267 (1980).

173 J. P. van der Ziel, W. T. Tsang, R. A. Logan, R. M. Mikulyak and W. M. Augustyniak, *Appl. Phys. Lett.* **39**, 525 (1981).

174 Y. Silberberg, P. W. Smith, D. J. Eilenberger, D. A. B. Miller, A. C. Gossard, and W. Wiegmann, *Opt. Lett.* **9**, 507 (1984).

175 P. W. Smith, Y. Silberberg and D. A. B. Miller, *J. Opt. Soc. Am.* **B 2**, 1228 (1985).

176 H. N. Islam, E. R. Sunderman, C. E. Soccolich, I. Bar-Joseph, N. Sauer, T. Y. Chang and B. I. Miller, *IEEE J. Quantum Electron.* **25**, 2454 (1989).

177 U. Keller, G. W. t'Hooft, W. H. Knox, T. K. Woodward, B. Tell, J. E. Cunningham, D. L. Sivco and A. Y. Cho, *in Technical Digest of Conference on Lasers and Electro-optics* (Optical Society of America, Washington D.C. 1991), paper JMA4.

178 U. Keller and T. H. Chiu, *IEEE J. Quantum Electron.* **28**, 1710 (1992).

179 U. Keller, K. J. Wiengarten, F. X. Kärtner, D. Kopf, B. Braun, I. D. Jung, R. Fluck, C. Hönninger, N. Matuschek and J. Aus der Au, *IEEE J. Sel. Topics Quantum Electron.* **2**, 435 (1996).

180 U. Keller, W. H. Knox and H. Roskos, *Opt. Lett.* **15**, 1377 (1990).

181 U. Keller, T. K. Woodward, D. L. Sivco and A. Y. Cho, *Opt. Lett.* **16**, 390 (1991).

182 U. Keller, G. W. 'tHooft, W. H. Knox and J. E. Cunningham, *Opt. Lett.* **16**, 1022 (1991).

183 U. Keller, W. H. Knox and G. W. 'tHooft, *IEEE J. Quantum Electron.* **28**, 2123 (1992).

184 U. Keller, D. A. B. Miller, G. D. Boyd, T. H. Chiu, J. F. Ferguson and M. T. Asom, *Opt. Lett.* **17**, 505 (1992).

185 J. Harrison, A. Finch, D. M. Rines, G. A. Rines and P. F. Moulton, *Opt. Lett.* **16**, 581 (1991).

186 K. Lamb, D. E. Spence, J. Hong, C. Yelland and W. Sibbett, *Opt. Lett.* **19**, 1864 (1994).

187 T. Baer, *J. Opt. Soc. Am.* **B 3**, 1175 (1986).

188 A. Ashkin, G. D. Boyd, J. M. Dziedzic, *IEEE J. Quantum Electron.* **2**, 109 (1966).

189 W. J. Kozlovsky, C. D. Nabors and R. L. Byer, *Opt. Lett.* **12**, 1014 (1987).

190 J. J. Zayhowski and A. Mooradian, *Opt. Lett.* **14**, 24 (1989).

191 C. Pederson, P. L. Hansen, T. Skettrup and P. Buchhave, *Opt. Lett.* **20**, 1389 (1995).

192 M. Oka and S. Kubota, *Opt. Lett.* **13**, 805 (1988).

193 L. Y. Liu, M. Oka, W. Wiechmann and S. Kubota, *Opt. Lett.* **19**, 189 (1994).

194 C. Yelland and W. Sibbett, *in Technical Digest of The Twelfth UK National Quantum Electronics Conference*, University of Southampton, 1995, Paper 2-4.

195 G. J. Valentine, *in Development of All-solid-state Modelocked Laser Sources at 1.55 μm*, PhD thesis, University of St.Andrews, (1998), Chapter 2.

196 Spectra Physics Millennia family of DPSS lasers, Spectra Physics, Santa Clara, California.

197 W. L. Nighan Jr, and B. Craig, *Laser Focus World*, **31**, no. 4, 63 (1996).

198 J. Aus der Au, D. Kopf, F. Morier-Genoud, M. Moser and U. Keller, *Opt. Lett.* **22**, 307 (1997).

199 C. Hönninger, G. Zhang, U. Keller and A. Giesen, *Opt. Lett.* **20**, 2402 (1995).

200 S.A.Payne, L.L.Chase, L.K.Smith, W.L.Kway and H.W.Newkirk, *J. Appl. Phs* **60**, 1051 (1989).

201 L. K. Smith, S. A. Payne, W. L. Kway, L. L. Chase and B. H. T. Chai, *IEEE J. Quantum Electron.* **QE-28**, 2612 (1992).

202 M. Fleischer, G. Y. Chao and C. A. Francis, *Amer. Mineralogist*, **66**, 878 (1981).

203 S.A.Payne, L.L.Chase, H.W.Newkirk, L.K.Smith and W F.Krupt, *IEEE J. Quantum Electron.* **24**, 2243 (1988).

204 I. Sorokina, S. Naumov, E. Sorokin, E. Wintner, and A. V. Shestakov, in *Technical Digest of* Conference on Lasers and Electro Optics Europe, (Optical Society of America, Washington, D. C. 1998), paper CTuK7.

205 P.F.Moulton, *Proc. IEEE* **80**, 340 (1992).

206 L. F. Johnson, H. C. Guggenhiem and R. A. Thomas, *Phys. Rev.* **149**, 179 (1966).

207 T. H. Maiman, *Nature* **187**, 493 (1960).

208 P.F.Moulton, *Proc. IEEE* **80**, 340 (1992).

209 J. A. Caird, in *Tunable Solid State Lasers II*, A. Budgor, L. Esterowitz and L. G. DeShazer Eds. (Springer-Verlag, Berlin 1986) p.20.

210 J. A. Cairn, *in Tuneable Solid-State Lasers*, P. Hammerling, A. B. Budgor and A. Pinto Eds. (Springer-Verlag, Berlin 1985).

211 S. A. Payne, L. L. Chase and W. F. Krupke, *J. Chem. Phys.* **86**, 3455 (1987).

212 M. L. Shand and J. C. Walling, *IEEE J. Quantum Electron.* **QE-18**, 1829 (1982).

213 M. L. Shand ans S. T. Lai, *IEEE J. Quantum Electron.* **QE-20**, 105 (1984).

214 S. T. Lai, *J. Opt. Soc. Am.* **B 4**, 1286 (1987).

215 M. L. Shand and H. P. Jenssen, *IEEE J. Quantum Electron.* **QE-19**, 480 (1983).

216 H. W. H. Lee, S. A. Payne and L. L. Chase, *Phys. Rev.* **B 39**, 8907 (1989).

217 D. L. Wood, J. Fergusson, K. Knox and J. F. Dillon, *J. Chem. Phys.* **39**, 890 (1963).

218 A. Miller, P. LiKamWa, B. H. T. Chai and E. W. Van Stryland, *Opt. Lett.* **17**, 195 (1992).

219 P. LiKamWa, B. H. T. Chai and A. Miller, *Opt. Lett.* **17**, 1438 (1992).

220 J. R. Lincon, M. J. P. Dymott and A. I. Ferguson, *Opt. Lett.* **19**, 1210 (1994).

221 N. H. Rizvi, P. M. W. French and J. R. Taylor, *Opt. Lett.* **17**, 877 (1992).

222 J. M. Evans, D. E. Spence, W. Sibbett, B. H. T. Chai and A. Miller, *Opt. Lett.* **17**, 1447 (1992).

223 R. Scheps, *IEEE J. Quantum Electron.* **QE-27**, 1968 (1991).

224 R. Scheps, J. F. Myers, H. B. Serreze, A. Rosenberg, R. C. Morris and M. Long, *Opt. Lett.* **16**, 820 (1991).

225 R. Scheps, *IEEE Photonics Technol. Lett.* **4**, 548 (1992).

226 H. B. Serreze and Y. C. Chen, *IEEE Photon. Technol. Lett.* **3**, 397 (1991).

227 P. M. Mellish, P. M. W. French, J. R. Taylor, P. J. Delfyett and L. T. Florez, *Electron. Lett.* **30**, 223 (1994).

228 M. J. P. Dymott and A. I. Fergusson, *Opt. Lett.* **19**, 1988 (1994).

229 M. J. P. Dymott and A. I. Fergusson, *Opt. Lett.* **20**, 1157 (1995).

230 M. P. Critten, in *All-solid-state Femtosecond Cr:LiSAF and Cr:LiSGaF Lasers*, PhD Thesis, University of St Andrews (1996).

231 P. W. Epperlein, G. L. Bona and P. Rontgen, *Appl. Phys. Lett.* **60**, 680 (1992).

232 D. P. Bour, in Quantum Well lasers, P. S. Zory Jr. Ed. (Academic, New York, 1993) chapter 9.

233 S. Tsuda, W. H. Knox, E A. de Souza, W. Y. Jan and J. E. Cunningham, *Opt. Lett* **20**, 1406 (1995).

234 K. Gäbel, P. Rußbüldt, R. Lebert, P. Loosen, R. Poprawe, H. Heyer and A. Valster, Opt. Commun. 153, 275 (1998).

235 D. Kopf, A. Prasad, G. Zhang, M. Moser and U. Keller, *Opt. Lett.* **22**, 621 (1997).

236 D. Kopf, K. J. Weingarten, L. R. Brovelli, M. Kamp and U. Keller, *Opt. Lett* **19**, 2143 (1995)

237 F. Falcoz, F. Balembois, P. Georges and A. Brun, *Opt. Lett* **20**, 1874 (1995).

238 A. Robertson, R. Knappe, K-J Boller and R. Wallenstein, *in 1996 Conference on Lasers and Electo-Optics Europe, (IEEE Catalog number 96TH8161), Paper CWA2.*

239 R. Mellish, N. P. Barry, S. C. W. Hyde, R. Jones, P. M. W. French, J. R. Taylor, C. J. van der Poel and A. Valster, *Opt. Lett* **20**, 2312 (1995).

240 S. Uemura and K. Miyazaki, *Opt. Commun.* **138**, 330 (1997).

241 K. M. Gäbel, P. Rußüldt, R. Lebert and A. Valster, *Opt. Commun.* **157**, 327 (1998).

242 S. Tsuda, W. H. Knox and S. T. Cundiff, *Appl. Phys. Lett.* **69**, 1538 (1996).

243 A. Robertson, R. Knappe and R. Wallenstein, *Opt. Commun.* **147**, 294 (1998).

Chapter 2: Towards low thresholds

2.1 Introduction

In chapter 1 an introduction to the some of the key aspects of ultrashort pulse generation and measurement have been presented. In this chapter a more detailed analysis of femtosecond lasers operating with low pump power requirements will be described, concentrating particularly on optimising the cw lasing threshold, the modelocking threshold and the dispersion compensation to ensure short pulse operation at low intracavity powers. Two preliminary laser systems based on Cr:LiSAF and Cr:LiSGaF crystals will then be described that take these considerations into account in their design and operation.

2.2 Factors affecting the self-modelocking thresholds of ultrashort pulse lasers

The CW threshold

Intuitively, it can be appreciated that a low modelocking threshold cannot be achieved without first ensuring a low cw threshold for a laser. In this section the cavity and material parameters that most dramatically influence this threshold will be examined.

As mentioned in the first chapter, a self-modelocked laser will contain a tightly focussed cavity mode in the gain medium to ensure that a sufficiently large nonlinear Kerr lens is induced. Therefore, to ensure efficient overlap between the pumped region and the cavity mode in the crystal and hence a low cw threshold, the pump beam must also be tightly focussed in the gain medium. For this reason and for reasons indicated earlier we will consider here only diffraction-limited pump beams, either from a master oscillator power amplifier (MOPA) or from a single narrow stripe laser diode or krypton-ion mainframe laser.

Alfrey derived a simple but effective model for the prediction of output power from a Ti:sapphire laser pumped longitudinally with a diffraction-limited pump beam[1].

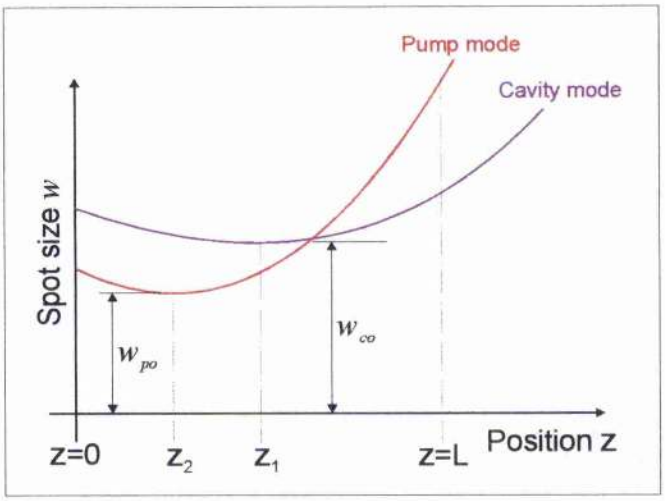

Figure 2.1 The collinear propagation of pump and cavity modes through a gain medium of length L.

Starting from the propagation of a focussed Gaussian pump and cavity mode through a gain medium of length L (Figure 2.1), Alfrey derived an expression for the pump power P_p required to produce an intracavity power of P_c

$$P_P = \frac{(T+\Lambda)hc\pi^2}{8\sigma\tau\lambda_P\alpha_P\int_0^L \frac{e^{-\alpha_P z}}{w_C{}^2(z)w_P{}^2(z)}Q(z)dz}$$

Equation 2.1

where P_c is embedded in $Q(z)$, z is the axial distance through the crystal, T is the transmission of the output coupling mirror, Λ represents the parasitic cavity losses in a round-trip including the mirror transmission and scattering losses and α_P is the absorption coefficient at the pump wavelength λ_P. σ and τ are the cross-section and lifetime of the upper-laser level respectively. The pump and cavity spot sizes $w_P(z)$ and $w_C(z)$ through the crystal are described by

$$w_C{}^2(z) = w_{C0}{}^2\left\{1+\frac{(z-z_1)^2\lambda_C{}^2}{\pi^2 w_{C0}{}^4 n_C{}^2}\right\}$$

$$w_P{}^2(z) = w_{P0}{}^2\left\{1+\frac{(z-z_2)^2\lambda_P{}^2}{\pi^2 w_{P0}{}^4 n_P{}^2}\right\}$$

Equation 2.2

where w_{C0} and w_{P0} are the pump and cavity mode waists respectively.

$Q(z)$ is the radial overlap integral of the pump and laser fields taking into account gain saturation:

$$Q(z) = 2\pi \int_0^{\infty} \frac{e^{-Ar^2} r dr}{1 + Be^{-Dr^2}}$$

Equation 2.3

Where,

$$A = \frac{2\left(w_P^{\,2} + w_C^{\,2}\right)}{w_P^{\,2} w_C^{\,2}},\ B = \frac{4P_C}{\pi w_C^{\,2} I_s} \text{ and } D = \frac{2}{w_C^{\,2}}$$

Equation 2.4

An expression for the threshold of a laser may be deduced from Equation 2.1 as we know from laser theory[2] that at threshold, the intracavity field intensity $I_c << I_s$ ($I_c = 0$). In this case $Q(z)$ becomes,

$$Q(z) \to 2\pi \int_0^{\infty} e^{-\frac{2\left(w_P^{\,2} + w_C^{\,2}\right)}{w_P^{\,2} w_C^{\,2}} r^2} r dr = \frac{\pi}{2} \frac{w_P^{\,2} w_C^{\,2}}{w_P^{\,2} + w_C^{\,2}}$$

Equation 2.5

Equation 2.1 at threshold therefore simplifies to:

$$P_{TH} = \frac{(T + \Lambda) hc\pi^2}{4\sigma\tau\lambda_P \alpha_P \int_0^L \frac{e^{-\alpha_P z}}{w_C^{\,2}(z) + w_P^{\,2}(z)} dz}$$

Equation 2.6

It is immediately obvious from Equation 2.6 that, as expected, a minimisation of the parasitic cavity losses Λ is crucial to achieving a low cw threshold. The pump absorption coefficient α_p and the trade-off between α_p and the parasitic cavity losses are also of utmost importance when optimising a laser for low threshold operation. It would be easy to assume that a laser threshold could be improved indefinitely by increasing the doping level of active ions in the host material, as the absorption coefficient is proportional to the doping. This, however, generally decreases figure of merit (FOM) of the gain crystal, which is given by:

$$F.O.M. = \frac{\text{peak absorption at the pump wavelength } (\alpha_p)}{\text{peak residual absorption at the lasing wavelength } (\alpha_l)}$$

Equation 2.7

where the residual absorption α_l also scales with doping concentration. The parasitic cavity losses, the figure of merit and the pump absorption are therefore all linked and there is a trade-off between optimising α_p and minimising Λ. As the values of α_p for the chromium-doped colquiriites, Cr:LiSAF and Cr:LiSGaF can be made quite large while still retaining a high FOM, they are ideal materials on which to base our study of low-threshold laser systems.

It is also evident from Equation 2.6 that the oscillation threshold is inversely proportional to the $\sigma\tau$ product of the laser gain material. This reinforces our choice of Cr:LiSGaF and Cr:LiSAF for low threshold gain materials because the $\sigma\tau$ products of Cr:LiSAF and Cr:LiSGaF are 32.2×10^{-19} cm^2 μs^{-1} and 29×10^{-19} cm^2 μs^{-1} respectively compared with 12.2×10^{-19} cm^2 μs^{-1} for Ti:sapphire. Another point in favour of the colquiriite crystals over Ti:sapphire is that the optimum pump wavelength, λ_P is longer (670 nm) and therefore the quantum defect is lower and the threshold power P_{TH} is proportional to the inverse of λ_P. The threshold is also inversely proportional to the pump and cavity spot sizes and their relative overlap within the medium, thereby highlighting the need to be able to tightly focus the cavity and pump beams simultaneously in the crystal. To maintain an efficient overlap between the two modes over the absorption length of the crystal it is necessary to ensure that similar waist sizes for pump and cavity occur at the same position in the crystal. Figure 2.2 and Figure 2.3 below show the effect of varying the waist sizes and positions on the threshold of a four-mirror Cr:LiSGaF laser with L = 10 mm, T = 1.5 %, η_p = 0.66, n = 1.41 and α_p = 4.5 cm^{-1}.

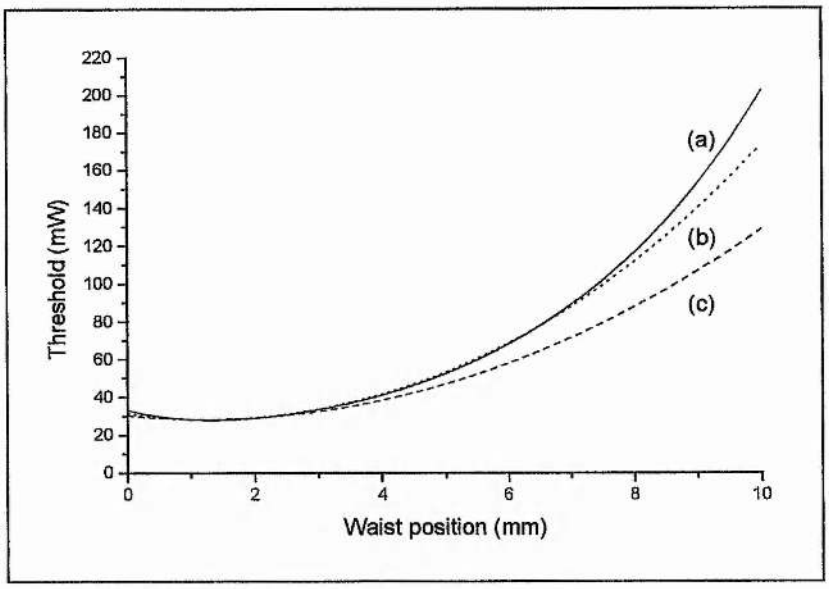

Figure 2.2 Variation in the threshold of a Cr:LiSGaF laser with position of (a) coincident pump and cavity waists, (b) the cavity waist with the pump waist fixed 1mm inside the crystal facet, (c) pump waist with the cavity waist fixed 1mm inside the crystal facet.

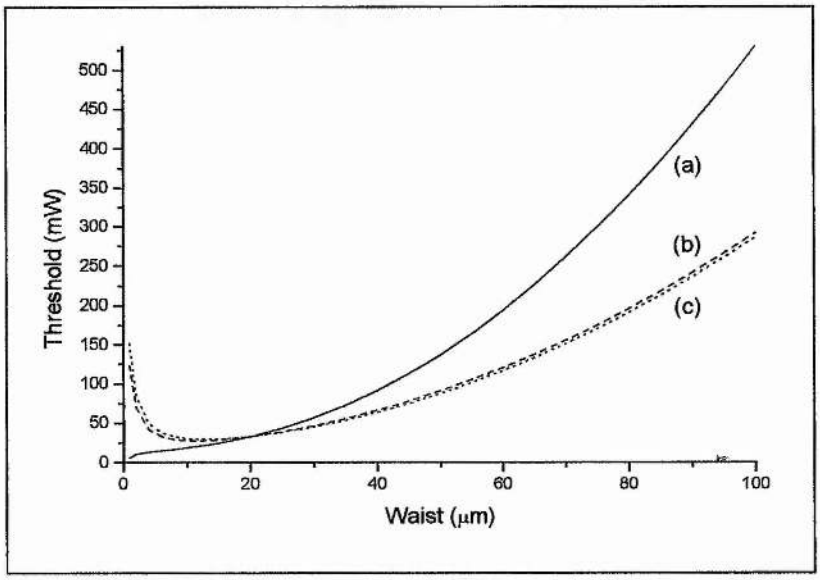

Figure 2.3 Variation in the threshold of a Cr:LiSGaF laser with waist spot size of (a) pump and cavity modes, (b) cavity mode, pump waist fixed at 20μm, (c) pump mode, cavity waist fixed at 20μm, all beams focussed at the crystal facet.

Figure 2.2 and Figure 2.3 indicate that the optimum low threshold condition is a resonator with pump and cavity modes tightly focussed at or just inside an end facet of the gain medium.

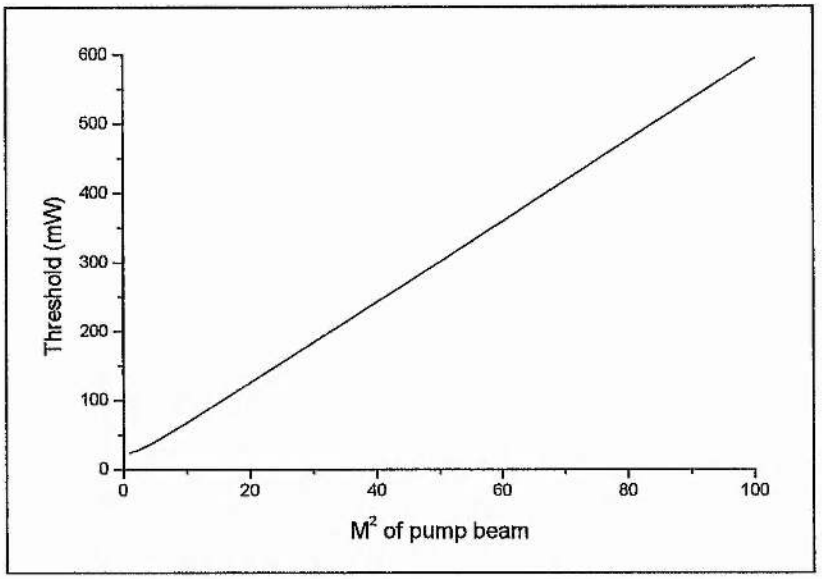

Figure 2.4 Variation of lasing threshold with the M^2 value of the pump beam.

Figure 2.4 above shows the effect of varying the M^2 value and hence the divergence of the pump laser on the threshold of the LiSGaF laser mentioned previously with $w_{C0} = 20$ μm, $w_{P0} = 12$ μm and $z_1 = z_2 = 1.3$ mm. It is clear from Figure 2.4 and the argument raised in chapter 1 that a deviation from a diffraction-limited pump source results in a rapid and detrimental effect on the cw oscillation threshold of a laser.

Optimisation of self-modelocking

The fundamentals of self-modelocking were introduced briefly in chapter 1 (section 1.4). We will now consider the manner in which this effect may be optimised, concentrating for the most part on a specific formalism suggested by Magni and co-workers[3].

Firstly we will look in more detail at the strength and position of an intensity dependent lens within a Kerr medium. Intuitively, an infinitely thin lens, present exactly at the cavity focus, will have no effect on the cavity mode. The same is also true for two equal strength lenses evenly distributed about the focus, as their effects will cancel. A cavity mode focus (the centre of the distributed Kerr lens) coincident with the centre of the gain medium will also, by the same argument, have no effect. The effect of self-focussing on the laser will therefore be most evident when the cavity mode is focussed one end of the gain medium. From our discussion of low cw thresholds the optimum

threshold will be achieved when the cavity and pump foci line up on or just inside the crystal facet (for large α_p), and in practice a compromise is reached between these two very similar conditions.

The strength of an infinitely thin slice of the distributed nonlinear Kerr lens[4] is proportional to w^{-4} and this is the reason for using a tightly focussed cavity mode in self-modelocked lasers. This is illustrated graphically in Figure 2.5 which shows that the localisation and strength of the Kerr lens dramatically increases with a slight reduction in the mode size at the cavity focus.

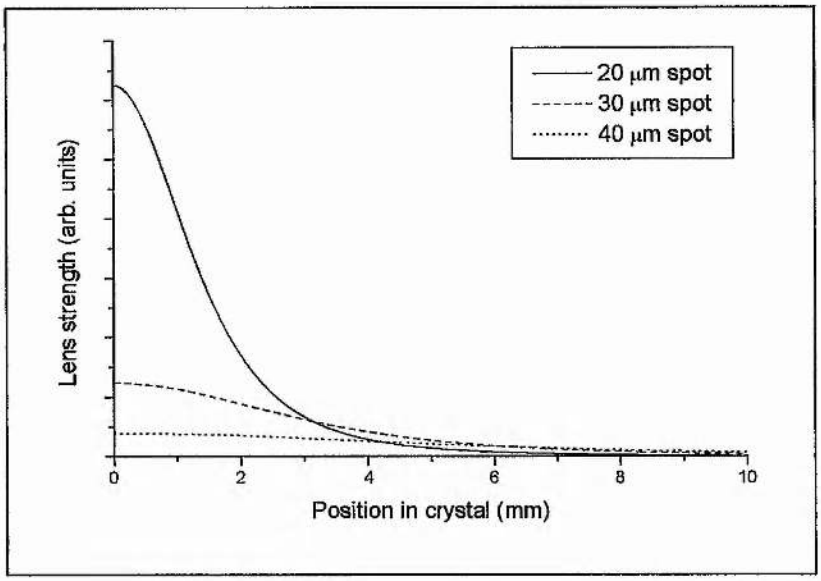

Figure 2.5 Relative variation of nonlinear lens strengths in a 10 mm crystal with different cavity foci incident at the crystal facet.

It becomes apparent from basic laser cavity modelling that the conventional 4-mirror, Z and X-folded laser cavities used for self-modelocking are not optimised for a maximum Kerr effect at the facet of the gain medium. This is due to the Brewster-angled crystals typically used to introduce the lowest insertion loss but which also introduce astigmatism that must be compensated for. Compensation for astigmatism is achieved by arranging the cavity so that a finite angle exists between the concave folding mirrors and each cavity arm. In this way the astigmatism from the angled curved mirrors can be made to cancel the effect of the Brewster-angled crystal. Astigmatism is still present, however, between the folding mirrors separating the foci in the sagittal and tangential planes to create a distributed focus in the gain medium (see Figure 2.6). This distribution of foci increases the cw operation threshold and reduces and displaces any Kerr lens within the rod. One solution is to use an antireflection (AR) coated, plane-plane cut crystal because this allows the foci to coincide in the tangential and sagittal

planes at the crystal facet. When using a plane-plane crystal the folding angles of the curved cavity mirrors must be kept as small as possible to avoid an astigmatic output beam but provided the half-angles can be made smaller than say 3°, this should not be a significant problem.

The ability to make the foci coincide in the gain medium and obtain an efficient intensity-dependent lens becomes increasingly important as we move to lasers with lower pump power requirements. For laser systems where the availability of pump power is not an issue, the lower insertion losses associated with Brewster-angled facets outweigh the advantage of being able to align the cavity foci with one another. Figure 2.6 and Figure 2.7 below show the distribution of the cavity foci and the corresponding nonlinear lens strength and position for a 10 mm Brewster-angled rod and a 10 mm AR coated plane-plane rod.

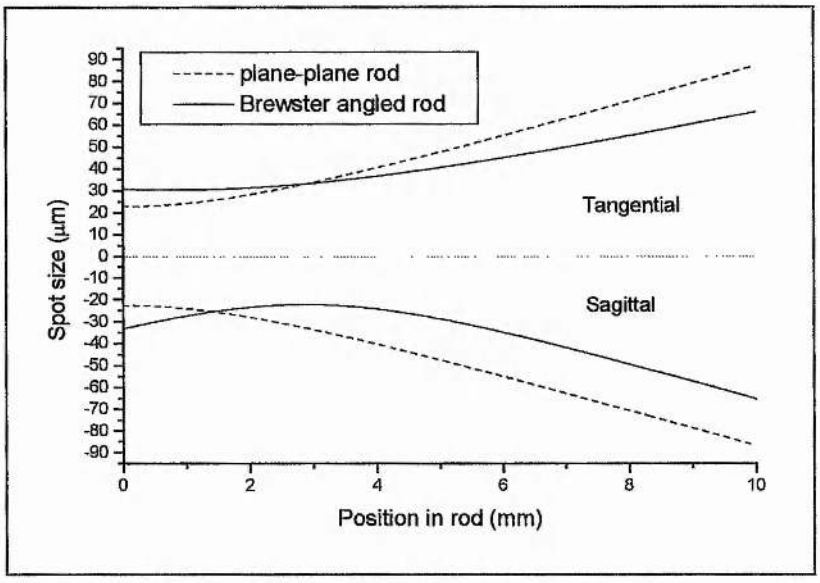

Figure 2.6 Distribution of tangential (positive) and saggital (negative) foci in a Brewster-angled (solid line) and a plane-plane (dotted line) gain medium.

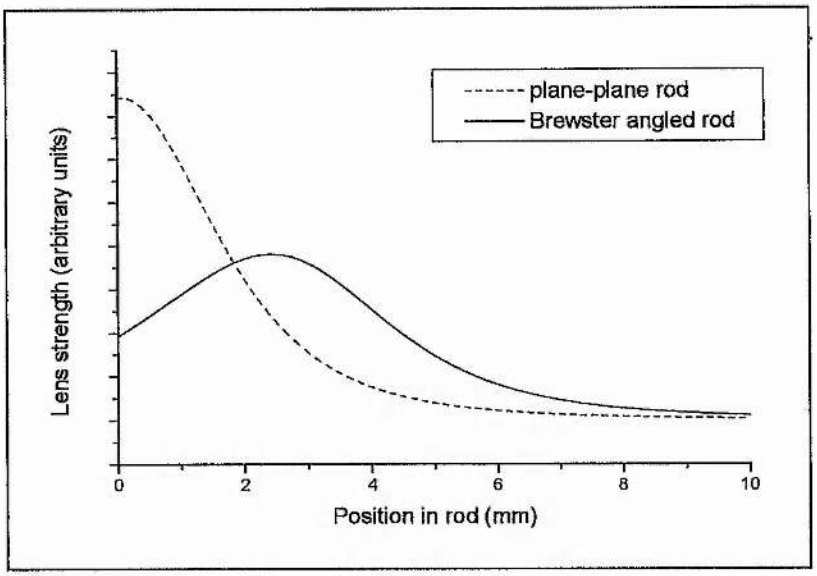

Figure 2.7 Effect on the Kerr lens strength and position of the distribution of tangential and saggital foci in a Brewster-angled (solid line) and a plane-plane (dotted line) gain medium.

Resonator stability

The ABCD matrix formalism 'ABCD law'[5,6] is a well-established method of determining the propagation of optical 'rays' and Gaussian beams through a given system of elements. The elements are represented by 2 × 2 (ABCD) matrices which may operate on an input Gaussian beam matrix $\mathbf{G_{in}}$,

$$\mathbf{G_{in}} = \begin{pmatrix} \hat{q}_{in} \\ 1 \end{pmatrix}$$

Equation 2.8

where $\hat{q}_{in}$ is the complex Gaussian beam parameter described by:

$$\frac{1}{\hat{q}_{in}} \equiv \frac{1}{R_{in}} - j\frac{\lambda_1}{\pi w_{in}^{\ 2}}$$

Equation 2.9

The associated operator of the element or elements is a 2 × 2 matrix **M** which operates on $\mathbf{G_{in}}$ in the following manner:

$$\mathbf{G_{out}} = \begin{pmatrix} \hat{q}_{out} \\ 1 \end{pmatrix} = \mathbf{M} \times \mathbf{G_{in}} = \begin{pmatrix} A & B \\ C & D \end{pmatrix} \times \begin{pmatrix} \hat{q}_{in} \\ 1 \end{pmatrix}$$

Equation 2.10

When considering a laser resonator, beam solutions are sought that are consistent over a cavity 'round trip' i.e. a beam that will become 'trapped' within the cavity. The consequence of this condition is that there will exist limits on the resonator parameters for the existence of a stable solution. For a cavity aligned outside these boundary limits there will be no self-consistent or stable solutions for a beam inside the resonator. These limits are defined by a stability parameter:

$$S = A_0 D_0 + B_0 C_0$$

Equation 2.11

where A_0, B_0, C_0 and D_0 are the elements of the matrix describing a single pass propagation from end mirror to end mirror. The resonator is only stable if $-1 < S < 1$. For the conventional 4-mirror resonators used for self-modelocking, the stability condition is highly dependent on the separation of the two cavity folding mirrors that provide a tight focus inside the gain element. More particularly, for a 4-mirror cavity with unequal arm lengths L_1 and L_2, there will exist two distinct stability regions or zones as the folding mirror separation is varied. Figure 2.8 below shows the stability parameter as a function of the folding mirror separation in a typical self-modelocked Ti:sapphire laser cavity (see fig1.14) with arm lengths L_1 = 500 mm and L_2 = 1100 mm and folding mirror radius of curvature (ROC) = 100 mm. The two stable regions where $-1 < S < 1$ exist from 113 mm to 115.3 mm and 118.3 mm to 120.4 mm respectively.

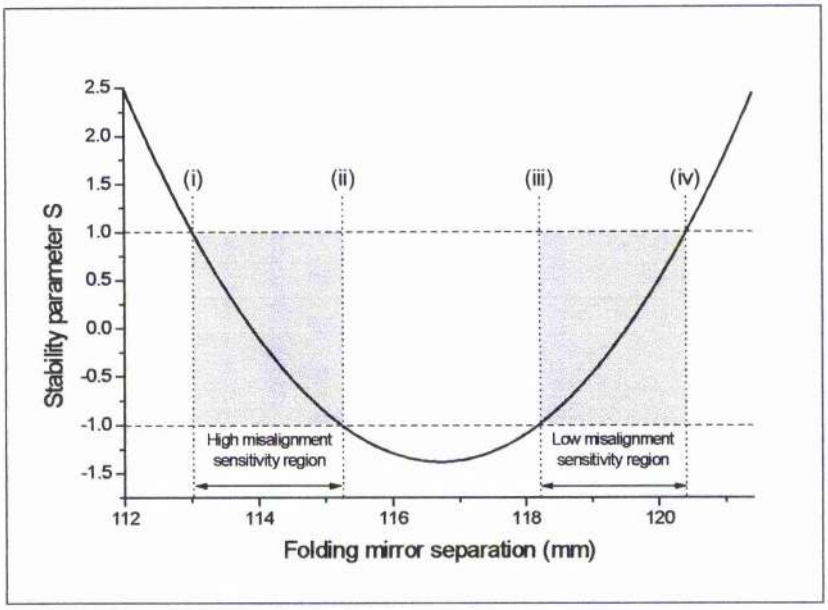

Figure 2.8 Variation of the stability parameter S with the folding mirror separation of a 4-mirror resonator, L1 = 500 mm, L2 = 1100 mm, folding mirror ROC. = 100 mm.

The figure above shows the four stability limits (i) – (iv) which mark the boundaries of the two stable regions. Starting from a short folding mirror separation the first stability limit reached (i) is known as the planar-confocal limit where the two folding mirrors act as lenses in a confocal arrangement whose separation is described by:

$$b_i = R + d\left(1 - \frac{1}{n^3}\right)$$

Equation 2.12

where R is the radius of curvature of the folding mirrors and d is the length of the gain element. The value n^3 assumes a rod with Brewster-angled facets and would reduce to n for a plane-plane cut rod. This limit corresponds to a collimated beam in each of the cavity arms, which are highly sensitive to end mirror misalignment. This limit is therefore critically stable. When the folding mirror separation is increased beyond this point the resonator passes through the first stability region, where the cavity mode is effectively focussing in the long arm of the cavity and collimated along the short arm. For this reason the cavity is highly sensitive to the alignment of the short arm end mirror and this region is referred to as the high misalignment sensitivity (HMS) region. When the second stability limit (ii), the weak-objective limit, is reached the effective focal length of the folding section is equivalent to the length of the long arm L_2.

$$b_{ii} = \frac{4L_2R - R^2}{4L_2 - 2R} + d\left(1 - \frac{1}{n^3}\right)$$

Equation 2.13

At this point an increase in the folding mirror separation corresponds to a focussing of the mode short of mirror M_2 and hence an unstable resonator. In direct comparison to stability limit (ii), limit (iii), the strong objective limit, corresponds to the mode focussing in the short arm and collimated in the long arm as the effective focal length of the folding section is now equivalent to the short arm length L_1.

$$b_{iii} = \frac{4L_1R - R^2}{4L_1 - 2R} + d\left(1 - \frac{1}{n^3}\right)$$

Equation 2.14

Increasing the folding section further traverses the second stability region, the low misalignment (LMS) region. In this region the cavity mode is weakly focussed at each end mirror and is therefore less sensitive to misalignment of the end mirrors. The final stability limit (iv), the conjugate-plane limit, is reached when the cavity mode is tightly focussed at each end mirror.

$$b_{iv} = \frac{4L_1L_2R - L_1R^2 - L_2R^2}{(2L_1 - R)(2L_2 - R)} + d\left(1 - \frac{1}{n^3}\right)$$

Equation 2.15

In this case the end mirrors lie in the conjugate planes of the folding section and an object at one end-mirror is imaged at the other. On this limit the cavity mode is vanishingly small at each end mirror and any increase in folding mirror separation will focus the mode short of M_1 and M_2. Figure 2.9 below shows graphically the beams in the same resonator as Figure 2.8 at each stability limit.

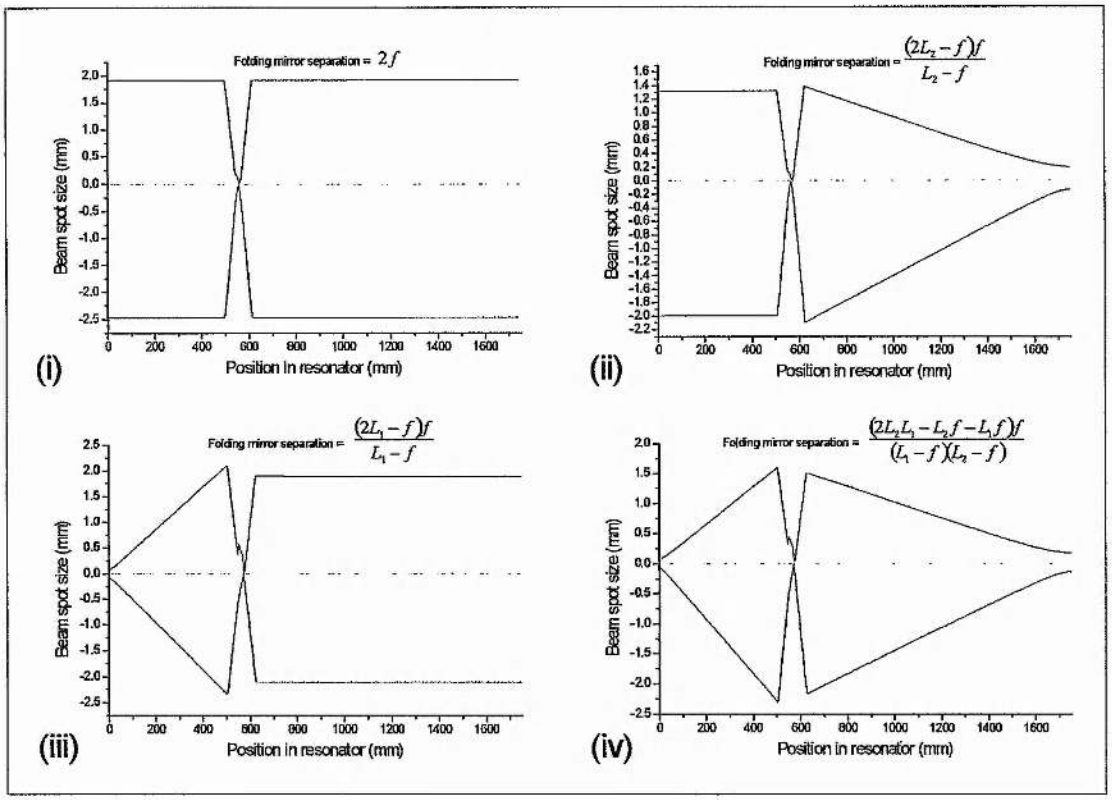

Figure 2.9 Behaviour of the cavity mode at each of the stability limits in the Ti:sapphire resonator of Figure 2.8, the folding mirror separation for each limit is shown as a function of f the focal length of the curved mirrors $(R/2)$ *and the arm lengths* L_1 *and* L_2.

Stability limit	Name	Folding mirror separation $(R_1 \neq R_2)$	Folding mirror separation $(R_1 = R_2 = R)$
b_i	planar-confocal limit	$\frac{1}{2}R_1 + \frac{1}{2}R_2$	R
b_{ii}	weak-objective limit	$\frac{2L_2R_1 + 2L_2R_2 - R_1R_2}{4L_2 - 2R_2}$	$\frac{4L_2R - R^2}{4L_2 - 2R}$
b_{iii}	strong objective limit	$\frac{2L_1R_1 + 2L_1R_2 - R_1R_2}{4L_1 - 2R_1}$	$\frac{4L_1R - R^2}{4L_1 - 2R}$
b_{iv}	conjugate-plane limit	$\frac{2L_1L_2R_1 + 2L_1L_2R_2 - L_1R_1R_2 - L_2R_1R_2}{(2L_1 - R_1)(2L_2 - R_2)}$	$\frac{4L_1L_2R - L_1R^2 - L_2R^2}{(2L_1 - R)(2L_2 - R)}$
Plane – Plane rod correction factor		$+d\left(1 - \frac{1}{n}\right)$	Brewster-angled rod correction factor $+d\left(1 - \frac{1}{n^3}\right)$

Table 2-1 Summary table of the mirror separations at the stability limits of a four mirror resonator with equal and unequal folding mirror ROC, the correction factors to the ultimate mirror separations for a plane/plane cut and a Brewster-angled rod between the folding mirrors is also given.

The Magni model

Since the first observations of self-modelocking[7], numerical and analytical models[4,8,9] have been suggested that describe the effect the nonlinear lensing has on the cavity modes. Building on a model which described the effect of a propagation through a Kerr medium on the complex Gaussian beam parameter[10], Magni and co-workers developed a practical formalism for a resonator incorporating a Kerr medium[3]. This formalism, based upon the aberrationless theory of self-focussing for propagating Gaussian beams showed that the Kerr nonlinearity could be represented by an ABCD matrix $\mathbf{M_k}$. This allowed the well-established 'ABCD law' of beam propagation in a linear optical system to be used for the design of a self-modelocked laser[11]. Although $\mathbf{M_K}$ is not strictly an ABCD matrix, as the individual elements depend on the input beam

parameters, the matrix can be used iteratively to model the effects of a Kerr medium within a laser resonator. Despite the apparent simplicity of the approach suggested by Magni *et al* the model gives a good agreement with more complex numerical investigations[8,12]. In the theory of aberrationless propagation a circularly symmetric Gaussian mode incident on a Kerr medium emerges as a Gaussian mode operated on by a scaling factor that varies with z. Expressions may then be derived for the spot size $w(z)$, wavefront radius of curvature $R(z)$ and phase $\phi(z)$ of this emerging mode:

$$w^2(z) = w_1^2\left[\left(1+\frac{z}{R_1}\right)^2+\left(\frac{\lambda z}{\pi n_0 w_1^2}\right)^2\left(1-\frac{P}{P_c}\right)\right]$$

Equation 2.16

$$\frac{1}{R(z)} = \left(\frac{w_1}{w(z)}\right)^2\times\left[\frac{1}{R_1}+\frac{z}{R_1^2}+z\left(\frac{\lambda}{\pi n_0 w_1^2}\right)^2\left(1-\frac{P}{P_c}\right)\right]$$

Equation 2.17

$$\phi(z)-\phi_1 = \frac{1-3P/2P_c}{\sqrt{1-P/P_c}}\left[\arctan\left(\frac{\pi n_0 w^2(z)}{\lambda R(z)\sqrt{1-P/P_c}}\right)-\arctan\left(\frac{\pi n_0 w_1^2}{\lambda R_1\sqrt{1-P/P_c}}\right)\right]$$

Equation 2.18

where w_1, R_1 and ϕ_1 are the initial values at $z = 0$, P is the intracavity power and P_c is the critical power for self-focussing given by,

$$P_c = \frac{c\varepsilon_0\lambda^2}{2\pi n_2}$$

Equation 2.19

where ε_0 is the permitivity of free space.

Note that as $P_c \to \infty$ Equations 2.17 to 2.19 revert to the expressions describing the propagation of a Gaussian beam in a homogeneous medium of refractive index n_0. When $P > P_c$ the spot size will vanish after a certain propagation distance through the medium depending on the initial beam parameters. Working backwards from Equations 2.17, 2.18 and 2.19 it is possible to define a ray transfer matrix **M** representing the Kerr medium as

$$\mathbf{M} = \sqrt{1-\gamma}\begin{pmatrix} 1 & d_{eff} \\ -\gamma/(1-\gamma)d_{eff} & 1 \end{pmatrix}$$

Equation 2.20

where $d_{eff} = d/n_0$ is the length of the medium for $P = 0$ and

$$\gamma = \left[1 + \frac{1}{4}\left(\frac{2\pi w_c^{\,2}}{\lambda d_{eff}} - \frac{\lambda d_{eff}}{2\pi w_0^{\,2}}\right)^2\right]^{-1} \frac{P}{P_c}$$

Equation 2.21

w_c is the spot size at the centre of the medium and w_0 is the spot size at the beam waist calculated at $p = P/P_c = 0$. As before when $p = 0$, **M** reduces to the ray transfer matrix for a dielectric block of refractive index n_0 and length d. We may separate the linear and nonlinear effects of **M** by factorising into two linear elements of length $d/2$ and a nonlinear element $\mathbf{M_K}$ in the following manner:

$$\mathbf{M} = \begin{pmatrix} 1 & d_{eff}/2 \\ 0 & 1 \end{pmatrix} \mathbf{M_K} \begin{pmatrix} 1 & d_{eff}/2 \\ 0 & 1 \end{pmatrix}$$

Equation 2.22

where to a first order approximation (γ small),

$$\mathbf{M_K} \approx \begin{pmatrix} 1 & -\gamma d_{eff}/4 \\ -\gamma/d_{eff} & 1 \end{pmatrix}$$

Equation 2.23

We can now more readily appreciate that $\mathbf{M_K}$ represents (to a first order approximation) the effect of a propagation through a thin lens of focal length $f_k = d_{eff}/\gamma$ 'self-focussing' and a propagation over a negative distance $z_k = -\gamma d_{eff}/4$ 'self-shortening'. By treating $\mathbf{M_K}$ as a linear element with a fixed value of γ as a starting point it is possible to express the spot size w and wavefront radius of curvature R in a plane within the resonator as functions of γ, $w = w(\gamma), R = R(\gamma)$. Starting from that reference plane, assuming linear propagation, the spot size in the centre of the Kerr medium and at the beam waist, may be determined. By substituting these expressions into Equation 2.21 the beam power $p = P/P_c$ can also be expressed as a function of γ, $p = p(\gamma)$. The

relationship between the intracavity power and the spot size at this plane is now described parametrically by γ.

For reliable self-modelocking it is important to consider the effect of increasing intracavity power on the spot size as the pulses will evolve initially from a cw field. For this reason the most useful parameter for optimisation of modelocking is the 'small signal relative spot size variation' or Kerr lens sensitivity δ evaluated at $p = 0$ defined as:

$$\delta = \left[\frac{1}{w}\frac{dw}{d(p)}\right]_{p=0}$$

Equation 2.24

For a negative value of δ any small increase in the intracavity power will cause the spot size at the plane in question to shrink, or more importantly at an aperture placed in this plane, and act as a fast saturable absorber. The Kerr lens sensitivity δ may be calculated for all points inside the cavity (except inside the gain medium) but is found to experience maximum values at a cavity end mirror where an explicit expression for δ may be derived:

$$\delta = -\frac{1}{2}\frac{\alpha + \alpha_2 S}{\alpha^2 + \alpha_2^2 + \alpha_1 + 2\alpha_1\alpha_2 S}$$

Equation 2.25

where S is the stability parameter and,

$$\alpha_1 = \frac{2B_1D_1}{d_{eff}} - \frac{A_1C_1d_{eff}}{2} \text{ and } \alpha_2 = \frac{2B_2D_2}{d_{eff}} - \frac{A_2C_2d_{eff}}{2}$$

Equation 2.26

where $A_0 \to D_0$, $A_1 \to D_1$ and $A_2 \to D_2$ are the elements of the ABCD matrices defined in Figure 2.10 below.

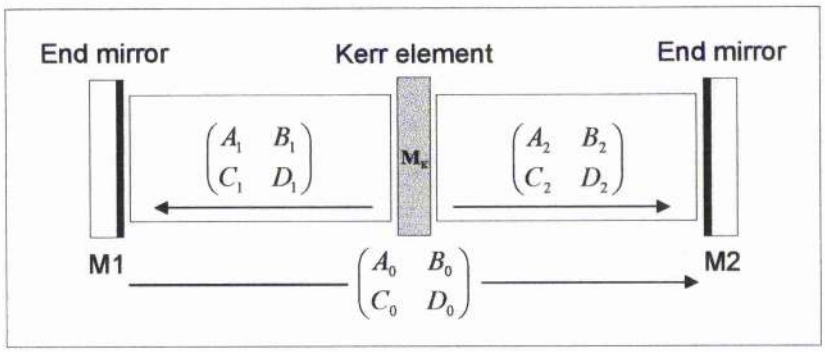

Figure 2.10 Definition of the single pass propagation ABCD matrices used in Equation 2.26.

The Magni Plot

Figure 2.11 shows a schematic of a typical Z-fold cavity used for self-modelocked Ti:sapphire lasers. The stability parameter described earlier is strongly dependent on the distance between the folding mirrors, and the focussing effect of the Kerr medium varies greatly with its position around the cavity focus[13]. For this reason it is useful to plot δ at the cavity end mirror (where an aperture is placed) as a function of the folding mirror separation b and the rod position a in order to optimise the cavity configuration for hard-aperture modelocking. It is immediately obvious from the plot (Magni plot) how to align the laser for a optimum nonlinear loss at the aperture.

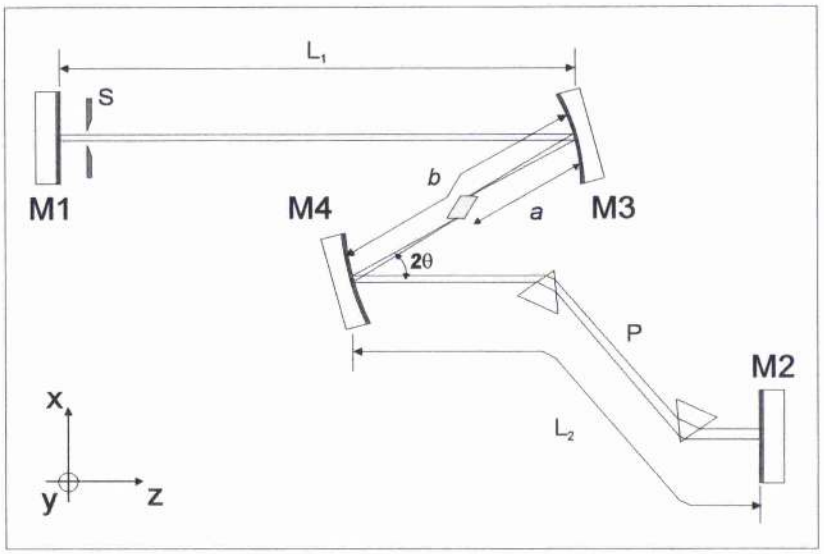

Figure 2.11 Typical resonator configuration of a self-modelocked Ti:sapphire laser where M1, M2 are planar mirrors, M3, M4 concave folding mirrors (100 mm ROC. $2\theta \approx 30°$), b is the folding mirror separation, a is the rod position, S is a slit used as a hard-aperture for modelocking and the gain medium is a 20 mm Brewster-angled Ti:sapphire rod.

Figure 2.12 shows a Magni-type plot of $\delta(a,b)$ for an asymmetric Ti:sapphire resonator where L_1 = 500 mm and L_2 = 1100 mm and the limits of stability (i), (ii), (iii) and (iv) are equivalent to those shown in Figure 2.8.

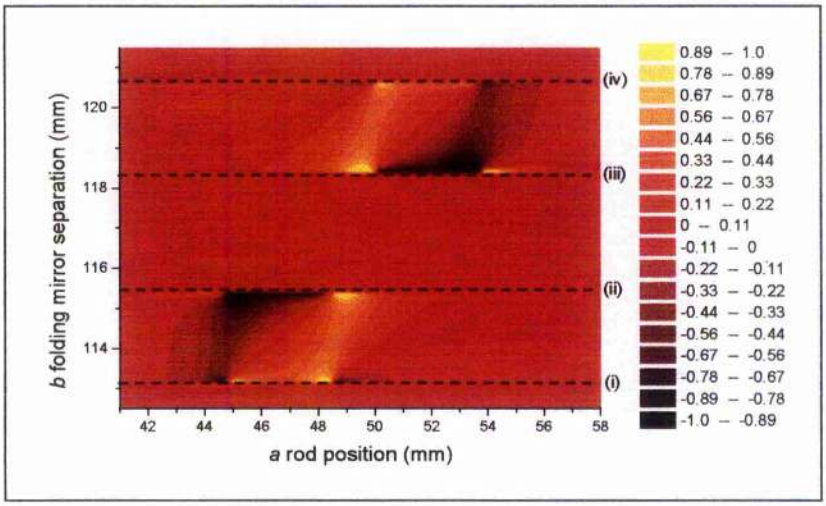

Figure 2.12 A Magni plot of δ(a,b) for an asymmetric Ti:sapphire resonator where L_1 = 500 mm and L_2 = 1100 mm and (i), (ii), (iii) and (iv) are the limits of stability.

It can be seen from Figure 2.12 that the maxima of δ lie close to the stability limits. This is because the maximum values of δ, δ_{max} *and* δ_{min} are related to the stability factor S by:

$$\delta_{\max,\min} = \pm\frac{1}{2\left(\sqrt{1-S^2}\right)}$$

Equation 2.27

and clearly as $|S| \to 1$, $\delta_{\max,\min} \to \pm\infty$. This implies, as has been verified experimentally[14,15], that a laser's propensity to modelock is greatly enhanced close to a cavity stability limit. It is obvious from our discussion of resonator stability that there will exist some optimum point for modelocking close to, but not on, a stability limit, as a resonator on its stability limit is critically stable, making reliable operation highly sensitive to cavity misalignment.

In the case of a symmetric resonator, however, with arms of equal length, the weak-objective (ii) and strong-objective (iii) limits will coincide resulting in a confocal resonator with a well-behaved transverse mode and no power reduction. In this configuration the laser may be operated close to the limit without compromising operation and hence the magnitude of δ may be made arbitrarily large. Figure 2.13 shows a Magni plot for the same resonator as Figure 2.12 but with equal length cavity arms $L_1 = L_2 = 800$ mm.

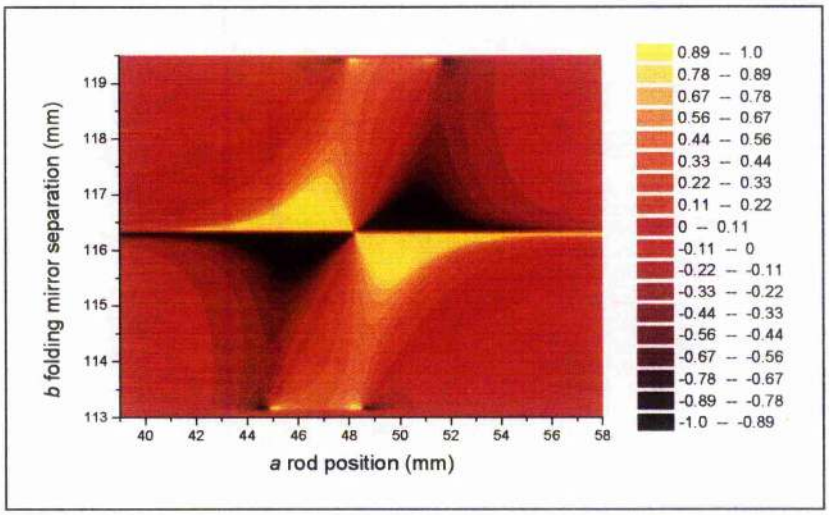

Figure 2.13 A Magni plot of δ(a,b) for a symmetric Ti:sapphire resonator where $L_1 = L_2 = 800$ mm.

Two conclusions may be drawn from the plots in Figure 2.12 and Figure 2.13, firstly the laser will become easier to modelock as the cavity arms approach an equal length due to the increase in size of the region where $\delta < 0$ and secondly the maxima of δ coincide with the cavity mode focussed on the end of the rod as predicted in the previous section. It is interesting to note here that although the strongest Kerr lens will occur when the

cavity waist, and hence the centre of a distributed lens, is coincident with the centre of the Ti:sapphire rod, this will, by the argument raised earlier, have minimal effect on the cavity mode but a lens centred on or near the end of a rod will have a maximum effect. This is due to the fact that the self-focussing and self-shortening effects mentioned earlier may not be treated independently and it is their combined effect that must be considered. It was thought that true self-starting operation of a self-modelocked laser was not possible, as pulsed operation must initiate from noise fluctuations that would not have the required intensity to experience sufficient self-focusing. For this reason the standard methods to initiate self-modelocking was to tap or vibrate an end mirror or to apply a loss modulation into the cavity, via a regenerative amplification scheme[16]. Cerullo *et al*[15] were able to show, using the model described in this chapter, that δ could be made very negative with careful alignment of the cavity and that noise already present within the cavity was sufficient for pulse build up and a self-starting of the modelocked operation.

Astigmatism

The model outlined above does not take into account the full effects of cavity mode asymmetry or astigmatism present in most conventional self-modelocked resonators. These so-called 'astigmatically compensated' resonators ensure a stable cavity with a near-circularly-symmetric mode in the cavity arms. As shown previously, (see Figure 2.7) the cavity mode in the folding section may be far from symmetric. In an extension to the above model the effects of astigmatism were initially investigated by splitting the cavity essentially into two separate resonators[14]. These two resonators described the behaviour of the laser in the tangential (xz) and sagittal (xy) orthogonal planes and hence a separate δ could be calculated for both cases. Although the model was derived for circularly symmetric Gaussian beams it was still possible to show that in general the value of the Kerr lens sensitivity increased in the tangential plane and decreased in the sagittal plane.

To more fully include the effects of astigmatic Gaussian beams in a resonator, Magni and co-workers derived an analytical formalism that took into account the coupled nature of the tangential and sagittal planes of the resonator[17]. The formalism was again based on the aberrationless propagation theory and low power approximation ($P << P_c$) and provided a set of coupled solutions to the propagation equations by splitting the

Kerr medium into thin slices and integrating over the length of the crystal. Magni showed that the propagation of an astigmatic beam could be substantially different to that of a symmetric beam. In the same manner as the previous model these solutions could be used in conjunction with the ABCD law to calculate, in closed form, the self-consistent Gaussian mode in an astigmatic resonator containing a Kerr medium. Firstly the spot-size variation on one of the end mirrors that is due to a thin slice of the Kerr medium is calculated

$$d\delta_{1x} = \left(\frac{1}{2\omega_{1x}}\frac{d\omega_{1x}}{d\phi_x}\right)_{\phi_x=0}\left(\frac{d\phi_x}{dp}\right)_{p=0}$$

Equation 2.28

where the subscript for δ_{1x} implies δ calculated in the tangential plane at end mirror M1 and ϕ_x is the dioptric power of the thin slice of Kerr medium given by:

$$\phi_x = p\left(\frac{\lambda}{n\pi}\right)^2\left(\frac{\omega_x}{\omega_y}\right)^{1/2}\frac{1}{\omega_x{}^2}dz$$

Equation 2.29

Describing the beam parameters in Equation 2.28 in terms of the elements of the ray matrices of the resonator (for $p=0$) and integrating over the length of the crystal yields,

$$\delta_{1x} = -\frac{1}{n}\left(\frac{1-S_y{}^2}{1-S_x{}^2}\right)^{1/4}\int_0^L\left|\frac{\tilde{B}_x}{\tilde{B}_y}\right|^{1/2}\times\frac{B_{2x}D_{2x}S_x + B_{1x}D_{1x}}{\tilde{B}_x{}^2}d\zeta$$

Equation 2.30

where ζ is the longitudinal co-ordinate of the thin slice $d\zeta$ in the crystal, $\tilde{B}_x$ and $\tilde{B}_y$ are the elements of the round-trip matrices in the tangential and sagittal planes starting from position ζ (see Figure 2.10), B_{ix} and D_{ix} are elements of the one-way propagation matrices from ζ to end mirror M*i* and S_x and S_y are the stability parameters in the two planes defined by:

$$S_i = \frac{\tilde{A}_i + \tilde{D}_i}{2} = A_iD_i + B_iC_i$$

Equation 2.31

where $A_i \rightarrow D_i$ are the elements of the one-way matrices from M1 to M2 and the condition for a stable resonator is $-1 < S_x, S_y < 1$.[18] The optical system for determining the elements of the ray matrices is shown below in Figure 2.14.

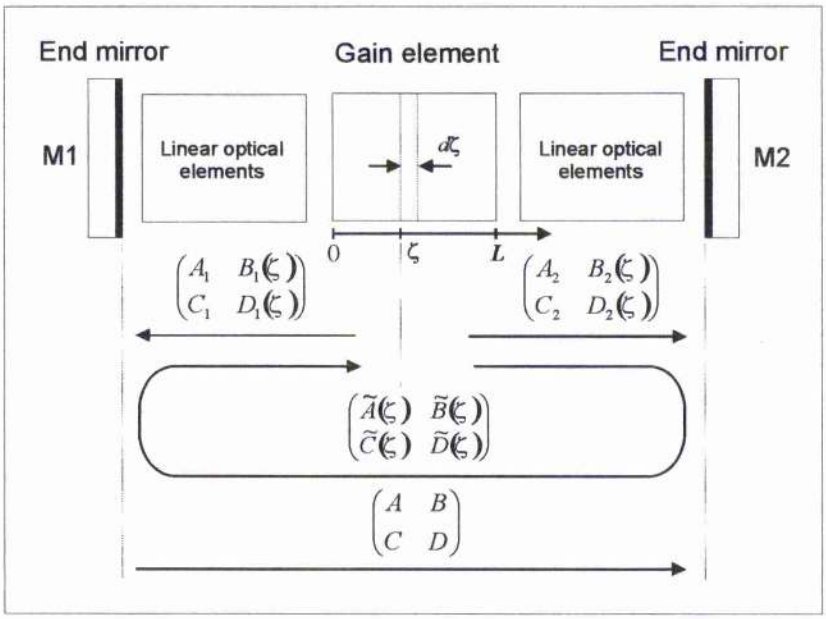

Figure 2.14 Definition of the single pass and round-trip matrices used in the full astigmatic treatment of a resonator containing a Kerr medium.

Figure 2.15 and Figure 2.16 below show Magni plots in the tangential and sagittal planes for an asymmetric (L_1 = 500, L_2 = 1100) and a symmetric ($L_1 = L_2$ = 800) Ti:sapphire laser.

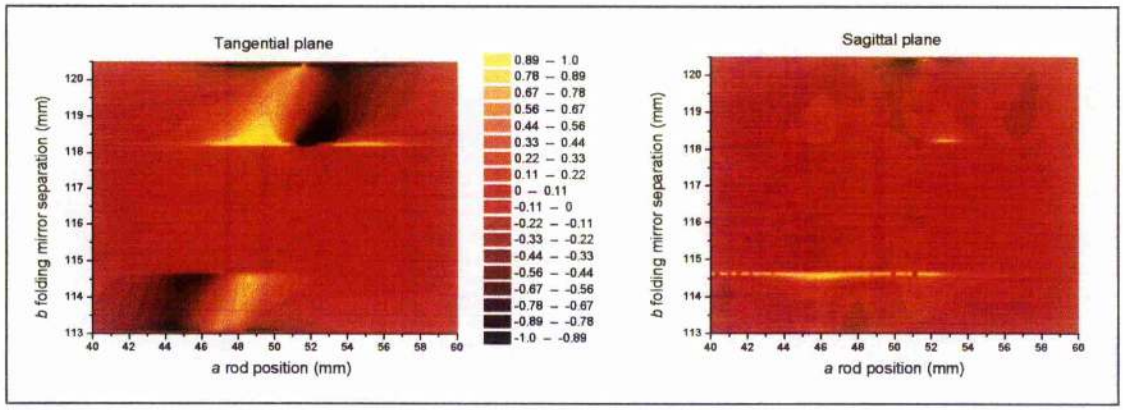

Figure 2.15 Magni plots in the tangential and sagittal planes for an asymmetric Ti:sapphire laser, L_1 *= 500,* L_2 *= 1100.*

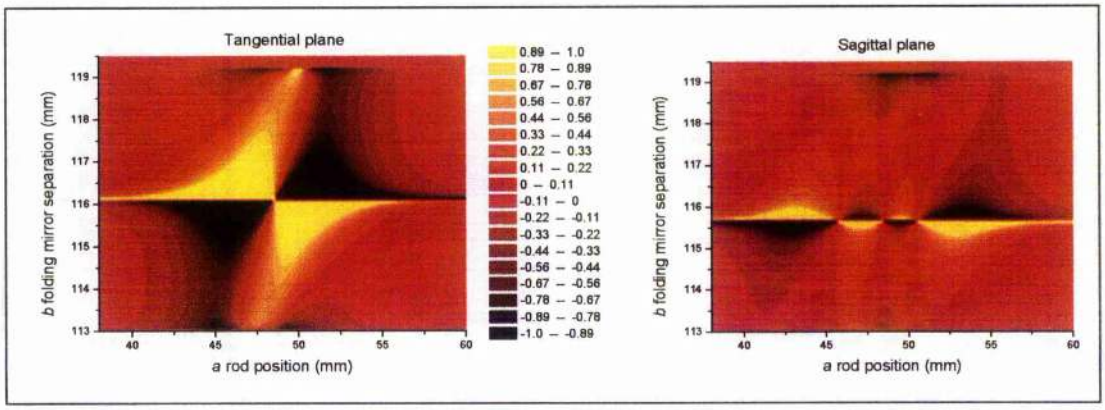

Figure 2.16 Magni plots in the tangential and sagittal planes for a symmetric Ti:sapphire laser, $L_1 = L_2 = 800$.

The conclusions of this full treatment are that the effects of astigmatism do indeed reduce the Kerr lens sensitivity in the sagittal plane and increase it in the tangential plane. Cerrulo verified experimentally[14,15] that hard-aperture modelocking could not be achieved in a nearly symmetric resonator with a slit shaped aperture cutting the beam in the sagittal plane. It can therefore be concluded that the optimum cavity configuration for the hard-aperture modelocking described by the Magni model is a symmetric cavity with a folding mirror separation

$$b_{optimum} = \frac{4LR - R^2}{4L - 2R} + d\left(1 - \frac{1}{n}\right)$$

Equation 2.32

such that the laser is aligned in the centre of its extended stability region ($S = -1$) and the distance from the folding mirror nearest the intracavity aperture is described by

$$a_{optimum} = \frac{b_{optimum} - d\left(1 - \frac{1}{n}\right)}{2}$$

Equation 2.33

This ensures that the cavity mode is focussed (in the tangential plane at least) at the rod facet for maximum Kerr effect on the cavity mode.

Soft-aperture considerations

The Magni model has been built upon by a number of groups to include effects such as soft aperturing by the pumped volume in the gain medium[19], gain guiding[20,21], thermal

lensing[22] and astigmatic pump beams[23] in the modelocking prescription. For the resonators, materials and power levels discussed in the remainder of this thesis it is necessary to only look at the former of these effects; the soft-aperture modelocking.

When considering these models to produce a practical recipe for a laser system their relative complexity must be weighed against the perturbation they add to the Magni model, as the precise measurement of the parameters a and b in a real laser system is not, in general, a trivial problem. While they are perfectly valid from a theoretical scientific standpoint and for understanding the dynamics of modelocking and resonator orientation it is often easier, within a lab environment, to optimise a laser system empirically after the laser has been set up using a simpler model. With this in mind a simple extension to the Magni model, is to calculate $\delta_x(a,b)$ at a plane coincident with the pumped end of the gain crystal. This gives a rudimentary picture of the cavity's ability to improve the cavity/pump laser mode overlap with increasing intracavity power. Firstly $\delta_{1x}(a,b)$ is calculated at the end mirror M1 as normal, then by calculating the linear spot size w_{1x} at this mirror and applying the following relation

$$\delta_x = \frac{A_x^{\,2} - \left(\lambda B_x/\pi\omega_{1x}\right)^2}{A_x^{\,2} + \left(\lambda B_x/\pi\omega_{1x}\right)^2}\delta_{1x}$$

Equation 2.34

where $A_x \rightarrow D_x$ are the elements of the propagation matrix from the end mirror M1 to the crystal facet. It may be noted from Equation 2.34 that $|\delta_x|$ is always less than or equal to $|\delta_{1x}|$, in other words, the maximum Kerr lens sensitivity always exists at a cavity end mirror. This approximation for the calculation of soft-aperture effects is valid for the scope of this thesis as the resonators presented are used in conjunction with tightly focussed pump beams at the surface of gain media that have sufficiently high coefficients. Figure 2.17 below shows Magni plots at the pumped crystal facet in the tangential and sagittal planes respectively for the symmetric cavity of a laser: Figure 2.11. It can be seen that there remain large regions in the tangential plane where δ is sufficiently large and negative for the laser to be modelocked.

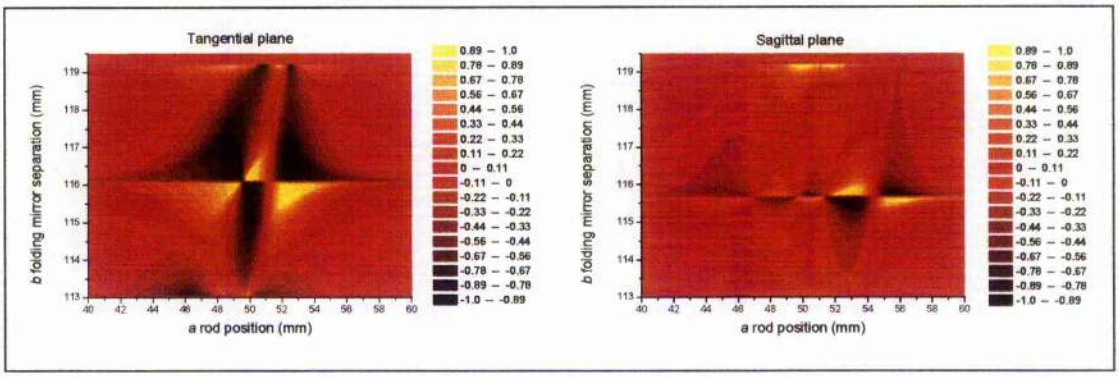

Figure 2.17 Magni plots at the pumped crystal facet in tangential and sagittal planes for a symmetric Ti:sapphire laser, $L_1 = L_2 = 800$.

Dispersion, intracavity power and pulse duration

Finally it is the optimisation of intracavity dispersion that ensures that a short pulse, once established in the cavity by the self amplitude modulation from the synthetic fast saturable absorber, will be stabilised across its corresponding bandwidth. The resulting steady-state pulse duration will be determined by the interplay of SPM and the net dispersion in a round-trip of the cavity. The relationship between the intracavity power, linear dispersion and pulse duration becomes increasingly important when designing a low-threshold laser. Based on the soliton approximation outlined in chapter 1 we may derive an expression for this relationship as:

$$E_p = \lambda w_{eff}^{\ 2} \frac{|k''|}{\Delta\tau_e n_2}$$

Equation 2.35

where E_p is the pulse energy, w_{eff} is the effective beam radius, k'' is the 2nd order dispersion or GVD parameter $d^2k/d\omega^2\big|_{\omega=\omega_0}$, $\Delta\tau_e$ is the 1/e pulse duration and n_2 is the nonlinear refractive index of the material. Figure 2.18 and Figure 2.19 below show plots of this relationship highlighting the dependence on k'' and the beam focussing respectively.

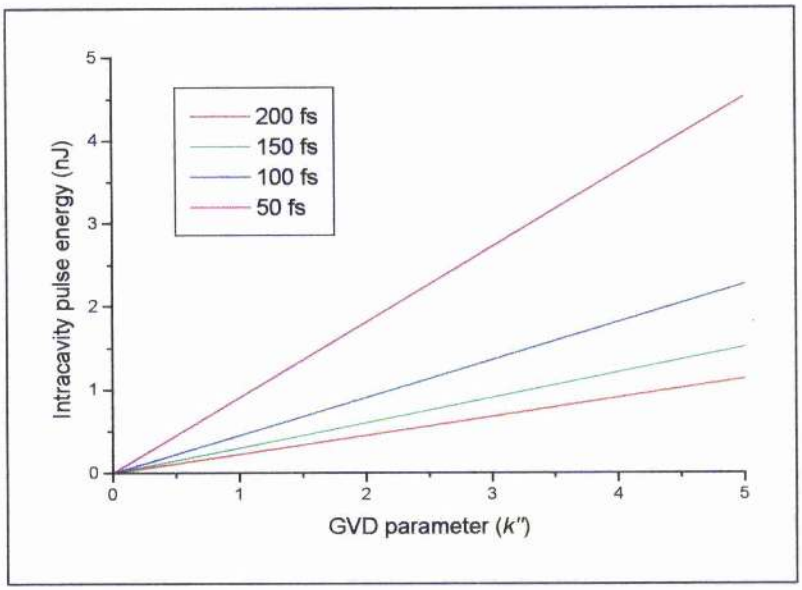

Figure 2.18 Plot of the pulse energy required to maintain particular pulse durations for different values of the GVD parameter in Cr:LiSGaF (beam waist fixed at 50 μm).

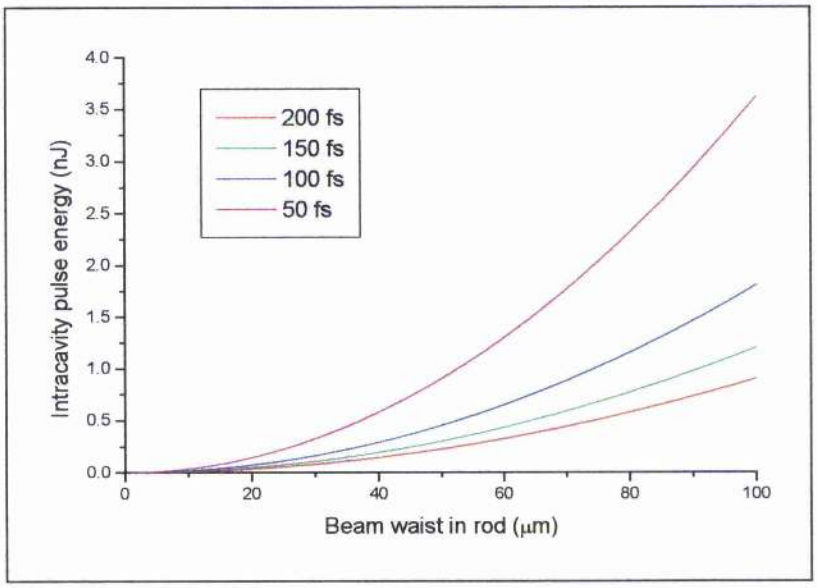

Figure 2.19 Plot of the required pulse energy to maintain a particular pulse duration as the cavity focussing is varied (GVD parameter fixed at 1 fs^2).

The figure above indicates that to maintain a pulse of minimum duration at low intracavity powers careful consideration of the net intracavity quadratic phase and cavity focussing must be made. From the earlier discussion of optimum self-focussing and low cw thresholds, however, the requirement for a tight intracavity focus has already been established. It is important to note here that the soliton model used in the derivation of Equation 2.35 becomes invalid for pulse durations substantially shorter than 100 fs or for beams that are too tightly focussed. Equation 2.35 also implies that

the required energy to sustain a pulse approaches zero as $k'' \to 0$, but this is unphysical and as this limit is reached the first-order soliton (N=1) will destabilise, forming higher-order solitons, as observed in multiple pulsing or harmonic modelocking[24]. The minimum pulse duration possible is also limited by higher order dispersive effects, which will have increasing dominance as $k'' \to 0$. Higher-order dispersion, namely cubic phase or TOD considerations become more important as the intracavity power and available pump power are reduced. Lemoff and Barty[25] used dispersive ray tracing to show that quadratic and cubic spectral phase may be simultaneously compensated by carefully considering the particular prism material and separation used in a Gordon and Fork prism pair. Figure 2.20 below shows the material cubic phase present in Cr:LiSAF and various prism glasses. The directly measured values of quadratic and cubic phase for bulk Cr:LiSAF[26] were used.

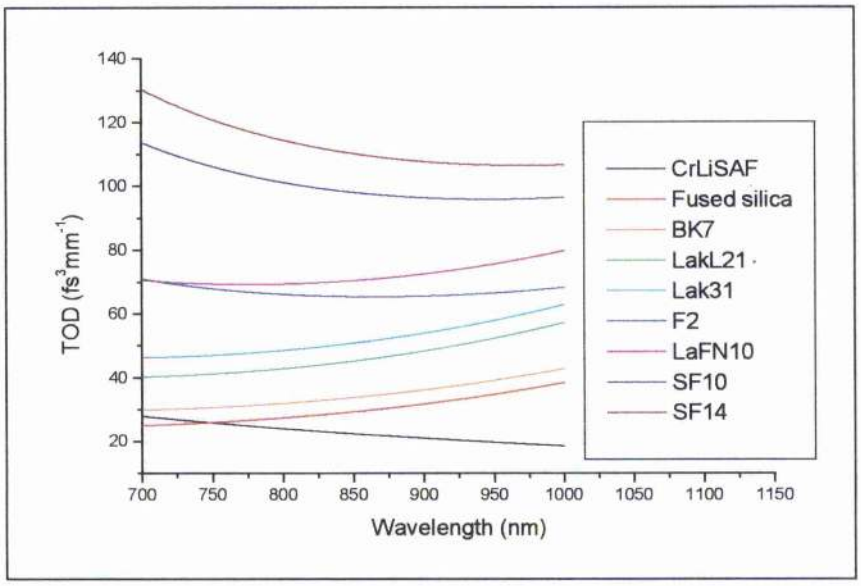

Figure 2.20 Material cubic phase present in Cr:LiSAF and various prism glasses between 700 and 1300 nm.

Although the cubic phase resulting from the bulk gain and prism material over the wavelength range of interest is always positive, the refractive or geometrical cubic phase introduced by the prism pair can be made sufficiently negative at a specific wavelength to compensate. The expression for the refractive cubic phase of a prism pair is[27]:

$$\frac{d^3P}{d\lambda^3} = l\cos\beta\left[\left(\frac{24}{n^3} - 48n\right)\left(\frac{dn}{d\lambda}\right)^3 - 24\frac{dn}{d\lambda}\frac{d^2n}{d\lambda^2}\right]$$

$$+ l\sin\beta\left[\left(\frac{12}{n^6} + \frac{12}{n^4} - \frac{24}{n^2} + 24n^2\right)\left(\frac{dn}{d\lambda}\right)^3 + \left(24n - \frac{12}{n^3}\right)\frac{dn}{d\lambda}\frac{d^2n}{d\lambda^2} + 4\frac{d^3n}{d\lambda^3}\right]$$

Equation 2.36

The net cubic phase in a cavity of this type is negative at shorter wavelengths and increases linearly with wavelength until at some point the cubic phase passes through zero and becomes positive. Increasing the intraprism path length shifts this zero cubic phase wavelength upwards. The fact that there must exist a finite amount of prism glass and a minimum separation of the prisms restricts the wavelengths for which the net cubic phase may be made equal to zero. The lower limit to the range over which compensation is possible λ_{0p} corresponds to the case of zero intraprism path (i.e. no prism glass) and here the cubic phase arising from any length of gain medium may be compensated for by the correct prism separation. The upper limit $\lambda_{\infty p}$ corresponds to an intraprism path length much greater than the gain medium length. In this case the contribution from the gain medium may be ignored and the geometrical cubic phase of the prism pair compensates for their material cubic phase. In theory, the zero cubic phase wavelength may be set anywhere between the bounds λ_{0p} and $\lambda_{\infty p}$, but in practice, the value of this wavelength will be restricted further by practical and realistic constraints on the prism pair. For example, the finite radius of the beam traversing the prism restricts the minimum intraprism path length achievable, because the entire beam must pass within the prism tips to avoid losses; typically ~4 mm is considered the minimum path length for a single prism pair (2 mm per prism). The separation of the prisms will also be constrained to an extent by the permitted footprint of the laser system.

Table 2-2 below gives the values of λ_{0p} and $\lambda_{\infty p}$ for 10 mm rods of Ti:sapphire and Cr:LiSAF with various prism materials.

Gain Medium	Ti:sapphire		Cr:LiSAF	
Prism Material	λ_{0p} (nm)	$\lambda_{\infty p}$ (nm)	λ_{0p} (nm)	$\lambda_{\infty p}$ (nm)
Fused Silica	852	847	833	847
BK7	877	880	868	881
LakI21	884	887	876	886
LaK31	904	917	906	916
F2	1006	1104	1097	1108
SF10	1038	1178	1197	1206
SF14	1056	1232	1225	1233

Table 2-2 Calculated zero-cubic-phase wavelength ranges for several combinations of Brewster prism and 10 mm of laser gain materials (zero quadratic phase assumed).

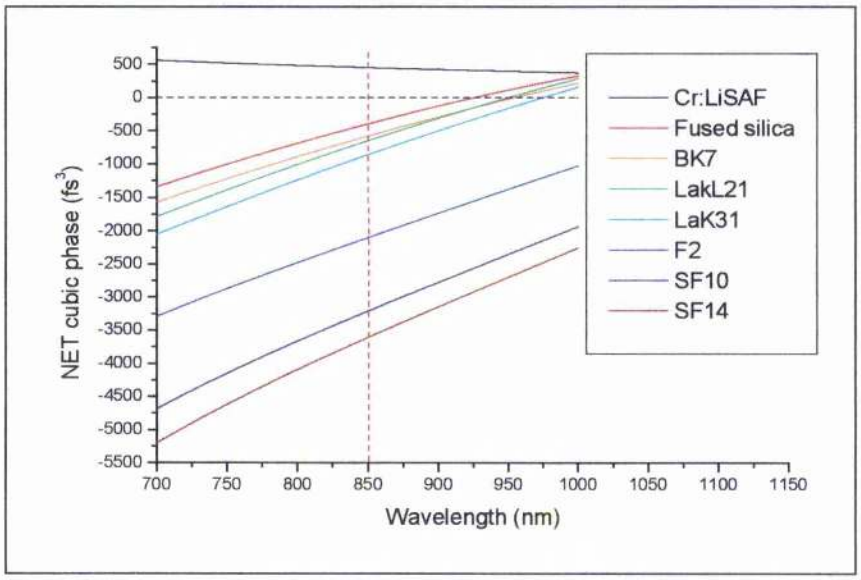

Figure 2.21 Calculated round-trip cubic phase for a 10mm crystal of Cr:LiSAF and the combined material and geometrical cubic phase of various prism materials with 4 mm of prism glass (assuming zero round-trip quadratic phase), the dashed line represents the typical centre operating wavelength of a Cr:LiSAF laser.

The graph in Figure 2.21 above shows separately the round-trip cubic phase for 4 mm of various types of prism glass and 10 mm of Cr:LiSAF calculated for zero round-trip quadratic phase. Indicated on the graph is the typical centre operating wavelength of a

Cr:LiSAF laser around 850 nm. The correct choice of prism material for a particular laser system will depend on the amount of excess negative quadratic and cubic phase required to compensate for SPM in the gain medium and cubic phase arising from the cavity mirrors and coatings. The table below indicates the required prism glass and wavelength to achieve the desired net round-trip quadratic and cubic phase at 850 nm for a laser with various prism materials and a 10 mm crystal of Cr:LiSAF.

	0 fs^2, 0 fs^3		-150 fs^2, 0 fs^3		-150 fs^2, -450 fs^3	
	λ (nm)	Separation (mm)	λ (nm)	Separation (mm)	λ (nm)	Separation (mm)
Fused Silica	839	347	882	457	747	532
BK7	874	272	918	358	785	416
LaKL21	881	175	921	225	804	259
LaK31	912	147	951	188	839	216
F2	1105	133	1155	175	1036	197
SF10	1204	93	1250	119	1149	133
SF14	1232	86	1277	108	1180	120

Table 2-3 Calculated prism glass and separation needed to achieve the required net quadratic and cubic phase at 850 nm for a laser containing a 10 mm crystal of Cr:LiSAF.

The above consideration may be extended for higher order dispersion terms and provide an optimised phase response of many orders. The successful use of this type of advanced dispersion compensation has led to the demonstration of a number of ultrafast laser systems with pulse durations ~11fs [28].

More compact dispersion compensating schemes such as Gires-Tournois interferometers (GTIs)[29] or chirped mirror structures[30] have also been used to good effect in Cr:LiSAF and other colquiriite host laser systems to minimise higher order dispersion and produce pulse durations as short as 65 fs. These systems, however, often incur higher insertion losses than a Brewster-angled prism pair and are therefore not as attractive for an efficient low-threshold femtosecond laser.

Summary of requirements

When considering the design of a laser cavity that will be used with limited or low pump powers the focussing of the pump and cavity laser modes in the gain medium is of utmost importance. The ability to make these tight foci coincide in the tangential and sagittal planes of the cavity is also very significant in reducing not only the CW lasing threshold but also the modelocking threshold as it will allow a much stronger more localised Kerr lens. Optimisation of the gain medium itself is also important as the threshold of a laser cavity depends greatly on the absorption coefficient, $\sigma\tau$ product and losses associated with the gain medium. The propensity of a resonator to modelock must be considered, at least to a first approximation. Finally, dispersive effects within the cavity must be carefully optimised to ensure efficient and reliable modelocked operation.

2.3 A Diffraction-limited pump source

The requirement of a diffraction-limited or near-diffraction-limited pump source in a low-threshold laser has already been highlighted. In order to develop efficient, ultrafast sources with low enough pump power requirements to allow pumping with narrow-stripe single-spatial-mode (SSM) laser diodes, it was first necessary to find a similarly near-diffraction-limited pump source with higher output power than generally obtainable from commercial SSM diodes. Under normal free-running conditions broad area semiconductor lasers emit higher powers than narrow-stripe laser diodes because the larger emission aperture reduces thermal and optical damage to the output facet and thus the risk of catastrophic damage. Unfortunately the width of these stripes, typically 50 μm, permit many spatial modes to oscillate and interfere to produce a broad, highly divergent beam in the far field (see Figure 2.22). It is possible, however, to spatially improve the output of these diodes dramatically to produce a near-diffraction-limited output using techniques known as injection-locking[31,32] and self-injection-locking.

Injection locking and Self-Injection Locking

Injection locking has been used widely in the improvement of laser output

characteristics[33-36]. In an injection-locked system, the output from a stable single longitudinal mode 'master' laser is used to seed a much higher power 'slave' oscillator. The injected signal locks the slave oscillator (essentially a multi-pass amplifier), to produce a higher power, more spectrally pure beam than the slave oscillator could possibly produce itself[37]. Injection locking was first demonstrated using He-Ne lasers[38], and has since been used in many other laser systems[39-46]. In semiconductor lasers injection-locking has significantly improved both the frequency and phase of an output beam to produce a more controlled laser source[33,34,47-53]. The phase control is essential in removing the far field interference and spatially improving the output of a diode. The models presented to describe spatial-injection-locking generally describe the laser as an emitter of a discrete set of 'spatial eigenmodes'[54] either as an array of small area emitters[55] or as one broad area emitter[56-59]. In general, an injected beam at a suitable angle will lock the phases of these emitters, altering the superposition of the eigenmodes to most closely match the beams profile.

In a self-injection-locked or cavity phase locked configuration[57,60-63], the injected beam takes the form of fluorescence which is fed back into the laser by a mirror placed just at the edge of the far-field free running output. In this manner a discrete number of spatial eigenmodes are selected to experience a lower threshold so they preferentially oscillate and produce a near-diffraction-limited quasi-Gaussian output in the far-field (see Figure 2.22).

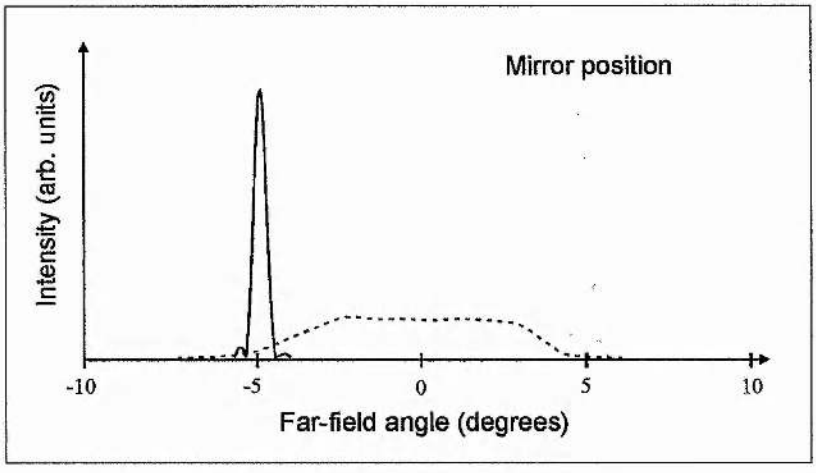

Figure 2.22 Resulting far-field output (solid line) of a broad area laser diode with a self-injection locking mirror just cutting the free-running far-field output (dashed line).

It is necessary to ensure that there is enough injected or 'fed-back' power to saturate the gain in the laser and suppress any free running or 'unlocked' laser output. The injected

power required to saturate the gain however, increases nonlinearly with the diode drive current. This is a problem when using the laser's own output to provide the injection-locking signal as the output power will increase only linearly with drive current. This implies that higher alignment precision is required for higher drive currents and that at some point the feedback will no longer be able to sustain single or near-single mode operation. As the diode drive current is increased beyond this point more and more modes will experience gain and the output beam quality will degrade. In practice a compromise will be reached between output power and injection alignment. Care must also be taken when optimising the output power from an SIL system as the power density across the diode facet is no longer uniform but highly localised at certain points and more likely to produce facet damage.

Using an injection locked system as a pump source is far from ideal because it requires an extended cavity and critical alignment for operation at high powers. However, as the key objective was to ultimately replace the broad area diode with narrow stripe single spatial mode diodes, high powers (>200 mW) were not a requirement and near-diffraction-limited beams with moderate output powers were readily achievable, lower current operation also reduced the risk of facet damage.

The Laser Diode

The extended cavity SIL broad area diode used initially in the development of low-threshold ultrafast sources at St. Andrews was an APT-Uniphase HB 067-500-130C semiconductor laser (see Figure 2.23) driven by a Spectra Diode Labs SDL-800 laser diode driver. This laser is a multiple quantum well AlGaInP device grown on a diamond substrate and antireflection coated for 670nm. The device was mounted on a thermoelectric cooler (TEC) and heat sink to allow more efficient operation and provide added protection against thermal damage. At room temperature and free-running the diode produced ~500mW for a drive current of approximately 1.1A. The same drive current produced ~750mW when the mounting plate was cooled to 13°C.

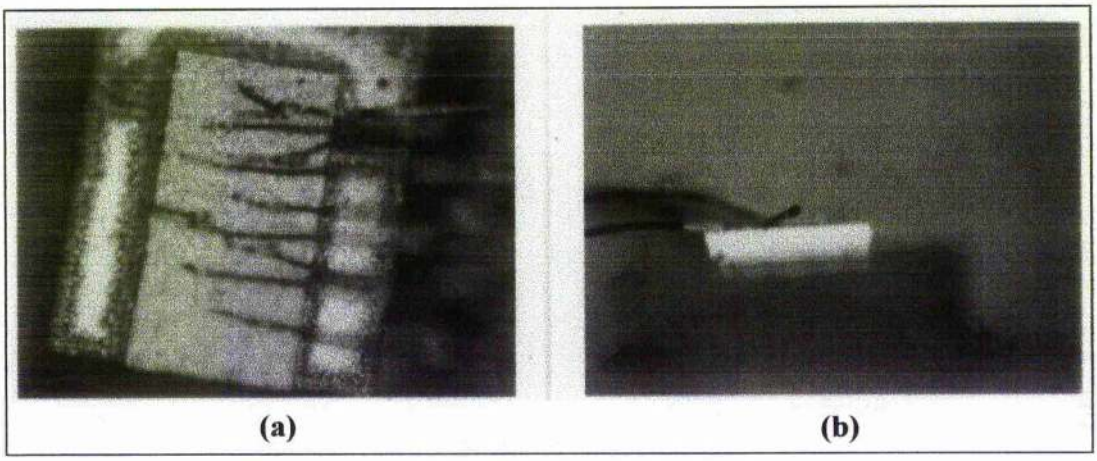

Figure 2.23 The APT-Uniphase HB-067-500-130-C semiconductor laser: (a) top surface (b) back facet, the bond wires are 25 μm in diameter.

The L-I characteristic of the laser is shown in Figure 2.24 below. When self-injection-locked the laser was supplied with ~600mA-650mA and the temperature maintained at ~15°C by a Marlowe Industries Inc. SE5020 Temperature controller.

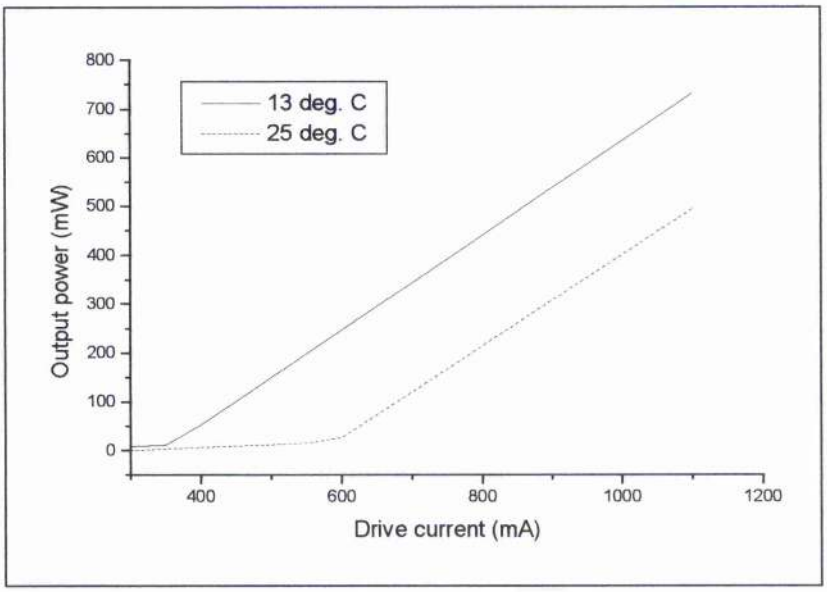

Figure 2.24 The L-I characteristics of the APT-Uniphase semiconductor laser HB-067-500-130-C at 13 °C and 25 °C.

The output of the laser was centred at 669nm ±0.2nm.

The Injection Locking Optics

To allow for an efficient feedback, the laser was focused in the diffraction-limited plane (perpendicular to the active stripe) and spatially extended in the non-diffraction-limited plane (parallel to the active stripe) at the feedback mirror. This was achieved by combining a 60mm focal length cylindrical lens in the non-diffraction-limited plane in conjunction with the initial tightly focusing (f~8mm) × 20 microscope objective collimating lens situated close to the diode facet (see Figure 2.25). The feedback mirror used was a high reflecting (HR) dielectric coated for 666 nm and cut with a flat edge to just clip the edge of the output from the diode.

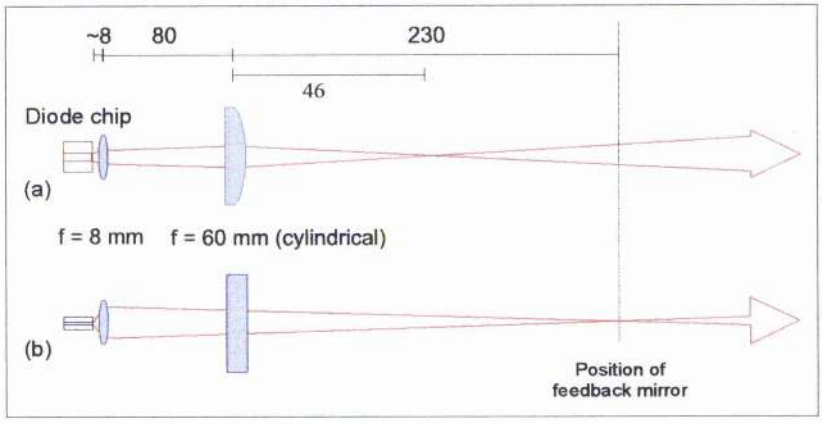

Figure 2.25 A schematic of the arrangement of the self-injection-locking optics, in the planes (a) parallel and (b) perpendicular to the diode active stripe, showing some typical dimensions of the self-injection-locked laser system (all lengths are in mm). The dashed line indicates the plane of the feedback mirror.

In the injection-locked plane the output from the diode takes the form of two lobes that appear either side of the path formerly taken by the unlocked beam (see Figure 2.26). The light within these contains ~85% of the beam energy within a quasi-Gaussian profile (see Figure 2.28).

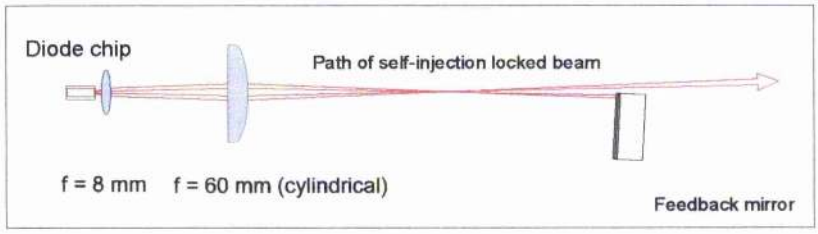

Figure 2.26 Schematic of the beams in the self-injection-locked laser cavity. The two beams sit at the edge of the unlocked beam profile. The output beam is collimated.

The coupling and injection locking optics together with some of the typical dimensions are described in Figure 2.27 below which clearly shows the extended nature of this type of pump source and hence this represents an undesirable feature for a compact laser

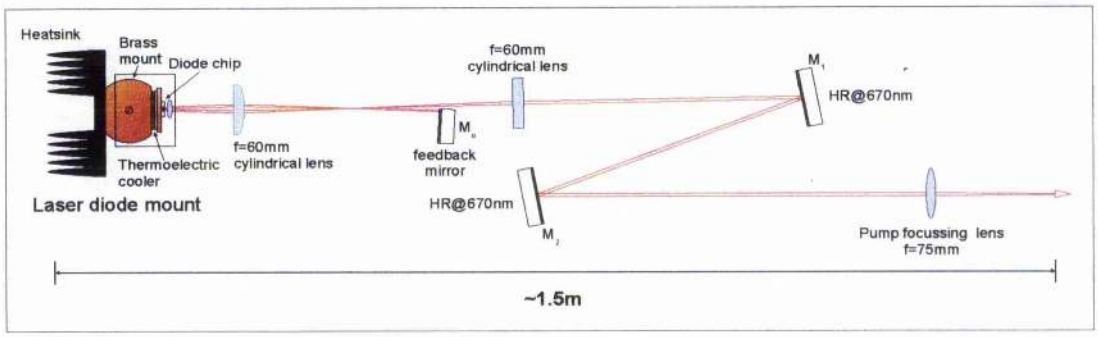

Figure 2.27 The injection-locked laser and the coupling optics required for the extended pump laser.

The two mirrors, M_1 and M_2, coated for high reflectivity at 666 nm allow the pump beam to be 'walked' ensuring an optimum overlap with the laser mode may be achieved. The second 60mm cylindrical lens collimates the pump beam in the diffraction-limited plane (perpendicular to the active stripe) and is necessary because the injection locking requires the laser to be focused onto the feedback mirror in this plane. The far-field output of the broad area AlGaInP laser in both injection-locked and unlocked conditions was measured using a linear CCD array and is shown in Figure 2.28. The laser produced ~170 mW at ~670 nm for 657 mA of drive current with a far-field divergence FWHM of 1.0±0.1°. The effect of the injection-locking can also be seen to narrow and upshift the spectrum as well as improving the beam quality. For the work presented in chapter 3 the Uniphase laser diode was replaced with a Coherent S-67-500C AlGaInP diode with almost identical specifications and characteristics. The Coherent diode was mounted in a hermetically sealed package with internal TEC and monitor photodiode adding extra facet protection against dust and condensation. A photograph of the extended SIL cavity with the Coherent diode is shown in Figure 2.29.

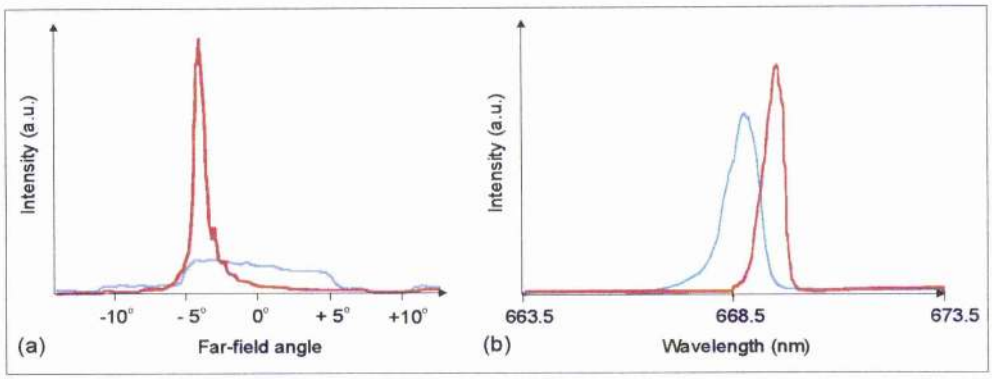

Figure 2.28 Output from the SIL laser under unlocked (blue) and locked (red) conditions at 657 mA drive current (169 mW output power): (a) far-field beam profiles of the locked (FWHM 1.0 ± 0.1°) and unlocked (FWHM 10 ± 1°) laser with the locking optics in place; (b) spectrum of the locked (FWHM 0.3 ± 0.2 nm) and unlocked (FWHM 0.5 ± 0.2 nm) laser.

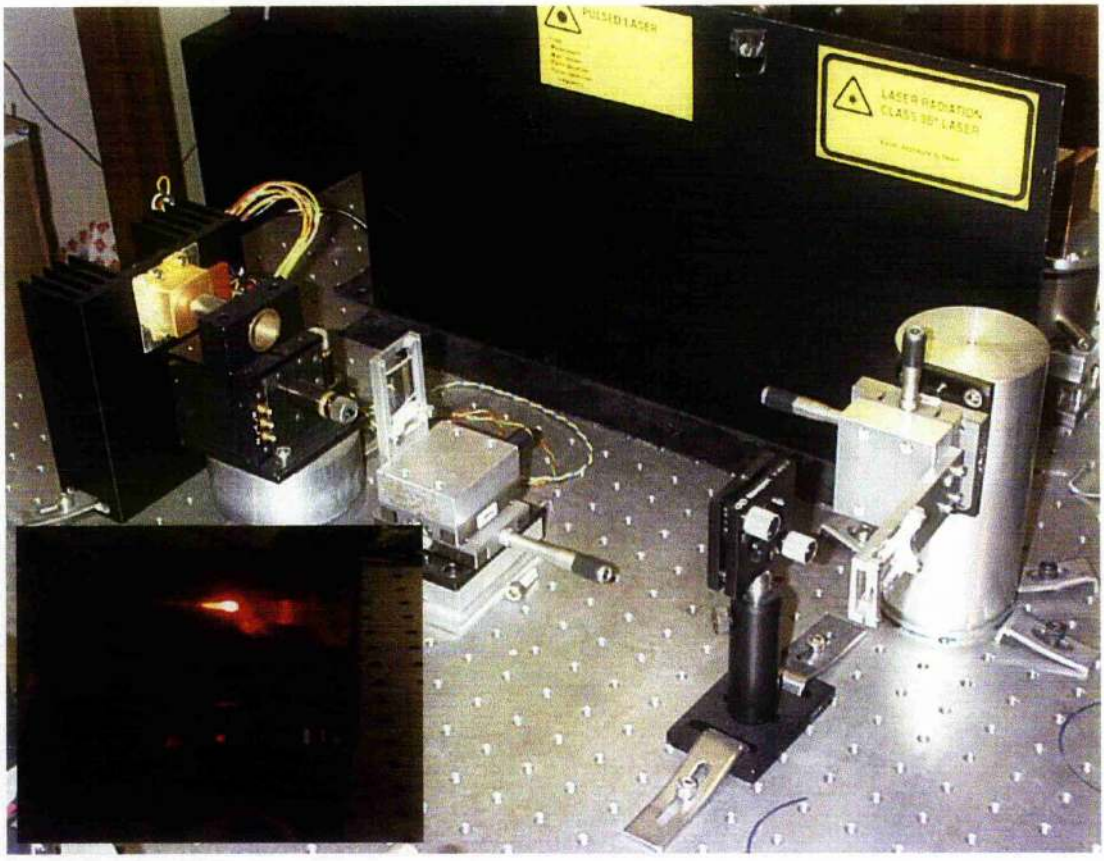

Figure 2.29 A Photograph showing the extended cavity of the self-injection locked Uniphase S-67-500C pump laser, the inset shows the injection-locked output beam.

The remainder of this chapter describes work primarily carried out by David Burns and Matthew P. Critten[64] although there was some overlap with the author on the Z-fold Cr:LiSGaF laser described in section 2.5. The reasons for including this work here are

three-fold: 1) it was the first system developed for the low-threshold work 2) several of the theoretical considerations of this chapter are elegantly demonstrated and 3) it is a useful comparison for subsequent laser systems. An introduction to the components common to the lasers described in this thesis is also given during the course of the following sections.

2.4 A low-threshold 'four-mirror' Cr:LiSAF laser

The Laser Cavity

The first laser system to take into account the points raised in the previous sections was the W-fold cavity configuration shown in Figure 2.30 below.

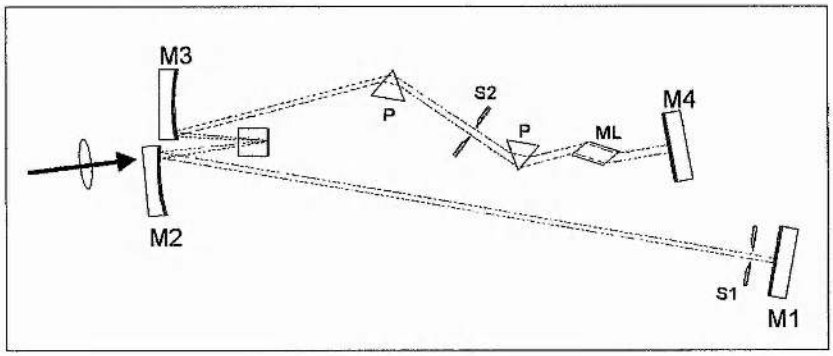

Figure 2.30 Schematic of the W-cavity: M1,M4 plane end mirrors; M2, M3 focusing mirrors; P dispersion compensation prisms; S1 tuning slit; S2 hard-aperture modelocking slit; ML quartz modelocker.

The gain crystal was a 3 % Cr^{3+} doped LiSAF crystal[65] cut in a 12 mm x 8 mm x 5 mm cuboid. One end of the crystal was coated for high reflectivity (HR) at 840 nm and anti-reflection (AR) for high transmission at 670 nm; the other end was AR-coated at 840 nm. The cavity mirrors were 25-mm diameter broadband coated BK7 substrates from LaserOptik GmbH. Each mirror had a reflectivity of 99.95% at 840 nm, >99.9% between 800 nm and 870 nm and was highly transmitting at 670 nm. The transmission loss of the mirrors was measured to be 0.08 % at the laser wavelength ~850 nm. The plane cavity end-mirrors M1 and M4 had a 30' wedge on the rear surface of each substrate to eliminate reflections back into the modelocked laser cavity. The folding section mirrors M2 and M3 were initially 100 mm radius of curvature (ROC) plano-convex mirrors; later replaced with 75 mm ROC mirrors. The Cr:LiSAF laser used an atypical 5-mirror 'W' cavity optically equivalent to the more conventional 4-mirror 'Z'

cavity arrangement, used most widely for self-modelocked lasers[66], except folded about the centre of the gain medium. Although it was never utilised this cavity configuration provided the possibility of pumping through the rear HR coated crystal facet with a tightly focused (highly divergent) beam from a broad area diode. To gain an optimum pump, cavity mode overlap for a low-threshold and efficient modelocking it was more efficient to focus the self-injection-locked pump beam through a folding section mirror. Intimate pumping through the crystal HR coating could have been used in conjunction with the SIL beam to increase the overall laser power once a low-threshold had been established. The pump laser light was focused into the Cr:LiSAF crystal by means of a 75 mm or 50 mm plano-convex lens placed closely behind the cavity folding mirror M2. The Cr:LiSAF laser cavity was symmetric with arms measuring 810 mm long with the 100 mm ROC mirrors and 820 mm with the 75 mm ROC mirrors.

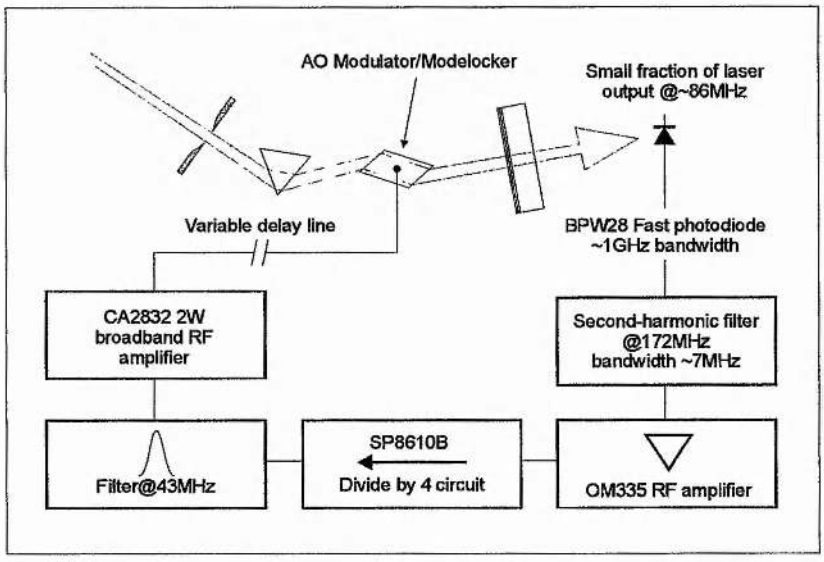

Figure 2.31 A schematic of the regenerative initiation scheme used with the W-cavity Cr:LiSAF laser.

Second-order dispersion or quadratic phase compensation was initially provided by an intracavity Brewster-cut SF14 prism pair. These were later replaced with prisms made from LaKL21, as they introduced less third-order dispersion into the cavity. A translatable intracavity slit was placed between the prisms as a tuning element. A second slit that acted as a hard modelocking aperture was placed at the end of the cavity arm adjacent to the pumped crystal facet. The light emitted from the end of the arm containing the prism pair was directed onto a fast photodetector to drive the regenerative initiation circuit shown in Figure 2.31 above. The circuit was connected to a 12 mm long Brewster-angled quartz AO modulator[67] placed at the end of this arm. The round-trip or intermode frequency of the cavity was ~86 MHz and the second

harmonic was used to drive the regenerative initiation circuit as this harmonic typically contains the most power.

CW Performance

By constantly reducing the pump power while adjusting the cavity for maximum output the laser was optimised for a low CW lasing threshold. The pump beam was attenuated with a variable neutral density (ND) filter wheel. The average output power from the Cr:LiSAF laser was monitored using a large-area silicon photodiode connected via a variable amplifier to an oscilloscope. Power measurements were made using a variety of calibrated thermal[68] and silicon power meters[69]. The CW threshold was 45mW with the 100 mm ROC mirrors and 35mW with the 75mm ROC mirrors. The maximum output power obtained for a pump power of 150 mW after the pump optics was ~1.2 mW from the rear surface of each HR mirror.

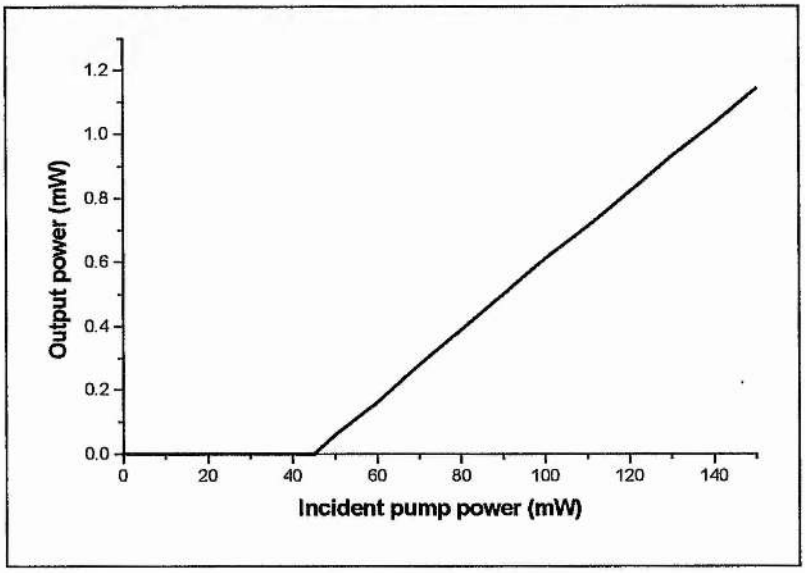

Figure 2.32 The CW power transfer characteristics of the diode-pumped Cr:LiSAF system with 100 mm ROC folding-section mirrors.

Modelocked Performance

The regenerative modelocking was initially optimised by slightly adjusting the cavity arm lengths. Once optimised the regenerative circuit was able to pick up and lock on to the second harmonic of the intermode beat frequency (172 MHz). In this state the laser was regeneratively modelocked producing picosecond pulses and the cavity required

only slight adjustment of the folding mirrors to become self-modelocked and give femtosecond pulses. Once the cavity was aligned for self-modelocking the 'regen' circuit initiated short pulse operation even after the pump path or cavity had been blocked for a time. Self-modelocking was initially achieved with 100 mm ROC folding mirrors and the SF14 prisms and as expected the Magni prescription for reliable self-modelocking (see Figure 2.33) coincided closely with the low CW threshold cavity alignments.

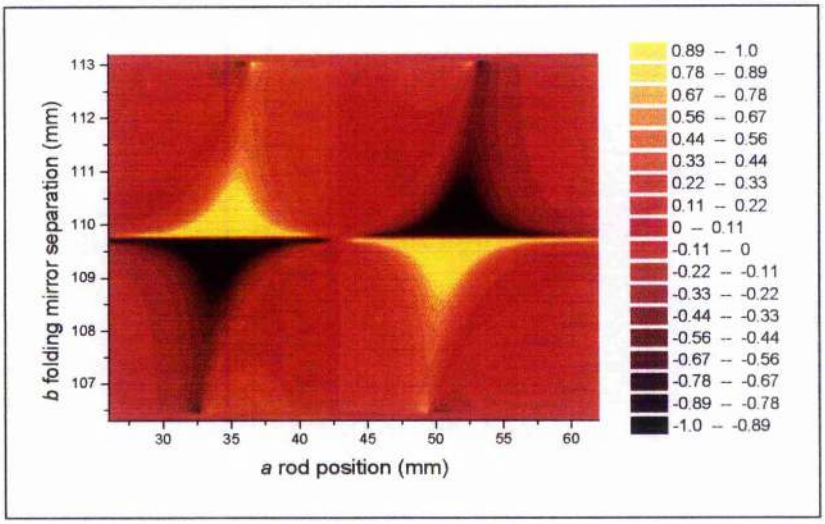

Figure 2.33 The Magni plot in the tangential plane for the W-cavity with 100 mm ROC folding-section mirrors.

With 150 mW of incident pump power the laser produced 60 fs pulses using LaKL21 prisms for lower cubic phase as described in section 2.2. Sub-100 fs pulses were obtained for incident pump powers as low as 88 mW. An interferometric autocorrelation and spectrum[70] for 97 fs pulses obtained with the 100 mm ROC. mirrors and LaK L21 prisms are shown in Figure 2.34.

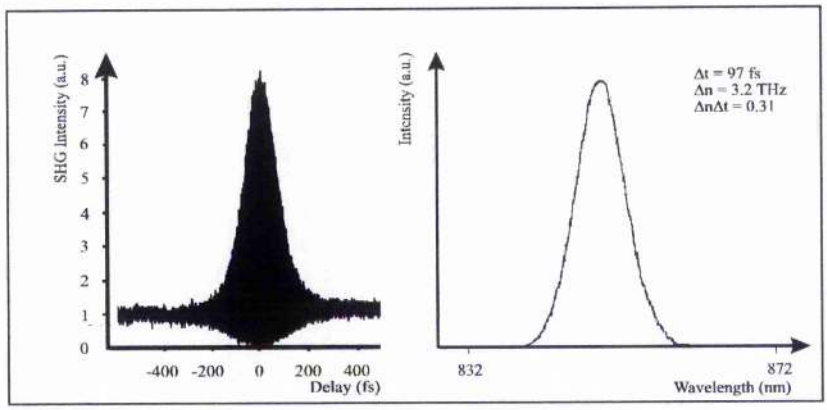

Figure 2.34 An interferometric autocorrelation and spectrum of a transform-limited 97 fs pulse obtained from the Cr:LiSAF laser with 100 mm ROC mirrors for 100 mW pump power.

The 100 mm ROC. folding mirrors were replaced with 75 mm ROC. mirrors to decrease the size of the cavity mode in the gain crystal reducing the cw threshold and increasing the power of the intensity dependent Kerr lens.

The shortest pulse durations achieved with 150 mW pump power and the 75 mm mirrors were 54 fs. Sub-100 fs pulses could be achieved with 70 mW incident pump power which represented a three-fold improvement over similar laser systems reported at the time[71] (193mW for sub-100fs pulses).

Table 2-4 below summarises the durations of the pulses obtained for each set of prisms combined with the different radius of curvature folding mirrors. As predicted in section 2.2 the reduction in the intracavity mode size in the crystal decreased the CW thresholds, modelocking thresholds and pulse durations. Careful consideration of prism material for cubic phase compensation also reduced the pulse durations. All the pulses were transform limited within the measurement errors assuming a $sech^2$ pulse shape. The cavity repetition rate was 86MHz in all cases.

	Prism material	Pump power 150 mW	Pump power 100 mW	Modelocking Threshold
100 mm ROC. mirrors	SF14	93 fs	140 fs	90 mW
	LaKL21	60 fs	99 fs	88 mW
75 mm ROC. mirrors	SF14	65 fs	77 fs	73 mW
	LaKL21	54 fs	65 fs	70 mW

Table 2-4 Pulse durations at 100 mW and 150 mW pump power for 100 mm ROC mirrors and 75 mm ROC. mirrors, and for SF14 and LaK L21 prisms.

Although the laser was based around the Magni prescription for hard-aperture modelocking, the laser often operated in a soft-aperture regime when adjustments to the modelocking slit had little or no effect on the output pulses. The Magni prescription seemed to lead to a cavity geometry that is good for both modelocking regimes. This soft-aperture operation did not occur at the exact configuration, which gave the best hard-aperture modelocking, but the laser needed little adjustment to get from one regime to the other. The most stable pulses were produced when the laser operated in the soft-aperture regime.

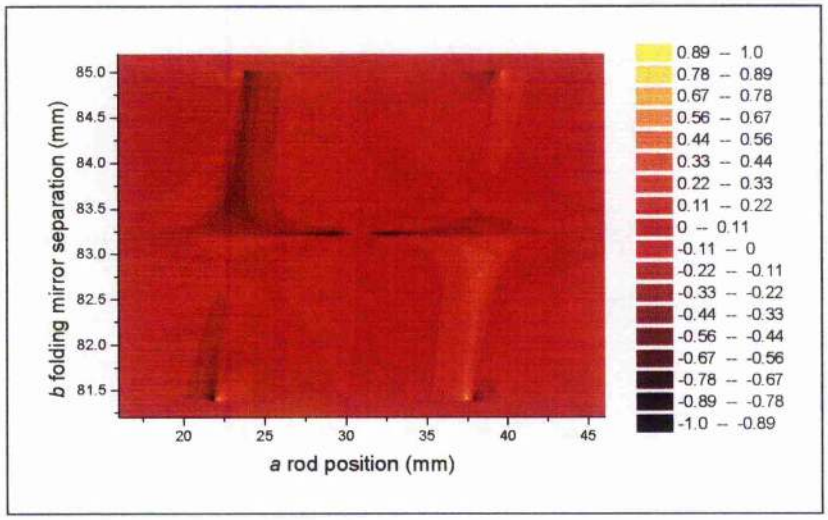

Figure 2.35 The Magni plot in the sagittal plane for the W-cavity with 75 mm ROC folding-section mirrors.

The efficient performance of this laser system can be attributed to, the use of the Magni prescription for reliable self-modelocking, the plane-plane rod geometry for low CW threshold and the regenerative initiation.

2.5 A low-threshold four-mirror Cr:LiSGaF laser

The second low threshold system was based around a crystal of Cr:LiSGAF. This material was chosen because it reputedly exhibited better thermal properties than Cr:LiSAF[72]. The Cr:LiSGaF crystal was grown[73] with a higher optical quality (lower scattering/absorption loss) than the Cr:LiSAF used previously and therefore had a lower insertion loss. The crystal was cut in a cylindrical rod 10 mm in length and the doping with Cr^{3+} ions was 3%. The crystal end facets were AR-coated for 850 nm and the reflection loss of each coating was measured at ~0.1% at 850 nm. The rod was mounted on a goniometer-gimbal mount that allowed lateral and axial rotation of the crystal. This greater orientational flexibility was used to eliminate birefringence effects that were experienced in the LiSAF laser when the crystal c-axis was not orientated correctly[74]. The inclusion of this mount allowed the laser to be tuned smoothly over the lasing bandwidth.

The Laser Cavity

The cavity configuration used was the more conventional 'Z' cavity shown in Figure 2.36 below. This effectively removed two mirror reflections per round-trip, reducing the number of reflections from 8 to 6, as the cavity no longer required a fold about the crystal. The optical components used were the same as those for the LiSAF laser but the lower insertion loss, and hence lower thresholds, associated with the Cr:LiSGaF crystal allowed the HR mirror M1 to be replaced with an output-coupling (OC) mirror.

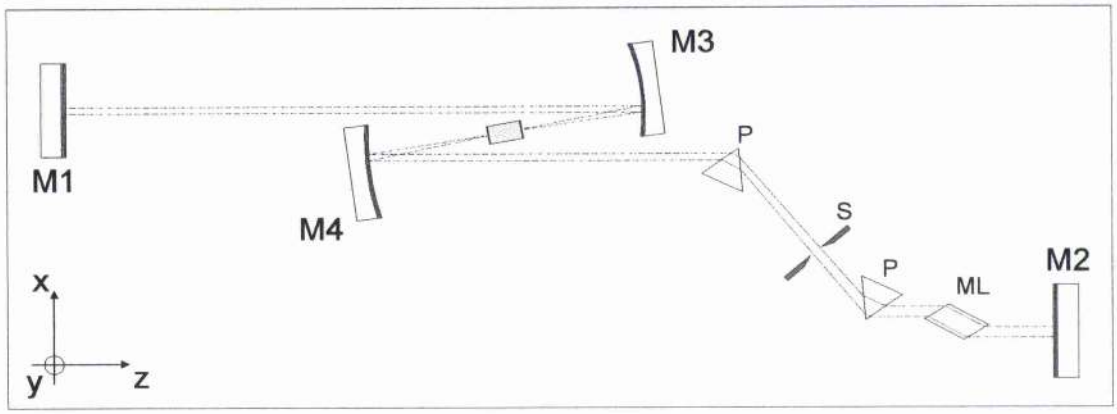

Figure 2.36 The Cr:LiSGAF laser 'Z'-cavity; M1,M4 plane end mirrors; M2, M3 focusing mirrors; P dispersion compensation prisms; S tuning slit; ML quartz modelocker.

The folding section mirrors M3 and M4 were 75mm ROC. orientated with folding angles of less than 3°. The intracavity prisms used were made of SF10 glass with a tuning slit placed between them in order to observe and eliminate birefringence. No modelocking slit was employed with this cavity and all self-modelocking achieved was soft-aperture. The pump laser was the SIL AlGaInP semiconductor laser focused through mirror M3 using a 50 mm focal length lens. The active 'modelocker' was the Brimrose FQM442 AO modulator as before.

CW Performance

With HR mirrors and all cavity elements present the lowest CW threshold achieved was 22.4 mW; almost a factor of two improvement over the LiSAF laser. The threshold when mirror M1 was replaced with a 1.5% output coupling mirror was 43 mW and the laser exhibited a slope efficiency close to 9%. The power transfer characteristic curve is shown in Figure 2.37.

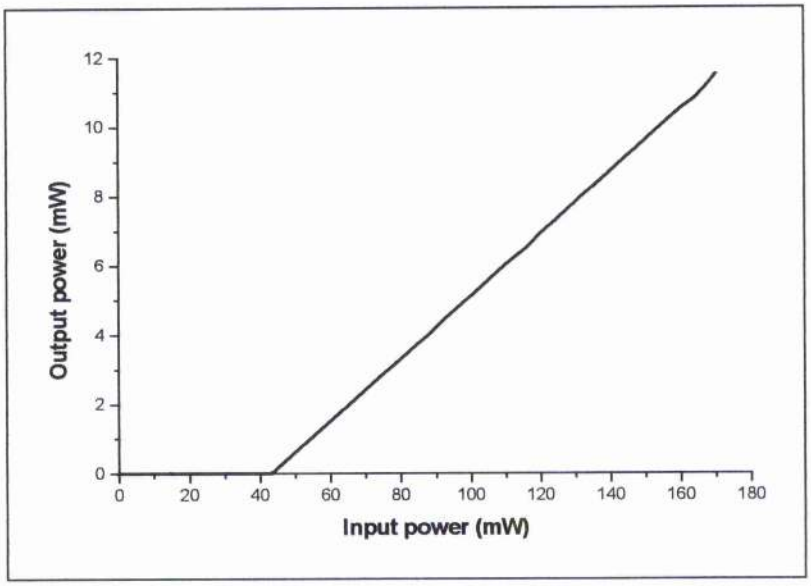

Figure 2.37 The CW power transfer characteristics of the diode-pumped Cr:LiSGaF system with 1.5% OC mirror M1

Modelocked Performance

The Z-cavity was always modelocked in the easier to align soft-aperture regime (see Figure 2.38).

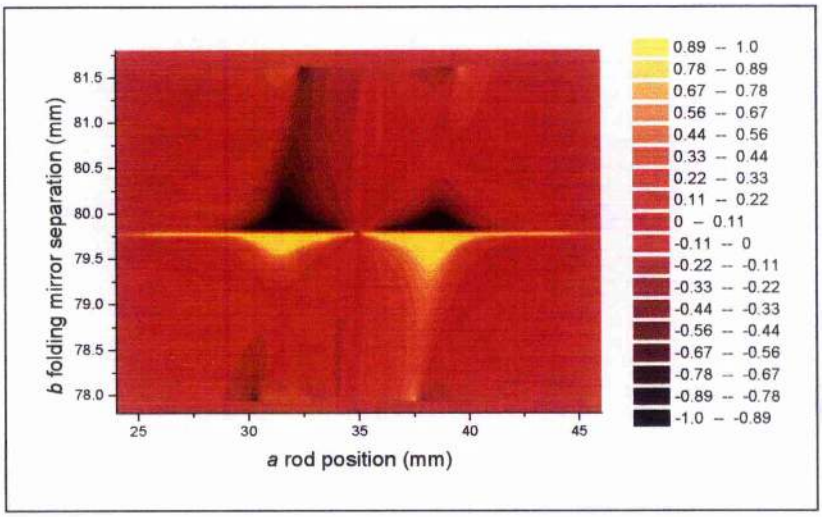

Figure 2.38 Soft-aperture Magni plot for the Cr:LiSGaF z-cavity laser.

When self-modelocked, the laser produced transform-limited, 87fs pulses for a pump power of 170mW (see Figure 2.39). These results are similar to the Cr:LiSAF laser although the cavity now contained an output-coupler and produced an average

modelocked output power of 11.5mW representing almost an order of magnitude increase in output power over the Cr:LiSAF laser of section 2.4. This increase was achieved by the reduction of intracavity losses in the crystal and the effective removal of two mirror reflections per round-trip.

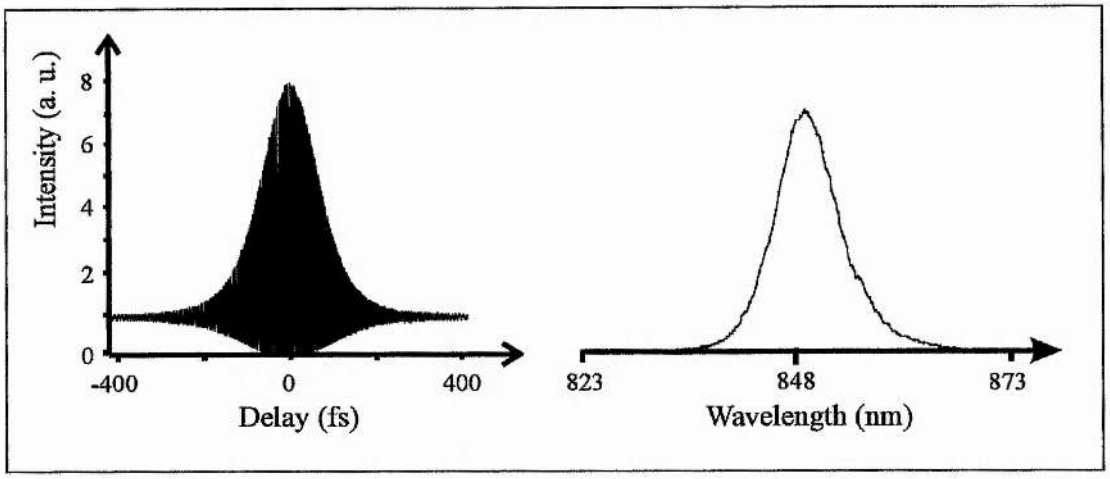

Figure 2.39 Interferometric autocorrelation and spectrum for pulses from the Cr:LiSGaF laser. The average output power of the pulses was 11.5 mW for 170 mW pump power and $\Delta\tau$ = 87 fs, λ = 850 nm, $\Delta\lambda$ = 8.3 nm and $\Delta\nu\Delta\tau$ = 0.30.

The Cr:LiSGaF laser demonstrated usable output powers with pump powers lower than the reported CW thresholds of many Cr^{3+} systems at the time! Shorter pulses may have been obtained from this system either by re-fitting an HR mirror to increase the intracavity power or by using fused-silica prisms as they would have provided the least third-order dispersion for the length of gain medium.

2.6 Conclusions

In this chapter, some of the key considerations to be made when designing a short pulse laser system with low pump power requirements have been introduced. Firstly, the material properties of the gain media, namely the pump absorption coefficient and the upper state lifetime/cross-section product ($\sigma\tau$) must be suited to a low cw threshold condition. Secondly, the parasitic losses within the laser cavity Λ must be minimised and the cavity must be configured to allow the best overlap of the pump beam and the cavity mode in the gain medium. This is achieved in gain media with relatively high pump absorption coefficients (α_p) by ensuring that both the pump beam and cavity

mode are tightly focussed and coincident at one end of the gain crystal. The geometry of the laser cavity must also be examined with regards to ensuring that an efficient modelocking mechanism can be produced. The conditions required for this efficient self-modelocking have been discussed and a simple geometrical model presented that gives the optimum cavity alignment for a hard-aperture modelocked femtosecond laser. The results of the model and an intuitive discussion both lead to the conclusion that the conditions for a low cw threshold namely the tightly focussed beam at one end of the laser rod (with high α_p), also give rise to the most efficient self-focussing effect on the cavity mode provided that the cavity is aligned near a stability limit. Finally, the dispersion of the laser cavity must be considered to ensure that the shortest pulses and therefore the lowest modelocking threshold may be achieved. Using a model suggested by Lemoff and Barty[25] both the quadratic and cubic phase present in the cavity may be compensated for by using a suitable prism arrangement. These prisms have the advantage over other compensation schemes in that they introduce the lowest insertion losses and therefore help to maintain a low cw threshold. Due to the requirement of a tightly focussed pump beam a diffraction-limited pump source based on a self-injection locked broad area laser diode that was used to pump the preliminary low threshold laser cavities was then described.

Two ultrashort pulse laser systems were described that used plane-plane cut gain crystal to ensure a very tight focus in both the tangential and sagittal plane of the laser resonator were possible. The first system used a crystal of Cr:LiSAF in a W-type cavity configuration which allowed the possibility of intimate pumping with broad area laser diodes for higher output powers. The second laser system used a crystal of Cr:LiSGaF in a more traditional Z cavity with two fewer mirror reflections than the W cavity. This laser permitted the use of an output coupler to provide close to an order of magnitude greater output power.

By carefully considering the aspects of a laser system that contribute to its modelocking threshold sub 100 mW thresholds for sub-100 fs operation were achieved.

Endnotes

1 A. J. Alfrey. *IEEE J. Quantum Electron.* **25**, 760 (1989).

2 A. E. Siegman, *in Lasers* (University Science Books, Sausalito, California 1986).

3 V. Magni, G. Cerullo, and S. De Silvestri, *Opt. Commun.* **96**, 348 (1993).

4 M. Piché, *Opt. Commun.* **86**, 156 (1991).

5 A. E. Siegman, *in Lasers (University Science Books, Sausalito, California 1986)*, chapter 20.

6 H. Kogelnik, *Bell System Tech. J.* **44**, 455 (1965).

7 D. E. Spence, P. N. Kean and W. Sibbett, *Opt. Lett.* **16**, 42 (1991).

8 F. Salin, J. Squier and M. Piché, *Opt. Lett.* **16**, 1674 (1991).

9 M. Sheik-Bahae, A. A. Said,D. J. Hagan, M. J. Soileau and E. W. Van Stryland, *Opt. Eng.* **30**, 1228 (1991), also see reference 13.

10 Y. R. Shen, *in The Principals of Nonlinear Optics* (Wiley, New York, 1984) Chapter 17.

11 V. Magni, G. Cerullo, and S. De Silvestri, *Opt Commun.* **101**, 365 (1993).

12 O. E. Martinez and J. Chilla, *Opt. Lett.* **17**, 1210 (1992).

13 V. Magni, D. De Silvestri and A. Cybo-Ottone, *Opt. Commun.* **82**, 137 (1991).

14 G. Cerullo, S. De Silvestri, V. Magni and L. Pallaro, *Opt. Lett.* **19**, 807 (1994).

15 G. Cerullo, S. De Silvestri, and V. Magni, *Opt. Lett.* **19**, 1040 (1994).

16 G. R. Huggett, Appl. Phys. Lett. **13**, 186 (1968).

17 V. Magni, G. Cerullo, S. De Silvestri and A. Monguzzi, *J. Opt. Soc. Am.* **B 12**, 476 (1995).

18 A. E. Siegman, *in Lasers (University Science Books, Sausalito, California 1986)*, chapter 21.

19 J. Herrmann, *J. Opt. Soc. Am.* **B 11**, 498 (1994).

20 S. Gatz and J. Herrmann, *Opt. Lett.* **20**, 825 (1995).

21 A. Ritsataki, G. H. C. New, R. Mellish, S. C. W. Hyde, P. M. W. French and J. R. Taylor, *J. Sel. Topics in Quantum Electron.* **4**, 185 (1998).

22 A. Agnesi, E. Piccinini and G. C. Reali, *Opt. Commun.* **135**, 77 (1997).

23 A. Ritsataki, P. M. W. French and G. H. C. New, *Opt Commun.* **142**, 315 (1997).

24 M. Lai, J. Nicholson and W. Rudolph, *Opt. Commun.* **142**, 45 (1997).

25 B. E. Lemoff and C. P. J. Barty, *Opt. Lett.* **18**, 57 (1993).

26 S. Uemura, *Jpn. J. Appl. Phys.* **17**, 133 (1998).

27 Note this expression is slightly different to the one presented in reference 25 and has recently been verified in reference 26.

28 M. T. Asaki, C. P. Huang, D. Garvey, J. P. Zhou, H. C. Kapteyn and M. M. Murnane, *Opt. Lett.* **18**, 977 (1993).

29 F. Gires and P. Tournouis, *C. R. Acad. Sci.* **258**, 6112 (1964).

30 R. Szipöcs and F. Krausz, *Opt. Lett.* **19**, 201 (1994).

31 J. Van der Pol, *Phil. Mag.* **3**, 65 (1927).

32 R. Adler, Proc. *IRE* **34**, 351 (1946).

33 K. Otsuka and S. Tarucha, *IEEE J. Quantum Electron.* **17**, 681 (1981).

34 K. Kobayashi, H. Nishimoto and R. Lang, *Electron. Lett.* **18**, 54 (1982).

35 C. L. Tang and H. Statz, *J. Appl. Phys.* **38**, 323 (1967).

36 R. H. Pantell, *Proc. IEEE* **53**, 474 (1965).

37 A. E. Siegman, *in Lasers (University Science Books, Sausalito, California 1986)*, Chapter 29.

38 H. L. Stover and W. H. Steier, *Appl. Phys. Lett.* **8**, 91 (1966).

39 C. J. Buczek, R. J. Freiberg and M. L. Skolnick, *J. Appl. Phys* **42**, 3133 (1971).

40 J. -L. Lachambre, P. Lavigne, G. Otis and M. Noel, *IEEE J. Quantum Electron.* **12**, 756 (1976).

41 C. J. Buczek and R. J. Freiberg, *IEEE J. Quantum Electron.* **8**, 641 (1972).

42 L. E. Erickson and A. Szabo, *Appl. Phys. Lett.* **18**, 433 (1971).

43 G. Magyar and H. J. Schneider-Muntau, *Appl. Phys. Lett.* **20**, 406 (1972).

44 I. J. Bigio and M. Slatkine, *IEEE J. Quantum Electron.* **19**, 1426 (1983).

45 J. J. Turner, E. I. Moses and C. L. Tang, *Appl. Phys. Lett.* **27**, 441 (1975).

46 R. E. Teets, *IEEE J. Quantum Electron.* **20**, 326 (1984).

47 J. -I. Nishizawa and K. Ishida, *IEEE J. Quantum Electron.* **11**, 515 (1975).

48 R. Lang and K. Kobayashi, *IEEE J. Quantum Electron.* **12**, 520 (1977).

49 S. Kobayashi and T. Kimura, *Electron. Lett.* **16**, 668 (1980).

50 S. Kobayashi, J. Yamada, S. Machida and T. Kimura, *Electron. Lett.* **16**, 746 (1980).

51 S. Kobayashi and T. Kimura, *IEEE J. Quantum Electron.* **17**, 681 (1981).

52 R. Lang, *IEEE J. Quantum Electron.* **18**, 976 (1982).

53 G. R. Hadley, *IEEE J. Quantum Electron.* **22**, 419 (1986).

54 E. Kapon, J. Katz and A. Yariv, *Opt. Lett.* **4** , 125 (1984).

55 L. Goldberg, H. F. Taylor, J. F. Weller and D. R. Scifres, *Appl. Phys. Lett.* **45**, 722 (1984).

56 J. -M. Verdiell and R. Frey, *IEEE J. Quantum Electron.* **26**, 270 (1990).

57 J. -M. Verdiell, R. Frey and J.-P. Huignard, *IEEE J. Quantum Electron.* **27**, 396 (1991).

58 G. R. Hadley, J. P. Hohimer and A. Owyoung, *Appl. Phys. Lett.* **49**, 684 (1986).

59 J. -M. Verdiell, H. Rajbenbach and J. -P. Huignard, *Appl. Opt.* **31**, 1992 (1992).

60 C. J. Chang-Hasnain, J. Berger, D. R. Scifres, W. Streifer, J. R. Whinnery and A. Dienes, *Appl. Phys. Lett.* **50**, 1465 (1987).

61 L. Goldberg and J. F. Weller, *Electron. Lett.* **25**, 112 (1989).

62 J. -M. Verdiell and R. Frey, *IEEE J. Quantum Electron.* **26**, 270 (1990).

63 G. R. Hadley, J. P. Hohimer and A. Owyoung, *Appl. Phys. Lett.* **49**, 684 (1986).

64 M. P. Critten, in *All-solid-state Femtosecond Cr:LiSAF and Cr:LiSGaF Lasers*, Phd Thesis, University of St Andrews (1996).

65 Grown by the Lightning Optical Corporation.

66 D. Spence, P. N. Kean and W. Sibbett. *Opt. Lett.* **16**, 42 (1992).

67 Brimrose FQM442 quartz acousto-optic modulator.

68 Photon Control, Newport.

69 Melles Griot universal optical power meter.

70 Anritsu M596A optical spectrum analyser (0.6 – 1.6 μm).

71 M. J. P. Dymott and A. I. Ferguson, *Opt. Lett.* **19**, 1988 (1994) and M. J. P. Dymott and A. I. Ferguson, *Opt. Lett.* **20**, 1157 (1995).

72 L. K. Smith, S. A. Payne, W. L. Kway, L. L. Chase and B. H. T. Chai, *IEEE J. Quantum Electron.* **28**, 2612 (1992).

73 Grown by the Lightning Optical Corporation.

74 D. Burns, M. P. Critten and W. Sibbett, Opt. Lett. 21, 477 (1996).

Chapter 3: Femtosecond Cr:LiSGaF and Cr:LiSAF lasers with 3-mirror resonators

3.1 Introduction

The traditional Z-fold or X-fold cavity arrangement for ultrashort pulse lasers has varied little since the first successful demonstration of self-modelocking[1]. The overall dimensions of the traditional ultrashort pulse (USP) Ti:sapphire lasers was not too much of an issue because the size of the Ar^+ pump laser often dwarfed the ultrafast laser and thus there was little point in concentrating effort on reducing the size of the USP laser footprints. By contrast, the advent of directly diode pumpable broadband solid-state materials has stimulated interest in the production of more compact and efficient ultrashort-pulse sources[2,3].

A significant factor in the performance improvement of the Z-fold Cr:LiSGaF laser over the W-cavity Cr:LiSAF laser in the previous chapter was the removal of parasitic cavity losses, namely, the two superfluous mirror reflections per round-trip. The Z-cavity, however, still experiences losses at 6 mirror reflections in a round-trip; 4 crystal AR coatings; 4 Brewster-modelocker surfaces and 8 Brewster-prism surfaces. To establish a laser system with a threshold conducive to narrow stripe diode pumping it is therefore necessary to further reduce the sources of loss. In this chapter, laser resonators with three cavity mirrors and therefore only four mirror reflections per round-trip will be described and the various merits of each discussed. Further measures to remove other sources of parasitic loss in two practical laser systems will also be described.

The first 3-mirror laser incorporates a Cr:LiSGaF crystal and provides a significant performance increase in terms of threshold and occupies almost half the bench space of the lasers described in the previous chapter. In the second 3-mirror laser the Cr:LiSGaF crystal was replaced with a Brewster-cut slab of Cr:LiSAF[4] as the reflection losses associated with the AR coatings of the Cr:LiSGaF crystal represented a major source of parasitic loss in the 3-mirror cavity. The lower losses associated with the Brewster-

angled crystal reduced the cavity losses considerably with a significant improvement in the cw threshold over the previous system. This in turn permitted, for the first time to our knowledge, the operation of a femtosecond laser with a single narrow-stripe diffraction-limited laser diode as the pump source.

The measurement and discussion of the noise present in a laser system is then presented showing the diode pumped colquiriite lasers to have superior noise properties than previous USP lasers. Finally, an application of the lasers in the assessment of a streak camera system is highlighted.

3.2 Resonators with 3 cavity mirrors

The reduction in the number of cavity mirrors from 4 to 3 reduces the total number of mirror reflections experienced in a round-trip from 6 to 4. This results in a more compact laser system with lower intracavity losses Λ and therefore a lower intrinsic cw threshold (see Figure 3.1).

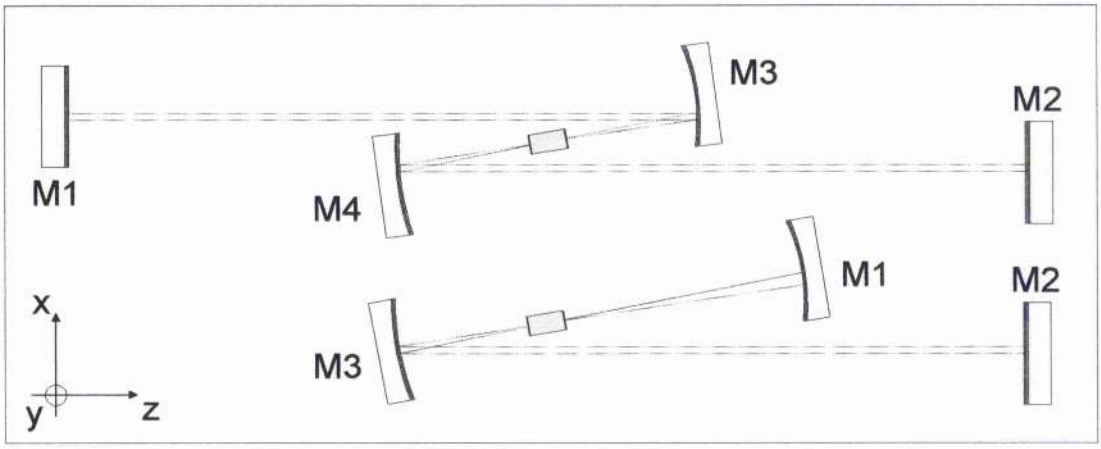

Figure 3.1 Schematic of a 4-mirror Z-fold and a 3-mirror cavity.

Stability

The variation of the stability parameter S and the folding mirror separation b is considerably different for the case of a 3-mirror resonator compared with the 4-mirror resonators discussed earlier. In the 4-mirror asymmetric Z-cavity the laser stability was characterised by a parabola forming two separate stable regions, the LMS and the HMS over which, $-1 < S < 1$, (see Figure 3.2a). These regions were bounded by four distinct stability limits, (i)-(iv), that related to the effective focal length of the folding section.

For the special case of a symmetric Z-cavity the stability parabola shifted up to join the stability limits (ii) and (iii) forming a single stability region which has been shown to improve the modelocking performance[5] (Figure 3.2b).

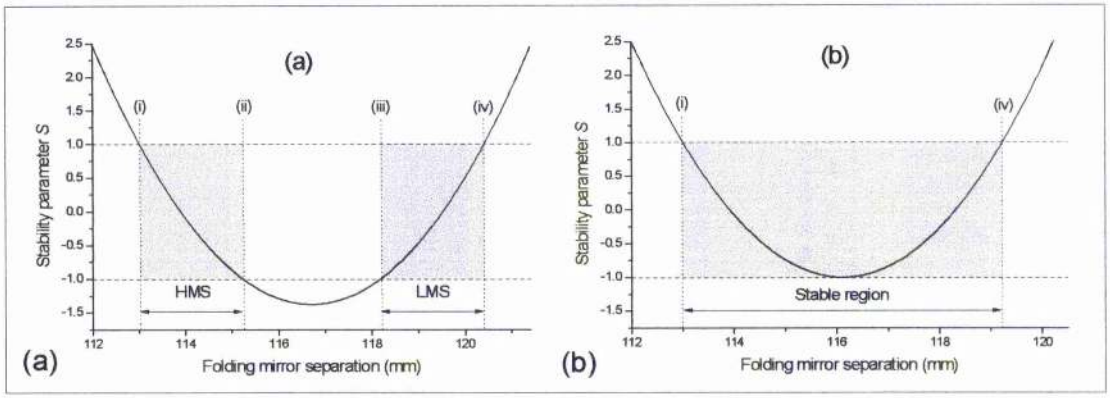

Figure 3.2 Stability diagrams for the (a) asymmetric and (b) symmetric 4-mirror Z-fold cavity, the shaded regions indicate the stable region.

For the case of a 3-mirror resonator supporting a TEM_{00} mode the stability condition again gives rise to two separate stability regions which are linked directly to $R(z)$ the wavefront radius of curvature of the cavity mode. Figure 3.3 below shows some of the fundamental properties of a TEM_{00} Gaussian beam indicating the waist w_0, the spot size $w(z)$, and the wavefront radius of curvature $R(z)$. The point at which the radius of curvature reaches a maximum is referred to as the Rayleigh range[6]

$$z_R = \frac{\pi w_0^{\,2}}{\lambda}$$

Equation 3.1

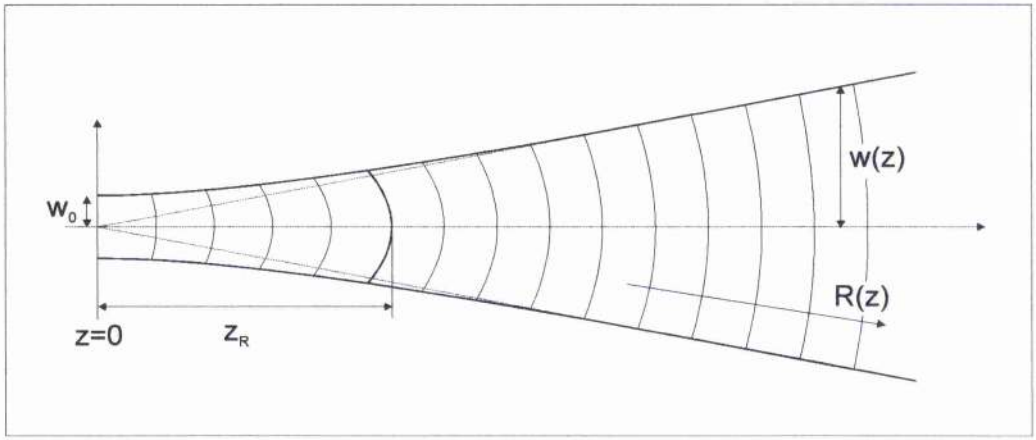

Figure 3.3 Schematic of a TEM_{00} Gaussian mode emanating from a waist w_0, z_R is the Rayleigh range, $w(z)$ is the spot size and $R(z)$ is the wavefront radius of curvature.

By fixing a mirror of finite radius of curvature R' to one side of the waist in the case of a simple 2-mirror cavity, there will exist two points beyond the waist either side of z_R for which a second mirror radius of curvature R will form a stable resonator cavity. These points exist at distances

$$z_1 = \frac{R}{2} - \frac{1}{2}\sqrt{R^2 - 4{z_R}^2} \text{ and } z_2 = \frac{R}{2} + \frac{1}{2}\sqrt{R^2 - 4{z_R}^2}$$

Equation 3.2

from the cavity waist (see Figure 3.4). We will refer to the two stability regions formed at these points as the near-field and far-field stability regions as they lie either side of the Rayleigh range.

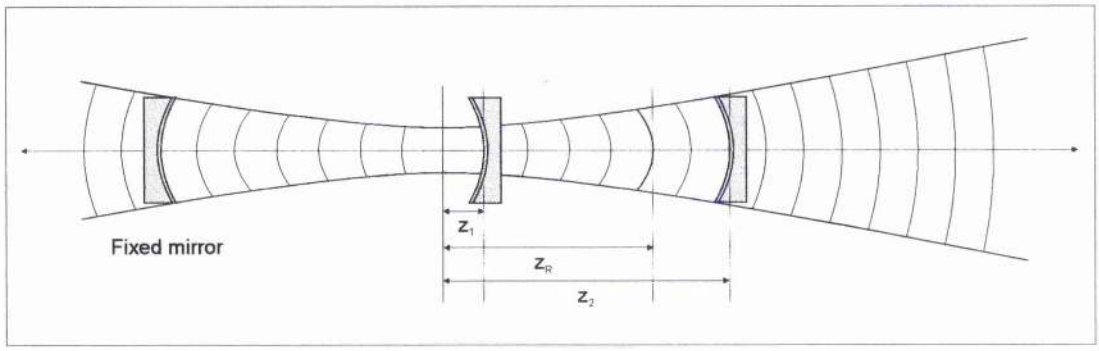

Figure 3.4 Schematic of a Gaussian mode about a cavity waist showing the two possible stable mirror positions z_1 and z_2.

The consideration of a folding section in a 3-mirror cavity is essentially the same as for this two mirror case and Figure 3.5 shows the variation of the stability parameter S with folding mirror separation b for a 3-mirror resonator. The stability limits (I) and (II) for each stable region correspond directly with the planar-confocal limit (i) and the conjugate-plane limit (iv) in Figure 3.2 where the mode degenerates into plane and spherical waves respectively in the cavity arm. These stability limits are equally important for the 3-mirror case as in the 4-mirror because the value of δ (Kerr lens sensitivity) will increase in magnitude towards these limits (Equation 2.28). The weak-objective limit (ii) and strong objective limit (iii) have no corresponding limits in a laser cavity with a single arm.

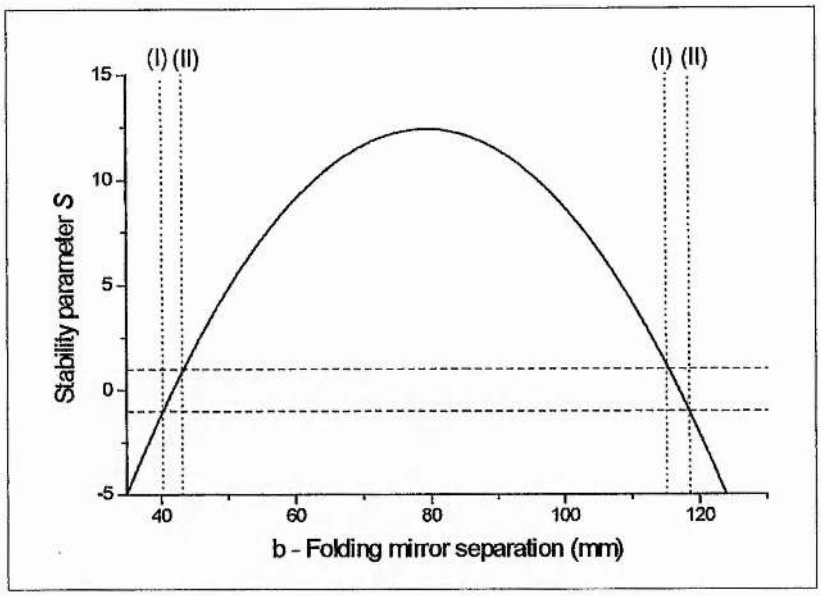

Figure 3.5 Variation of the stability parameter S with varying mirror separations in a 3-mirror cavity containing a 10mm Cr:LiSGaF crystal and 75 mm ROC mirrors resulting in a near-field stability region and a far-field stability region each with stability limits (I) and (II).

In the case of a 4-mirror cavity the HMS and LMS regions often lie within the travel of a standard translation stage, whereas, it may be observed from Figure 3.5 that for the 3-mirror case the two stability regions lie far apart. The theoretical point when these two regions meet occurs when $R = 2z_R$ but as the ROC of the mirror approaches this value the resonator waist, w_0, becomes smaller, thus further separating the two regions. In the 3-mirror laser it is in fact impossible to make these two regions intersect and therefore the special case of the symmetric 4-mirror resonator for modelocking has no analogy in a 3-mirror cavity. As the two stability regions will never coincide there will exist two types of resonator based on a 3-mirror geometry; the near-field resonator and the far-field resonator.

Semimonolithic resonator geometry

A near-field resonator for self-modelocking will in general require a mirror placed close to the cavity waist as, due to the tight intracavity focus required, resulting in z_R being typically of the order of a couple of millimetres. For this reason the most practical near-field resonator is the special case, of a plane mirror placed at the cavity waist, where the radius of curvature is infinite, the so-called semimonolithic resonator[7]. In this special case there is only one mirror separation which corresponds to a stable cavity because the

second stable region lies an infinite distance beyond z_R. This cavity configuration lends itself to using a gain medium with an HR coated plane cut facet as this forces the cavity waist position to always exist at the surface of the crystal the merits of which for low cw and modelocking thresholds were discussed in detail in chapter 2. In this configuration the cavity is then optically equivalent to half of a symmetric Z-cavity divided about the centre of the crystal (Figure 3.1) and represents a major simplification over previous modelocked solid-state laser designs. Fujimoto and colleagues first investigated this type of cavity for the purpose of modelocking[8,9].

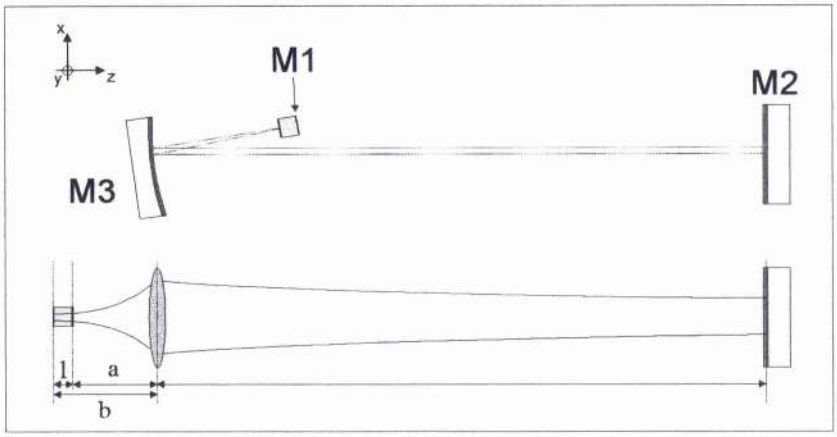

Figure 3.6 Schematic of the semimonolithic cavity and optical equivalent for consideration of small signal Kerr lens sensitivity δ.

The combination of gain medium and end mirror reduces the number of degrees of freedom in the laser by two. In the 4-mirror cavity the position of the crystal a, the folding mirror separation b and the lengths of each cavity arm could be adjusted independently. In the 3-mirror cavity the waist or focus is fixed at the mirror coated crystal facet and the mirror separation and crystal position become equivalent (b = a + l, where l is the length of the crystal). Optimisation of modelocking therefore becomes a one-dimensional problem significantly simplifying the alignment and operation of the laser. Figure 3.7 below shows the variation of the stability parameter S with the folding mirror separation b in a 3-mirror semimonolithic cavity containing a 10 mm plane/plane Cr:LiSGaF crystal and 75 mm ROC mirrors. Figure 3.8 shows how δ varies with b using the full implementation of the Magni model[10] for the same cavity. It can be seen that δ can only be made sufficiently negative at the crystal facet while it is never negative at the plane end mirror M3 hence the laser will only operate in a soft or gain-aperture regime. Bouma[9] was the first to use the Magni prescription to successfully predict the behaviour of a soft-aperture laser system in this manner.

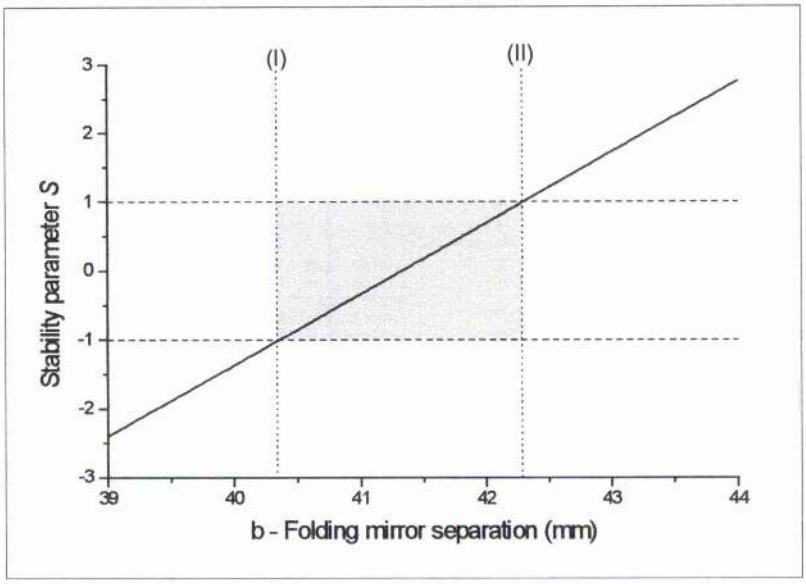

Figure 3.7 Variation of the stability parameter S with mirror separation b in a 3-mirror semimonolithic laser containing a 10 mm plane/plane cut Cr:LiSGaF crystal and 75 mm ROC mirror.

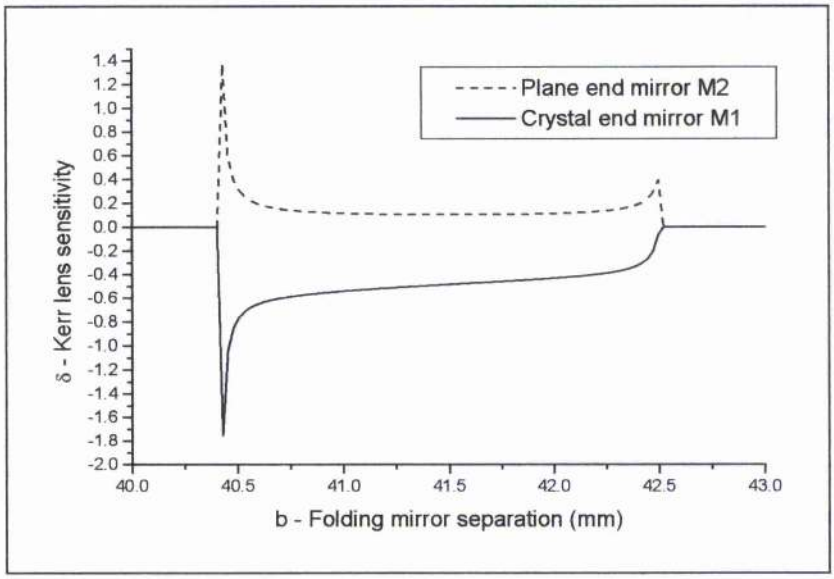

Figure 3.8 Variation of δ with mirror separation b in a 3-mirror semimonolithic laser containing a 10 mm plane/plane cut Cr:LiSGaF crystal and 75 mm ROC mirror.

The semimonolithic 3-mirror cavity lends itself to high power end pumping with diode lasers as the highly divergent pump light can be closely coupled and tightly focussed into the gain medium,

Retroreflecting resonator geometry

By removing degrees of freedom in the resonator, modelocking may be achieved more easily when available pump power is not an issue. However, with limited pump power the loss of too many adjustable parameters will have a detrimental effect on the alignment and performance of the laser. To retain as many degrees of freedom as possible while still removing a cavity mirror it is necessary to keep the folding section of the cavity intact. In this manner the crystal position and the folding mirror separation may be independently adjusted as in the case of the 4-mirror cavity, and a full two-dimensional Magni modelling consideration can be made. This configuration corresponds to a cavity aligned in the far-field stability region and is termed a 'retroreflecting resonator' because the curved mirror re-images the cavity mode through the crystal (see Figure 3.9).

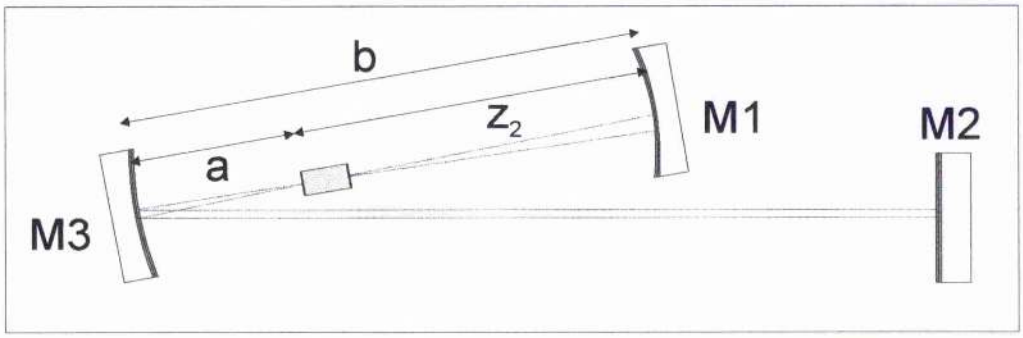

Figure 3.9 Schematic of the retroreflecting cavity showing the crystal position, a, the folding mirror separation, b, and the stable separation, z_2, of mirror M1 from the cavity waist assuming the pump light is focussed through M3.

Figure 3.10 below shows in more detail the stability condition for the particular retroreflecting laser taken from Figure 3.5. The retroreflecting curved mirror sits at a distance from the cavity waist equivalent to its radius of curvature and the intervening distance may be regarded as 'dead space' as far as laser operation is concerned. The stability limits (I) and (II) in Figure 3.10 are equivalent to those in Figure 3.5 and correspond to the mode degenerating into plane and spherical waves in the cavity arm respectively.

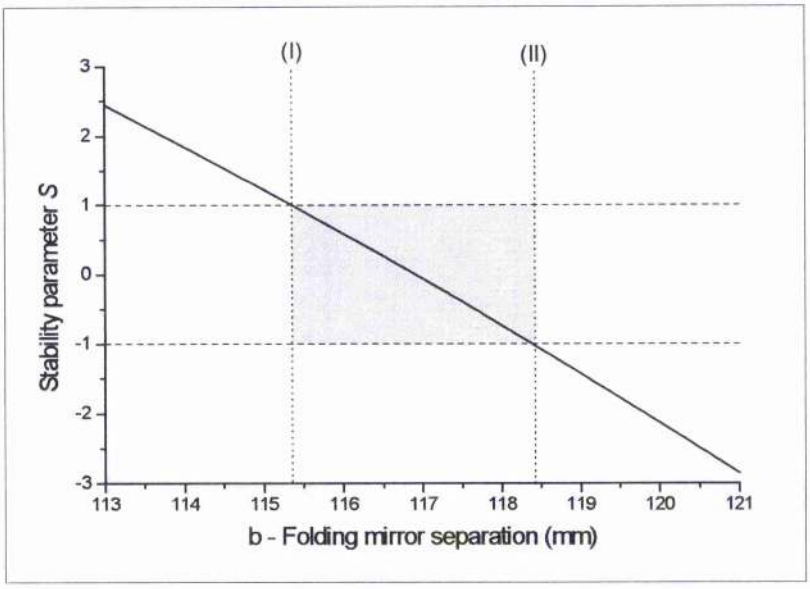

Figure 3.10 Variation of the stability parameter S with mirror separation b in a 3-mirror retroreflecting laser containing a 10 mm plane/plane cut Cr:LiSGaF crystal and 75 mm ROC mirror.

The Magni plots in Figure 3.11 and Figure 3.12 below show the variation of the Kerr-lens sensitivity δ in the tangential plane of the resonator at the plane end-mirror M2 and the cavity waist position (the pumped crystal facet).

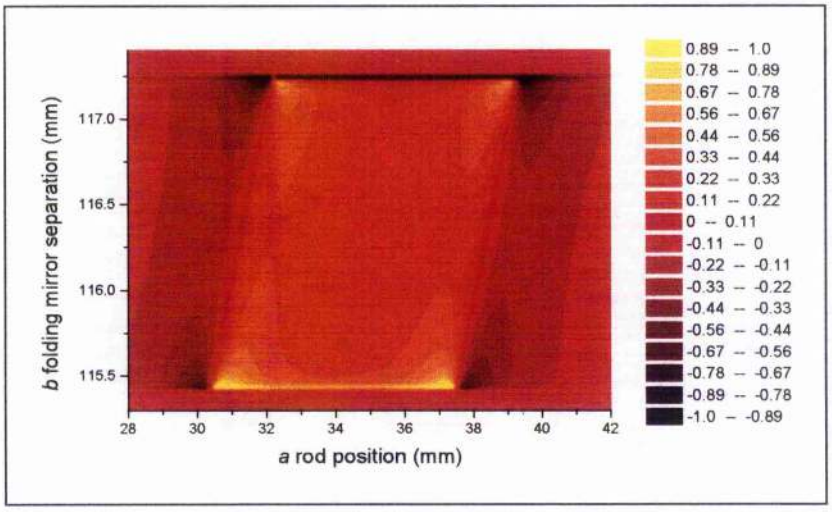

Figure 3.11 A Magni plot of δ(a,b) in the tangential plane at the plane end mirror M2 for a 3-mirror retroreflecting laser containing a 10 mm plane/plane cut Cr:LiSGaF crystal and 75 mm ROC mirrors.

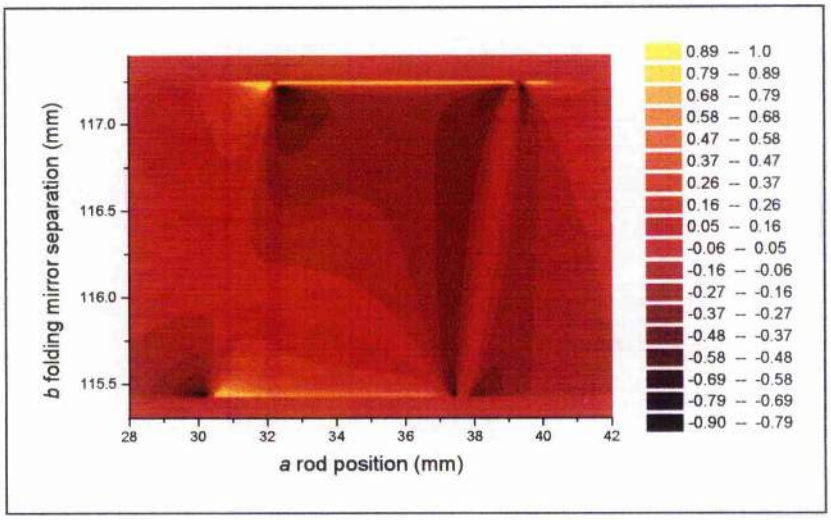

Figure 3.12 A Magni plot of δ(a,b) in the tangential plane at the pumped crystal facet nearest mirror M3 for a 3-mirror retroreflecting laser containing a 10 mm plane/plane cut Cr:LiSGaF crystal and 75 mm ROC mirrors.

The two diagrams describe the propensity of the laser to operate in a hard-aperture or soft-aperture modelocking regime. Figure 3.11, the hard-aperture case, shows that the spot size at the end-mirror only decreases when the cavity waist lies outside the crystal and the mirror separation is close to the stability limit. As in the case of the semimonolithic cavity the laser will be impossible to hard-aperture modelock, in a low-threshold system at least. In addition to this argument if we were to use a prism pair for dispersion compensation, the cavity mode will be spatially dispersed at this end-mirror and therefore an aperture would also limit the bandwidth. It is obvious from Figure 3.12 that a laser of this type will be much more suited to soft-aperture modelocking as the region where δ becomes negative extends well within the stability limits and corresponds to the cavity waist on or just inside the crystal facet. It may be observed from Figure 3.13, which shows the variation of δ at the crystal facet in the sagittal plane, that in the case of the 3-mirror cavity the magnitude and variation of δ can be similar in both the sagittal and tangential planes of the resonator. This indicates that uniform beam focussing in both planes may be achieved, reinforcing the 3-mirror cavity's potential to soft-aperture modelock.

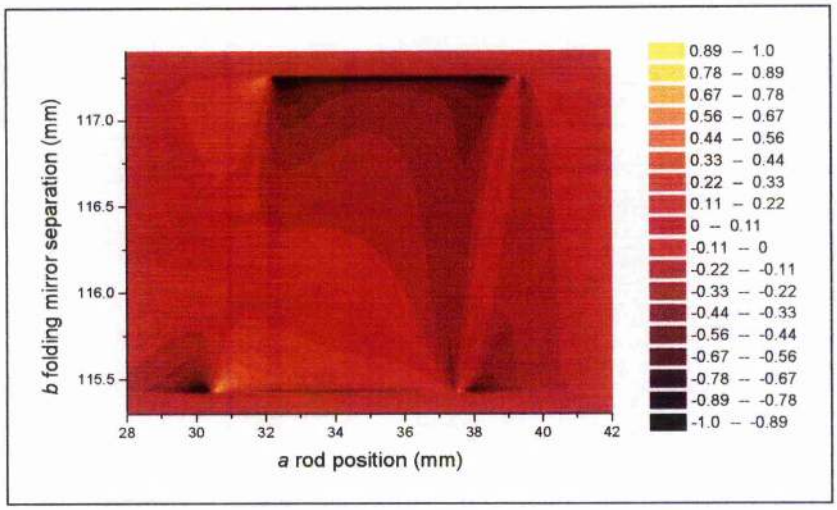

Figure 3.13 A Magni plot of δ(a,b) in the sagittal plane at the pumped crystal facet nearest mirror M3 for a 3-mirror retroreflecting laser containing a 10 mm plane/plane cut Cr:LiSGaF crystal and 75 mm ROC mirrors.

In addition to the benefits for the optimisation of self-modelocking the ability to position the crystal at any point about the cavity waist is also a necessary condition for optimising the cw threshold. For these reasons the retroreflecting geometry was adopted for the laser systems described in the remainder of this chapter.

3.3 A 3-mirror Cr:LiSGaF laser

The laser cavity

The first implementation of a retroreflecting resonator was the simple removal of a cavity arm from the 4-mirror Cr:LiSGaF laser described in the previous chapter. Figure 3.14 below shows the cavity configuration of the resulting 3-mirror Cr:LiSGaF laser.

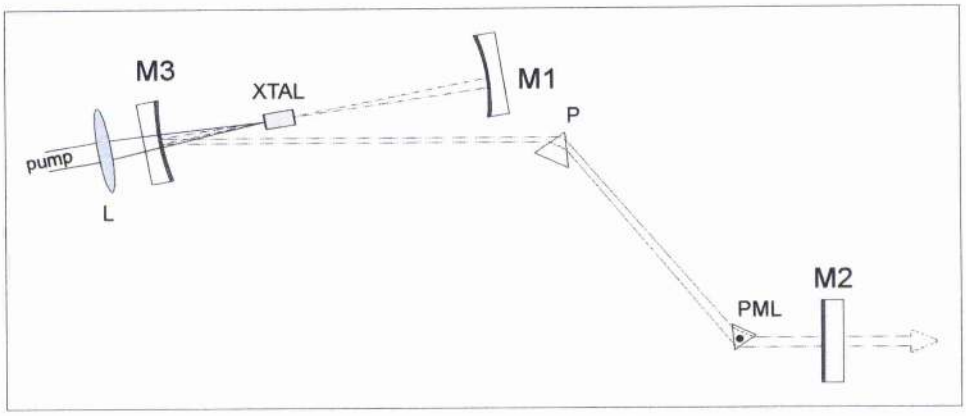

Figure 3.14 Schematic of the 3-mirror cavity: M1, M3 focusing mirrors; M2 plane end mirror; P dispersion compensating Infrasil prism; PML fused silica prism modelocker L 50 mm pump focussing lens, XTAL 10 mm 3% doped Cr:LiSGaF crystal mounted on a goniometer.

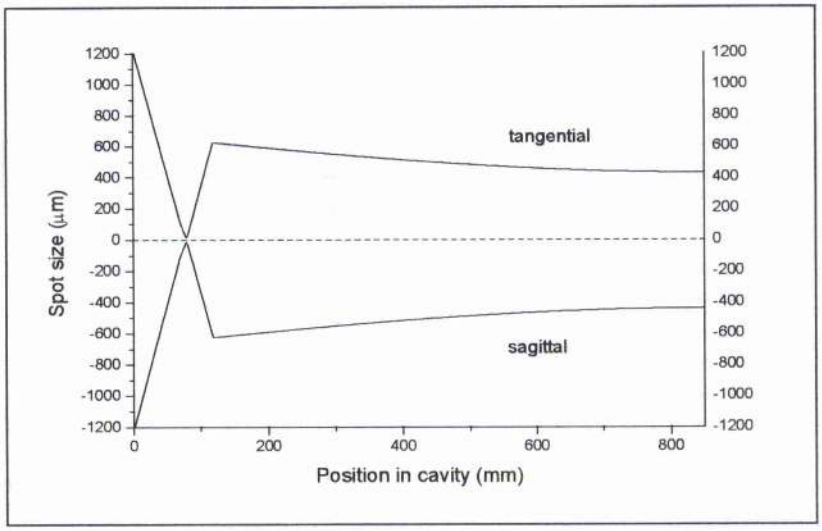

Figure 3.15 Spot size in the tangential (positive) and saggital (negative) planes of the 3-mirror Cr:LiSGaF resonator with an overall cavity length of 850 mm.

The mirrors were all HR coated (R>99.95% @ 840 nm) with the two folding mirrors M1 and M3 having a 75 mm radius of curvature. A low-loss 'Infrasil' fused silica prism and a combined fused silica prism modulator from an Ar^+ laser (Spectra Physics model 342A acousto-optic prism-modelocker) provided dispersion compensation. Fused silica was used as it provided the minimum third-order dispersion for this combination of prism pair and 10 mm crystal of Cr:LiSGaF. A fast photodiode and RF amplifier circuit connected to the prism modelocker provided regenerative initiation (see Figure 3.16). The regenerative circuit was seeded with the loss from one of the AR coatings of the CR:LiSGAF crystal. The combination of prism and modelocker permitted regenerative initiation to be implemented without the inclusion of additional intracavity elements.

This helped to remove parasitic reflection losses from the cavity and further reduce the lasing threshold.

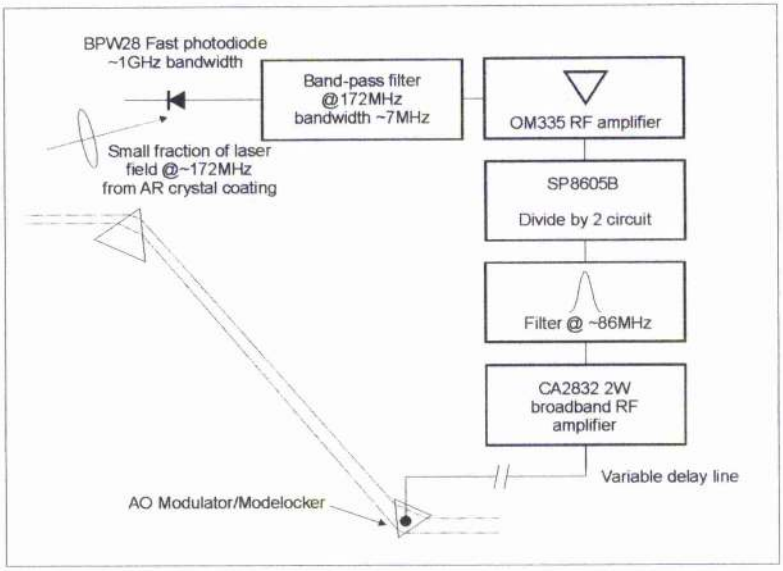

Figure 3.16 Schematic of the regenerative initiation scheme used with the 3-mirror Cr:LiSGaF laser.

The laser cavity measured approximately 850 mm and the repetition or intermode frequency was close to 180 MHz. As this laser was almost half the length of the 4-mirror laser, the circuit in Figure 3.16 is slightly different to the one used with the 4-mirror laser. The SP8610B divide by 4 circuit was replaced with a SP8605B divide by 2 circuit and a couple of the RF filters were tuned to the new cavity length. The pump source used throughout the work on this laser was the self-injection-locked system described in section 2.3. Figure 3.17 shows the configuration of the SIL laser with a variable neutral density (ND) filter wheel used to reduce the pump power, and a pinhole/slit arrangement used to remove any excess pump light that did not contribute to the operation of the Cr:LiSGaF laser.

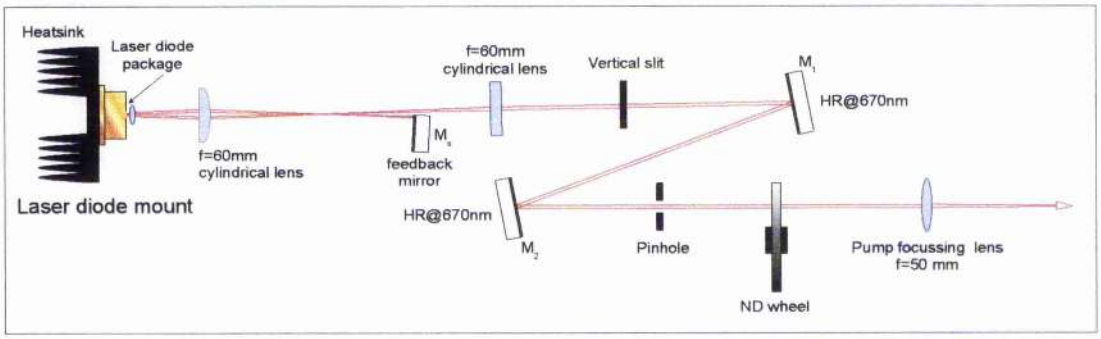

Figure 3.17 Self-injection locked Coherent S-67-500C AlGaInP laser diode with a vertical slit and pinhole to aperture beam and a variable ND filter wheel to attenuate the pump power.

CW performance

The laser was aligned for a low cw threshold by optimising performance while continually reducing the pump power. The slit and pinhole were then placed in the pump beam and closed until their effect on the output of the Cr:LiSGaF laser was just detectable. In this manner the slit and pinhole could be made to reduce the pump power by ~11% without affecting the operation of the laser. The cw threshold with the SIL pump beam apertured in this manner was typically ~14 – 15 mW measured after the pump focussing lens and cavity mirror M1. Placing the power meter head immediately in front of the crystal indicated thresholds as low as 13 mW. When the laser was pumped with 160 mW, cw output powers as high as 2.5 mW were observed. Figure 3.18 below shows a typical power characteristic for the 3-mirror LiSGaF laser.

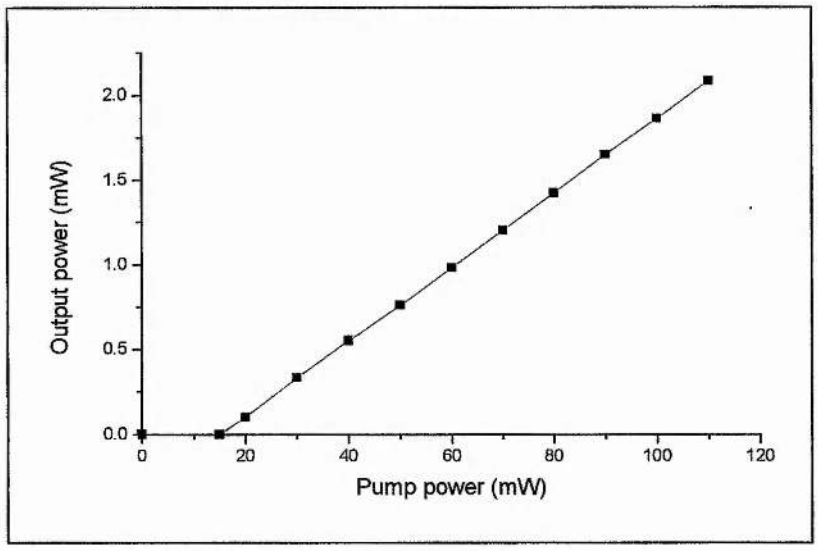

Figure 3.18 Typical power characteristic of the 3-mirror Cr:LiSGaF laser, pump powers measured before the pump focussing lens after steering optics and slit/pinhole arrangement.

Initial modelocked performance

After initial alignment of the autocorrelator and connection of the regenerative circuit the laser was modelocked almost immediately. Initial pulse durations of 300 fs were quickly optimised by careful adjustment of the intracavity dispersion and folding mirror/crystal separations. Pulse durations of 84 fs were obtained for a pump power of 130 mW (see Figure 3.19) and sub 100 fs pulse durations could be achieved for pump powers as low as 93 mW. The prism separation was 560 mm.

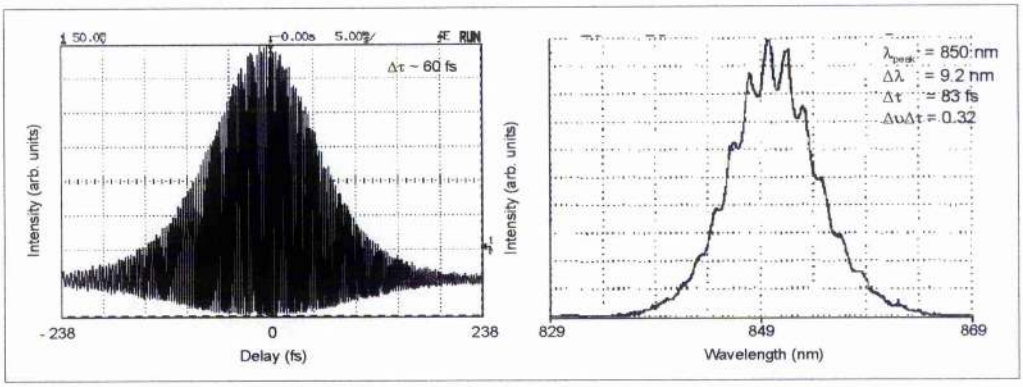

Figure 3.19 Interferometric autocorrelation and spectrum obtained for 84 fs pulses with an average output power of ~ 1 mW obtained for 130 mW pump.

The structure observed in the spectrum of Figure 3.19 is due to the multi-mode nature of the fibre used to couple the light into the optical spectrum analyser and could be all but removed by bending the fibre appropriately. During these initial measurements stability problems arose in the cw output of the laser in the form of longer timescale fluctuations of the order of ~ 30 s. These fluctuations were thought to be due to feedback from the plane crystal facet into the pump laser and slight misalignment of the Cr:LiSGaF crystal removed this effect. To further stabilise the laser system a protective cover was constructed to reduce air currents and dust contamination.

Another stability issue for this laser concerned the regenerative initiation system and prism modelocker. A standing-wave, acousto-optic modulator exhibits resonances for which a much higher proportion of RF power is absorbed. These resonances occur at intervals defined by the physical thickness of the modulator and in the case of the prism modelocker this was approximately 400 Hz. Ideally, a modelocker should not be operated on a resonance for regenerative initiation as this can result in thermal effects. However, in order to sustain modelocked operation in the lasers presented here a larger modulation than could be achieved between resonances was often required due to the relatively low intracavity intensities. For this reason the lasers ran on, or near, a resonance of the modelocker. During the course of taking of results for this laser system the modelocker was replaced with an identical model that exhibited stronger resonances between 80 and 90 MHz. The second modulator made modelocked operation easier to achieve but unfortunately suffered more from heating resulting in a shift in the resonance frequencies and less stable pulses. Stable modelocking could still be achieved if the modelocker was allowed to thermally stabilise and an equilibrium position reached.

Modelocked Performance

The initial performance was hampered by the incorrect alignment of the prism modelocker, which was not Brewster angled properly. Once this was corrected and the laser was pumped with the maximum available pump power of 150 mW, the laser produced 65 fs bandwidth-limited pulses (assuming $sech^2$ pulse profiles) at average output powers of the order of 1 mW. This indicates an intracavity average power of 1.25 W and a peak power of ~ 100 kW. Pulse durations of ~70 fs were achieved for pump powers as low as 85 mW. The typical prism separation was 545 mm. By carefully adjusting the cavity parameters to retain short pulse operation while the pump power was reduced the modelocking threshold of this laser system was investigated. Ultrashort pulse operation of the laser could be achieved for pump powers as low as 25 mW and sub-100 fs pulses achieved for pump powers less than 50 mW. Figure 3.20 below shows an interferometric autocorrelation and spectrum of transform-limited 104 fs pulses obtained with 45 mW pump and Figure 3.21 shows data of 250 fs pulses with a time-bandwidth product of 0.3 obtained with 25 mW. The noise evident in the autocorrelation in Figure 3.21 is due to the limits of the SHG detection.

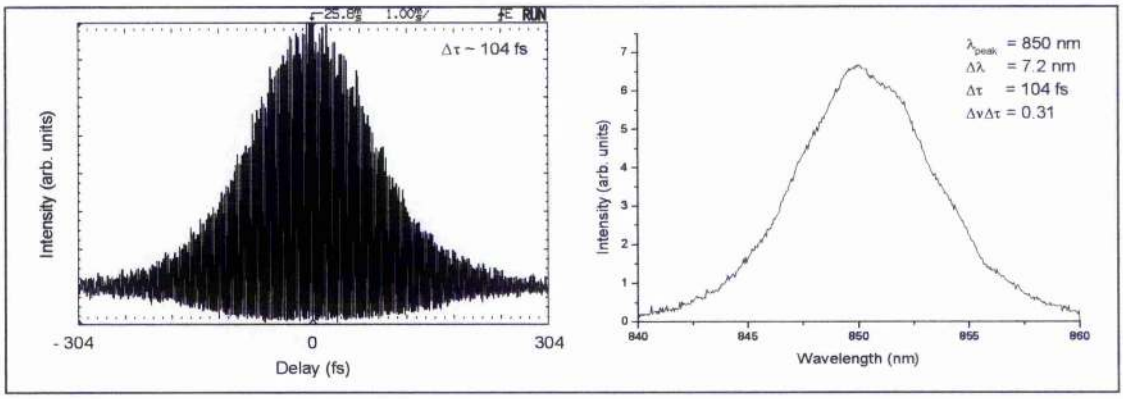

Figure 3.20 Interferometric autocorrelation and spectrum of 104 fs pulses obtained for 45 mW pump.

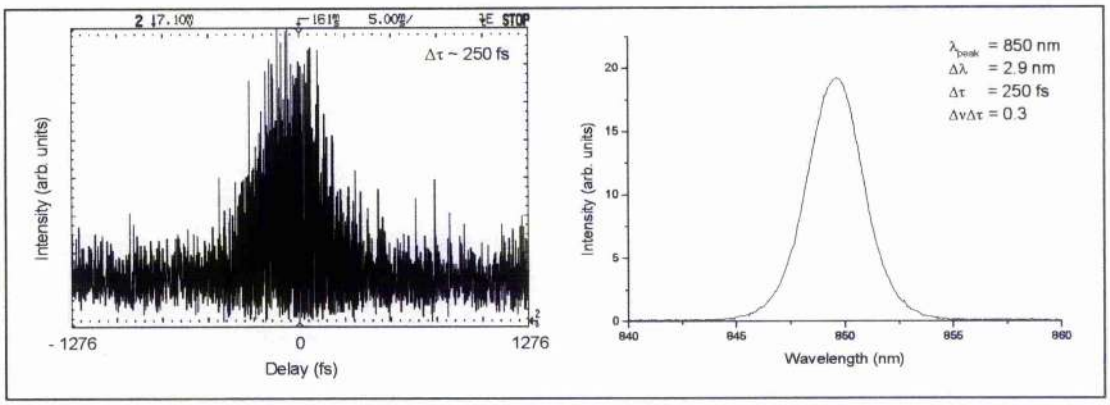

Figure 3.21 Interferometric autocorrelation and spectrum of 250 fs pulses with an average output power of 95 μW obtained for 25 mW pump.

3.4 A 3-mirror Cr:LiSAF laser

The laser cavity

In section 2.2 the astigmatic effect of using a Brewster-angled gain medium on the cavity foci and hence the threshold of a symmetric 4-mirror cavity was discussed. This detrimental effect on the cavity focus may be removed in a 3-mirror cavity if the pump light is focussed through the retroreflecting end mirror. Assuming the angle of the folding mirror compensates for the astigmatism introduced by the Brewstered crystal the cavity foci in the tangential and sagittal planes may coincide on the opposite face of the crystal, i.e. the pumped end of the crystal adjacent to M1. A tight localised focus is therefore achieved at a low-loss Brewstered crystal surface: the optimum low-threshold condition. Figure 3.22 shows graphically the cavity focal positions at the pumped crystal facet in a symmetric 4-mirror laser and the retroreflecting 3-mirror laser respectively.

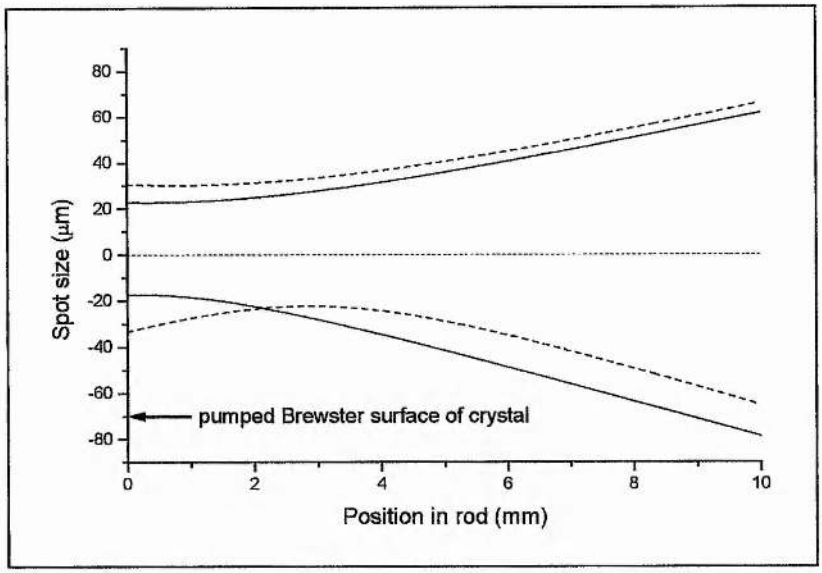

Figure 3.22 Spot size and position of the cavity foci in the tangential (positive) and sagittal (negative) planes for a symmetric 4-mirror cavity (dotted line) and an end-pumped retroreflcting 3-mirror cavity (solid line) containing a 10 mm Brewster-angled slab of Cr:LiSAF.

Figure 3.23 below shows a schematic of the 3-mirror cavity with the Brewster-cut crystal, which was a 7 mm long Cr:LiSAF slab with 1.5% Cr^{3+} doping ($\alpha_p \sim 9\ cm^{-1}$). The mirrors were identical to those used in the previous laser except the radius of curvature of the retroreflecting end mirror M1 was reduced from 75 mm to 50 mm. This allowed the use of the shorter 50 mm focal length lens and therefore a more tightly focussed pump mode to exist at the crystal face helping to reduce the cw threshold. The 75 mm ROC folding mirror M3 was set at a half-angle of 14.5° to compensate for the astigmatism due to the Brewster-angled crystal. The modulator was the same prism modelocker as before and together with an Infrasil fused silica prism provided negative intracavity GVD and minimum third-order dispersion. Pumping the gain crystal in a resonator of this type through the retroreflecting end mirror has a consequence on the stability of the laser. The fact that the pump beam must pass through this mirror implies that obtaining feedback from the cavity arm during initial alignment could be non-trivial as the placing of a photodetector behind this mirror is obviously impossible. Also, any deviation or adjustment in the angle or position of this mirror results in either the reduction of overlap between the pump and cavity modes or a defocusing of the pump mode at the crystal facet. It was found that this resonator configuration was quite tolerant of these issues even at low pump powers and that optical feedback and subsequent lasing, were easily obtained. (This cavity has also been used successfully in a self-modelocked Cr^{4+}:YAG laser[11]).

The pump-focussing lens situated behind mirror M1 had a focal length of 50 mm. The laser cavity again measured ~850 mm with an intermode frequency of ~180 MHz. The regenerative initiation circuit was identical to the circuit in Figure 3.16 and was driven using the leakage from mirror M3.

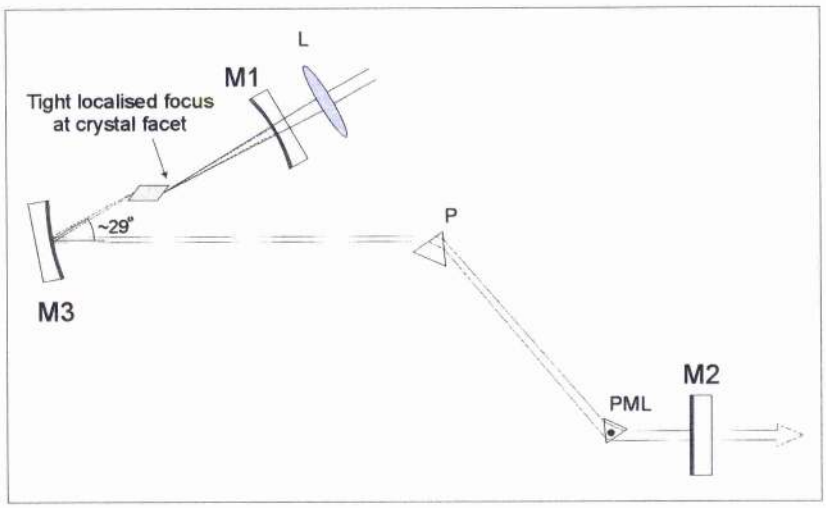

Figure 3.23 Schematic of the 3-mirror Cr:LiSAF cavity: M1, M3 focusing mirrors; M2 plane end mirror; P dispersion compensating Infrasil prism; PML fused silica prism modelocker, L pump focussing lens.

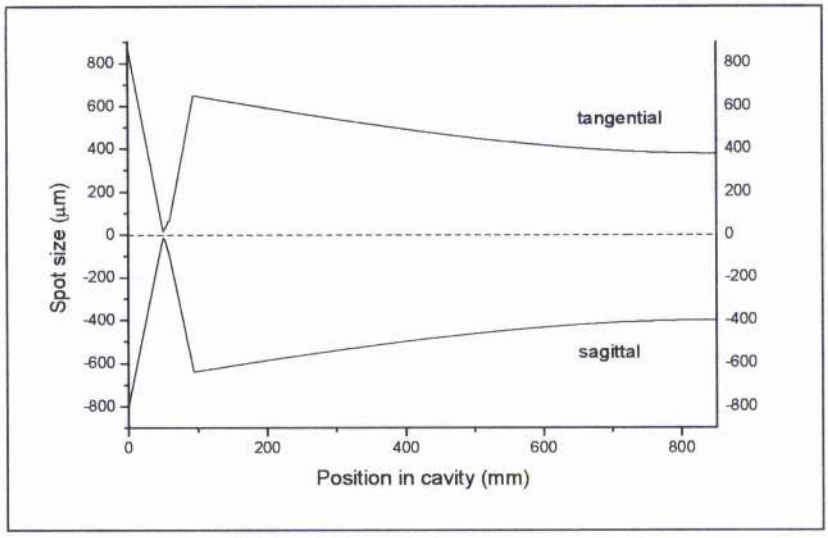

Figure 3.24 Spot size in the tangential (positive) and saggital (negative) planes of the 3-mirror retroreflecting resonator with an overall cavity length of 850 mm.

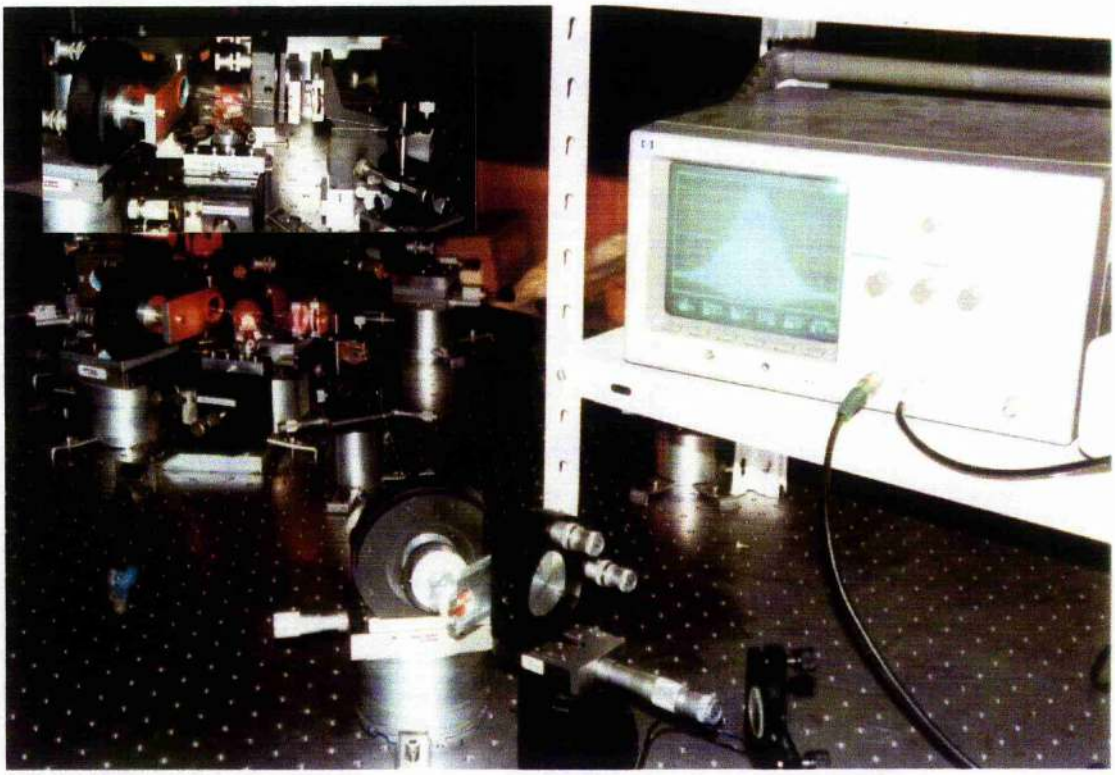

Figure 3.25 Photograph of the 3-mirror Cr:LiSAF laser, inset: close-up of the folding section showing the Cr:LiSAF crystal and the Infrasil prism.

The pump system was reconstructed for the Cr:LiSAF laser and consisted of the SIL laser polarisation combined with a commercial narrow-stripe single-spatial-mode (SSM) AlGaInP laser diode (SDL 7311-G1). The SSM diode chip was housed in a 9 mm TO3 package that was mounted on the heatsink and TEC arrangement shown in Figure 3.26. The SSM laser diode was rated for 33 mW maximum output at 670 nm but was limited to 30 mW when used to pump the Cr:LiSAF laser. The diode was driven using a Wavelength Electronics LFI4352 3.25 A laser diode driver and the temperature of the laser can was maintained at ~ 15°C with a Wavelength Electronics LF3526 2.25 Amp temperature controller. Figure 3.27 shows a typical power characteristic of the SDL device.

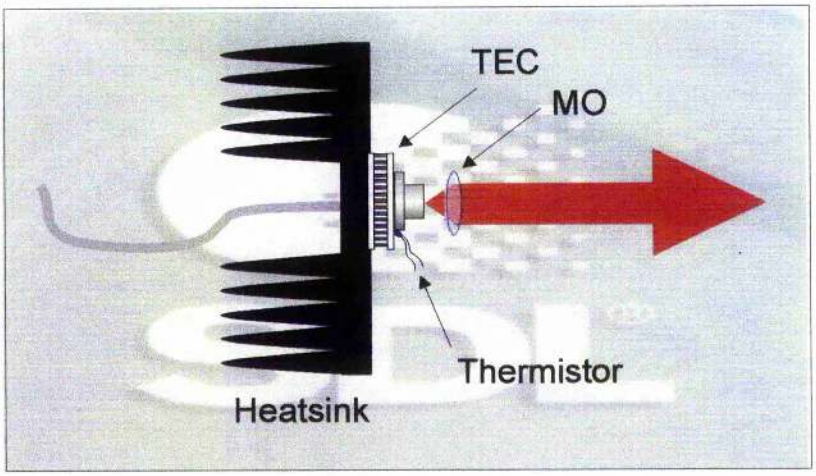

Figure 3.26 Mounting for SDL single-spatial-mode diode laser, TEC – thermoelectric cooler, MO - × 20 microscope objective, the table insert details some characteristics of the laser diode.

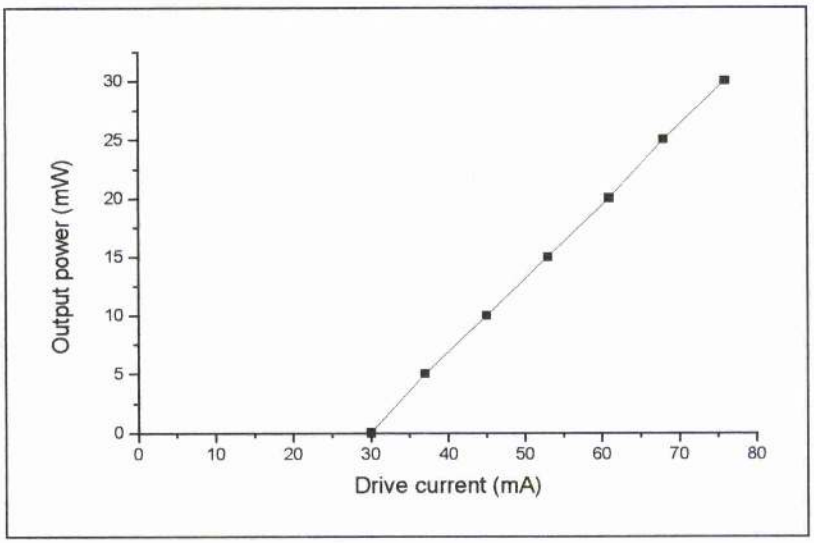

Figure 3.27 Typical power characteristic of the SDL-7311-G1 laser diode.

The emitter facet of the SSM diode measured less than 5 × 1 μm and produced a near-diffraction-limited beam in planes both parallel and perpendicular to the active region. The output beams had a characteristic ellipticity of ~ 3:1 and could be collimated with a simple aspheric or microscope objective lens thus dispensing with the need for more elaborate and extended beam shaping schemes. Figure 3.28 shows the scheme used to combine the SSM and the SIL lasers. The SSM diode was p-polarisation oriented for optimal absorption in the Cr:LiSAF crystal and the SIL laser was polarisation rotated to be s-polarised with a periscope. The maximum available power at the pump-focussing lens was 25 mW from the SSM diode and 99 mW from the SIL diode.

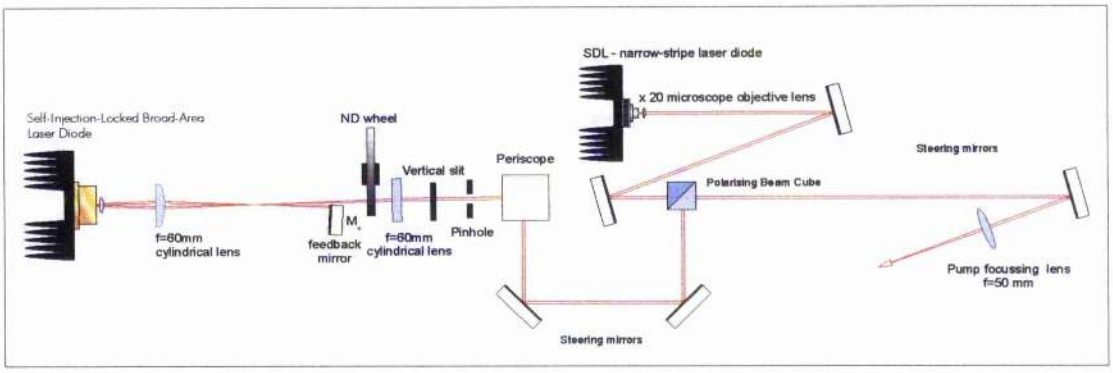

Figure 3.28 Schematic of the full pump system to combine the outputs from the SIL and SSM diodes used initially with the Cr:LiSAF laser.

Various beam shape optimisation schemes were investigated in the SSM beam path including diode collimating optics, an anamorphic prism pair with a spherical telescope and a cylindrical telescope in conjunction with the standard × 20 microscope objective shown above. The conclusion of these investigations was that although some of these schemes produced a more uniform beam shape with minimal aberrations they made insignificant improvements to the threshold of the Cr:LiSAF laser and introduced too much loss for the low power SSM diode.

CW performance

For optimum KLM operation the laser was first aligned for a low cw threshold. Just 8.5 mW of power was required from the p-polarised SSM diode to achieve lasing with all the cavity elements in place. The threshold when using the s-polarised SIL diode was 19 mW indicating the lower absorption of Cr:LiSAF in the plane perpendicular to the crystal c-axis. Figure 3.29 below shows a power characteristic for the Cr:LiSAF laser when aligned for low threshold.

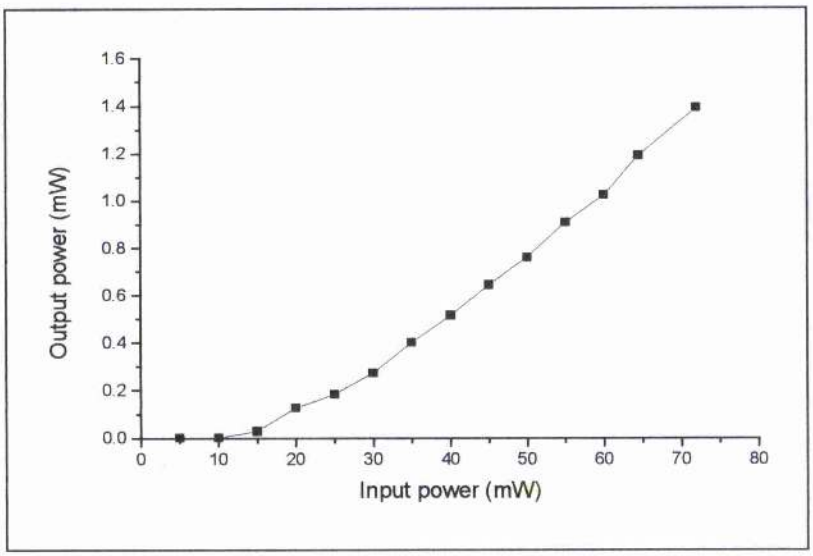

Figure 3.29 Power characteristic of the 3-mirror Cr:LiSAF laser.

Initial modelocked performance

Figure 3.30 and Figure 3.31 below show Magni-type plots for the 3-mirror retroreflecting laser at the end mirror M1 and the pumped crystal facet adjacent to M1 respectively.

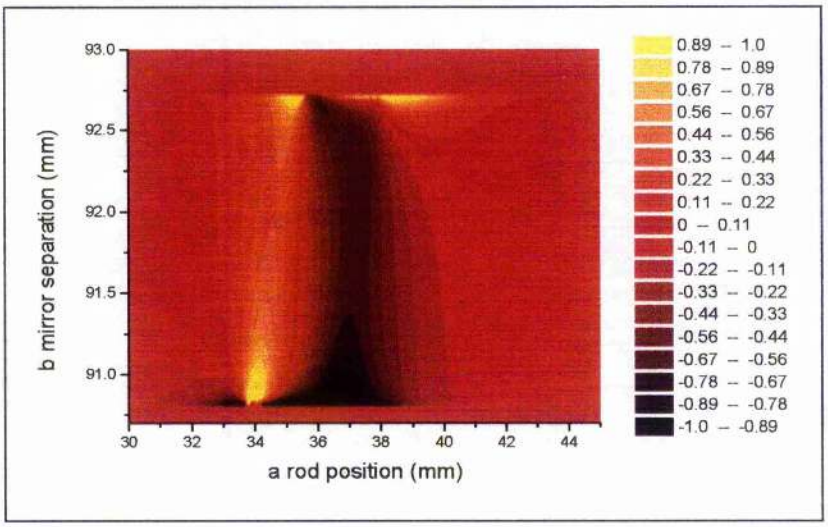

Figure 3.30 A Magni plot of δ(a,b) in the tangential plane at the retroreflecting end mirror M1 for a 3-mirror retroreflecting laser containing a 7 mm Brewster cut Cr:LiSGaF crystal with 50 mm (M1) and 75 mm (M3) ROC mirrors.

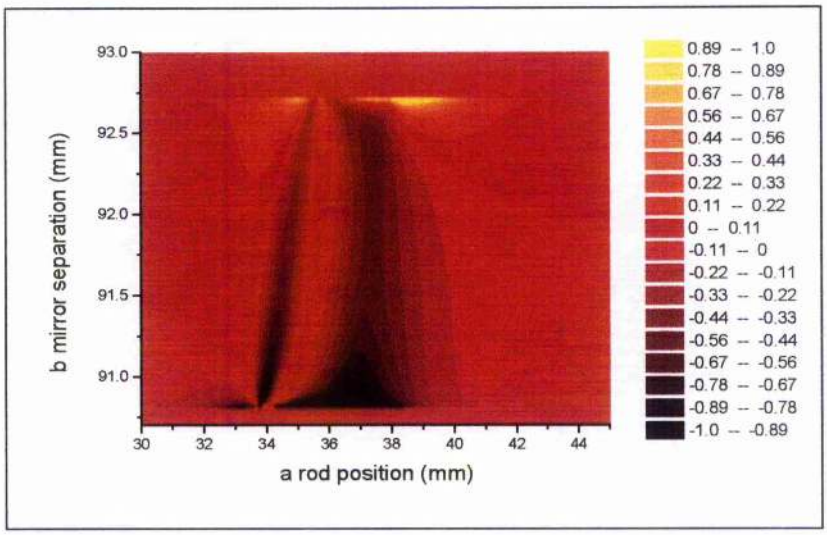

Figure 3.31 A Magni plot of δ(a,b) in the tangential plane at the pumped crystal facet (nearest mirror M1) for a 3-mirror retroreflecting laser containing a 7 mm Brewster cut Cr:LiSGaF crystal with 50 mm (M1) and 75 mm (M3) ROC mirrors.

Figure 3.31 indicates clearly that the cavity is well suited to soft-aperture self-modelocking as δ is negative over a large proportion of the stable region. Hard-aperture modelocking at M1 is impossible because the pump light must also pass through this mirror and an aperture placed before this mirror will obviously obstruct the pump beam.

The laser produced 89 fs pulses within five minutes of connecting the regenerative initiation circuit to the modelocker. The power from the combined pump diodes at the pump focussing lens was 114 mW and the average output power from the laser was 870 μW. When the pump power was reduced to 40 mW the laser produced 196 fs pulses. After initial optimisation the laser produced 70 fs pulses for 100 mW of pump light. When pumped with only the SSM diode (25.5 mW) the laser produced ~200 fs pulses at an average output power of 150 μW and with a time-bandwidth product of 0.35 (see Figure 3.32). The corresponding intracavity average and peak powers were ~ 0.2 W and 5 kW respectively. This result represented the first femtosecond pulses from a laser pumped with a laser diode more commonly used in a supermarket barcode reader or CD writer!

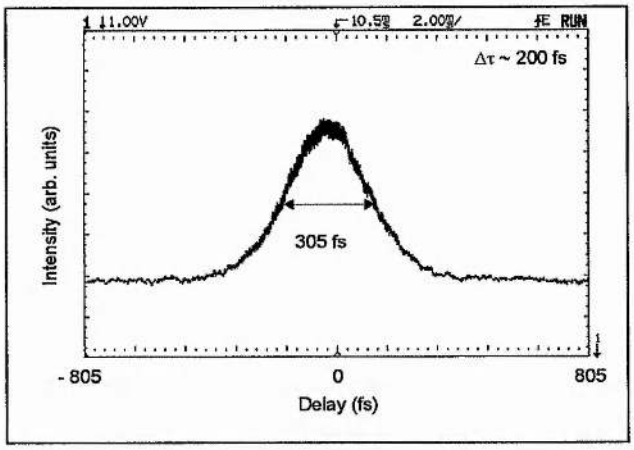

Figure 3.32 Intensity autocorrelation of 200 fs pulses obtained with the SSM pump laser only.

The pump system was then replaced with a pair of prototype 50 mW 680 nm SSM narrow-stripe diodes[12,13] from the Philips Optoelectronics Research Centre (CQL806/D5)[14]. These diodes were based on a selectively buried ridge structure[15] and were fabricated using strain overcompensation to increase the bandgap near the emitter facet thereby reducing absorption and the risk of catastrophic optical mirror damage. The diodes were supplied 'as is' with no specified lifetime so they were mainly kept to a maximum output of 42 mW and each was cooled to 15°C using the same mounting configuration as the SDL SSM diode. Figure 3.33 below shows a typical power characteristic for the prototype devices showing similar thresholds and slope efficiencies as the SDL devices.

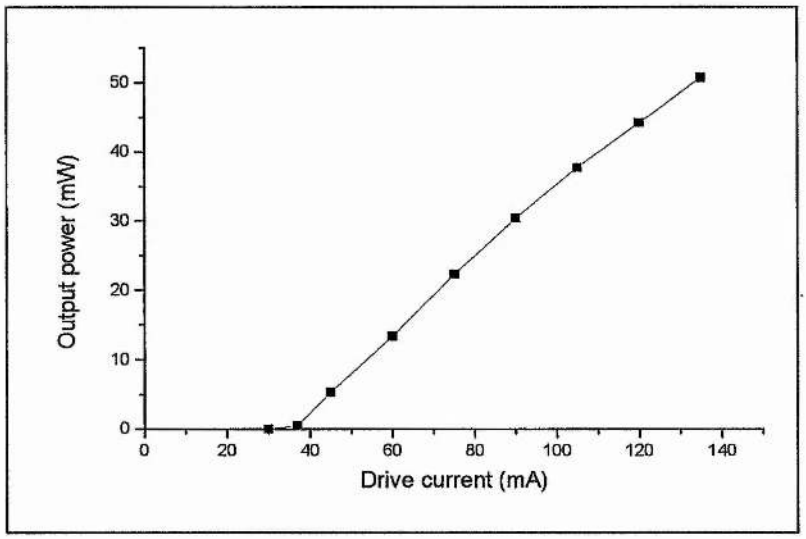

Figure 3.33 Typical power characteristic of the Philips CQL806/D5 laser diodes.

The diodes were mounted orthogonally with respect to each other and polarisation combined to give 76 mW of power incident at the pump-focussing lens. The emitter facet of each diode measured 4.5 × 1 μm producing a similar ~ 3:1 elliptical beam as the SDL devices and as before, no beam reshaping was used which resulted in a cross shaped pump beam (see Figure 3.34).

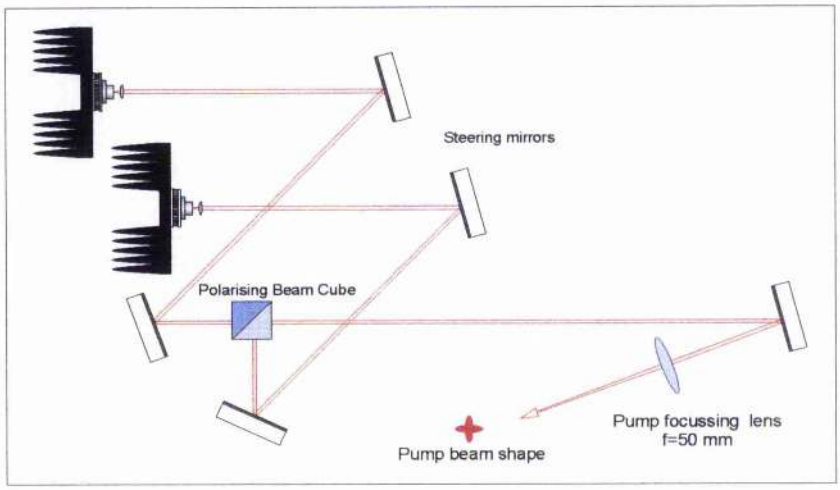

Figure 3.34 Configuration of the two orthogonally mounted prototype Philips laser diodes.

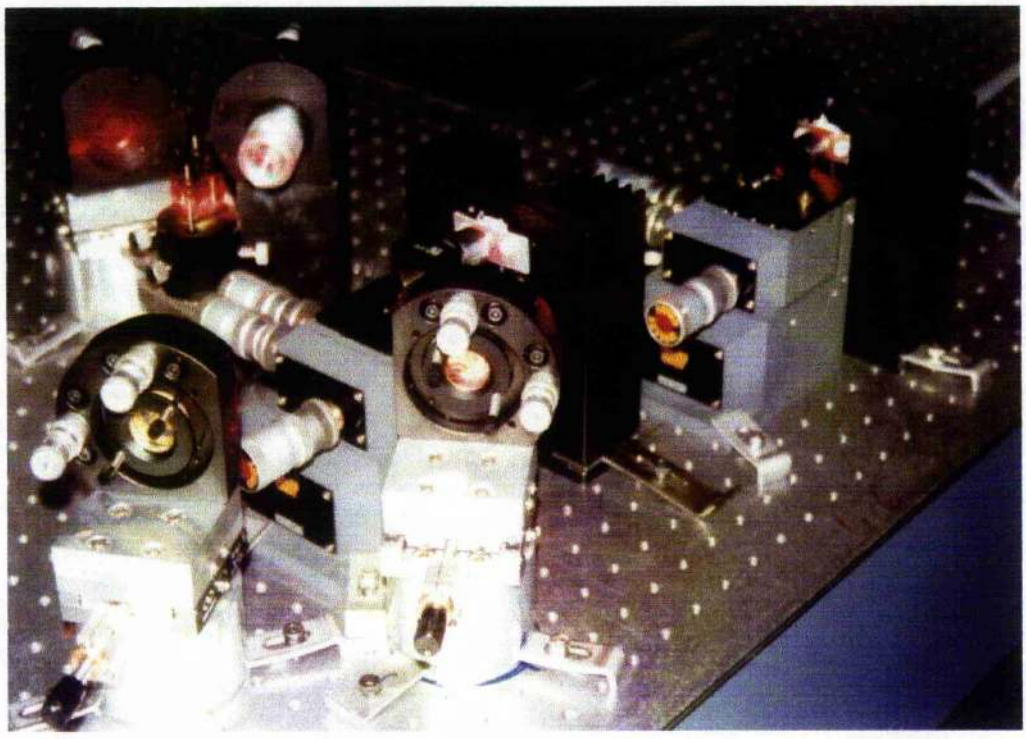

Figure 3.35 Photograph showing the layout of the Philips SSM laser diodes and the coupling optics used.

Modelocked performance

Stable, bandwidth-limited pulses of 60 fs duration were readily obtained with an average output power of 1.57 mW available through each HR mirror (see Figure 3.36). The corresponding intracavity average and peak powers were ~ 2 W and 185 kW respectively. Had a suitable output coupling mirror of slightly lower reflectivity (R~99.75 %) been available at the time it should have been possible to increase the useful output power to >3.5mW, but the modelocked performance might have been compromised. Once stable femtosecond operation was accomplished using this arrangement, the regenerative-modelocking electronics could be switched off, at which point the laser operated in a purely passively modelocked manner. To assess the stability of the pulse train, a phase-noise measurement was carried out using the methodology described later in this chapter the results of which are also presented later.

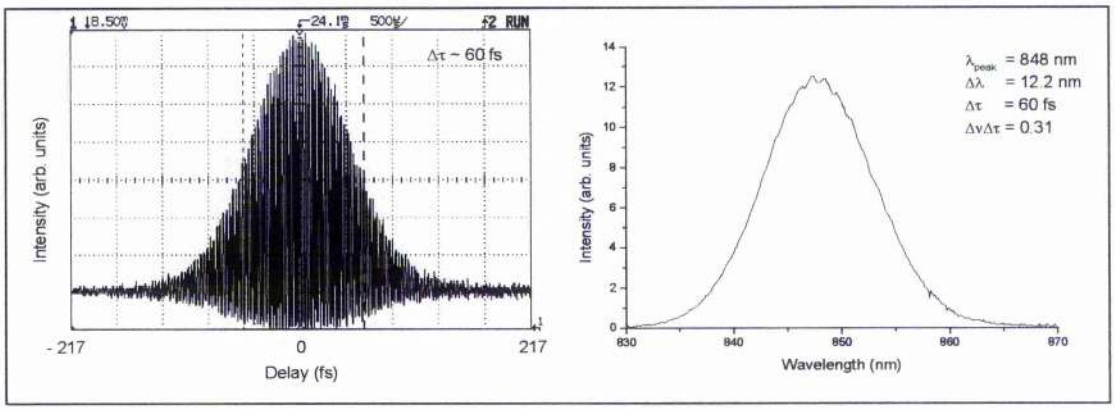

Figure 3.36 Interferometric autocorrelation and spectrum of 60 fs pulses with an average output power of 1.57 mW obtained for 76 mW pump.

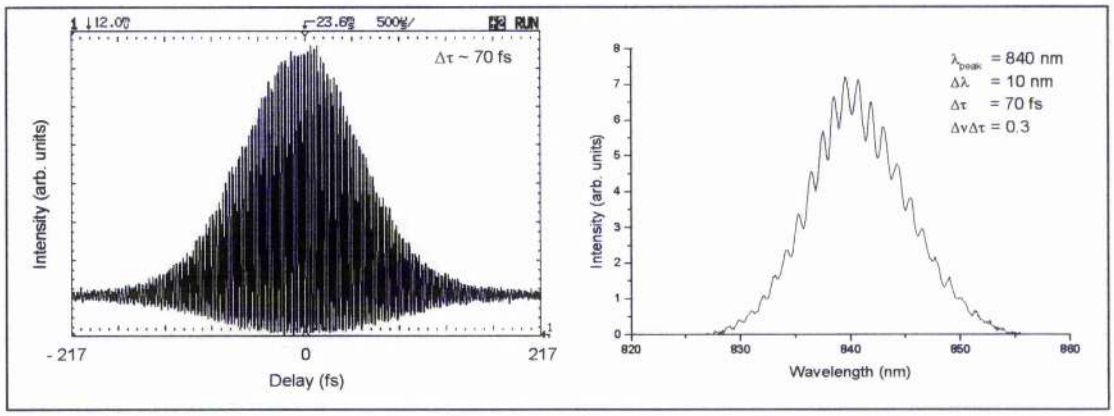

Figure 3.37 Interferometric autocorrelation and spectrum of 70 fs pulses with an average output power of 730 μW obtained for 36 mW pump.

Finally, the s-polarised laser was switched off and the cavity dispersion optimised for pumping with one p-polarised Philips diode by introducing more prism material into the

cavity. This compensates for the reduction in the total effective positive dispersion, as the lower intracavity power induces less self-phase modulation[4]. With only 36 mW of incident pump power, bandwidth-limited pulses as short as 75 fs duration at 730 μW output power were obtained (see Figure 3.37). Sub-100 fs pulsed operation ceased when the pump power dropped below ~30 mW. To demonstrate the potential of this low-threshold laser system for low running costs and portability, the laser diode power supply was replaced with three AA penlight cells (Duracell MN1500) connected in series. An adjustable LP2952, low dropout voltage regulator allowed the drive voltage to the Philips laser diode to be set to give the required 36 mW of incident pump power (see Figure 3.38). This efficient power supply allowed constant output power from the narrow stripe laser diode to be maintained for over 18 hours of operation before excessive battery discharge had occurred.

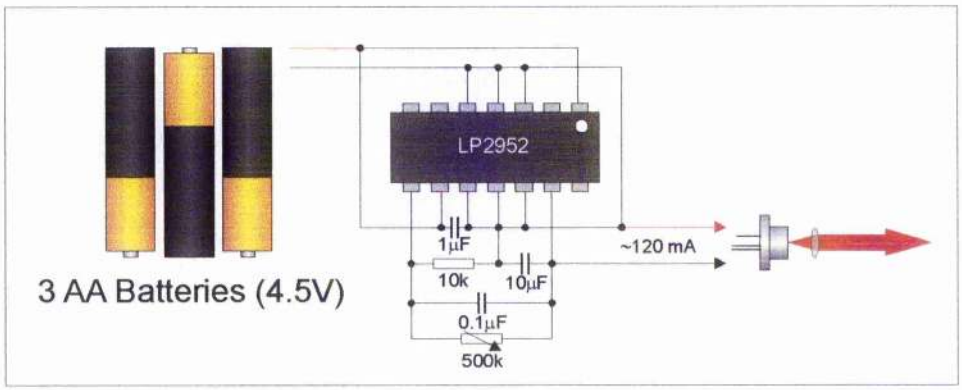

Figure 3.38 Schematic of the simple battery powered low-voltage-drop-out regulator circuit used to power the Philips laser diodes.

3.5 Noise

In any physical system noise, in the form of random fluctuations or deterministic (spurious) fluctuations is an unavoidable phenomenon. These fluctuations originate from a variety of sources including thermal effects, quantum effects and mechanical vibrations. The principal sources of random noise in a laser system are numerous but often include fluctuations in the pump source/laser thermal noise acting on the lasing process, air currents/dust, mechanical vibrations, mixing/interference and mode coupling effects[16]. Systematic noise may also be caused by oscillations from adjacent mechanical or electrical systems, it was found for example that a resonance from the surface of an optical table added a frequency component at ~200 Hz to the noise of a system[17]. Noise therefore must be taken account of, and to a first approximation at least

quantified when investigating or using such a laser system. The noise present in an ultrashort pulse laser system manifests itself in the quality and repeatability of the output train of pulses. The majority of fluctuations in a train of Fourier transform limited or near transform limited pulses from a self-modelocked laser are found to occur, in general, on timescales much longer than the repetition time between the pulses and certainly much longer than the duration of the pulses themselves. It is possible therefore in this case to think of the pulseshape as being relatively unaffected by these fluctuations which will appear as perturbations in the amplitude of the pulses (amplitude noise) and in the time between subsequent pulses (temporal jitter or phase noise). If one considers a perfectly modelocked train of pulses $F_o(t)$ then the same train of pulses $F(t)$ in the presence of this noise can be represented by

$$F(t) = F_o(t) + F_o(t) \cdot A(t) + \dot{F}_o'(t) \cdot T \cdot J(t)$$

Equation 3.3

where $\dot{F}_o'(t)$ is the first-order time derivative of $F_o(t)$, T is the average pulse repetition time and $A(t)$ and $J(t)$ are random fluctuations with respect to time. Figure 3.39 below shows the physical interpretation of Equation 3.3.

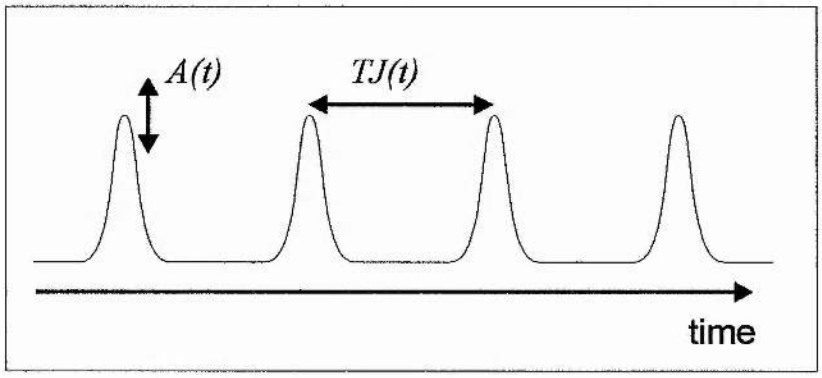

Figure 3.39 Pulse train in the presence of fluctuations in amplitude and time, $A(t)$ and $J(t)$.

To be able to utilise to the full an ultrashort pulse laser system in say a pump-probe experiment or in the characterisation of a pulse measurement system such as the streak cameras in section 3.6 a knowledge of and an ability to characterise its amplitude and phase noise properties is paramount to the experimenter. It has been shown[18] that the relative presence of these distinct effects may be readily determined from direct measurements of the RF power spectrum of the laser source. Such spectra can be readily measured using a suitable combination of fast photodetector and RF spectrum analyser.

This type of measurement naturally combines the noise from the laser and any 'two-port' or contributed noise from the photodetector and analyser. Von der Linde[18] derived an expression for the power spectrum of an 'imperfectly' modelocked laser as

$$P_F(\omega) = \left(2\pi/T\right)^2 \left|\tilde{f}(\omega)\right|^2 \sum_{\mu} \left[\delta(\omega_\mu) + P_A(\omega_\mu) + (2\pi\mu)^2 P_J(\omega_\mu)\right]$$

Equation 3.4

where $\tilde{f}(\omega)$ is the Fourier transform of the pulse envelope slowly varying with respect to the more rapidly varying term in square brackets, $\omega_\mu = (\omega - 2\pi\mu/T)$ and μ is an integer between plus and minus infinity. A plot of $P_F(\omega)$ normalised to the spectral envelope $\left|\tilde{f}(\omega)\right|^2$ is shown below in Figure 3.40.

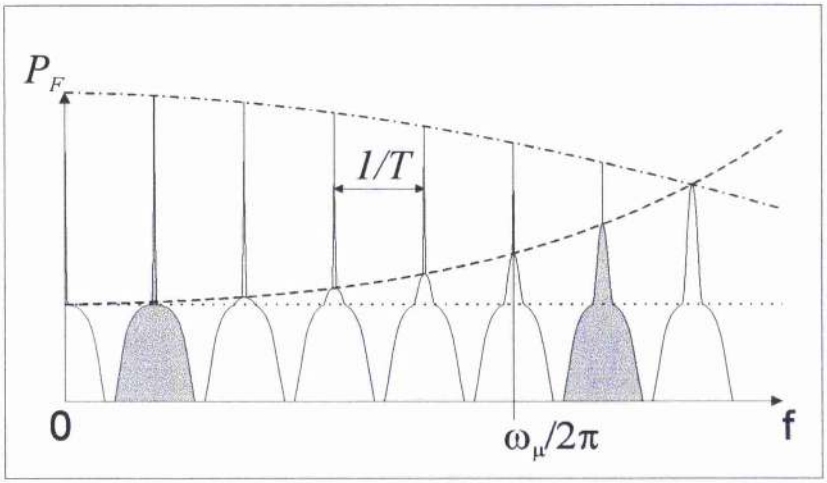

Figure 3.40 Normalised power spectrum P_f of a train of pulses with a fluctuating pulse amplitude and repetition time. T is the average repetition time. The dotted line indicates the maxima of the amplitude noise contribution to the noise bands. The dashed line is proportional to ω^2 and marks the maxima of the narrower jitter noise contribution to the noise bands. The dashed-dot line represents the frequency response of the detection system.

The plot represents the discrete frequency bands or harmonics associated with the laser denoted by harmonic order μ and respective central frequency ω_μ. Figure 3.40 illustrates the differences in the effect of each type of noise represented in the sum of Equation 3.4. The first term in the sum $\delta(\omega_\mu)$ represents the δ function like contribution to the power spectrum by a perfectly modelocked laser. The second term is the part of P_f derived from the amplitude fluctuations of the pulses and is indicated in the figure by the broad pedestals of constant volume under the dotted, line i.e. the frequency shifted power spectrum of the amplitude noise A(t). The third term involves the power

spectrum of the jitter function, J(t) and exhibits a characteristic ω^2 dependence (the dashed line). It is this dependence that allows us to break down the noise in a laser system into its constituent parts and distinguish the relative amounts of each. The dashed-dot line indicating a cut-off at higher frequencies is due to the combined truncated response of the measurement system. By comparing the RF power spectra of low and high order harmonics of a laser system (see Figure 3.41) it is possible to calculate values for the amplitude and phase noise present. In this manner pulse jitter values of less than 100 fs can be obtained from a photodetector with a rise time of the order of nanoseconds.

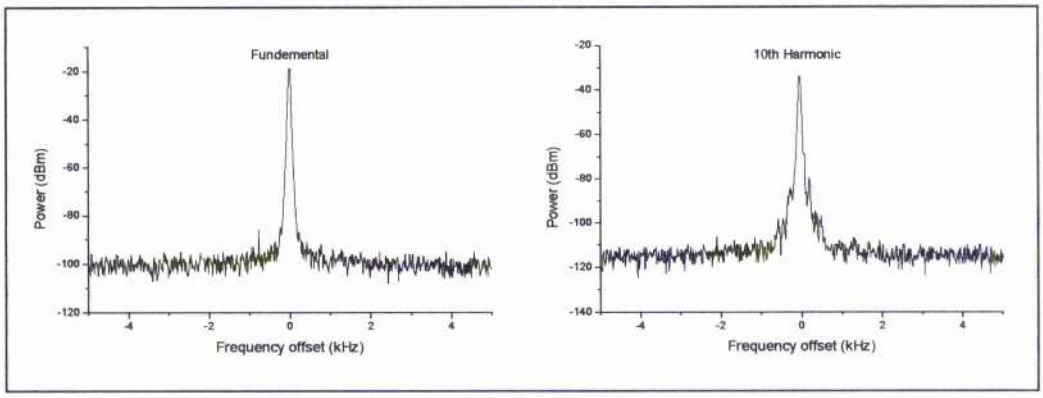

Figure 3.41 Typical RF spectra of the fundamental and 10th harmonic of a femtosecond laser running at 170 MHz measured with a 10 kHz span.

The output from the 3-mirror LiSAF laser was focussed using a 1.5 cm plano-convex lens onto a BPW28-B silicon fast photodiode with a nominal bandwidth of ~2 GHz. The diode was biased to 135 V using a smoothed voltage supply to ensure as low-noise and linear response as possible. The photodiode was connected via the terminated bias circuit to an HP 70000 series RF spectrum analyser unit as shown below in Figure 3.42.

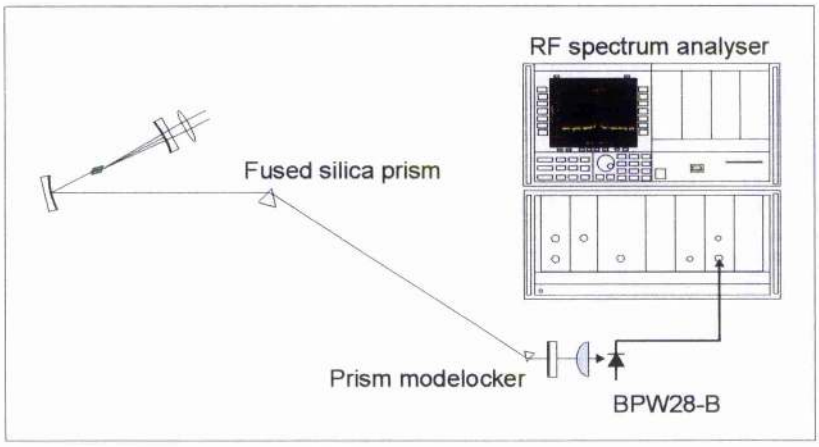

Figure 3.42 Typical noise measurement set-up.

The RF spectrum for each harmonic was measured over different frequency spans (10 MHz, 1 MHz, 10kHz, 1kHz) in order to determine a respectable resolution across the entire harmonic spectra. These spectra were automatically measured and logged by an IBM compatible PC connected to the analyser system running a program written in Pascal. Typically the fundamental, 10^{th} and 15^{th} harmonics were used to determine the noise. The noise floor of the system was also measured in this manner. Once the measurements of each harmonic at different resolutions had been carried out the computer calculated plots of amplitude and phase noise as well as timing jitter values for a variety of frequency bands. Figure 3.43 below shows the amplitude and phase noise power spectra for the self-modelocked Cr:LiSAF laser.

Some typical rms timing jitter values are plotted in Table 3-1 for various frequency bands of the 3-mirror Cr:LiSAF laser compared with a free running KLM Ar^+-ion pumped Ti:sapphire laser[19] and an actively stabilised, frequency locked Ti:sapphire laser connected to a noise eater system[19].

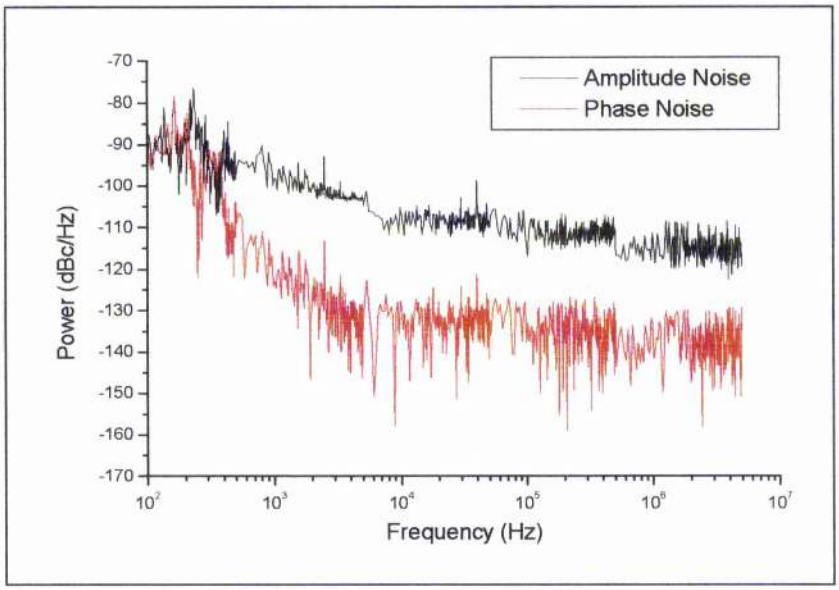

Figure 3.43 The single-sideband amplitude and phase noise power spectra of the self-modelocked Cr:LiSAF laser, calculated using the fundamental and 10^{th} harmonic Fourier components.

Frequency range	3-mirror, low-threshold, KLM Cr:LiSAF laser	Free-running, KLM Ti:sapphire laser[19]	Actively-stabilised, KLM Ti:sapphire laser[19]
50 – 1000 Hz	2200 fs	-	-
100 – 500 Hz	680 fs	3400 fs	150 fs
500 – 5000 Hz	73 fs	800 fs	80 fs

Table 3-1 Rms timing jitter values for the 3-mirror self-modelocked Cr:LiSAF laser, a self-modelocked Ti:sapphire laser and an actively stabilised self-modelocked Ti:sapphire laser.

In contrast to the laser described in reference 19 the only attempt to remove sources of noise from the Cr:LiSAF laser was to ensure that all mirror/component mounts were attached firmly to the optical table and the construction of a light aluminium framework covered with a thin polythene sheeting to reduce air currents to a minimum. Battery operation of the two pump diodes also ensured a clean noise-free pump beam for the laser. The table clearly shows the advantage of pumping directly with diode lasers as the performance of this purely passive system is comparable with the actively stabilised system.

3.6 Investigation of a prototype streak camera system

Time-resolving, electron-optical streak cameras provide a direct measurement of the temporal profile of an optical pulse over a very large wavelength range and therefore represent an invaluable diagnostic tool for a wide variety of optical pulse systems. In turn, low-noise ultrashort pulse lasers provide a means of characterisation and calibration of these streak camera systems. During the course of the experimental work for this thesis a number of intermediate prototype camera tubes were investigated using the basic experimental technique outlined in the following section.

Figure 3.44 below shows the configuration of a typical streak camera system consisting of some input optics, the streak image tube and an intensifier/detection system (not shown).

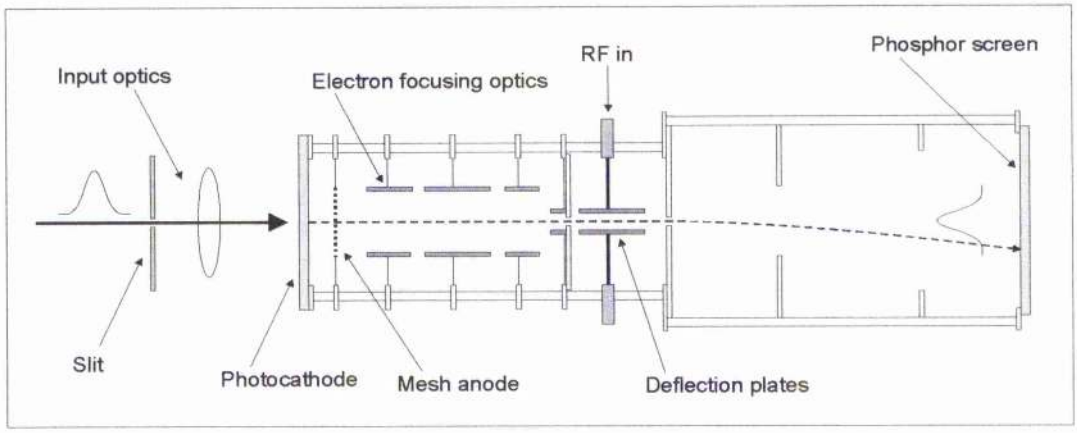

Figure 3.44 Schematic of an electron-optical streak camera.

The streak tube consists of a photocathode an acceleration anode mesh, an electron focussing lens, deflection electrodes and a phosphor screen. An incoming light pulse passes through a narrow slit and is imaged through some input optics onto the photocathode liberating a packet of electrons with the intensity profile related to that of the of the original optical pulse. These electrons are then accelerated across a high electric field (typically ~ 20 $kVcm^{-1}$) between the cathode and an anode mesh electrode. The electrons then pass through a set of deflection plates that focus them onto the phosphor screen at the output of the camera tube. Before reaching the screen the electron pulse passes between deflection plates to which, in synchroscan operation, a sinusoidal frequency synchronised with the repetition frequency of the incoming pulses is applied. This sinusoidal deflection effectively turns the pulses and scans or 'streaks' them across the phosphor screen thereby converting the temporal profile of the electron packet (and therefore the incident optical pulse) into a spatial profile. The image on the screen is made up of many subsequent pulses integrated by the response time of the phosphor. Improvements in tube design have meant that the resolution of commercially available streak cameras have been pushed down from ~ 50 ps to ~ 1 ps in synchroscan operation and ~ 300 fs in single-shot mode.

In single-shot mode, as its name suggests, a single pulse is recorded with a single voltage ramp applied across the streak plates. The operation of a camera in this mode is more complex as sufficient intensity must be contained within a single pulse to overcome the noise present in the camera without degrading the temporal response due to space charge effects and Coulomb repulsion of the liberated electrons[20]. Intensifiers are also required in order to detect the signal at the output of the camera.

Due to the added difficulties in making a single-shot measurement it is advantageous therefore to further improve the resolution available to synchroscan operation. The resolution of a streak camera in both modes of operation is dependent on a number of factors such as the finite diffraction limited width of the input slit, the response time, energy and angular spread of photoelectron emission of the cathode, the non-linear deflection field and the phase noise present in both the camera itself and the input pulse train. In order to assess the resolution of a streak tube, as many of the external noise sources as possible must be eliminated. To remove any temporal smearing due to the input pulse train it is necessary to use an ultrashort pulse source with pulse duration much shorter than the ultimate resolution of the camera (ideally a delta function) with as little temporal jitter or phase noise as possible. The improved phase noise properties of the low threshold colquiriite laser systems has been show previously[21] to provide a great simplification to the types of laser systems used for streak camera evaluation.

Typically the image is recorded with a conventional camera system and viewed on an optical multi-channel analyser (OMA).

The streak cameras tested with the lasers during the course of the development of the low threshold colquiriite lasers were all intermediate prototypes toward the development of a more compact, self-contained camera with CCD array detection system[22]. The tubes were modified versions of the Photocron V streak camera developed at St Andrews[20] with an S1 photocathode for longer wavelength operation (UV to 1.5 μm). The primary modifications to the tubes assessed here were a lower anode voltage (~ 5 kV) to avoid damage to an internal electron-bombarded CCD array and to improve the dynamic range. The slower electrons will not liberate as many carriers in the charge-coupled device and saturate so readily and are easier to scan across the detector. New mesh designs for better photoemission and lower distribution of electron velocities were also a feature of this project.

Figure 3.45 below shows the typical experimental set-up used in the assessment of electron-optical streak camera tubes during the course of this thesis.

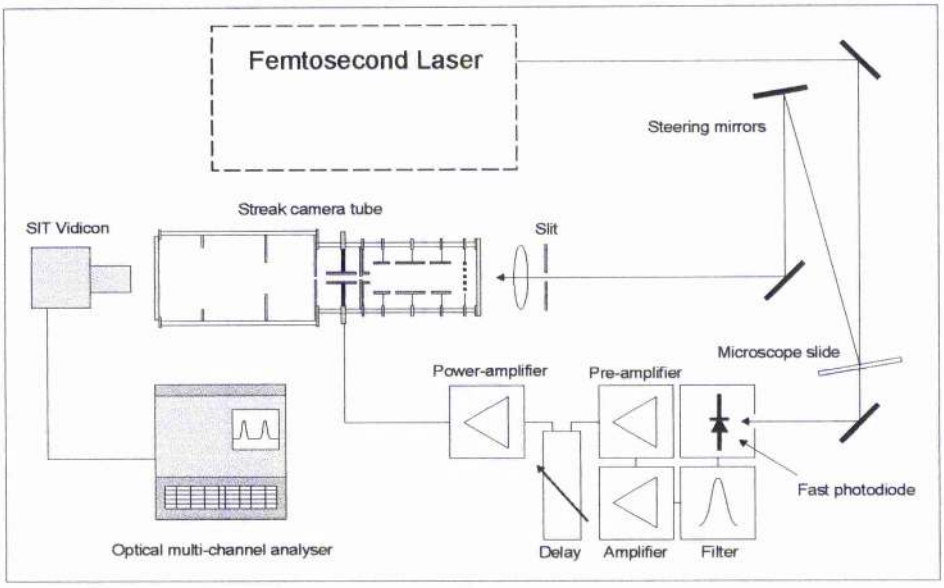

Figure 3.45 Schematic of the experimental set-up for the assessment of streak camera tubes.

The laser output was reflected from a 1 mm thick uncoated glass microscope slide at near normal incidence providing a pair of pulses separated by 10 ps for calibration of the camera output. To accurately determine the repetition frequency of the laser cavity for the streak sweep the leakage from the slide was used to illuminate an AEPX 65 fast photodiode and tuned filter/amplifier (OM355) combination circuit. This signal was then amplified using a CA2820 broadband amplifier (30 dBm) and passed through a variable delay line to match the electrical and optical path lengths. The correctly phased signal was then amplified by a BG45C power amplifier with a 20 MHz bandwidth and passed to the deflection plates via a high Q tuned circuit. The screen image from the camera was recorded using a B+M OSA 500 silicon intensified target (SIT) Vidicon camera and optical multi-channel analyser arrangement.

Figure 3.46 below shows a typical output trace from an intermediate tube with a temporal resolution ~ 0.8 ps. This is the best directly measured temporal resolution for a Photocron-type synchroscan streak camera to be recorded to date. This is attributable to the exceptionally low phase noise in the self-modelocked Cr:LiSAF laser.

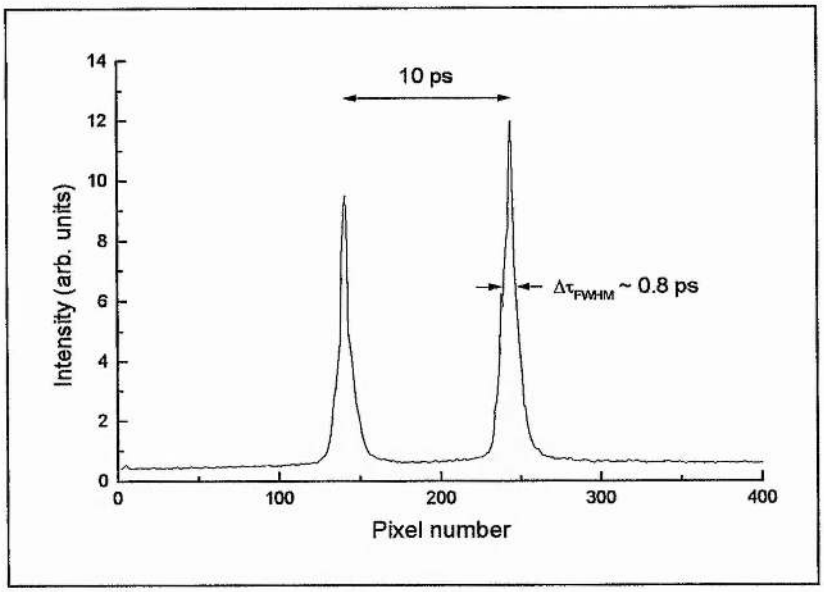

Figure 3.46 Streak camera trace of two ultrashort pulses separated by 10 ps the resolution of this camera is ~ 0.8 ps.

3.7 Conclusions

In this chapter a brief description and the merits of laser resonators with three cavity mirrors designed for the purpose of low-threshold ultrashort pulse self-modelocked operation has been given. The cw, modelocked and low noise performance of two regeneratively initiated directly diode-pumped Cr^{3+}:colquiriite lasers were then detailed. These laser systems exhibited very low cw thresholds and noise properties that were superior to traditional Ar^{+} pumped Ti:sapphire lasers. The first 3-mirror laser based around a plane/plane cut crystal of Cr:LiSGaF produced pulses as short as 65 fs and provided sub-100 fs pulse operation for pump powers as low as 50 mW. The modelocking threshold was measured to be 25 mW. The second 3-mirror laser incorporated a Brewster-angled Cr:LiSAF crystal and produced pulses as short as 60 fs. The laser provided sub-100 fs pulse operation for pump powers as low as 30 mW and ultrashort pulse operation ceased when the pump power was reduced below 22 mW. The superior performance of the Cr:LiSAF laser permitted a single, narrow-stripe, diffraction limited laser diode to be used as the pump source. This laser system provided a cheap, efficient and low noise source of femtosecond pulses, which potentially could be made to occupy a small area. Finally, a description of the experimental set-up used in conjunction with these novel short pulse sources for the evaluation of a number of prototype streak camera tubes was described. Using this experimental configuration the best temporal resolution for a synchroscan streak image was recorded.

Endnotes

1 D. E. Spence, P. N. Kean, and W. Sibbett, *Opt. Lett.* **16**, 42 (1991).

2 B. E. Bouma, M. Ramaswamy-Paye and J. G. Fujimoto, *Apl. Phys.* **B 65**, 213 (1997).

3 G. J. Valentine, M. P. Critten, G. T. Kennedy, J-M. Hopkins, P. Loza-Alvarez, and W. Sibbett in *Technical Digest of Conference on Lasers and Electro Optics*, (Optical Society of America, Washington, D. C. 1997), paper CMI1.

4 Kindly donated by Dr. David Burns and the Optical Materials Research Centre of the University of Strathclyde.

5 G. Cerullo, S. De Silvestri, V. Magni, and L. Pallaro, *Opt. Lett*, **19**, 807 (1994).

6 A. E. Siegman, *in Lasers (University Science Books, Sausalito, California 1986)*, Chapter 17.

7 D. T. Reid, C. McGowan, W. Sleat, M. Ebrahimzadeh and W. Sibbett, Opt. Lett. 22, 525 (1997).

8 Malini Ramaswamy-Paye and J. G. Fujimoto, *Opt. Lett*, **19**, 1756 (1994).

9 B. E. Bouma and J. G. Fujimoto, *Opt. Lett*, **21**, 134 (1996).

10 V. Magni, G. Cerullo, S. De Silvestri and A. Monguzzi, *J. Opt. Soc. Am.* **B 12**, 476 (1995).

11 G. J. Valentine, and W. Sibbett, *in Technical Digest of the Conference on Lasers and Electro-optics Europe (Optical Society of America, Washington D.C. 1998)*. paper CtuM47.

12 A. Valster, A. T. Meney, J. R. Downes, A. R. Adams, A. A. Brouwer, and A. J. Corbijn, in *Digest of 15th Intl. Semiconductor Laser Conference* (IEEE, New York, NY, USA, 1996), pp. 139.

13 A. Valster, A. T. Meney, J. R. Downes, D. A. Faux, A. R. Adams. A. A. Brouwer and A. J. Corbijn, *IEEE J. Sel. Topics Quantum Electron.* **3**, 180 (1997).

14 Kindly donated by Dr. Ad Valster, Philips Optoelectronics Research, Prof. Holstlaan 4, 4656 AA Eindhoven, The Netherlands.

15 M. Ishikawa, Y. Ohba, Y. Watanabe and G. Hatakoshi, in *Ext. Abst. 18th Conf. Solid-state Dev. Mater.*, Bus. Ctr. For Academic Soc., Tokyo, Japan, 1986, p.153.

16 T. Baer, *J. Opt. Soc. Am.* **B 3**, 1175 (1986).

17 J.M. Evans, in *Linear and Nonlinear Pulse Characterisation*, Phd Thesis, University of St Andrews (1989).

18 D. von der Linde, Appl. Phys. B. 39, 201 (1986).

19 D. E. Spence, J. M. Dudley, K. Lamb, W. E. Sleat, and W. Sibbett, Opt. Lett., **19**, 481 (1994).

20 Y. Liu, in *Design and Evaluation of Ultrafast Electron-optical Streak and Framing Cameras*, Phd Thesis, University of St Andrews (1996).

21 M. P. Critten, in *All-solid-state Femtosecond Cr:LiSAF and Cr:LiSGaF Lasers*, Phd Thesis, University of St Andrews (1996), Chapter 4.

22 DRS Hadland Ltd. Harrow Yard, Akeman Street, Tring, HERTS, HP23 6AA, U.K.

Chapter 4: Femtosecond Cr:LiSAF lasers with highly asymmetric resonators

4.1 Introduction

In chapter 3, two low-threshold, self-modelocked laser arrangements were described that exhibited an impressive performance with relatively low intracavity powers. These lasers had a number of drawbacks however, because the lower intracavity powers necessitated the use of a regenerative initiation of the modelocking and this was not always reliable and added an extra degree of complexity into an otherwise simple laser resonator. Also, the two cavities could not be operated in a 'hard aperture' modelocking regime at an end-mirror, because this was physically impossible and although this did not have a detrimental effect on the final performance of the two lasers, the absence of this degree of freedom was unwelcome.

In this chapter, a number of laser systems based on a more versatile highly asymmetric 4-mirror resonator geometry will be described. The resonators are designed to retain as many of the advantages of the 3-mirror retroreflector geometry as possible while addressing the above issues. They provide the possibility of 'hard-aperture' or, more importantly, saturable absorber modelocking in a more compact cavity than traditional self-modelocked or saturable-absorber-based lasers. The application of this new cavity geometry in conjunction with an semiconductor saturable absorber mirror (SESAM) will be shown to produce a laser system that is both low-threshold and efficient. The inclusion of the an antiresonant Fabry-Perot saturable absorber (A-FPSA) permitted the use of an output coupling mirror allowing an order of magnitude greater average output power to be obtained. This new resonator configuration also provided more reliable, entirely self-starting, femtosecond pulse operation. Two laser systems based on this resonator geometry will be described and the modelocking and noise properties discussed. As a proof of principle and a demonstration of the stable modelocking

achieved at low pump powers an intracavity frequency doubling experiment will also be detailed.

4.2 A highly asymmetric 4-mirror resonator

The primary benefits of the 3-mirror Cr:LiSAF laser in the previous chapter were the reduced parasitic losses from the reduction of cavity elements and the simultaneous positioning of tight localised foci in the tangential and sagittal planes at the surface of the Brewster-angled gain medium. This was achieved by ensuring all the astigmatic elements in the cavity were located on one side of the Cr:LiSAF crystal.

Many of the benefits realised in the 3-mirror cavity may be implemented in a 4-mirror cavity, provided that the fold angle of the curved mirror adjacent to the pump lens is kept to a minimum and the angle of the opposite folding mirror used to compensate for astigmatic effects. The use of a cavity of this type has a number of advantages: it permits the use of a hard aperture for self modelocking, and therefore an extra degree of control; the stability properties of the cavity revert to the traditional high misalignment (HMS) and low misalignment (LMS) stability regions described in chapter 2; and the output from the second cavity arm is not spatially dispersed due to the intracavity prisms. Reducing the radius of curvature (ROC) of one of the cavity folding mirrors has been shown to allow a more closely coupled and tightly focused pump beam[1], which is particularly advantageous for diode pumping, without significantly reducing the stability region for alignment purposes. In addition, alignment of the 4-mirror cavity in the LMS region permits a very tight focus to be achieved on the 4th end-mirror providing the second arm length is kept short. This tight focus has the advantage of producing a high incident pulse fluence at this mirror, which may be used to facilitate fast saturable absorber modelocking even with moderate intracavity powers. Alignment of a 4-mirror laser in the LMS region corresponds to folding mirror separation of

$$\frac{2L_1R_1+2L_1R_2-R_1R_2}{4L_1-2R_1}\le b-d\left(1-\frac{1}{n^3}\right)\le\frac{2L_1L_2R_1+2L_1L_2R_2-L_1R_1R_2-L_2R_1R_2}{(2L_1-R_1)(2L_2-R_2)}$$

Equation 4.1

where R_1 and R_2 are the ROC of the folding mirrors and L_1 and L_2 are the lengths of the corresponding cavity arms.

The resulting 4-mirror laser when all these considerations are taken into account is therefore highly asymmetric in almost every degree of freedom: the cavity arms are of differing lengths; the folding mirrors have different radii of curvature and each folding mirror subtends a different angle to the gain medium. The laser systems presented in this chapter are all based around the highly asymmetric 4-mirror cavity geometry shown below in Figure 4.1.

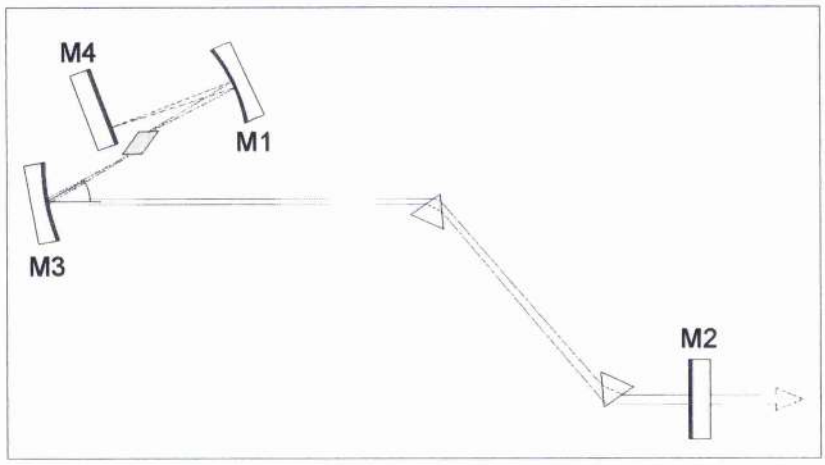

Figure 4.1 Schematic of the highly-asymmetric 4-mirror resonator: M1 - 50 mm ROC, M3 – 75 mm ROC, M2, M4 – plane end-mirrors.

The tight localised focus is retained at the pumped crystal facet, as the angle of the folding mirror M1 is kept small (near normal incidence). This ensures that a low cw threshold and non-distributed Kerr lens remain possible. The astigmatism introduced by the Brewster-cut gain medium is again compensated entirely by the angle (~30°) of the opposite folding mirror (M3). The inclusion of the short arm provides a point at which an intracavity slit or for the case of the lasers presented here, some form of saturable absorber mirror may be placed to facilitate modelocking. Figure 4.2 shows a Magni plot of Kerr lens sensitivity (KLS) at an aperture placed in front of mirror M4 for such a cavity with short arm length ~88 mm and the pump light focussed through M1.

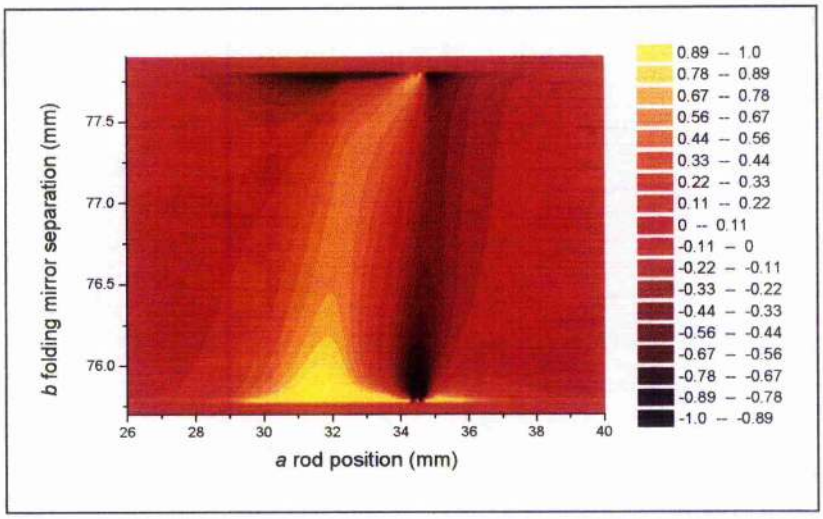

Figure 4.2 Magni plot for a highly asymmetric resonator, short arm length 88 mm, M1 50 mm ROC, M3 75 mm ROC.

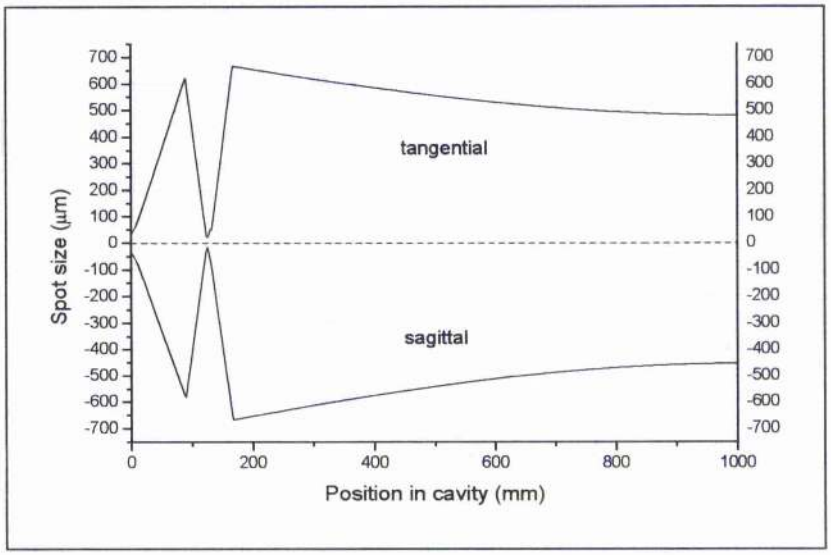

Figure 4.3 Spot size in the tangential (positive) and saggital (negative) planes of the highly symmetric resonator for a short arm length of 88 mm and an overall cavity length ~ 1 m.

A major advantage of the highly asymmetric resonator geometry is that by simply adjusting the length of the short arm the spot size at the short arm end mirror may be easily changed (see Figure 4.3). The ability to alter the spot size without replacing any cavity optics becomes significant when saturable absorber mirrors are used as this allows the incident fluence and subsequent saturation of the absorber to be optimised for varying intracavity powers. Figure 4.4 below shows the linear relationship between the spot size at M4 and the length of the short arm. The fluence at M4 in μJcm^{-2} is given by

$$F_{M4} = \frac{P_c}{f_{cav}\pi r^2} \times 10^{14}$$

Equation 4.2

where P_c is the intracavity power, f_{cav} is the intermode or round-trip cavity frequency and r is the spot radius at the focus.

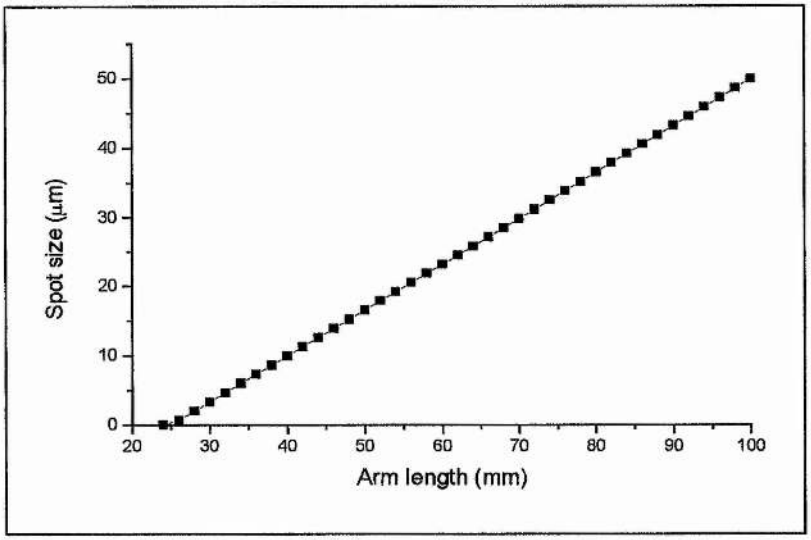

Figure 4.4 Spot size at mirror M4 as a function of short arm length.

It is possible to achieve a very tight cavity focus at the end mirror and as this cavity design has many advantages for lasers with relatively low pump power requirements and low intracavity powers.

Although cavity optics need not be replaced while adjusting the spot size at M4 the length change of the short arm does require a slight adjustment in the position of folding mirror M1 to maintain a stable cavity. Because the pump beam passes through this mirror, optimisation of the pump lens is required to counter any displacement of the pump beam. As in the previous 3-mirror resonators the long cavity arm accommodates the dispersion compensating prism pair and provides an output from the laser.

4.3 A low-threshold, highly asymmetric self-modelocked Cr:LiSAF laser

To more closely compare the highly asymmetric cavity with previous resonators, the regenerative initiation scheme and prism modelocker were used initially in conjunction with soft-aperture modelocking, as before.

The laser cavity

The Cr:LiSAF crystal used was the 7 mm, 1.5% Cr^{3+} doped Brewster-angled slab from the laser detailed in section 3.4. The configuration of the Cr:LiSAF cavity and pump diodes is shown in Figure 4.5. The short arm folding mirror M1 was a 50 mm ROC mirror through which the pump beam was focussed using a 50 mm focal length lens. A 75 mm ROC mirror was used as the second folding mirror M3. All the cavity mirrors were broadband HR (> 99.9%) coated for 840 nm. The total cavity length was approximately 840 mm giving a pulse repetition frequency of ~178 MHz. The two pump lasers used were the prototype, narrow stripe, SSM diodes from Philips (CQL 806/50) described earlier. The diode outputs were once again combined using a Glan-Thompson polarising beam splitter cube to provide 76 mW of 680 nm light at the pump lens. Instead of mounting the diodes orthogonally they were mounted parallel to one another and a half wave plate used in the path of the s-polarised diode thus avoiding the cross-shaped pump beam used previously. The regenerative initiation circuit used to drive the prism modelocker was the same as that of chapter 3 and was seeded with the loss from the first Brewster prism surface.

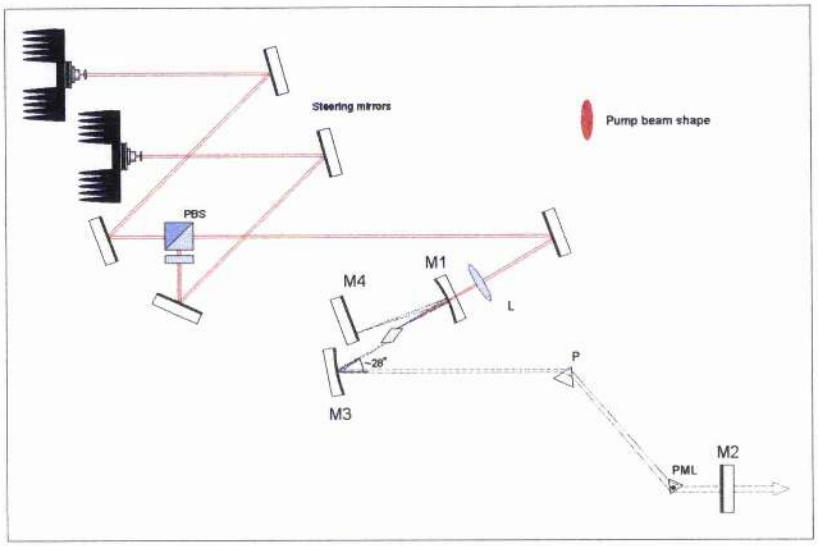

Figure 4.5 Schematic of the highly asymmetric Cr:LiSAF laser and pump diode configuration, M2 and M2 - plane mirrors, M1 - 50 mm ROC mirror, M3 - 75 mm ROC mirror, P - Infrasil fused silica prism, PML - fused silica prism modelocker, L - 50 mm pump focussing lens, PBS – polarising beam splitter cube, HWP – half-wave plate.

CW performance

The lowest pump power required to achieve lasing in the highly asymmetric Cr:LiSAF cavity was just 9 mW from the p-polarised diode with the s-polarised diode switched off and 18 mW from the s-polarised diode alone. A typical power characteristic is shown in Figure 4.6 below.

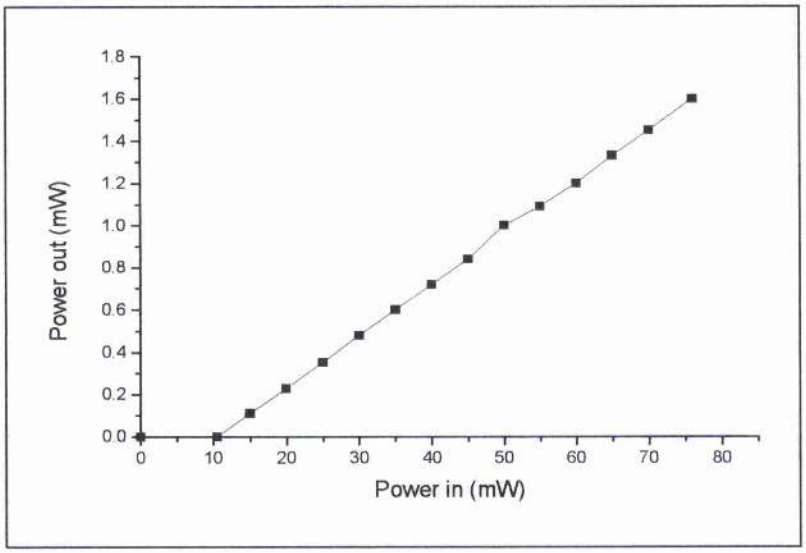

Figure 4.6 Typical power characteristic for the highly asymmetric cavity with 4 × HR mirrors shown in Figure 4.5.

Initial modelocked performance

The Magni plot in Figure 4.7 shows that the cavity should be well suited to soft-aperture modelocking as over a significant proportion of the LMS stability region as an increase in intracavity power will result in a decrease in the size of the cavity mode at the pumped crystal facet.

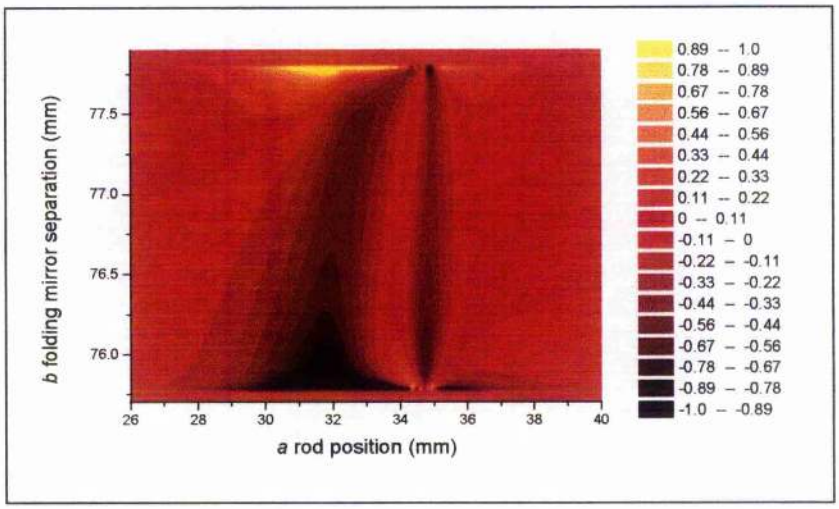

Figure 4.7 Magni plot calculated at the crystal facet for a highly asymmetric resonator, short arm length 88 mm, M1 - 50 mm ROC, M3 - 75 mm ROC.

After alignment of the autocorrelator and careful adjustment of the folding mirror separation the laser produced stable 230 fs pulses for many hours (see Figure 4.8). The stability of these moderate length pulses allowed the optical input to the regen to be blocked with no effect on the modelocking. To provide a preliminary characterisation of the noise in the laser system the regen was switched off and the pulse train detected using a BPW28B, 2 GHz silicon fast photodetector connected to a fast oscilloscope. The two traces of the pulse train shown in Figure 4.9 below were taken with an oscilloscope camera over 100 ns and 1 ms and show no obvious instabilities. Slower scans (~100's ms) revealed no discernible change in the peak power of the pulses. By way of a more sensitive measurement the second harmonic (SHG) amplitude noise was recorded by blocking one arm of the autocorrelator and recording the photomultiplier response on a digital storage scope over a 500 ms time period (see Figure 4.10). The SHG amplitude noise was measured as 3.8 % rms over this time scale indicating very good pulse amplitude and duration stability.

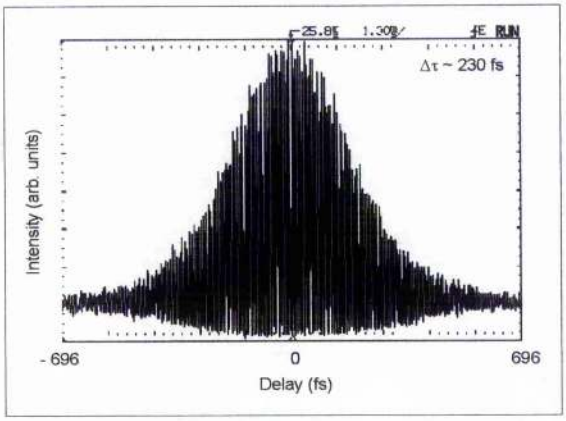

Figure 4.8 Interferometric autocorrelation of 230 fs self-modelocked pulses.

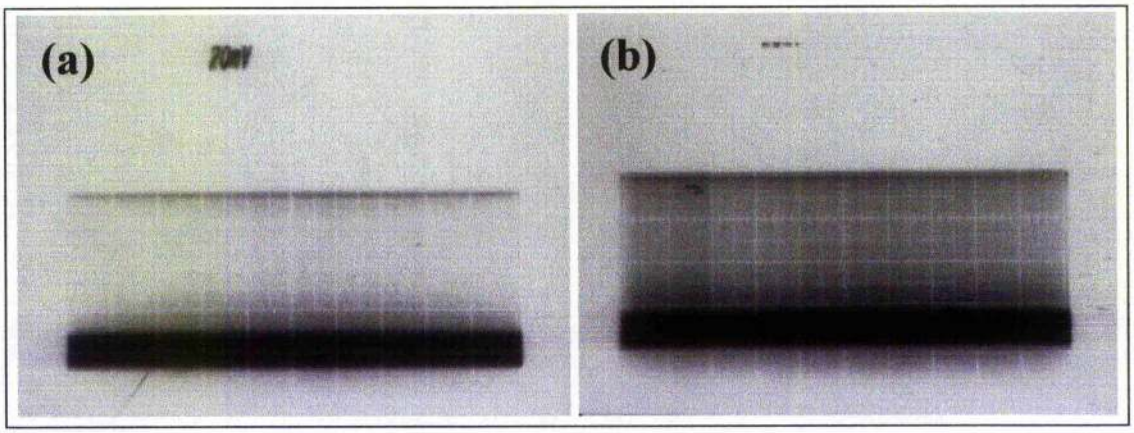

Figure 4.9 Amplitude pulse train noise of the highly asymmetric Cr:LiSAF laser for (a) 100 ns span (b) 1 ms span.

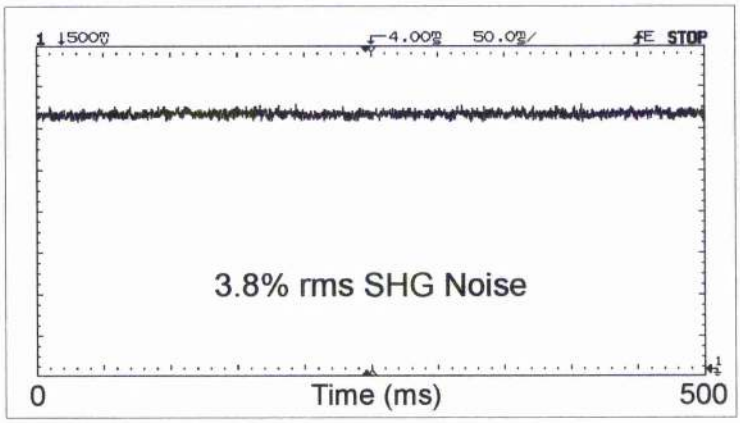

Figure 4.10 Oscilliscope trace of the second harmonic amplitude noise recorded by blocking one arm of the autocorrelator.

Attempts to optimise the modelocked performance of this laser highlighted some of the drawbacks of the regenerative initiation scheme. The translation of the first prism to optimise dispersion displaced the optical input to the regen circuit causing the modelocked operation to become unstable. Translation of the prism modelocker meant

that the position of the transducer on top of the prism moved in relation to the beam path in the prism thereby causing the diffractive effect experienced by the laser mode to alter. The ability of the regenerative circuit to track cavity length drifts was also hampered by the resonance problem described in the previous chapter. While all of these issues are resolvable with appropriate optics and optimisation they are indicative of the difficulties encountered using a 'regen' circuit coupled with self-modelocking at low intracavity powers. The presence of a large number of electronic components also removes some of the advantages gained in moving to a more compact pump source and laser cavity geometry. For these reasons the cumbersome regenerative electronics were removed and an intracavity semiconductor saturable absorber[2] was used to initiate, stabilise and maintain modelocked operation.

4.4 Semiconductor saturable absorbing mirrors

The behaviour of a passively modelocked or Q-switched laser incorporating a SESAM depends heavily on the macroscopic properties of the saturable absorber and mirror structure. The most important properties typically used to define a SESAM are: the maximum modulation depth, the non-saturable loss, the saturation fluence, the unsaturated low intensity reflectivity and the absorption recovery time (see Figure 4.11).

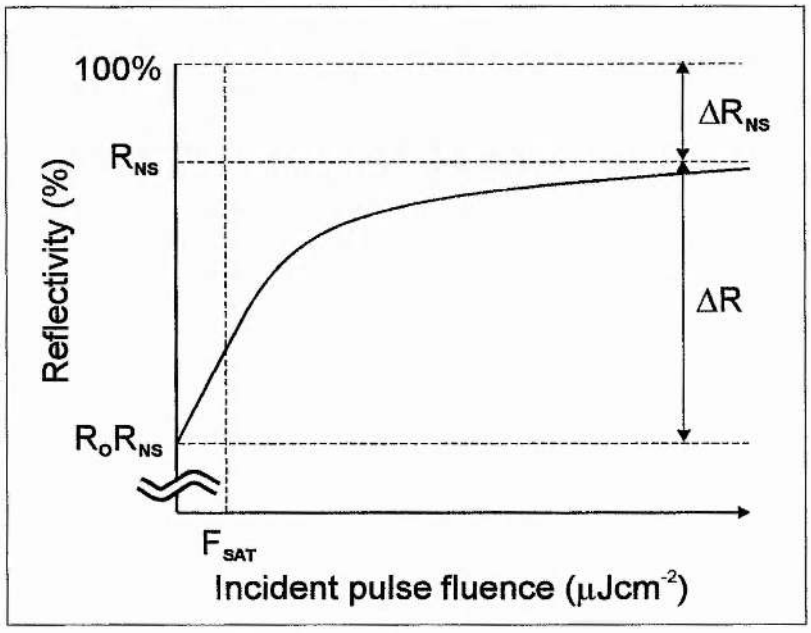

Figure 4.11 SESAM reflectivity as a function on pulse fluence.

The maximum modulation depth ΔR, is the maximum saturable loss that may be bleached by the incident pulse and is inversely proportional to the final pulse duration τ_p. The non-saturable loss, ΔR_{ns} represents the remaining losses experienced by a pulse with fluence F_p much greater than the saturation fluence F_{sat} given by

$$F_{sat} = \frac{h\nu}{2\sigma_A}$$

Equation 4.3

where $h\nu$ is the photon energy and σ_A is the absorber cross-section. The non-saturable losses ΔR_{ns} arise mainly from the transmission of the bottom mirror structure, scattering and residual absorption losses. The unsaturated low intensity reflectivity $R_0 R_{ns}$ is the reflectivity of the SESAM when $F_p \to 0$ and R_{ns} is the reflectivity when the SESAM is fully saturated or bleached ($\tau_p \to \infty$). The recovery time τ_A of the absorption is the final defining parameter and relates the saturation fluence to the saturation intensity I_{sat}

$$I_{sat} = \frac{F_{sat}}{\tau_A}$$

Equation 4.4

Modelling[3,4] predicts that the reflectivity R_f after a pulse with fluence F_p has bleached the absorber is

$$R_f = \frac{R_0}{R_0 - (R_0 - 1)\exp(-F_p / F_{sat})}$$

Equation 4.5

And that the reflectivity experienced by the pulse is

$$R(F_p) = \frac{F_{out}}{F_p} = R_{ns} \frac{\log\left(\frac{R_o - 1}{R_f - 1}\right)}{\log\left(\frac{R_o - 1}{R_f - 1}\right) - \log\left(\frac{R_o}{R_f}\right)}$$

Equation 4.6

As a rule of thumb for the shortest pulses the pulse fluence should be about three to five times the saturation fluence. Larger fluences result in multiple pulse instabilities[5] as the

induced cavity conditions more readily support the formation of more than one less intense pulses. Significantly larger fluences (~50-100 times) will ultimately exceed the damage threshold of the SESAM.

The recovery time of the absorber τ_A is a very important factor when predicting the behaviour and stability of a passively modelocked laser. The intrinsic impulse response of a semiconductor saturable absorber is bitemporal thereby effectively giving rise to two distinct responses. The faster response is due to intraband carrier scattering and thermalisation typically of the order of 10-100 fs[6] i.e. equivalent to the nonlinear reactive fast saturable absorption in a purely self-modelocked laser. The slower response, which is still fast compared to the slow saturable absorbers described earlier, is due to interband trapping and relaxation and is typically of the order of picoseconds to nanoseconds depending on the growth parameters. When designing a SESAM for a picosecond laser system the ultrafast recovery can all but be ignored and it is this slower fast saturable absorption that will define the behaviour of the laser.

Traditionally grown semiconductors do not typically have sufficiently fast recovery times to avoid Q-switching in solid-state lasers. It is therefore necessary to improve the response time in some way. This is achieved in a number of ways including low temperature (LT) growth to add point defects for fast carrier trapping and recombination[7] or ion bombardment, which introduces damage[8]. There are trade-offs between increasing non-saturated losses and reducing the nonlinearity and the induced recovery time improvement. It has been shown that beryllium doping and annealing can keep the non-saturable losses and the degradation in nonlinearity to a minimum while allowing significant improvement in the recovery time of a device[9].

In the femtosecond regime both the faster and slower of the two 'fast' recovery times play important roles. The faster recovery time is important for the stabilisation of a soliton like pulse once established. It can be shown this fast recovery time alone can gate the gain and modelock a laser in the same way as the optical Kerr effect in a self-modelocked laser[10]. Optimising a SESAM for this type of modelocking may be achieved by either exciting carriers high into the conduction band in quantum wells although this is bandwidth limited and harder to saturate or by utilising excitonic nonlinearities which can be very fast and easily saturated but have a very narrow bandwidth. To release the SESAM from some of these more demanding design specifications it is possible to use it as a starting mechanism for soliton modelocking. The faster recovery time may then be up to 30 times longer than the final desired pulse

duration[11] and it is possible to use the saturable absorption of a suitably grown bulk semiconductor. The use of bulk semiconductors has permitted 50 nm tunability from a diode pumped Cr:LiSAF laser[37] and over 300 nm tuning of 30 fs pulses from a Ti:sapphire laser[12]. The ability of a SESAM to passively modelock a femtosecond laser is one of their most attractive strengths as this permits the complete decoupling of the gain medium and modelocking mechanism allowing a greater flexibility on cavity design. This is a very useful feature in direct diode pumped lasers, for example, whose pump diodes do not have diffraction-limited output beams as a more efficient 'gain at end' cavity may be used[13,14]. SESAMs may also be used to initialise self-modelocking as this method generally gives rise to the shortest pulses.

The longer recovery time allows the build up of modelocked pulses from background noise bursts. The upper limit for the longer recovery time is again set by the onset of Q-switch instabilities which will occur earlier for gain media with longer upper state lifetimes, for example a Ti:sapphire (~ 3 μs) laser will have less of a tendency to Q-switch than a Yb:glass laser (~ 1 ms). Careful design consideration of the SESAM slow response time is necessary (especially in picosecond systems)[15].

The effect of each particular SESAM design on the modelocking/Q-switching behaviour and stability in each of the possible modes of operation; passive-ps, passive-fs, self- or soliton-modelocking initiation has been extensively discussed and reviewed elsewhere[16] and it is unnecessary to report this here.

Summary of SESAM structures

Virtually all of the demonstrated intracavity SESAMs have a similar basic parent structure, the antiresonant Fabry-Perot saturable absorber (A-FPSA)[17]. The structure is essentially a Fabry-Perot cavity of thickness d defined by a bottom high reflecting mirror (usually a Bragg mirror comprising of a stack of alternating quarter-wavelength layers of semiconductor material) and a top mirror structure. The Fabry-Perot satisfies the antiresonance condition to provide a broad flat reflection bandwidth and minimal quadratic phase dispersion. The F-P etalon contains the absorber and any spacer layers required in positioning the absorber at an appropriate point while maintaining the antiresonance condition. The absorber may consist of either single[18] or multiple quantum wells[19] (MQW) or in some cases bulk fast recovery semiconductor[20]. The modulation depth of the SESAM is governed by the reflectivity of the top mirror, if the

reflectivity is high the resulting modulation depth is low and if the reflectivity is low the modulation depth is higher although this increases the non-saturable losses introduced by a particular thickness of absorber layer. The presence of the F-P between the two mirrors allows precise control of the saturation fluence of the device F_{sat}^{eff} given at antiresonance by

$$F_{sat}^{eff} = F_{sat} \times \left(\frac{\left[1 + \sqrt{R_t R_b}\,\exp(-2\alpha d_A)\right]^2}{1 - R_t} \right)$$

Equation 4.7

F_{sat} is the saturation fluence of an AR coated SESAM, R_t and R_b are the intensity reflectivity's of the top and bottom mirrors respectively, α is the amplitude absorption coefficient of the absorber layer and d_A is the combined thickness of all the absorbers. The two extremes of A-FPSA design are the high-finesse A-FPSA[17] with a highly reflecting top mirror and the antireflection (AR) coated SESAM. The bandwidth of an A-FPSA, discounting absorber and the mode of operation is ultimately limited by the free spectral range and the bandwidth of the mirror structures. Figure 4.12 below shows some of the more common designs of A-FPSA.

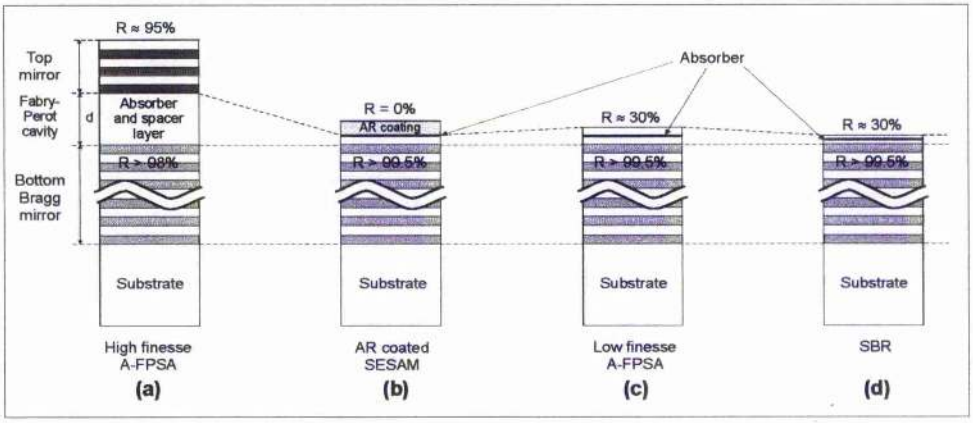

Figure 4.12 Schematic diagram of various SESAM structures

High finesse A-FPSA

The first type of SESAM, the high-finesse A-FPSA, (see Figure 4.12a) had a F-P defined between the bottom Bragg mirror and a top high reflecting (HR) dielectric Bragg mirror typically comprised of alternating SiO_2/TiO_2 layers. High-finesse A-FPSAs have been used to modelock Nd:YLF[17,20], Nd:glass[21], Nd:YVO_4[20],

Yb:YAG[22] and Nd:LSB[23] in the picosecond regime and Nd:glass[24], Yb:YAG[22] and Ti:sapphire[25] in the femtosecond regime.

AR coated SESAM

The other extreme of top mirror reflectivity is an A-FPSA with an antireflection coating dubbed the AR coated SESAM (see Figure 4.12b). The saturation fluence of the device may still be optimised by changing the position of the absorber within the F-P spacer layer and hence the position relative to the standing wave intensity pattern within the F-P. This type of device has been used to modelock Ti:sapphire[19,26], Ar^+ pumped Cr:LiSAF[27], diode pumped Cr:LiSAF[28] and Er:fibre lasers[29]. Many of these early devices, however, used multiple quantum wells (MQW) and introduced large non-saturable losses.

Low-finesse A-FPSA

The most successful and widely used SESAM design is the more simple low-finesse A-FPSA (see Figure 4.12c) where the F-P is formed between the bottom mirror and the Fresnel reflectivity of the semiconductor air interface ($R \approx 33\%$) on top of the absorber/spacer layer. The first low-finesse A-FPSA to be used intracavity consisted of a AlAs/GaAlAs Bragg mirror grown on a GaAs substrate with a thin single quantum well (QW) absorber grown into the topmost quarter wavelength mirror layer[30]. This device was termed the saturable Bragg reflector (SBR). The use of a thin absorber layer permitted the SBR to be incorporated in a Cr:LiSAF laser with very little non-saturable loss[18]. Although at first, the term SBR was reserved for the specific structure in Figure 4.12d the nomenclature SBR and low-finesse A-FPSA have since become interchangeable. This SESAM structure has been used to passively modelock and initiate self and soliton modelocking in a wide variety of laser systems including Nd:LSB[23], Nd:YVO_4[20,31], Nd:YLF[20], and Nd:$YAlO_3$[32] in the picosecond regime and Nd:glass[22,33,14], Ti:sapphire[34,35] , Yb:YAG[22], Yb:phosphate-glass[36], Yb:silicate-glass[36], Cr^{3+}:LiSAF[13,37], Cr^{4+}:YAG[38,39] and Cr^{4+}:fosterite[40] in the femtosecond regime. Low-finesse A-FPSAs have also been used for the modelocking of Er[41], Yb[41], Nd[42] and Tm[43]-doped fibre lasers.

4.5 A low-threshold Cr:LiSAF laser modelocked with an A-FPSA

The semiconductor saturable absorbing mirror shown in Figure 4.13 was inserted in the highly asymmetric cavity in place of HR mirror M4. The SESAM was a broadband low-finesse, antiresonant Fabry-Perot saturable absorber (A-FPSA) mirror structure[44,45]. The low finesse Fabry-Perot cavity is defined by the Fresnel reflectivity of the semiconductor-air interface at the top of the device ($R \approx 31\%$) and the MOCVD grown AlAs/AlGaAs Bragg mirror centred at 850 nm ($R > 99.5\%$). The A-FPSA was designed to give a relatively flat low-intensity (unsaturated) reflectivity of $98.5 \pm 0.7\%$ across a wavelength range of 50 nm. A 15 nm, low-temperature (LT - 400°C) MBE-grown GaAs quantum well layer is positioned within a half-wavelength thick transparent AlAs spacer layer satisfying the antiresonance condition of the F-P structure. The bandgap of the GaAs quantum well corresponded to an absorption edge at 860 nm. The A-FPSA had a saturation fluence of $160\mu Jcm^{-2}$ at 830nm which was not significantly different at the preferred operating wavelength around 860nm. Its associated maximum reflectivity when saturated was 99.5% giving a modulation depth of ~1.4%.

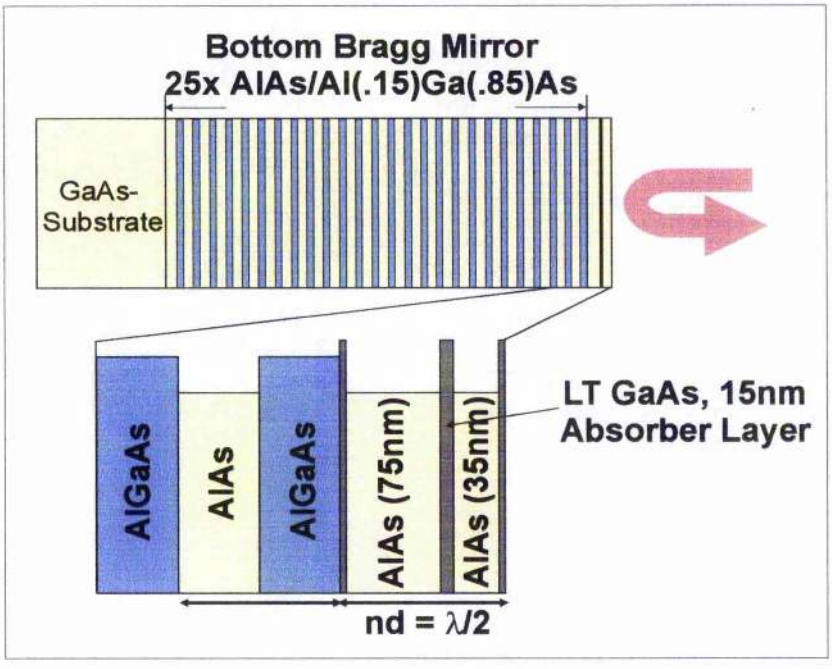

Figure 4.13 Schematic of the GaAs A-FPSA used in the highly asymmetric Cr:LiSAF laser.

The cavity

Figure 4.14 shows a schematic of the asymmetric cavity used for the femtosecond Cr:LiSAF laser. The long and short arm HR folding mirrors M3 and M1, had radii of curvature of 50mm and 75mm respectively. The plane end mirror was either HR coated or an output-coupling mirror with a transmission of 1.5% at 850 nm. A slit placed in front of this end-mirror allowed the laser wavelength to be tuned to the absorption edge of the A-FPSA close to 860nm. The cavity length was no longer limited by the regen system and measured approximately 1 m corresponding to a pulse repetition frequency of ~150 MHz. Intracavity dispersion compensation was provided by a pair of low insertion loss Infrasil fused-silica prisms separated by 510 mm. Fused-silica was chosen initially to minimise the intracavity third-order dispersion originating from the prism pair and gain medium (the 7 mm crystal of Cr:LiSAF). Initially, the intracavity field was focused to a 22μm spot radius on the A-FPSA by setting the short arm length to 54mm. The shortest possible cavity length while still permitting an adequate prism separation was 750 mm which corresponded to a repetition frequency of 200 MHz, typically however, the lasers were operated nearer 150 MHz. The pump laser configuration was the same as that for the self-modelocked version of this cavity. Figure 4.15 shows the behaviour of the cavity mode in the tangential and sagittal planes of this resonator.

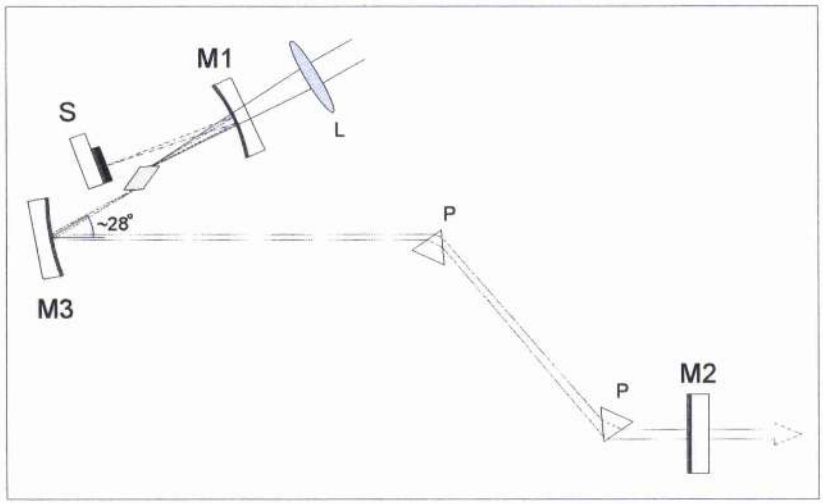

Figure 4.14 Schematic of the highly asymmetric Cr:LiSAF laser, S – A-FPSA, M2 - plane mirror, M1 - 50 mm ROC mirror, M3 - 75 mm ROC mirror, P - Infrasil fused silica prisms, L - 50 mm pump focussing lens.

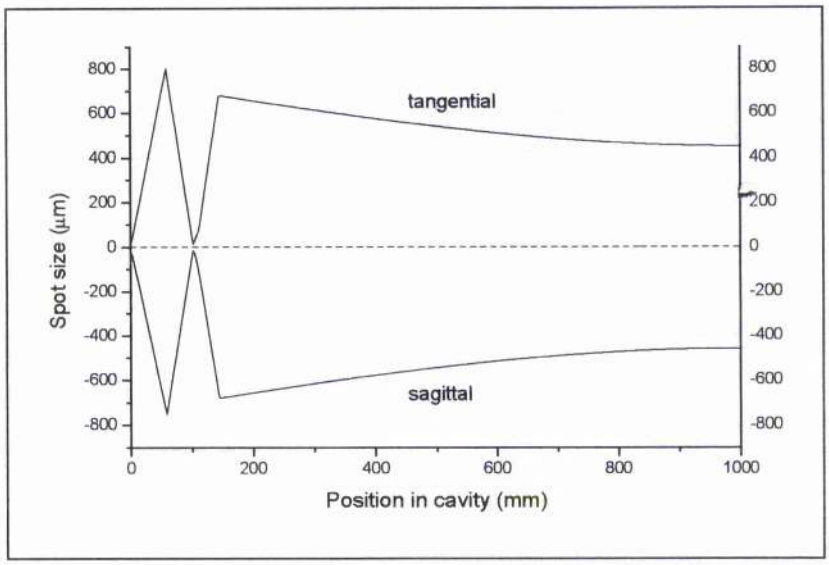

Figure 4.15 Spot size in the tangential (positive) and saggital (negative) planes of the highly symmetric resonator for a short arm length of 54 mm and an overall cavity length ~ 1 m.

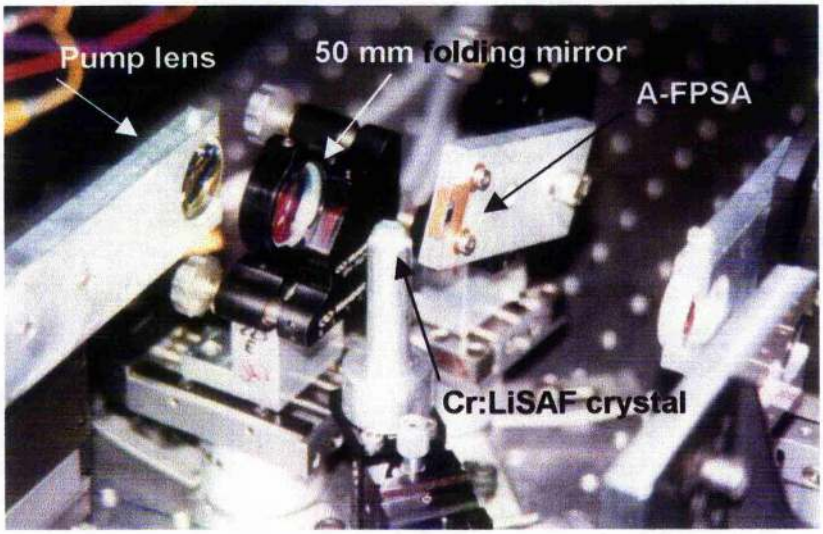

Figure 4.16 Photograph of the folding section of the highly asymmetric cavity showing the short arm containing the A-FPSA mounted on a copper block and the Cr:LiSAF crystal mounted on a pedestal with no external cooling, the 50 mm pump focussing lens is also visible.

CW performance

The cw-threshold of the laser with an HR end-mirror was measured to be ~ 20 mW when pumped with the p-polarised diode. With both diodes at full power (76 mW) the laser produced cw output powers typically around 1.5 mW. When the HR mirror was replaced with a 1.5% output coupling mirror the threshold for the p-polarised diode rose

to ~30 mW. With this mirror in place the slope efficiency was 36% and output powers as high as 6.5 mW were observed. Figure 4.17 below shows typical power characteristics of the cavity with an HR coated end mirror and the 1.5% output coupler.

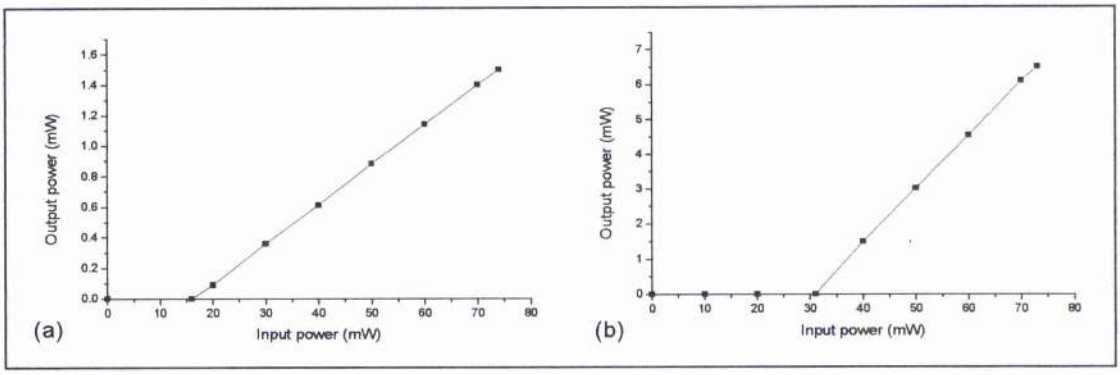

Figure 4.17 Typical power characteristics for the highly asymmetric cavity for (a) HR coated end-mirror and (b) 1.5% output coupling end mirror, prisms and A-FPSA present in cavity.

Initial modelocked performance

In order to monitor the spectral output in real time the output from the laser was directed into a monochromator[46] with a 1 μm (visible) grating with a linear CCD array at its output. Almost from the moment the A-FPSA was placed in the cavity 68 fs pulses were recorded at the autocorrelator (see Figure 4.18). These significantly shorter pulses obtained with the A-FPSA in an identical cavity indicate that dispersion was not the limiting factor on the pulse durations for the self-modelocked laser in section 4.2.

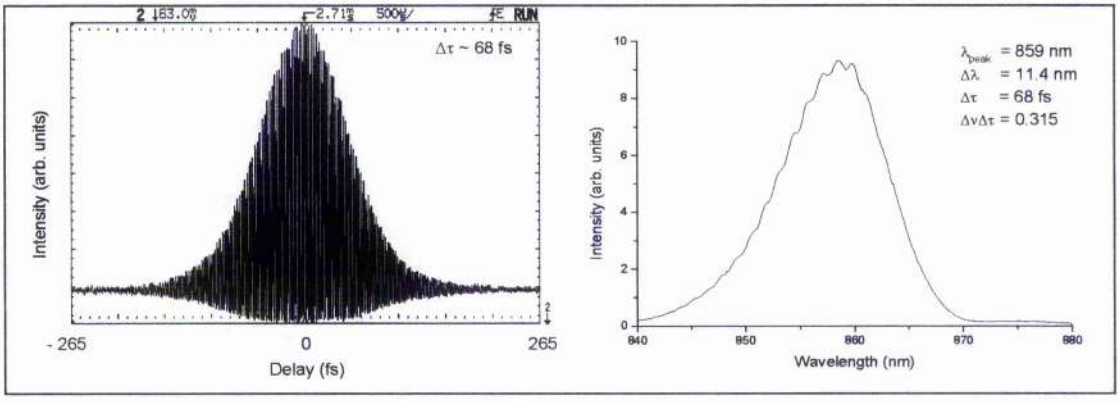

Figure 4.18 Interferometric autocorrelation and corresponding spectrum of 68 fs pulses with average output power of 800 μW obtained for a pump power of 76 mW.

Modelocked performance

Adjusting the orientation of the prisms while maintaining optimum GVD conditions, yielded a stable self-starting train of transform-limited 65 fs pulses from the laser (see Figure 4.19). An average output power of 920 μW was obtained from each of the HR-mirror reflections for an incident pump power of 76 mW. The fluence at the A-FPSA in this condition was ~ 490 μJcm^{-2}. The s-polarised single narrow-stripe diode was then switched off and the laser pumped with the remaining p-polarised diode giving a maximum power of 38 mW incident at the pump lens (35 mW at the crystal). At this lower pump power the laser produced 77 fs pulses (see Figure 4.20) at an average output power of 460 μW (~250 μJcm^{-2} at the A-FPSA). Sub-100 fs pulses could be produced for pump powers as low as 24 mW. Modelocked operation ceased only when the pump power was reduced below 23 mW corresponding to 21.5 mW incident at the crystal facet and fluence at the A-FPSA of only 157 μJcm^{-2}. This modelocking threshold is close to the cw-threshold of the laser and is an indication of the higher reflectivity available from the A-FPSA when saturated.

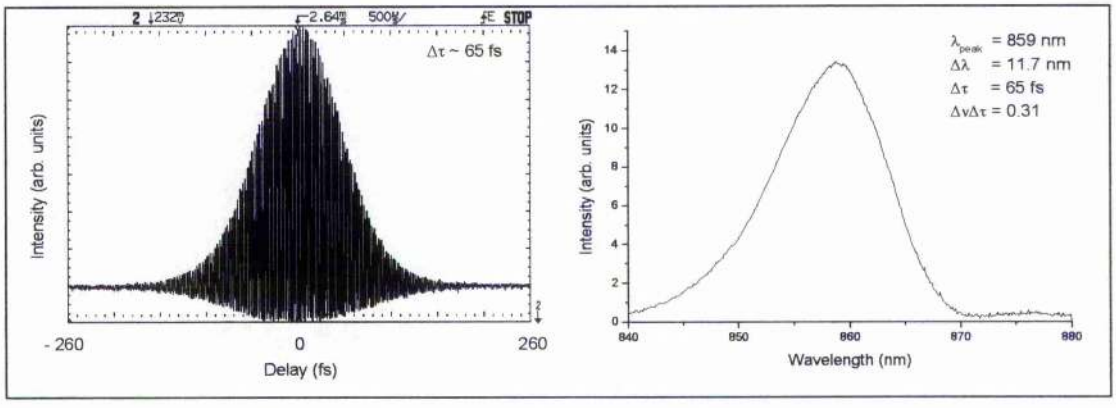

Figure 4.19 Interferometric autocorrelation and corresponding spectrum of 65 fs bandwidth limited pulses with average output power of 920 μW obtained for a pump power of 76 mW.

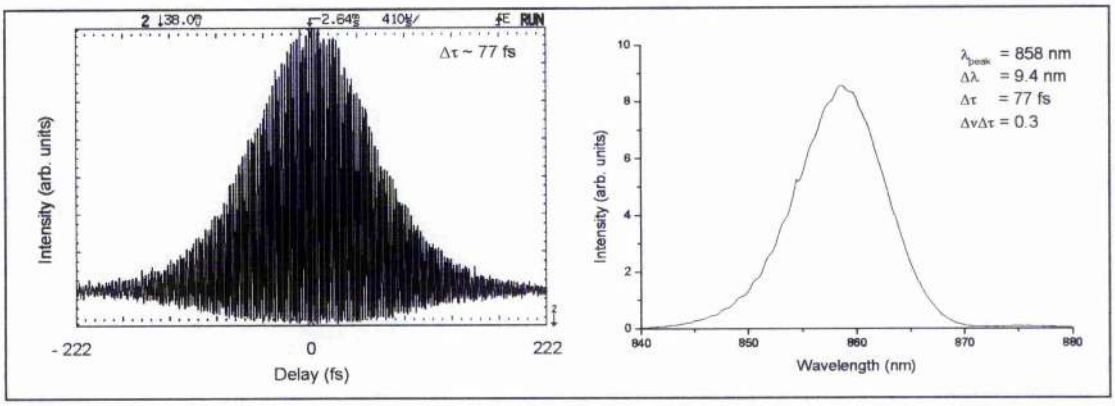

Figure 4.20 Interferometric autocorrelation and corresponding spectrum of 77 fs bandwidth limited pulses with average output power of 460 μW obtained for a pump power of 38 mW.

The self-starting operation and added modelocking stability provided by the A-FPSA at low intracavity powers permitted the use of an output coupler and a larger proportion of the laser field to be extracted. When the high-reflectivity plane mirror was replaced with the 1.5% output coupler the laser produced 88 fs pulses at an average output power of 5.5 mW and 95 fs pulses at 6.1 mW. By replacing the mains electrical power supplies to the laser diodes by a battery pack containing six 1.5V AA-type penlight batteries and a low drop-out voltage regulator circuit (LP2952), the diodes were operated closer to their maximum output power specification providing up to 86 mW at the pump lens. With the pumped in this manner and the 1.5% output coupler in place, the laser produced transform-limited 90 fs pulses at an average output power of 9 mW (see Figure 4.21). The fluence on the A-FPSA in this case was 261 μJcm^{-2}. This performance represented the attractive overall electrical-to-optical efficiency for an ultrashort pulse source of approximately 1%. Modelocked laser operation could be sustained for over 14 hours using the battery power supply. The operation of the diodes at these higher output powers was found, however, to reduce their lifetime so the original ceiling of 40 mW was reinstated for subsiquent experiments.

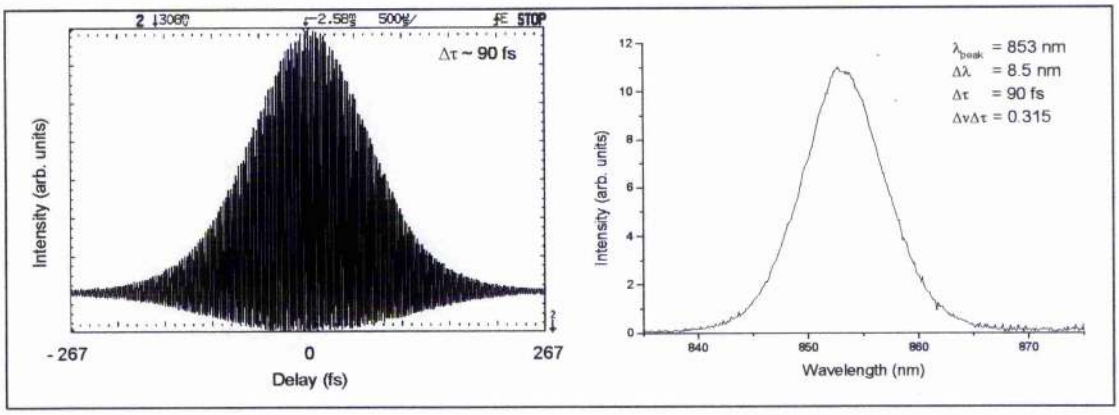

Figure 4.21 Interferometric autocorrelation and corresponding spectrum of 90 fs bandwidth limited pulses with average output power of 9 mW obtained for a pump power of 86 mW.

To further improve pulse durations with the output coupler in place, the spot size on the A-FPSA was reduced to 13μm by shortening the A-FPSA folding mirror separation to 45 mm. As a result of the increased cavity focussing and fluence, the tuning slit was no longer necessary to instigate modelocked operation. In addition, due to increased focussing in the gain crystal (see Figure 4.22), the cw threshold fell to 15 mW when pumped with the p-polarised diode and 27 mW when pumped with the s-polarised diode.

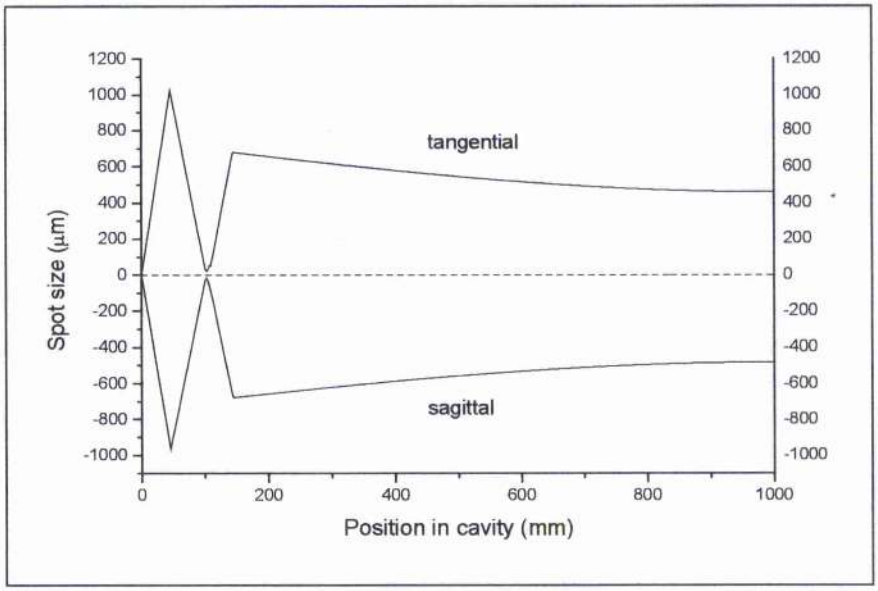

Figure 4.22 Spot size in the tangential (positive) and saggital (negative) planes of the highly asymmetric resonator for a short arm length of 45 mm and an overall cavity length ~ 1 m.

In this configuration the laser produced pulses as short as 70 fs at an output power of 6 mW (~ 500 μJcm^{-2} incident on the A-FPSA) for an incident pump power at the at the pump lens of 76 mW (72 mW at the crystal facet).

Using a complex matrix analysis of its multilayer structure[47], the A-FPSA was found to contribute a minimal amount of group-velocity or second-order dispersion as expected but a significant amount of positive third-order dispersion (~ 400 fs^3) was introduced into the cavity. For this reason the fused silica prisms were replaced with LaK31 prisms separated by 27 cm. This prism arrangement provided a net negative third-order dispersion of a few hundred fs^3 that compensated for the dispersive effect of the A-FPSA[10]. In this configuration the laser produced 57 fs pulses at an average output power of 6.5 mW for an incident pump power of only 76 mW (see Figure 4.23).

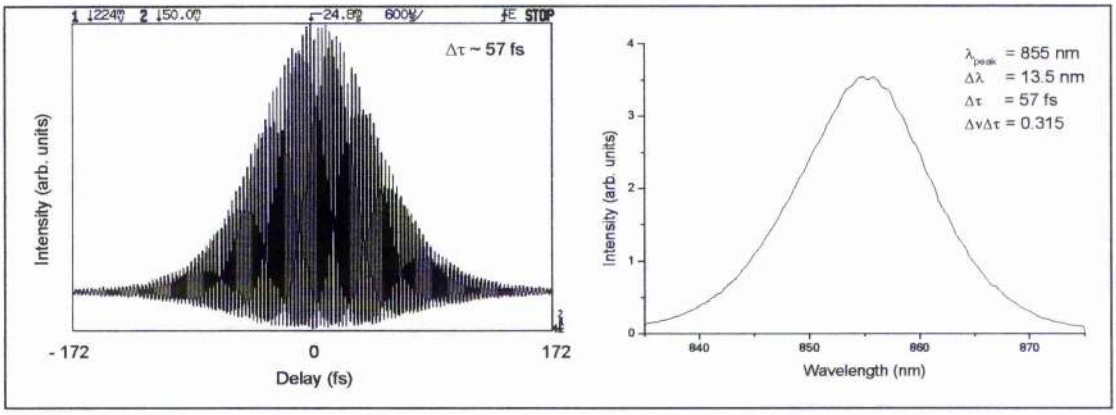

Figure 4.23 Interferometric autocorrelation and corresponding spectrum of 57 fs bandwidth limited pulses with average output power of 6.5 mW obtained for a pump power of 76 mW.

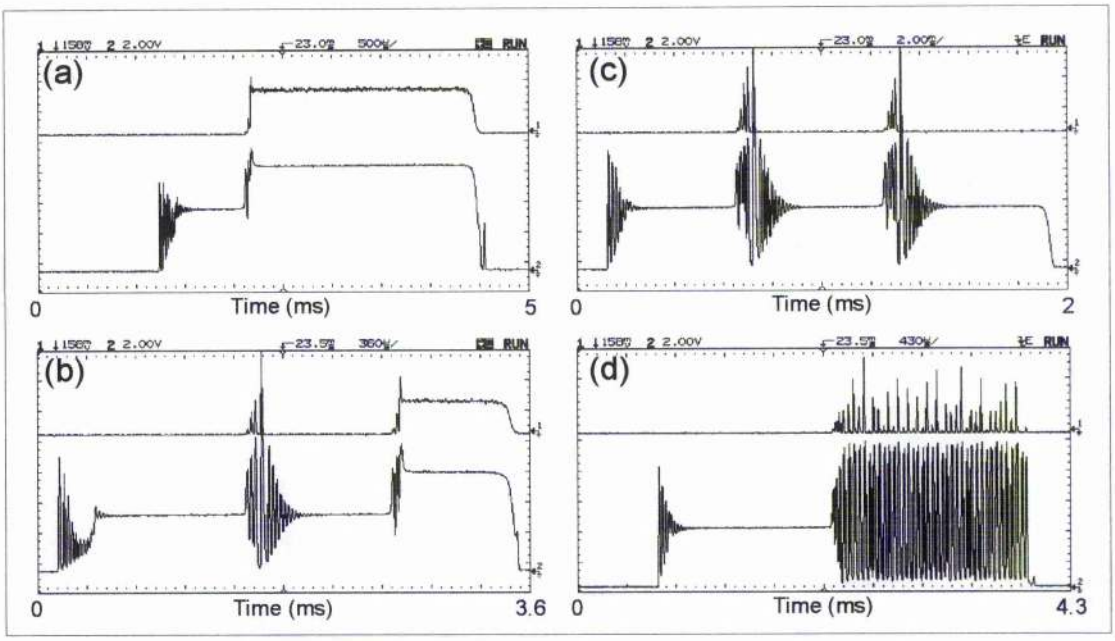

Figure 4.24 Pulse build up for (a) normal modelocked operation, (b) Q-switching burst and eventually modelocking, (c) Q-switched bursts when the dispersion is not optimised, (d) Q-switching. In each case, the top trace is the SHG signal and the bottom trace is the photodiode signal.

Quantitative measurements of the modelocking were made by placing an optical chopper wheel in the cavity and recording the fundamental and second harmonic output of the laser on a storage oscilloscope. Figure 4.24 shows four images obtained in this manner where the top trace in each panel is the SHG signal and the bottom trace is the fundamental. The first panel (a) shows the laser in normal modelocked operation. When the cavity becomes unblocked the laser exhibits relaxation oscillations for a short time (~300 μs) followed by a characteristic pulse build up time (~ 100's μs). The initiation of modelocking is indicated by the sudden jump in the fundamental output and the appearance of a second harmonic signal. The second panel (b) shows the presence of Q-switching and eventual modelocking due to a slight misalignment of the A-FPSA. Panel (c) shows the operation of the laser with too much dispersion or a closed intracavity slit as the laser attempts to initiate modelocking periodic bursts of Q-switched operation are visible. The final panel (d) shows the laser in a state when the wavelength is tuned significantly away from the absorption edge resulting in repetitive Q-switching.

Phase noise

Using the methods described in chapter 3, phase-noise measurements of the laser output were carried out. The laser beam was focused onto a BPW28 fast silicon-avalanche photodiode and the resulting signal displayed on a HP7000 microwave spectrum analyser system. Figure 4.25 shows fundamental and harmonic spectra obtained from the Cr:LiSAF laser running at ~139.6 MHz.

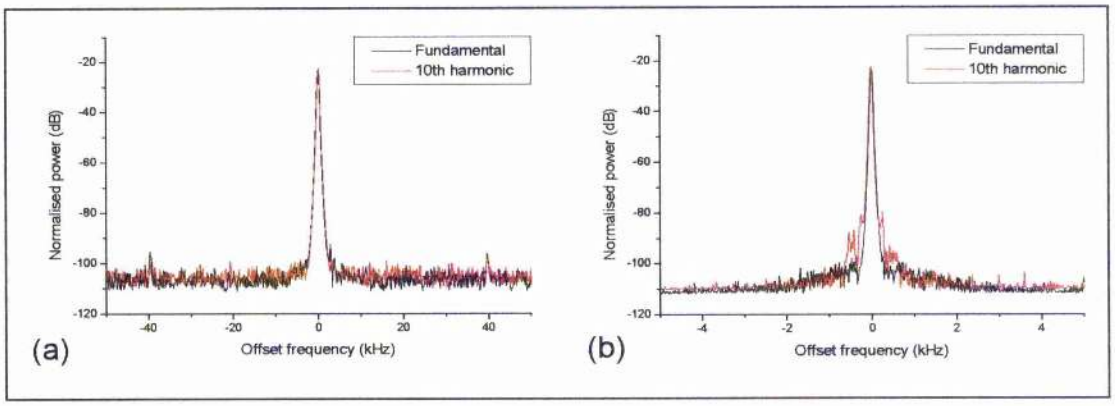

Figure 4.25 Spectra of the fundamental at 139.59 MHz and 10th harmonic for (a) 100 kHz span, 300 Hz resolution bandwidth and (b) 10 kHz span, 30 Hz resolution bandwidth.

The calculated single sideband phase-noise spectrum is shown in Figure 4.26. Table 4-1 indicates the rms timing jitter for this laser as compared to a low noise, KLM Cr:LiSAF laser pumped with narrow-stripe laser diodes[6], a free running KLM Ti:sapphire laser[12] and an actively-stabilised, cavity-referenced KLM Ti:sapphire laser which was coupled to a noise-eating system[12]. The noise figures compare favourably with these earlier system configurations, as the modelocking mechanism was completely passive with no external noise reduction. A 'worst case' amplitude noise spectrum could only be recorded because the noise performance of this battery operated laser was below the noise floor of our measurement system.

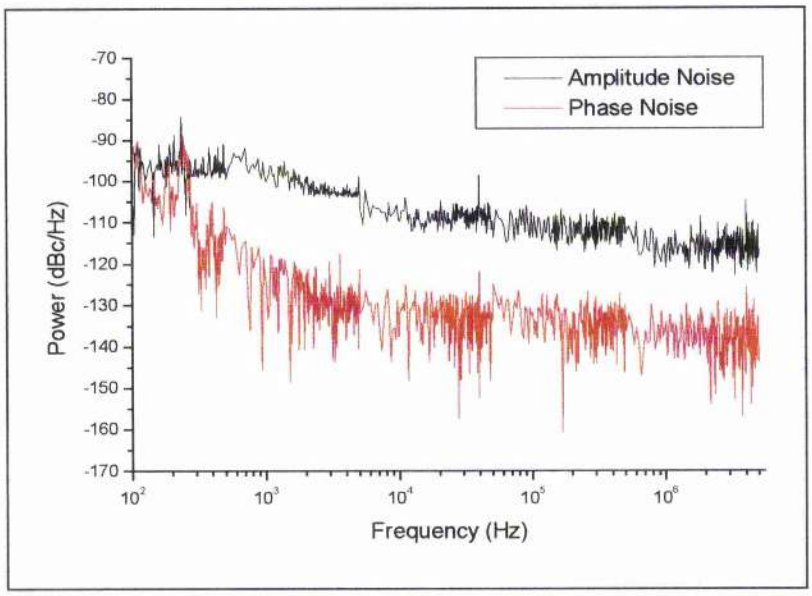

Figure 4.26 The single-sideband amplitude and phase noise power spectra of the highly asymmetric Cr:LiSAF laser, calculated using the fundamental and 10th harmonic Fourier components.

Frequency	Free-running, Cr:LiSAF laser with A-FPSA	Free-running, 3-mirror, low-threshold, KLM Cr:LiSAF laser	Free-running, KLM Ti:sapphire laser	Actively-stabilised, KLM Ti:sapphire laser
50 – 1000 Hz	1200 fs	2200 fs	-	-
100 – 500 Hz	302 fs	680 fs	3400 fs	150 fs
500 – 5000 Hz	73 fs	73 fs	800 fs	80 fs

Table 4-1 Rms timing jitter values for the highly asymmetric Cr:LiSAF laser, the 3-mirror self-modelocked Cr:LiSAF laser, a self-modelocked Ti:sapphire laser and an actively stabilised self-modelocked Ti:sapphire laser.

A saturable Bragg reflector

A GaAs saturable Bragg reflector (SBR)[48] shown in Figure 4.27 was used in the highly asymmetric cavity. The SBR consisted of a AlAs/AlGaAs Bragg mirror stack with a GaAs quantum well absorber grown into the first mirror layer. Unlike the A-FPSA the quantum well is not placed within an antiresonant cavity and hence the field at the absorber is not optimised. The resulting structure is a higher quality mirror with lower

unsaturated losses but with a lower modulation depth and higher saturation fluence. For this reason the SBR did not function as well in the low threshold cavity as the perturbation provided was not sufficient for the shortest pulses. The laser produced 120 fs pulses with an output power of ~ 4 mW (see Figure 4.28).

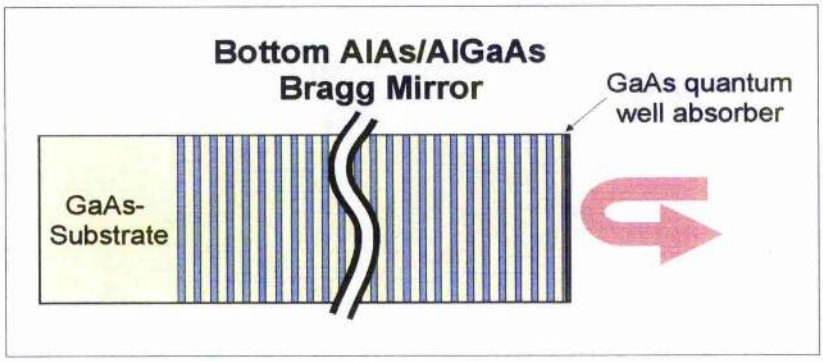

Figure 4.27 Schematic of the saturable Bragg reflector.

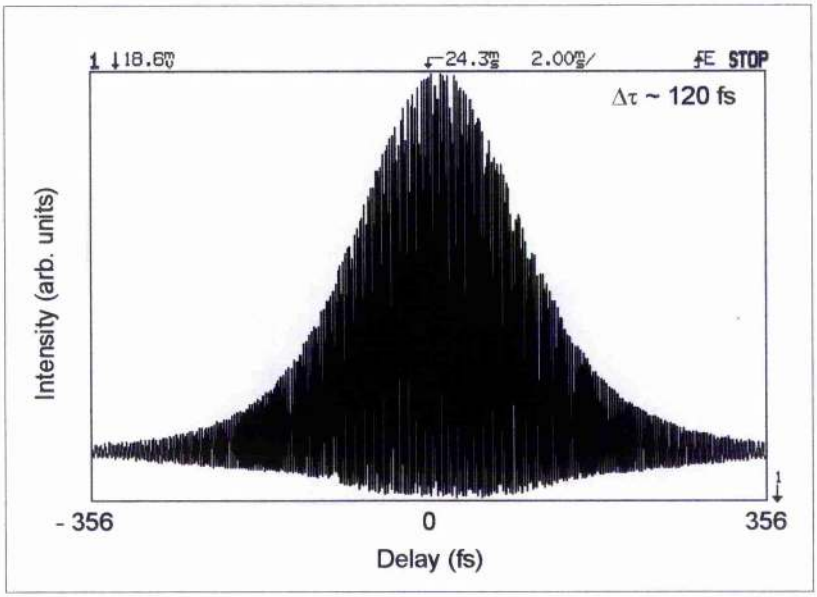

Figure 4.28 Interferometric autocorrelation of 120 fs pulses obtained with the SBR in the Cr:LiSAF laser cavity.

A laser diode autocorrelator

Recently, pioneering work by Ried *et al*[49] and others[50-53] has allowed the realisation of more compact pulse autocorrelation systems[54] by replacing the traditional SHG crystal and photomultiplier tube with two-photon induced free carrier generation in semiconductor devices such as photodiodes and LEDs.

Using a similar method to that described by Burns *et al*[55] a laser diode was incorporated in an autocorrelator arrangement to measure the pulses from the Cr:LiSAF laser. The laser diode used was the SDL 7311-G1 SSM laser used in chapter 3, which had a cracked window. The use of a diode laser or any waveguide device for the purpose of autocorrelation has a number of advantages. Once the light is coupled into the waveguide the interaction of the two pulses is confined and therefore the nonlinear interaction is many (~ 100) times more sensitive. The resulting correllator is compact and although one would think the alignment of a waveguide would be more difficult, given appropriate mounts, the laser may be forward biased to provide its own alignment beam. Figure 4.29 below shows a schematic of the compact laser diode autocorrelator and Figure 4.30 shows an interferometric autocorrelation of 100 fs pulses obtained from the autocorrelator.

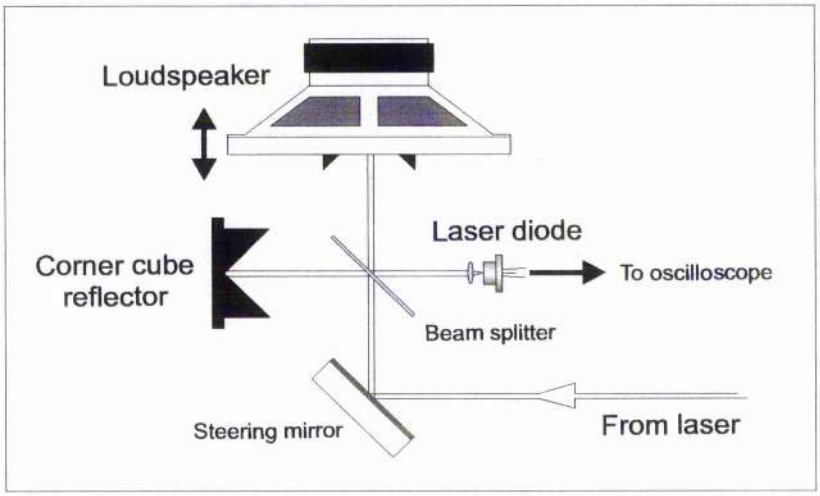

Figure 4.29 Schematic of the laser diode autocorrelator.

The laser diode autocorrelator was able to detect pulses when the average input power was reduced below 30 μW. The most interesting thing to note about the use of a AlGaInP laser diode in an autocorrelator is that the same type of narrow-stripe laser diode is used both to pump and record the output of the femtosecond laser. At a couple of hundred dollars each this represents a considerable saving over typical pump diodes and photomultiplier tubes.

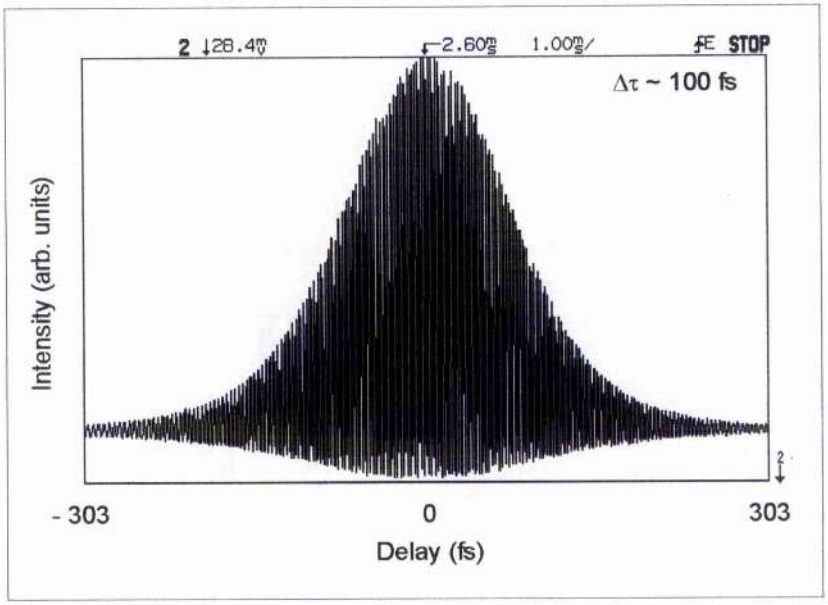

Figure 4.30 Interferometric autocorrelation of 100 fs pulses with the laser diode autocorrelator.

4.6 A frequency doubled Cr:LiSAF laser operating at 430 nm

Femtosecond pulse sources in the blue region of the visible spectrum have been of particular recent great interest. Such sources have important practical applications in the spectroscopy of GaN structures and emerging II-VI semiconductor materials as well as lithographic and medical applications. As direct sources of femtosecond pulses in the blue-green to UV spectral regions do not as yet exist, continuum[56], harmonic and

parametric[57] generation techniques have been used to extend the wavelength ranges accessible to existing ultrafast sources. Continuum generation involves multi-pass amplification and subsequent fibre-grating compression of a chirped ultrafast laser and have been used to generate ~10 fs pulses in the blue-green (450 nm and 500 nm). While widely tuneable (from UV into the IR[58]) these types of sources add a great deal of complexity to a system and operate at low (kHz) repetition frequencies[56]. Harmonic generation, specifically SHG or frequency doubling on the other hand is relatively simple as it requires only as single cw pump laser and preserves the high (~100 MHz) repetition rates of the fundamental pulse source. In addition frequency doubling produces fewer fluctuations in the output pulses and a much higher signal to noise than continuum techniques. CPM dye lasers have produced pulses at wavelengths as short as 493 nm and 554 nm directly[59,60] and in conjunction with extracavity[61,62] and intracavity doubling with potassium dihydrogen phosphate[63] (KDP) and more efficient beta-barium borate[64], β-BaB_2O_4 (BBO) have produced sub-50 fs pulses with milliwatt outputs in the UV ~310 nm.

As a fundamental pulse source Ti:sapphire and other solid state alternatives offer an attractive replacement to the dye lasers in that the intracavity intensities are typically an order of magnitude greater and the lasers exhibit wider tunability. Extracavity[65,66] and intracavity[67-69] frequency doubling of Ti:sapphire lasers have produced sub-20 fs pulses with effective conversion efficiencies as high as 75% (single pass conversion efficiencies ~2%). Extracavity doubling offers the most convenient doubling mechanism in that the ultrafast laser itself need not be disturbed, Pulses as short as 10 fs at 438 nm have been produced using extracavity doubling schemes in BBO[65]. Although extracavity doubling to sub-20 fs pulse durations is possible, group velocity mismatch (GVM) limits the nonlinear crystal lengths to ~100 μm and efficient conversion thus requires relatively high peak powers. In addition, the generation of such short pulses requires the use of prism-grating sequences[70] to compress the fundamental signal before the doubling crystal and second harmonic signal after the crystal. The multiple reflections from the gratings needed to minimise the third-order dispersion in both cases often reduces the available output power from such a system by more than 50%. If ultrashort pulses are not required (say for lithographic applications) then thick (~ mm) crystals may be utilised to provide efficient extracavity doubling[66]. Employing a high degree of focussing in the SHG crystals also enhances harmonic generation though temporal dispersion.

Intracavity frequency doubling is preferred in most cases because it offers the highest conversion efficiencies for the simplest configuration. The higher intensities present within a laser cavity (greater than 10 × that of extracavity output) allow efficient conversion processes to take place even in very thin crystals[67]. Ultrashort pulses as short as 14 fs and at a repetition frequency ~90 MHz have been produced by incorporating a 100 μm lithium triborate, LiB_3O_5 (LBO) crystal in an intracavity folding section with an external prism-grating compressor combination[69]. Intracavity doubling was therefore the method of choice for the lasers in this thesis which exhibit quite modest intracavity powers.

The reconfigured highly asymmetric cavity

The asymmetric cavity used as the basis for the doubling experiment was slightly different than the cavity presented in section 4.2. The two curved folding mirrors were transposed and folding angle of the 75 mm ROC mirror M1 was again used to compensate for the astigmatism due to the Brewster-angled crystal. The folding angle of the shorter 50 mm ROC mirror M3 in front of the pump focussing lens was placed at near normal incidence. In this way the cavity allowed the A-FPSA position and subsequent fluence to be more simply adjusted without disturbing the primary pump beam. The spot size on the A-FPSA was set at to 10 μm and the cavity mode focus reduced from 20 μm to 15 μm lowering the cw-threshold to 10 mW. The reconfigured cavity is shown below in Figure 4.31 and the behaviour of the cavity mode is shown in Figure 4.32.

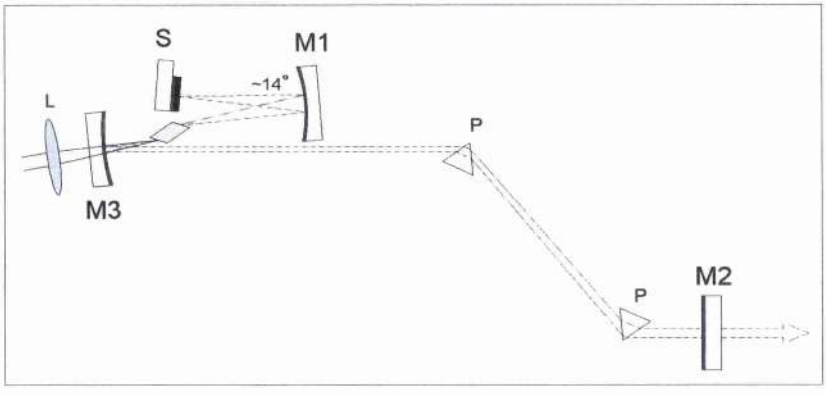

Figure 4.31 Schematic of the reconfigured asymmetric cavity M3 at near normal incidence and the folding angle of M1 ~ 14° to compensate for astigmatism.

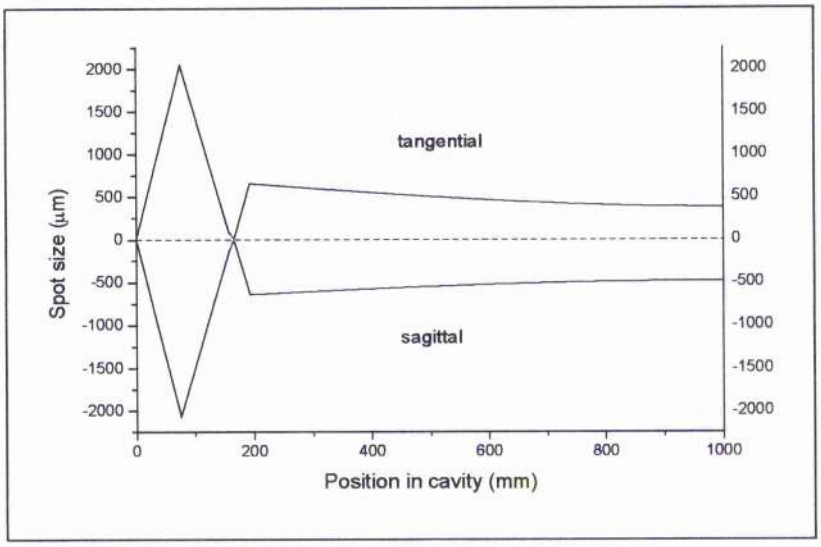

Figure 4.32 Spot size in the tangential (positive) and saggital (negative) in the reconfigured asymmetric resonator.

The laser produced transform-limited 60 fs pulses with an average output power of 5.5 mW using the primary pump diodes (see Figure 4.33).

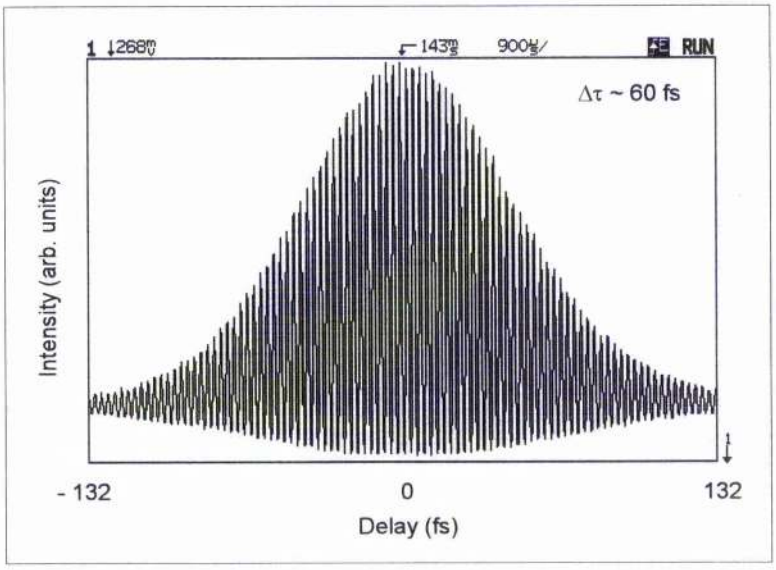

Figure 4.33 Interferometric autocorrelation of 60 fs pulses at ~860 nm from the HR end mirror.

This new orientation of the laser allowed the optimum fluence on the A-FPSA to be exceeded and double and multiple pulse operation was observed (see Figure 4.34).

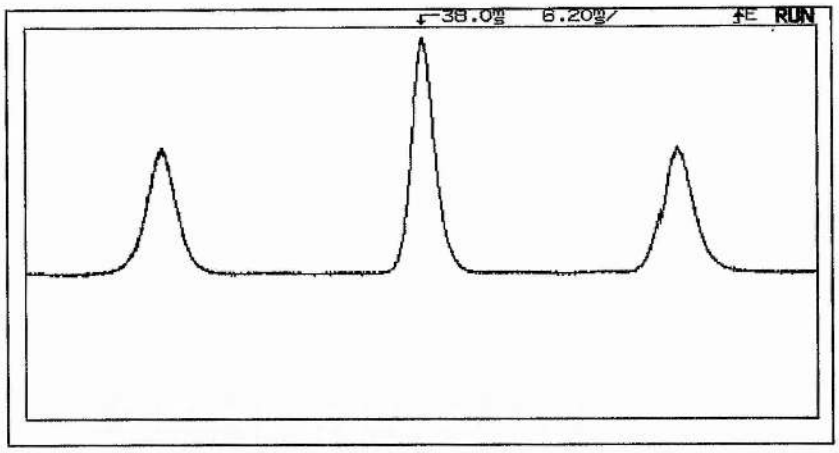

Figure 4.34 Oscilloscope trace of multiple pulsing in the highly asymmetric Cr:LiSAF laser.

The intracavity frequency doubled Cr:LiSAF laser

The long arm of the highly asymmetric Cr:LiSAF laser cavity was extended by 100 mm and a second folding section, consisting of two 75 mm ROC mirrors was included. A Brewster-cut crystal of BBO measuring $10 \times 5 \times 0.5$ mm was inserted between the folding mirrors after external alignment externally for maximum SHG in the output beam from a short pulse (<100 fs) Ti:sapphire laser. The BBO crystal was cut for Type I phase matching ($\theta = 27.5°$, $\phi = 0°$) and minimum transmission loss at 860 nm ($\theta_B = 59°$). The excessive thickness of 500 μm for the non-linear crystal was used as the intracavity power levels available in the laser were not large and sub-50 fs pulse durations were not required/expected/desired. This thickness of crystal would undoubtedly result in chirped pulses as the GVM of BBO is 225 fsmm^{-1} at 750 nm (twice that of KDP). A schematic of the cavity configuration and behaviour of the cavity mode are shown in Figure 4.35 and Figure 4.37 below.

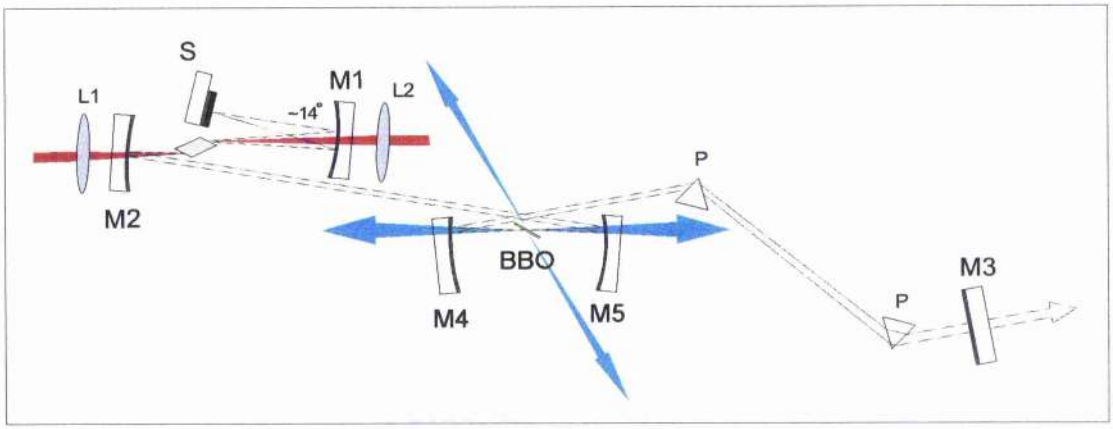

Figure 4.35 Schematic of the highly asymmetric resonator with the included 75 mm ROC mirror folding section, S - A-FPSA, M1 - 75 mm ROC mirror, M2 - 50 mm ROC mirror, M3 - plane mirror, M4 and M5 - 75 mm ROC folding mirrors, P - Infrasil fused silica prisms, BBO - BBO crystal, L1 - 50 mm pump focussing lens, L2 - 100 mm pump focussing lens.

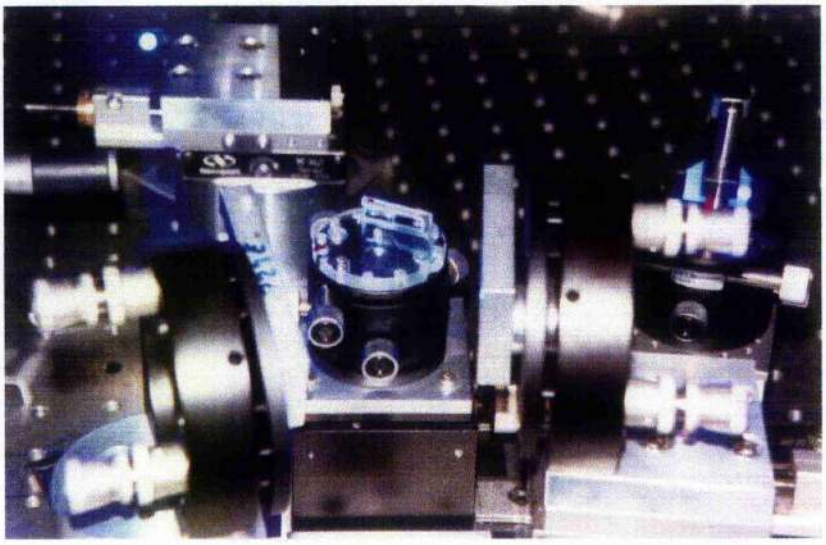

Figure 4.36 Photograph of the folding section and the Brewster angled BBO crystal, the first Lak31 prism is visible at the right.

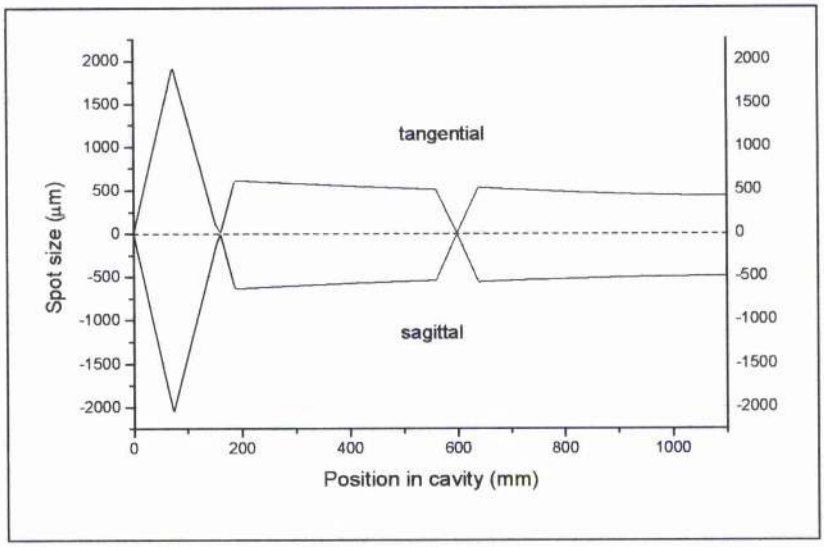

Figure 4.37 Spot size in the tangential (positive) and saggital (negative) in the highly asymmetric resonator with the included 75 mm ROC mirror folding section.

The primary pump laser was improved slightly by removing the four steering mirrors between the diodes and the polarising beam splitter cube. In doing so the available pump power at the pump lens was increased to 80 mW while still operating the diodes below specification (<45 mW). A second pair of Philips diodes were mounted and polarisation combined in an identical set-up to provide the possibility of a secondary pump beam through the mirror M1. The secondary pair of pump diodes provided 77 mW at the 100 mm focal length lens L2 which typically increased the output power by 50%. A full schematic of the cavity and four laser diodes is shown in Figure 4.38.

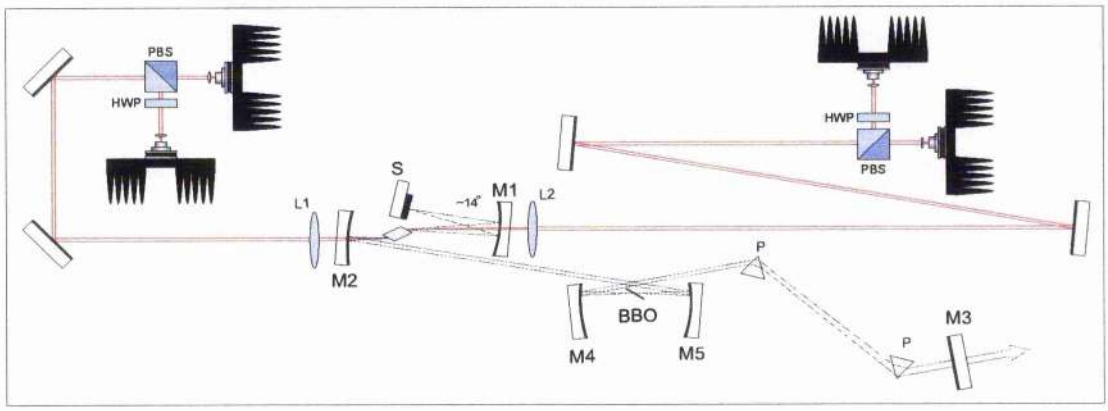

Figure 4.38 Schematic of the doubled Cr:LiSAF laser cavity with the primary and secondary pair of pump laser diodes.

Performance

With the folding section in place the cw threshold of the cavity was 20 mW when using the primary p-polarised diode which rose to 24 mW when the BBO crystal was placed between the mirrors. When the LaK31 prisms were placed 350 mm apart 61 fs duration pulses at an average output power of 550 μW at the fundamental wavelength, 860 nm were measured from the HR end mirror (see Figure 4.39). Over a milliwatt of doubled power at 430 nm was measured when the laser produced sub-65 fs pulses. Introducing more glass via the prisms increased the pulse durations ~80 fs and increased slightly the doubled output power. With the secondary diodes switched off and appropriate dispersion optimisation the laser produced 62 fs pulses at an average output power of ~300 μW and over 400 μW of blue. With the p-polarised diode from the primary diode alone the laser produced 67 fs pulses at an average output power of ~144 μW and over 250 μW of blue light.

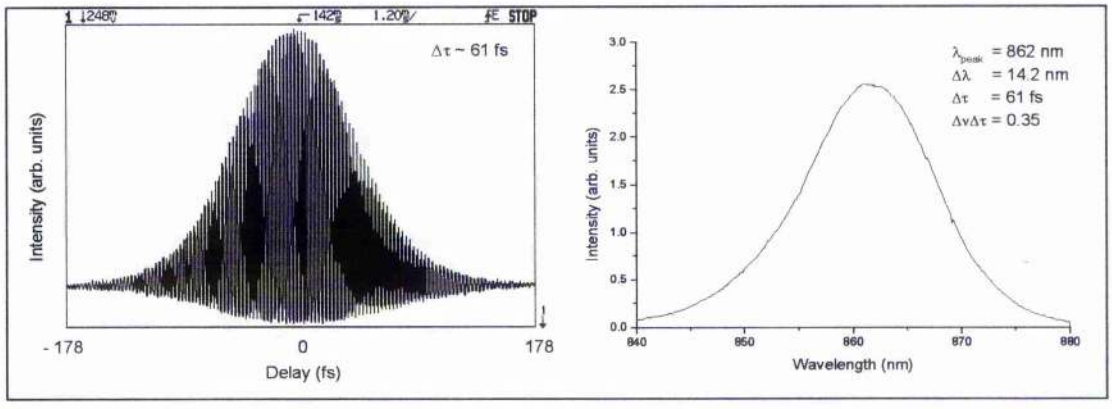

Figure 4.39 Interferometric autocorrelation and corresponding spectrum of 61 fs bandwidth limited pulses with average output power of 550 μW obtained for a pump power of 157 mW.

Due to the lack of appropriate dichroic mirrors a more exact measurement of the output power at 430 nm was not possible. Many reflections existed from the back and front surfaces of the folding mirrors, the crystal surfaces and various multiple reflections thereof. A significant proportion of the second harmonic power was measured in eight separate beams! The brightest beams were generated by pulses moving from the Cr:LiSAF crystal towards the prism pair. Two approaches to measuring the duration of the pulses would be to use a second BBO crystal in an autocorrelator with a UV enhanced, solar-blind photomultiplier tube or to use two-photon absorption in a SiC[71]

photodiode. Unfortunately, autocorrelation of the second harmonic was not possible, as there was not an adequate amount of power in a single beam. Spectral data were collected by placing a 50 mm ROC gold mirror behind mirror M4 which in conjunction with a long focal length (1 m) lens collimated the second harmonic output. The light was directed into a scanning monochromator[46] that was connected to a BBC X-Y chart plotter. A photograph and spectrum of the SHG signal recorded at the same time as the pulse data in Figure 4.39 is shown in Figure 4.40 and Figure 4.41 below. The pulses would undoubtedly be chirped due to the thickness of the BBO crystal but with appropriate compression the bandwidth implies 26 fs pulses are possible.

Figure 4.40 Photograph of the doubled output from mirror M4 hitting the back of the mount for the secondary pump lens.

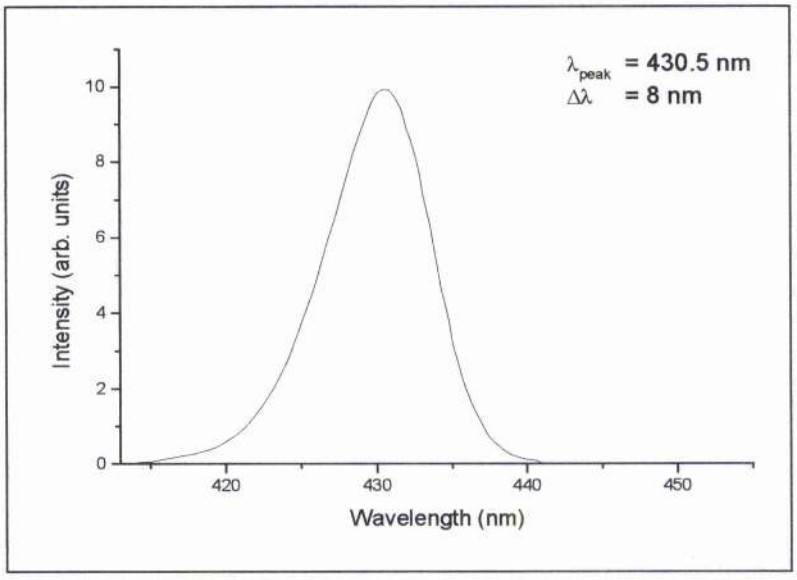

Figure 4.41 Spectrum of the doubled output obtained from the back of mirror M4 with 157 mW of pump power.

The laser remained stable and modelocked for many hours and although the laser did not provide substantial amounts of blue light this was never expected due to the relatively low intracavity powers and thickness of the BBO crystal. It is expected that more compact, future laser cavities will have significantly higher intracavity powers will result in greater conversion efficiencies and shorter SH pulses. A thinner crystal could mean less chirped pulses but possibly less efficient generation.

Figure 4.42 Photograph of the intracavity doubled low-threshold Cr:LiSAF laser.

4.7 Conclusions

In this chapter the design and operation of highly asymmetric 4-mirror directly diode pumped Cr:LiSAF lasers has been detailed. These laser cavities have been shown to retain many of the benefits of the 3-mirror resonators presented in the previous chapter in terms of low cw and modelocking thresholds and compactness while allowing the implementation of saturable absorber modelocking with a SESAM. Efficient operation of lasers with low pump power requirements and moderate intracavity powers was demonstrated and the modelocking stability allowed an output-coupling mirror to be included into the cavity. Continuous-wave operation of the lasers could be achieved

with pump powers as low as 10 mW. The laser produced pulses as short as 57fs in at an average output power of 6.5mW with an incident pump power of only 72mW. Pump powers of this order could be maintained for over 14 hours using just six 1.5V AA batteries as the electrical power source and modelocking could be sustained for pump powers as low as 21.5 mW. Modelocked output powers as high as 9 mW were observed when the pump power was increased to 80 mW. The stability and noise properties of these lasers were also shown to be some of the quietest systems yet reported. Using the highly asymmetric cavity as a starting point for an intracavity doubling experiment average output powers greater than 1 mW at 428 nm were observed and pulses as short as 60 fs at the fundamental wavelength when a 500 mm thick BBO crystal was included in a tightly focussing folding section. The highly asymmetric 4-mirror laser resonator was shown to be a versatile and efficient laser cavity for direct pumping with diffraction limited laser diode sources and provided the potential of a low cost and compact femtosecond laser system.

Endnotes

1 S. Uemura and K. Miyazaki, *Opt. Commun.* **138**, 330 (1997).

2 Kindly donated by Professor U. Keller, Ultrafast Laser Physics, Institute of Quantum Electronics, Swiss Federal Institute of Technology, ETH Hönggerberg-HTP, CH-8093 Zürich, Switzerland.

3 A. E. Siegman, *in Lasers (University Science Books, Sausalito, California 1986).*

4 G. P. Agrawal and N. A. Olsson, *IEEE J. Quantum Electron.* **25**, 2297 (1989).

5 F. X. Kärtner, J. Aus der Au and U. Keller, *IEEE J. Sel. Topics Quantum Electron.* **4**, 159 (1998).

6 J. Shah, in Ultrafast Spectroscopy of Semiconductors and Semiconductor Nanostructures, (Springer-Fverlag, Berlin, 1996).

7 U. Siegner, R. Fluck, G. Zhang and U. Keller, *Appl. Phys. Lett.* **69**, 2566 (1996).

8 M. J. Lederer, B. Lyther-Davies, H. H. Tan and C. Jagadish, *Appl. Phys. Lett.* **70**, 3428 (1997).

9 M. Haiml, U. Siegner, F. Morier-Genoud, U. Keller, M. Luysberg, P. Specht and E. R. Weber, *Appl. Phys. Lett.* **74**, 1269 (1999).

10 U. Keller, *in Nonlinear Optics in Semiconductors*, E. Garmire, A. Kost, Eds. (Academic Press, Inc., Boston, 1999), vol. 59, Chapter 4, pp.211-286.

11 F. X. Kärtner and U. Keller, *Opt. Lett.* **20**, 16 (1995).

12 D. H. Sutter, I. D. Jung, N. Matuschek, F. Morier-Genoud, F. X. Kärtner, U. Keller, V. Scheuer, M. Tilsch and T. Tschudi, *in Technical Digest of Conference on Lasers and Electro-Optics,* (Optical Society of America, Washington, D. C. 1998) paper CThC5.

13 D. Kopf, K. J. Weingarten, G. Zhang, M. Moser, M. A. Emanuel, R. J. Beach, J. A. Skidmore and U. Keller, *Appl. Phys.* **B 65**, 235 (1997).

14 J. Aus der Au, F. H. Loesel, F. Morier-Genoud, M. Moser and U. Keller, *Opt. Lett.* **23**, 271 (1998).

15 C. Hönninger, R. Paschotta, F. Morier-Genoud, M. Moser and U. Keller, *J. Opt. Soc. Am.* **B 16**, 46 (1999).

16 U. Keller, K. J. Wiengarten, F. X. Kärtner, D. Kopf, B. Braun, I. D. Jung, R. Fluck, C. Hönninger, N. Matuschek and J. Aus der Au, *IEEE J. Sel. Topics Quantum Electron.* **2**, 435 (1996).

17 U. Keller, D. A. B. Miller, G. D. Boyd, T. H. Chiu, J. F. Ferguson and M. T. Asom, *Opt. Lett.* **17**, 505 (1992).

18 S. Tsuda, W. H. Knox, E. A. de Souza, W. Y. Jan, J. E. Cunningham, *Opt. Lett.* **20**, 1406 (1995).

19 R. Mellish, P. M. W. French, J. R. Taylor, P. J. Delfyette and L. T. Florez, *Electron. Lett.* **29**, 894 (1993).

20 R. Fluck, G. Zhang, U. Keller, K. J. Wiengarten and M. Moser, *Opt. Lett.* **21**, 1378 (1996).

21 K. J. Weingarten, U. Keller, T. H. Chiu and J. F. Fergusson, *Opt. Lett.* **18**, 640 (1993).

22 C. Hönninger, G. Zhang, U. Keller and A. Giesen, *Opt. Lett.* **20**, 2402 (1995).

23 B. Braun, C. Hönninger, G. Zhang, U. Keller, F. Heine, T. Kellner and G. Huber, *Opt. Lett.* **21**, 1567 (1996).

24 U. Keller, T. H. Chui and J. F. Ferguson, *Opt. Lett.* **18**, 1077 (1993).

25 I. D. Jung, L. R. Brovelli, M. Kamp, U. Keller and M. Moser, *Opt. Lett.* **20**, 1559 (1995).

26 L. R. Brovelli, I. D. Jung, D. Kopf, M. Kamp M. Moser, F. X. Kärtner and U. Keller, *Electron. Lett.* **31**, 287 (1995).

27 N. H. Rizvi, P. M. W. French, J. R. Taylor, P. J. Delfyette and L. T. Florez, *Opt. Lett.* **18**, 983 (1993).

28R. Mellish, P. M. W. French, J. R. Taylor, P. J. Delfyette and L. T. Florez, *Electron. Lett.* **30**, 223 (1994).

29 E. A. de Souza, C. E. Socolich, W. Pleibel, R. H. Stolen, J. R. Simpson and D. J. DiGiovanni, *Electron. Lett.* **29**, 447 (1993).

30 S. Tsuda, W. H. Knox, E. A. de Souza, W. Y. Jan, J. E. Cunningham, *in Technical Digest of Conference on Lasers and Electro-Optics,* (Optical Society of America, Washington, D. C. 1995), paper CWM6.

31 T. Graf, A. I. Ferguson, E. Bente, D. Burns and M. D. Dawson, *Opt. Commun,* **159**, 84 (1999).

32 T. Kellner, F. Heine, G. Huber, C. Hönninger, B. Braun, F. Morier-Genoud and U. Keller, *J. Opt. Soc. Am.* **B 15**, 1663 (1998).

33 J. Aus der Au, D. Kopf, F. Morier-Genoud, M. Moser and U. Keller, *Opt. Lett.* **22**, 307 (1997).

34 S. Tsuda, W. H. Knox, S. T. Cundiff, W. Y. Jan, J. E. Cunningham, *IEEE J. Sel. Topics Quantum Electron.* **2**, 454 (1996).

35 I. D. Jung, F. X. Kärtner, N. Matuschek, D. H. Sutter, F. Morier-Genoud, G. Zhang, U. Keller, V. Scheuer, M. Tilsch and T. Tschudi, *Opt. Lett.* **22**, 1009 (1997).

36 C. Hönninger, F. Morier-Genoud, M. Moser, U. Keller, L. R. Brovelli and C. Harder, *Opt. Lett.* **23**, 126 (1998).

37 D. Kopf, A. Prasad, G. Zhang, M. Moser and U. Keller, *Opt. Lett.* **22**, 621 (1997).

38 B. C. Collings, J. B. Stark, S. Tsuda, W. H. Knox, J. E. Cunningham, W. Y. Jan, R. Pathak and K. Bergman, *Opt. Lett.* **21**, 1171 (1996).

39 S. Spälter, M. Böhm, M. Burk, B. Mikulla, R. Fluck, I. D. Jung, G. Zhang, U. Keller, A. Sizmann and G. Leuchs, *Appl. Phys.* B **65**, 335 (1997).

40 P. T. Guerreiro, S. Ten, E. Slobodchikov, Y. M. Kim, J. C. Woo and N. Peyghambarian, *Opt. Commun.* **136**, 27 (1997).

41 W. H. Loh, D. Atkinson, P. R. Morkel, M. Hopkinson, A. Rivers, A. J. Seeds and D. N. Payne, *IEEE. Photon. Technol. Lett.* **5**, 35 (1993).

42 M. H. Ober, M. Hofer, U. Keller and T. H. Chui, *Opt. Lett.* **18**, 1532 (1993).

43 R. C. Sharp, D. E. Spock, N. Pan and J. Elliot, *Opt. Lett.* **21**, 881 (1996).

44 D. Kopf, K. J. Weingarten, G. Zhang, M.Moser, M. A. Emanuel, R. J. Beach, J. A. Skidmore, and U. Keller, *Appl. Phys.* **B. 65**, 235 (1997).

45 D. Kopf, A. Prasad, G. Zhang, M. Moser, and U. Keller, *Opt. Lett* **22**, 621 (1997).

46 Applied photonics, f/3.4 monochromator.

47 E. J. O. Williams, in *Optimisation of a Colliding Pulse Modelocked Dye Laser*, PhD thesis, University of St.Andrews.

48 Kindly donated by Dr. David Burns and the Institute of Photonics, University of Strathclyde, Wolfson Centre, 106 Rottenrow, Glasgow G4 0NW, Strathclyde, Scotland, UK.

49 D. T. Reid, M. Padgett, C. McGowan, W. E. Sleat and W. Sibbett, *Opt. Lett.* **22**, 233 (1997).

50 Y. Takagi, T. Kobayashi, K. Yoshihara and S. Imamura, *Opt. Lett*, **17**, 658 (1992).

51 F. R. Laughton, J. H. Marsh, D. A. Barrow and E. L. Portnoi, *IEEE J. Quant. Electron.* **QE-30**, 838 (1994).

52 W. Rudolph, M. Sheik Bahae, A. Bernstein and L.F. Lester, *Opt. Lett.* **22**, 313 (1997).

53 J. K. Ranka, A. L. Gaeta, A. Balatuska, M. S. Pshenichnikov and D. A. Wiersma, *Opt. Lett.* **22**, 1344 (1997).

54 Timewarp Autocorrelator, Elliot Scientific, 3 Allied Business Centre, Coldharbour Lane, Harpenden, Herts, AL5 4UT, U.K.

55 D. Burns, S. T. Lee, M. D. Dawson and A. I. Fergusson, *in Technical Digest of Conference on Lasers and Electro-optics* (Optical Society of America, Washington D. C., 1998), paper CtuI66.

56 R. W. Schoenlien, J.-Y. Bigot, M. T. Portella, and C. V. Shank, *Appl. Phys. Lett.* **58**, 801 (1991).

57 D. T. Reid, M. Ebrahimzadeh and W. Sibbett, *Appl. Phys.* **B 60**, 437 (1995).

58 R. L. Forkm, C. V. Shank, C. Hirlimann, R. Yen, and W. J. Tomlinson, *Opt. Lett.* **8**, 1 (1983).

59 P. M. W. French, and J. R. Taylor, *Opt. Lett.* **13**, 470, (1988).

60 P. M. W. French, M. M. Opalinska, and J. R. Taylor, *Opt. Lett.* **14**, 217 (1989).

61 J. H. Glownia, J. Misewich, and P. P. Sorokin, *J. Opt. Soc. Am.* **B 4**, 1061 (1987).

62 F. Laermer, J. Dobler, and T. Elsaesser, *Opt. Commun.* **67**, 58 (1988).

63 G. Focht and M. C. Downer, *IEEE J. Quantum Electron.* **QE-24**, 431 (1988).

64 D. C. Edelstein, E. S. Wachman, L. K. Cheng, W. R. Bosenberg, and C. L. Tang, *Appl. Phys. Lett.* **52**, 2211 (1988).

65 D. Steinbach, W. Hügel, and M. Wegener, *J. Opt. Soc. Am.* **B 15**, 1231 (1998).

66 A. M. Weiner, A. M. Kan'an, and D. E. Leaird, *Opt. Lett.* **23**, 1441 (1998).

67 R. J. Ellingson, C. L. Tang, *Opt. Lett.* **17**, 343, (1992).

68 V. Petrov, D. Georgiev, and U. Stamm, *Appl. Phys. Lett.* **60**, 1550 (1992).

69 S. Backus, M. T. Asaki, C. Shi, H. C. Kapteyn, and M. M. Murnane, *Opt. Lett.* **19**, 399 (1994).

70 R. L. Fork, C. V. Shank, C. Hirlimann, R. Yen and W. J. Tomlinson, *Opt. Lett.* **8**, 1 (1983).

71 T. Feurere, A. Glass and R. Sauerbrey, *Appl. Phys.* **B 65**, 295 (1997).

Chapter 5:
Highly compact femtosecond lasers

5.1 Introduction

With the demonstration of directly diode pumped Cr:LiSAF and Cr:LiSGaF lasers with output powers as high as 125 mW[1-3] and 500 mW[4], producing pulses with durations as short as 12 fs[5] and 50 fs[6] respectively, came the realisation of potentially compact and robust 'real world' ultrashort pulse laser systems. More recently, on the back of this work, demonstrations of self-modelocking and passive modelocking in alternative and more compact cavities have helped to expand the potential market and applications of ultrafast laser sources. Such systems could be employed in many medical, microscopy and imaging applications as well providing as portable, low-noise sources for diagnostic measurements and calibration of pulse characterisation equipment such as electron-optical streak cameras.

There are a number of methods of improving and removing many of the size constraints in an ultrashort pulse laser cavity. The first and most obvious method is to reduce the overall dimensions (and cost) of the laser cavity by removing superfluous cavity optics. Ramaswamy-Paye, Bouma and Fujimoto[7,8] successfully demonstrated the reduction in SML Ti:sapphire laser cavities using a variety of three-mirror resonator geometries. A laser cavity with fewer fundamental elements is inherently more mechanically stable and compact and has been shown to allow more simple alignment for modelocking[8-11]. Cavities of this type have been demonstrated in both Cr^{4+}:YAG[12,13] and Cr:LiSAF[14] and were reviewed in chapter 3. The use of asymmetric cavity arrangements for the optimisation of ultrashort-pulse lasers for direct diode pumping has also been suggested[15] and demonstrated[16]. These cavities retain the larger alignment stability properties of the more standard 4-mirror, 7-element short-pulse lasers while tightly focussing the cavity mode in the gain medium and reducing the overall cavity length. Asymmetric cavities have permitted the use of a single pump laser diode thereby simplifying the pump geometry by reducing the number of required optics. Further

reduction in the complexity and cost of the pump arrangement has been demonstrated with the use of diffraction-limited narrow-stripe AlGaInP lasers diodes[14,17].

One of the main limitations to the reduction of the cavity length or overall footprint has been the required minimum separation of the typical prism pair in order to provide sufficient negative geometric dispersion within the laser. Alternative and more compact dispersion schemes have been demonstrated which include the use of specially cut laser crystals media and prismatic output coupling mirrors[7] or the minimisation of the sources of positive dispersion and dispensing with compensation altogether[8]. In this manner cavity lengths as short as 150 mm with repetition frequencies ~ GHz have been reported[8,12]. The use of dispersive mirrors[18] and dispersive SESAMs (DSAMs)[19] in prismless cavities has also produced more compact, or potentially compact, femtosecond laser sources.

Continuing the work in low-threshold all-solid-state laser sources a more compact or 'ultracompact' cavity geometry was sought that retained many of the benefits of the systems described in the previous chapters. For the reasons associated with their low insertion losses, already described, the dispersion compensating prisms were retained throughout the work. This was also convenient as no specially cut crystals or cavity optics would then be required releasing standard 'off the shelf' laser optics and components to be used in the compact resonators.

In this chapter a number of highly compact resonators will be described that are based on a cavity design by Aoshima *et al*[20] which use conventional components and occupy less than 200 cm^2 of bench space. More detailed analysis of the dispersion in these cavities leads to the conclusion that only one prism is needed to provide a net negative dispersion and femtosecond pulse operation of a laser of this type is then detailed. Combined with a compact pumping geometry for the single spatial mode diodes these lasers provide the potential for a economically priced, highly compact, portable and low-noise laser source.

5.2 Compact cavities with a pair of prisms for dispersion compensation

As already mentioned, prism pairs used for dispersion compensation are restrictive to the minimum cavity length of an ultrashort pulse laser and therefore to the overall footprint of these sources. Aoshima[20] showed that a standard prism pair could be

incorporated in a more compact symmetric self-modelocked z-fold cavity by placing one prism in each of the cavity arms. In this way the necessary distance between the folding mirrors for tight focussing and the interprism path could be combined. 90 fs pulses were achieved at a repetition frequency > 230 MHz in a laser incorporating elements from a standard 4-mirror 7-element cavity with a Brewster-angled Cr:LiSAF crystal as the gain medium. The cavity footprint measured 38 × 20 cm and represented a considerable reduction in the size of an ultrashort pulse laser (see Figure 5.1). The pump lasers used for this laser did not represent a very compact system because two MOPAs (SDL 7350-A6) providing up to 800 mW of pump power were used and, although these provide diffraction-limited beams, the modelocking threshold was quite high (370 mW). The output power was limited to 4.5 mW through each HR mirror as an output coupler was not used. Improvements could have immediately been made to this cavity by simply using smaller radius of curvature folding mirrors or by angling the mirrors asymmetrically as described in chapter 4.

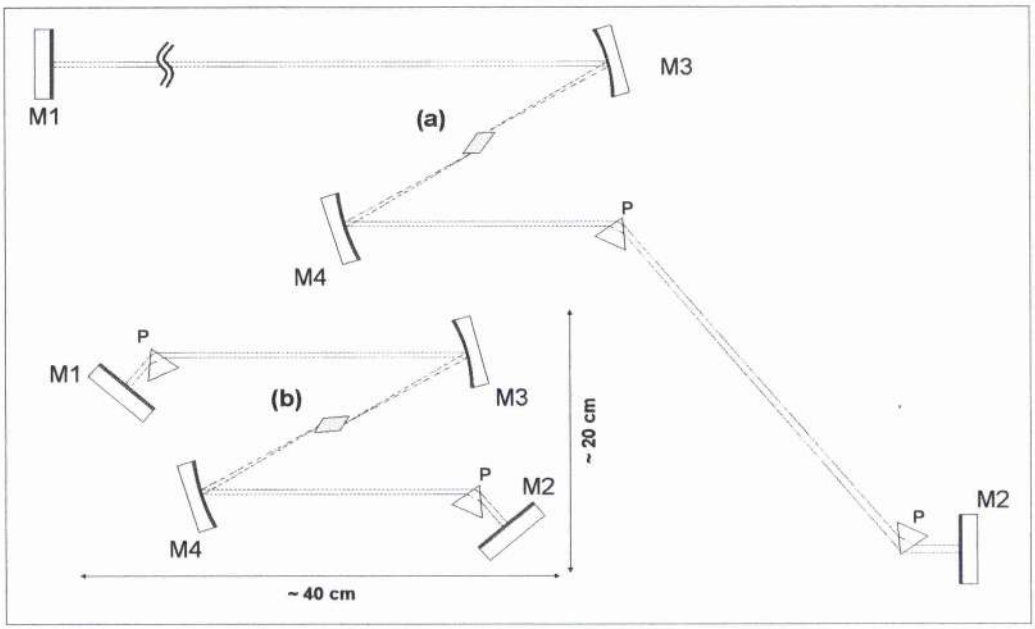

Figure 5.1 Schematic of (a) a standard z-fold, 4-mirror 7-element self-modelocked laser cavity and (b) a compact z-fold cavity as demonstrated by Aoshima et al[20].

Aoshima[20] assumed that the prisms were simply acting in the same geometrical manner as if they occupied a single arm of the cavity and set their separation accordingly. This resulted in a significant increase in pulse duration from 30 fs to 90 fs which was attributed to the spatially dispersed beam in the Cr:LiSAF crystal acting as a bandwidth filter[7]. The simple adopted ray picture shown in Figure 5.2 led Aoshima[20] to believe the

prisms should be oriented with the apices pointing in the same direction due to the crossing of the rays at the cavity focus. While the rays do indeed sometimes cross at this point this is not necessarily the case and this simplistic picture will be shown later not to accurately describe the behaviour of the cavity mode. Firstly, however, two practical demonstrations of this compact dispersion technique combined with the highly asymmetric low-threshold laser cavities of chapter 4 will be described. This has also been implemented in an all-solid state Cr^{4+}:YAG laser[21].

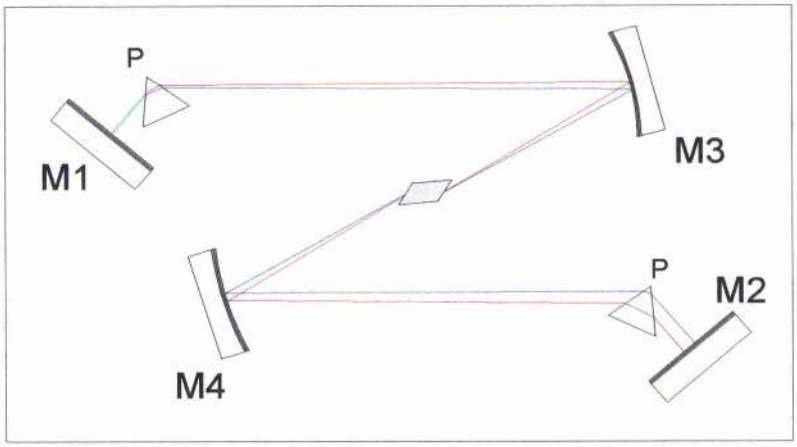

Figure 5.2 Schematic of the simple ray picture for the compact femtosecond laser.

5.3 Highly compact and asymmetric femtosecond lasers with a prism in each cavity arm

The first laser cavity

The novel dispersion compensation scheme was combined with the highly asymmetric 4-mirror, A-FPSA modelocked laser cavity. Figure 5.3 below shows a schematic of the 4-mirror cavity with the 7 mm long Brewster-angled Cr:LiSAF crystal (1.5% Cr^{3+} doping, $\alpha_p \sim 9\ cm^{-1}$). The mirrors were identical to those used in the previous laser systems, M3 50 mm radius of curvature (ROC) and M1 75 mm ROC. The 75 mm ROC folding mirror M1 was set at a half-angle θ of 18° to compensate for the astigmatism due to the Brewster-angled crystal. The dispersion compensating prisms in each of the 'long' and short arms were made from LaK31. The pump-focussing lens situated behind mirror M1 had a focal length of 50 mm.

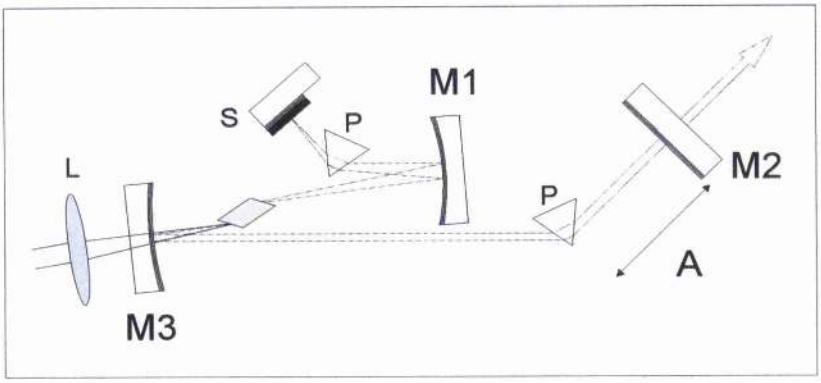

Figure 5.3 Schematic of the 4-mirror highly asymmetric Cr:LiSAF cavity: M1 75 mm ROC focusing mirror; M3 50 mm ROC focusing mirror, M2 plane end mirror; S GaAs A-FPSA, P dispersion compensating Lak31 prisms; L 50 mm pump focussing lens, A variable 'long' arm length.

The laser cavity initially measured ~721 mm representing an intermode frequency of ~208 MHz with the variable length A set to 375 mm. The pump system was the same as for the highly asymmetric laser in chapter 4 (see Figure 4.38). When the distance A was shortened to 40 mm the cavity length was ~390 mm and the repetition frequency 386 MHz. Figure 5.4 below shows a photograph of the laser cavity in this configuration.

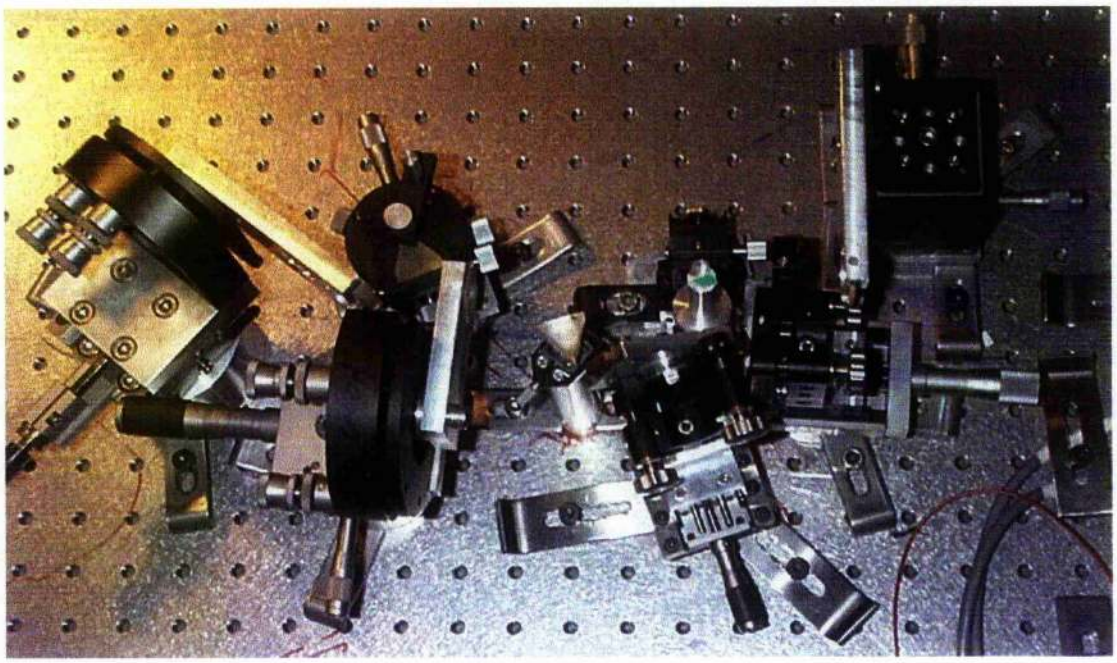

Figure 5.4 Photograph of the 4-mirror highly asymmetric Cr:LiSAF cavity.

CW performance

The cw threshold of the laser was 20 mW from the p-polarised SSM diode with all the cavity elements in place. With both diodes supplying a total of 76 mW at the pump lens the laser produced ~1.5 mW with a high reflecting (HR) plane end-mirror and 5.9 mW from a 1.5 % output coupling (OC) mirror.

Initial modelocked performance

The laser produced 150 fs pulses at an average output power of 590 μW with the length A set to 375 mm (see Figure 5.5). The longer arm was then shortened to 72 mm and the modelocked performance optimised. The repetition frequency of the laser was then 362 MHz and 115 fs pulses were produced at an average output power of 1.1 mW (see Figure 5.6). Modelocking was very stable over a period of several hours. Interferometric autocorrelations indicating pulses as short as 103 fs were obtained but these exhibited obvious distortions (see Figure 5.7). Intensity autocorrelation traces indicated 115-120 fs pulses. Modelocked operation with the 1.5 % output coupler was not achieved.

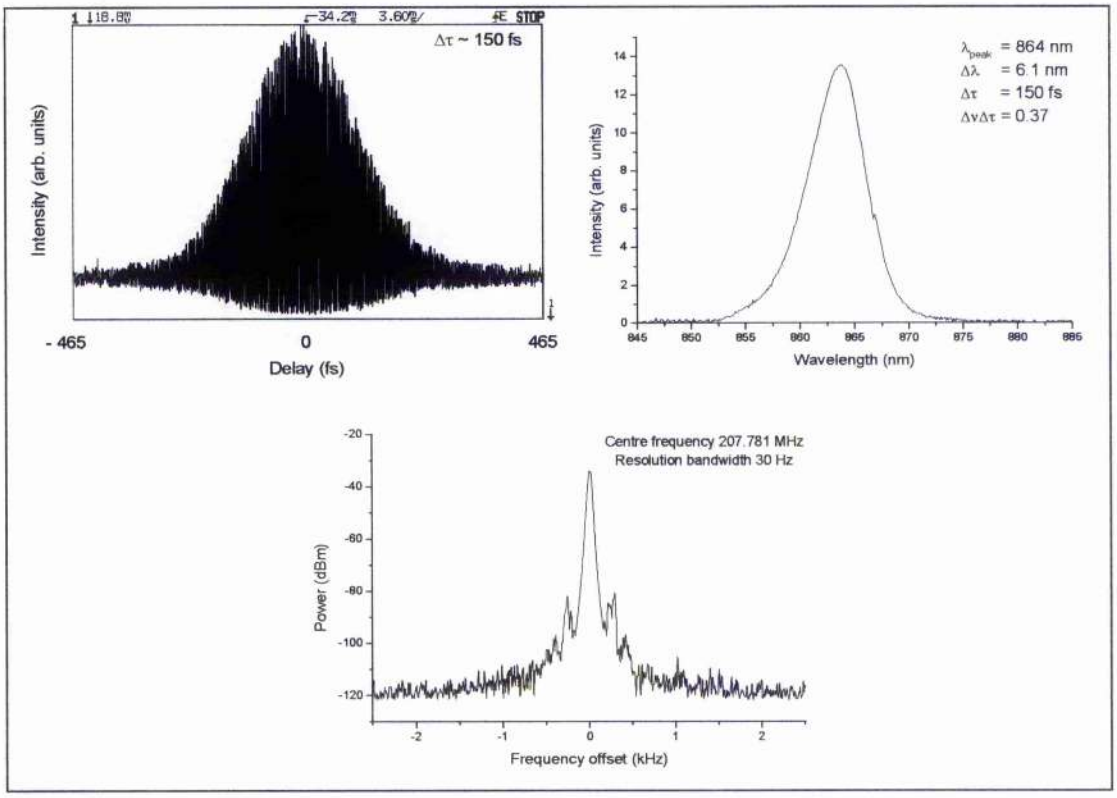

Figure 5.5 Interferometric autocorrelation, optical and RF spectra of 150 fs pulses obtained from the asymmetric Aoshima-type cavity[20].

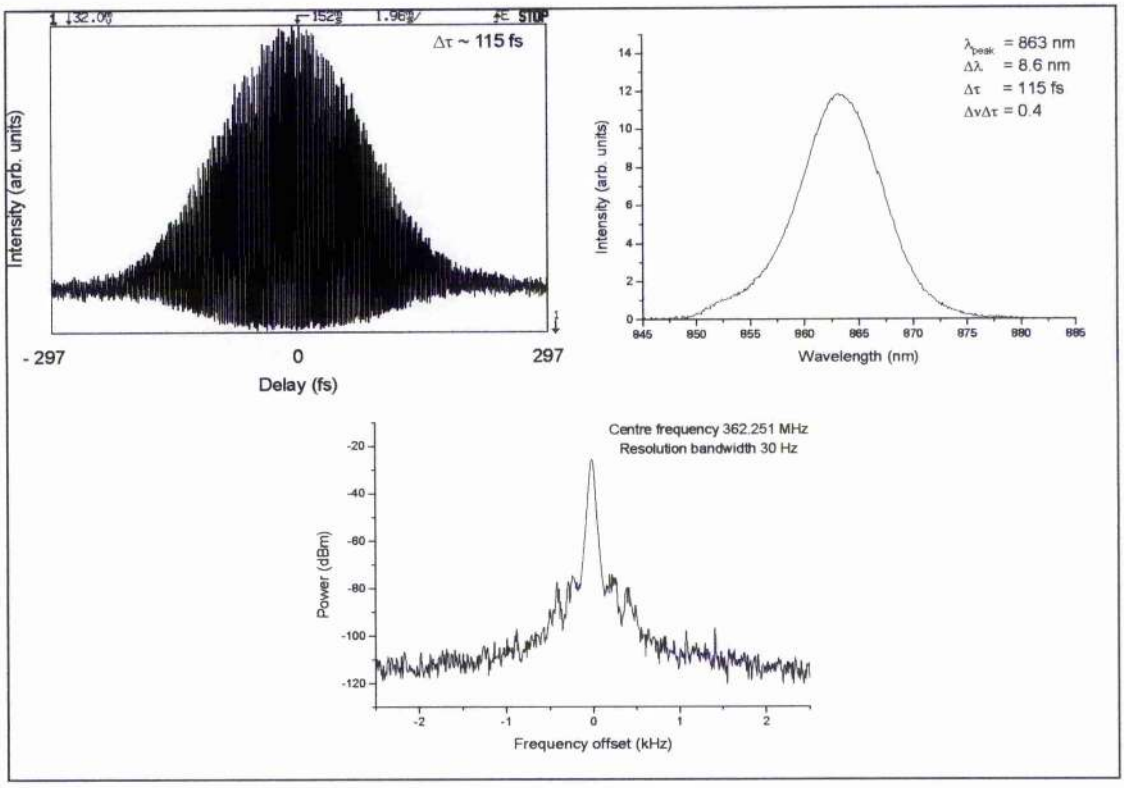

Figure 5.6 Interferometric autocorrelation, optical and RF spectra of 115 fs pulses obtained from the asymmetric Aoshima-type cavity.

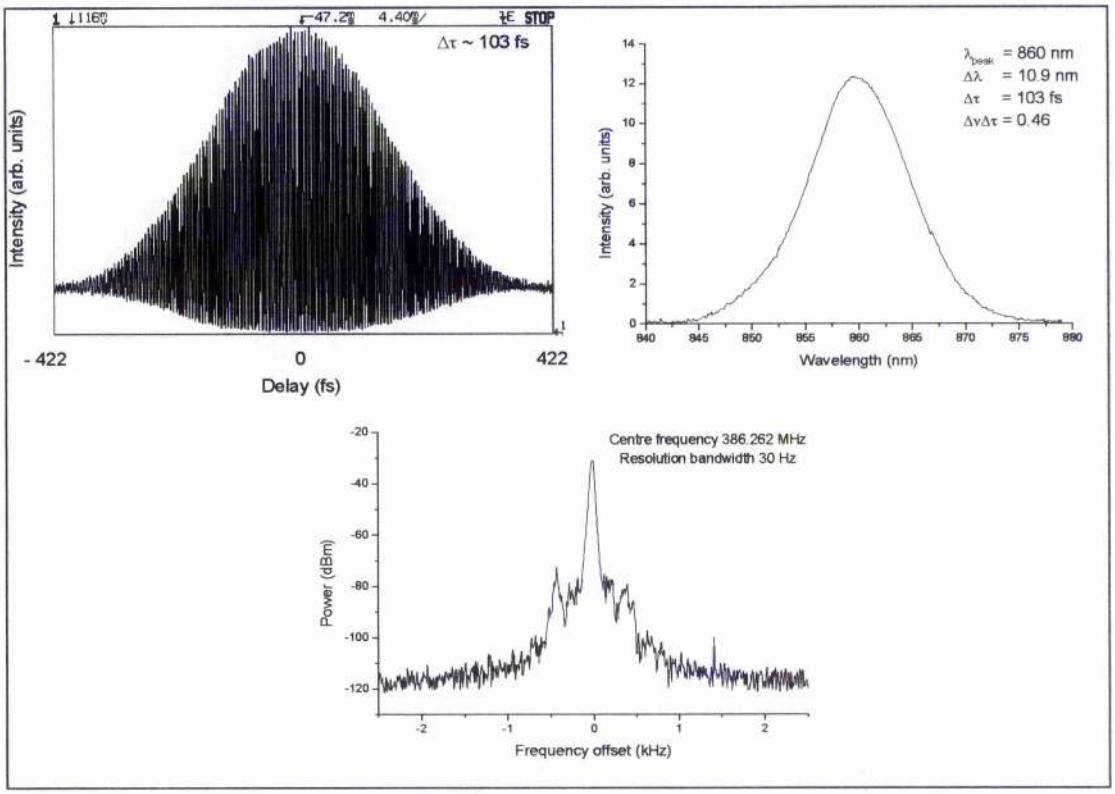

Figure 5.7 Interferometric autocorrelation, optical and RF spectra of 115 fs pulses obtained from the asymmetric Aoshima-type cavity.

Stability considerations in an asymmetric Aoshima-type cavity

The spot size incident on the A-FPSA for the initial compact resonators referred to in the previous section was calculated to be ~ 20 μm and was thought to be a contributing factor to the higher modelocking thresholds and longer pulse durations. To address this issue a similar cavity was constructed with a longer distance between the rear facet of the crystal and the folding mirror M1 and a shorter distance from this mirror to the A-FPSA. The effect of reducing the folding mirror SESAM separation from 75 mm to ~ 55 mm reduced the incident spot size to ~ 10 μm (see Figure 5.8).

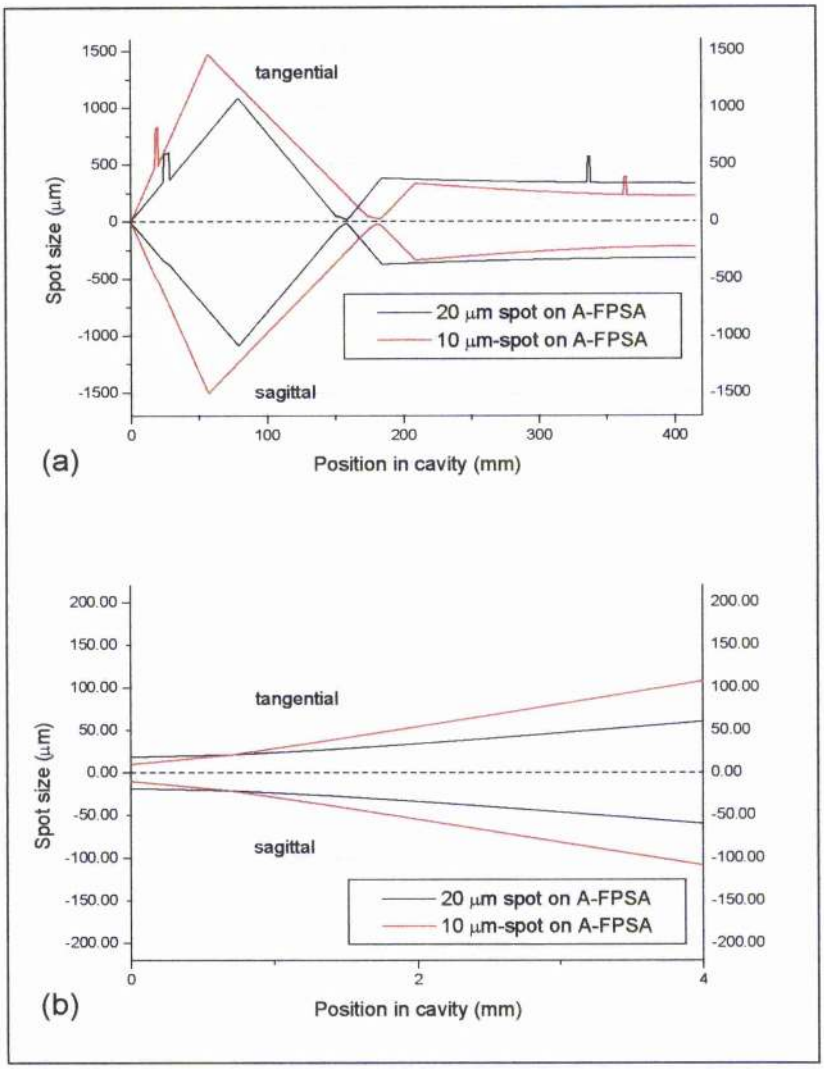

Figure 5.8 (a) Cavity mode behaviour in an asymmetric Aoshima-type cavity, with a folding mirror/crystal separation of 75 mm resulting in a spot size of 20 μm at the A-FPSA (black line), and with a folding mirror/crystal separation of 116 mm resulting in a spot size of 10 μm at the A-FPSA (red line), (b) Close up of the modes at the surface of the A-FPSA.

In practice, however, the cw threshold of this new cavity configuration was quite high and it proved very difficult to set up. After several attempts an explanation was sought as to the increased difficulty in aligning what seemed to be a very similar cavity to the initial asymmetric Aoshima-type laser. The first and most obvious explanation was that the prism apex was clipping the cavity mode between the crystal and the folding mirror. This was because the necessary fold angle for astigmatism compensation closed down as the folding mirror/crystal separation was increased and the shorter length of the arm to the A-FPSA meant that the prism sat closer to the fold mirror where the beam was wider (see Figure 5.9). Also, the beam width at this point increased slightly as the folding mirror was pulled back further compounding this problem (see Figure 5.8).

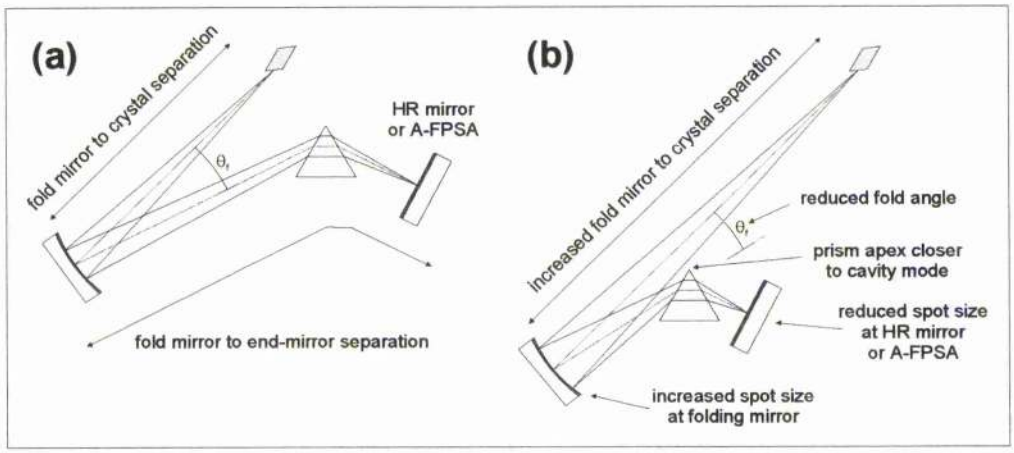

Figure 5.9 Schematic of the cavity mode in the short arm of the asymmetric Aoshima-type resonator for (a) small foldimg mirror/crystal separation and (b) large folding mirror/crystal separation.

A more fundamental reason for the inability to insert a prism in the short arm of the cavity is that the stability limits of the permitted intraprism path in this arm shrank as the spot size at the SESAM was reduced. In other words, the difference in the amount of glass traversed by the extrema of the cavity mode exceeded that permitted by the stability condition. Figure 5.10 below shows the prism in the short arm in more detail. It is immediately obvious that by focussing tightly through the prism the differences in intraprism path for the upper and lower most edges of the cavity mode are exaggerated. Through simple geometrical modelling the path difference for these two extremes of the beam or mode Δ_p can be shown to approximately equal the sum of the spot sizes w_1 and w_2 at the facets of the prism

$$\Delta_p = dp_1 + dp_2 \approx w_1 + w_2$$

Equation 5.1

where dp_1, dp_2, w_1 and w_2 are defined in Figure 5.10.

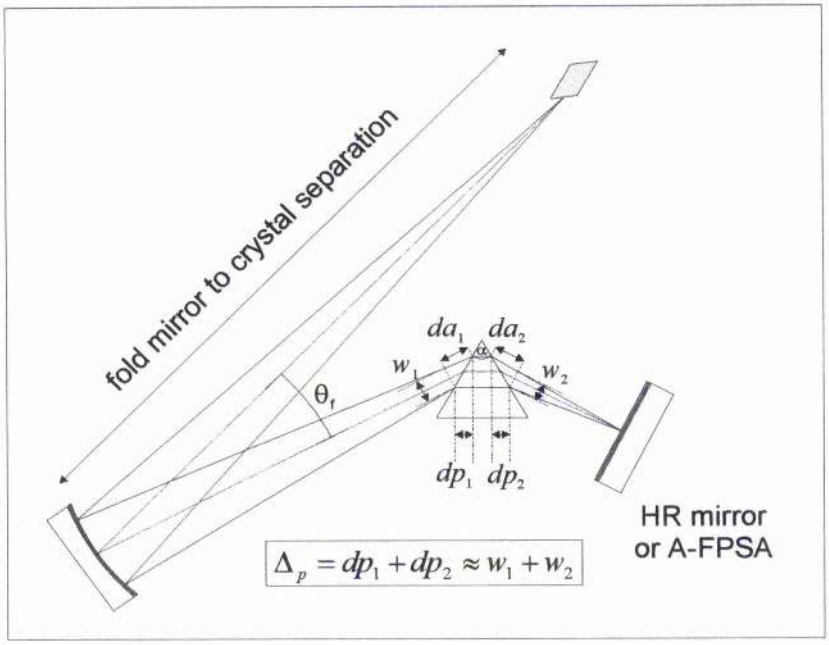

Figure 5.10 Schematic of the intraprism path length difference for the extremes of the cavity mode in the tightly focussed short arm of the asymmetric Aoshima-type cavity.

The stability diagrams in Figure 5.11 below show the permitted amounts of prism material for the specific cases of a longer and shorter folding mirror/crystal separation in Figure 5.8. The variation in permitted path in the sagittal plane of the resonator is much smaller in the case of a more tightly focussed arm with longer folding mirror/crystal separation. Also indicated in each diagram is the intraprism path length difference Δ_p for each resonator. It is clear from the figure that the second cavity with a folding mirror/crystal separation of 116 mm cannot support the full cavity mode as the value of Δ_p lies outside of the stable region. This is the reason why this particular resonator configuration would not operate with a prism in the short arm and explains the high cw threshold since the diffraction losses were so high.

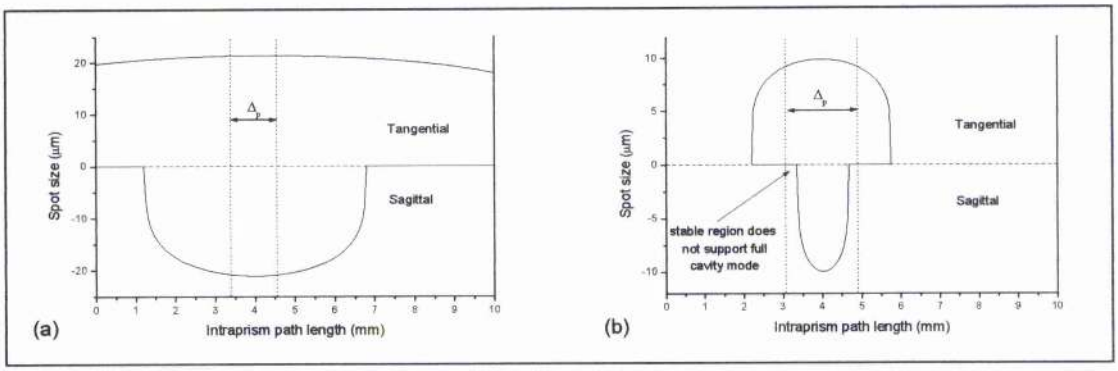

Figure 5.11 Variation of resonator stability with intraprism path length in the tangential and sagittal planes of the asymmetric Aoshima-type cavity for (a) 75 mm folding mirror/ crystal separation and 20 μm spot on the short arm end-mirror, (b) 116 mm folding mirror/ crystal separation and 10 μm spot on the short arm end-mirror.

The second laser cavity

A reasonable compromise between the mode spot size at the A-FPSA and the stability condition was calculated to be given by the resonator arrangement shown in Figure 5.12. The folding mirror/crystal separation was set at ~ 91 mm with a corresponding folding angle θ of 17° and spot size at the A-FPSA of ~ 15 μm. The cw threshold when the laser was pumped with the horizontally p-polarised diode was ~ 21 mW and with the full available pump power of 76 mW at the pump lens the laser produced a cw output of 1.4 mW from the HR end-mirror. The cavity optics including the pump lens fitted within a 20 × 6 cm footprint.

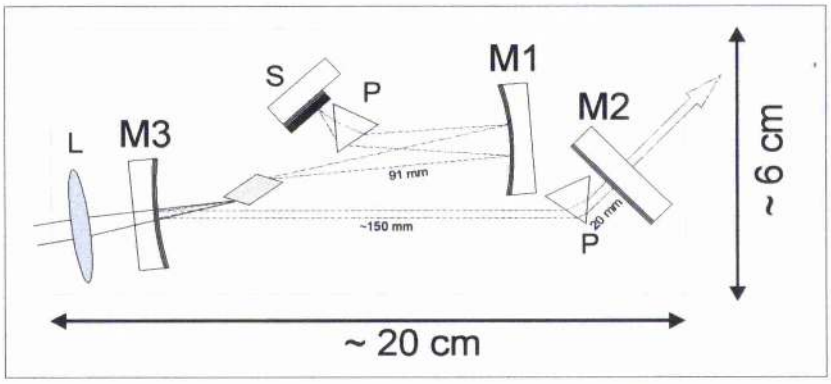

Figure 5.12 Schematic of the 4-mirror highly asymmetric Cr:LiSAF Aoshima-type cavity: M1 75 mm ROC focusing mirror; M3 50 mm ROC focusing mirror, M2 plane end mirror; S GaAs A-FPSA, P dispersion compensating Lak31 prisms; L 50 mm pump focussing lens..

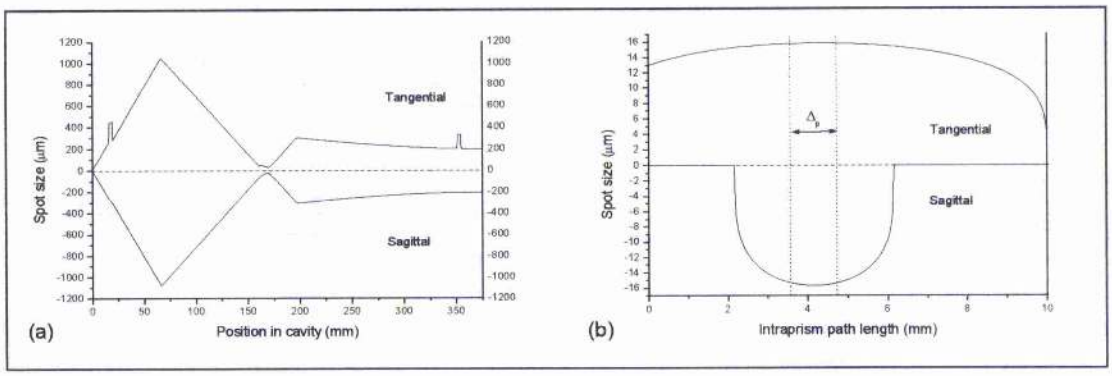

Figure 5.13 (a) Cavity mode behaviour: in the asymmetric Aoshima-type cavity with a folding mirror/crystal separation of 91 mm resulting in a spot size of 15 μm at the A-FPSA, (b) Variation of resonator stability with intraprism path length in the tangential and sagittal planes of the asymmetric Aoshima-type cavity showing the difference in prism path lengths traversed by the edges of the cavity mode lies well within the stable region.

The cavity operated with a repetition frequency of 407 MHz and stable, bandwidth-limited pulses of 115 fs duration with an average output power of 1.1 mW were readily obtained from the HR end-mirror (see Figure 5.14). As before, the laser could not be successfully modelocked with the 1.5% OC mirror in place of the HR end-mirror, but, had a suitable output coupling mirror of slightly lower reflectivity (R~99.25 %) been available at the time it should have been possible to slightly increase the useful output power.

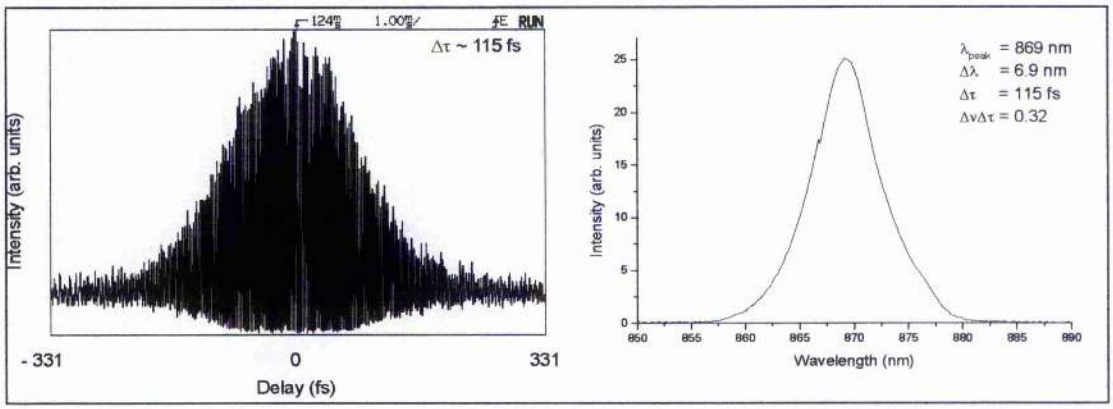

Figure 5.14 Interferometric autocorrelation and spectrum of 115 fs pulses with an average output power of 1.1 mW obtained for 76 mW pump.

An alternative compact femtosecond laser with oppositely oriented prisms in each arm

As it was unclear as to the precise action of the prisms in each of the cavity arms the prism in the longer of the arms was 'flipped' so that the apex pointed in the opposite direction to the prism in the short arm (see Figure 5.15). In this configuration the laser produced 100 fs pulses with a time-bandwidth product of 0.43 at a repetition frequency of 353 MHz. The average output power from the flipped prism cavity was ~1.1 mW for a pump power of 76 mW. The modelocking threshold was 61 mW. The separation between the pump folding mirror M3 and the prism was ~ 200 mm and the prism and the end-mirror M2 was 25 mm. This longer cavity length was necessary to achieve femtosecond pulse operation. The cavity optics including the pump lens fitted within a 25 × 7 cm footprint.

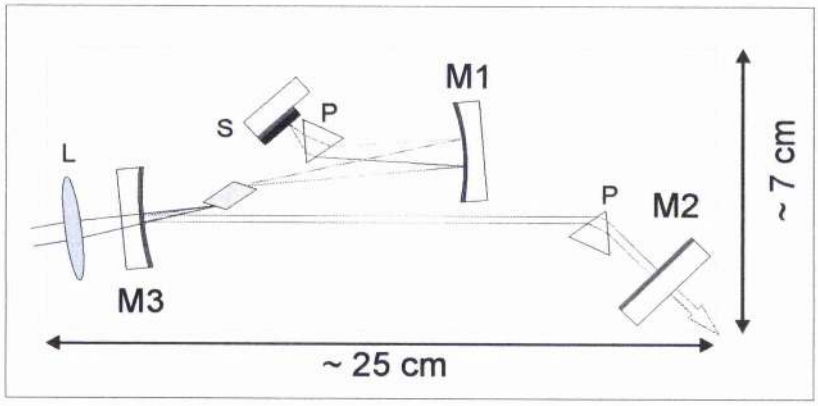

Figure 5.15 Schematic of the 4-mirror highly asymmetric Aoshima-type cavity with 'flipped' prism: M1 - 75 mm ROC focusing mirror; M3 - 50 mm ROC focusing mirror, M2 - plane end mirror; S - GaAs A-FPSA, P - dispersion compensating Lak31 prisms; L - 50 mm pump focussing lens.

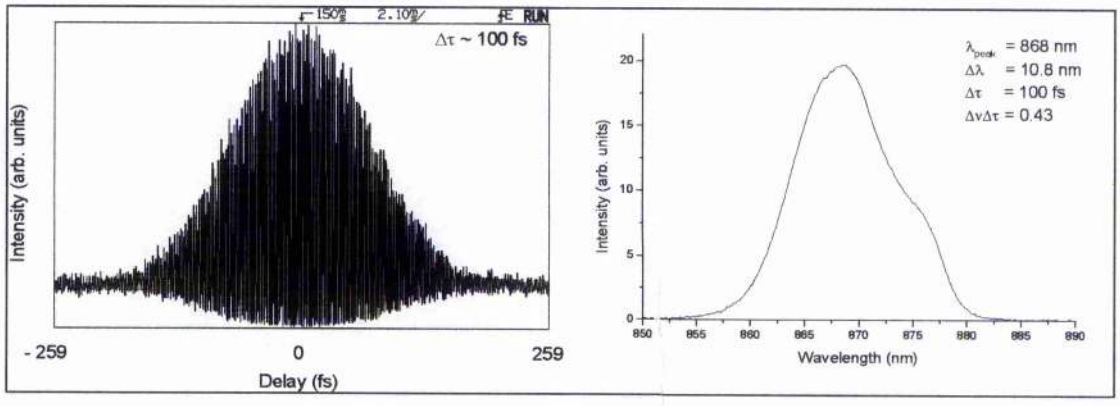

Figure 5.16 Interferometric autocorrelation and spectrum of 115 fs pulses with an average output power of 1.1 mW obtained for 76 mW pump.

5.4 A dispersive model for the compact resonator geometry's

More detailed analysis of the Aoshima-type cavities were required to explain the behaviour and contributions towards dispersion of the prisms in the resonators.

Kostenbauder[22] suggested a model for simplifying the analysis of complex dispersive optical systems, such as pulse compressors and femtosecond laser cavities. The model includes both spatial and temporal variations in the propagating signal and can calculate dispersive effects up to and including quadratic phase. Based on the ABCD matrix representation of paraxial optical systems Kostenbauder used a 1×4 'ray-pulse' vector to describe the spatial displacement x, slope θ, arrival time t and frequency f of a propagating monochromatic pulse with respect to a spatially and temporally transform limited midband reference pulse. This reference pulse provides a well-defined spatial and temporal origin at each transverse reference plane within the system.

The effect of any optical system on an input ray-pulse vector can then be described by:

$$\begin{bmatrix} x_{out} \\ \theta_{out} \\ t_{out} \\ f_{out} \end{bmatrix} = T\left\{ \begin{bmatrix} x_{in} \\ \theta_{in} \\ t_{in} \\ f_{in} \end{bmatrix} \right\}$$

Equation 5.2

where the elements x, θ, t and f of each ray-pulse vector are the relative offsets with respect to the reference ray and T is a 4×4 transfer matrix completely describing the optical system, $(T\{0\} = 0)$.

An individual element of any optical system operating on an input ray-pulse vector is represented by its corresponding 4×4 element matrix. As with standard ABCD matrix considerations the effect of arbitrary sequence of optical elements on an input pulse is described by the cascaded product of these element matrices

$$T = M_i \cdot M_{i-1} \cdots M_2 \cdot M_1$$

Equation 5.3

where M_i is the ith optical element and the system transfer matrix T has the general form

$$T = \begin{bmatrix} \frac{\partial x_{out}}{\partial x_{in}} & \frac{\partial x_{out}}{\partial \theta_{in}} & \frac{\partial x_{out}}{\partial t_{in}} & \frac{\partial x_{out}}{\partial f x_{in}} \\ \frac{\partial \theta_{out}}{\partial x_{in}} & \frac{\partial \theta_{out}}{\partial \theta_{in}} & \frac{\partial \theta_{out}}{\partial t_{in}} & \frac{\partial \theta_{out}}{\partial f_{in}} \\ \frac{\partial t_{out}}{\partial x_{in}} & \frac{\partial t_{out}}{\partial \theta_{in}} & \frac{\partial t_{out}}{\partial t_{in}} & \frac{\partial t_{out}}{\partial f_{in}} \\ \frac{\partial f_{out}}{\partial x_{in}} & \frac{\partial f_{out}}{\partial \theta_{in}} & \frac{\partial f_{out}}{\partial t_{in}} & \frac{\partial f_{out}}{\partial f_{in}} \end{bmatrix}$$

Equation 5.4

Immediate simplification of the transfer matrix in Equation 5.4 may be made as the invariance of the centre frequency for linear systems, $(f_{in} = f_{out})$, implies that the fourth row becomes $(0 \quad 0 \quad 0 \quad 1)$. Also the third column representing the dependence of the output ray-pulse on the arrival time of the input pulse becomes $(0 \quad 0 \quad 1 \quad 0)$. The transfer matrix therefore simplifies to

$$T = \begin{bmatrix} A & B & 0 & E \\ C & D & 0 & F \\ G & H & 1 & I \\ 0 & 0 & 0 & 1 \end{bmatrix}$$

Equation 5.5

where the elements A – I correspond to the remaining elements in Equation 5.4. The intersection of the first two rows and columns in the transfer matrix is the equivalent of the standard ABCD matrix for monochromatic ray propagation such that $AD - BC = 1$. A summary of the 4×4 element matrices for some of the more common laser cavity components is given in Appendix A.

To model the laser resonators, the transfer matrix that describes a complete round-trip of the cavity must be calculated and each ray-pulse of relative frequency f_{in} shown to be self reproducing in order for it to exist within the cavity such that

$$\begin{bmatrix} x \\ \theta \\ t_{out} \\ f \end{bmatrix} = \tilde{T} \begin{bmatrix} x \\ \theta \\ t_{in} \\ f \end{bmatrix}$$

Equation 5.6

where $\tilde{T}$ is the transfer matrix describing a complete round-trip of the cavity.

Combined with the conditions for a stable resonator the relative positions of rays of different frequency and delays of pulses of different frequency may be calculated. In this manner the axial position of a ray of frequency separation from the reference pulse f_{in} is given by

$$x_{out} = x_{in} = f_{in} \frac{E(1-D)+BF}{(D-1)(A-1)-BC}$$

Equation 5.7

and the slope of the ray is

$$\theta_{out} = \theta_{in} = f_{in} \frac{F(1-A)+CE}{(D-1)(A-1)-BC}$$

Equation 5.8

In the following sections, the compact resonators described at the beginning of this chapter will be examined using this using this comprehensive matrix analysis. The symmetric Aoshima-type cavity[20] will be examined first.

Modelling the symmetric Aoshima-type cavity

To determine the behaviour of a resonator mode the relative positions and slopes of a frequency upshifted and downshifted ray with respect to the midband reference ray are calculated. The round trip matrices from each reference plane in the stable resonator are used in conjunction with Equation 5.7 and Equation 5.8 to determine the behaviour of the rays in each element space. Figure 5.17 below shows the stable resonator mode for the tangential plane in the symmetric cavity and the positions of the cavity elements.

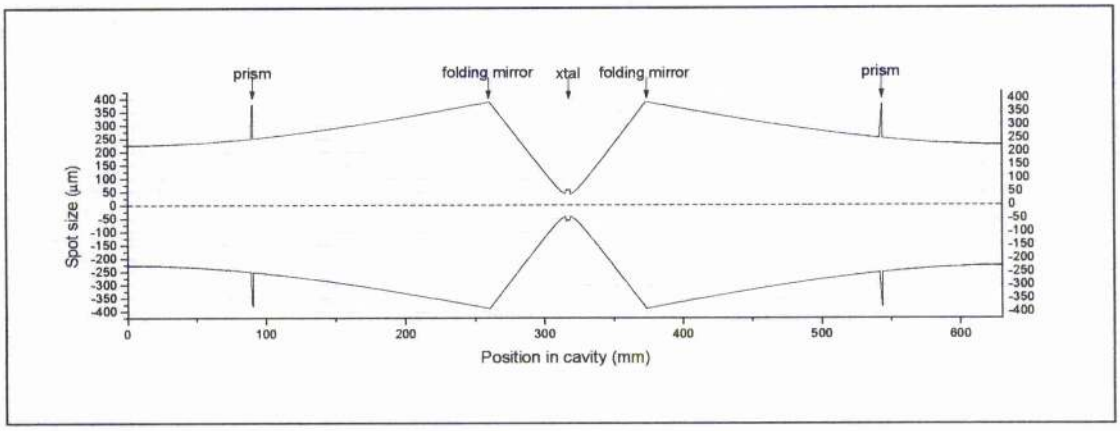

Figure 5.17 Behaviour of the tangential transverse beam in the symmetric Aoshima-type cavity, the positions of the various optical elements are shown above.

Using the method described above implemented in a Mathsoft MATHCAD™ model[23] (see Appendix B) the self sustaining rays at 900 nm and 920 nm were calculated with respect to a line centre reference ray at 910 nm and plotted in Figure 5.18.

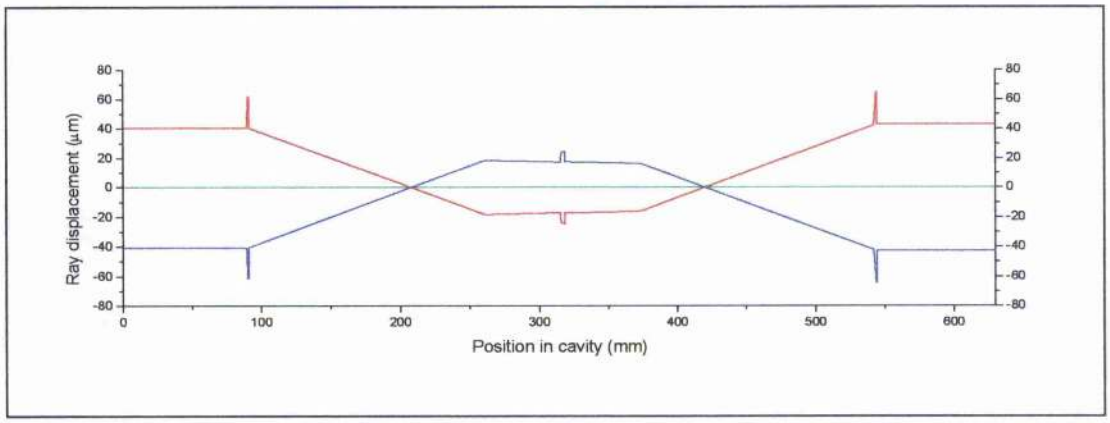

Figure 5.18 Relative paths traced by two rays separated by 20 nm, 900 nm (blue), and 920 nm (red) with respect to an arbitrary reference ray at 910 nm (green) in the symmetric Aoshima-type cavity.

It is important not to confuse the ray picture in Figure 5.18 with Figure 5.17 which describes the beam spot size ($1/e^2$ point) of the cavity mode throughout the cavity. For clarity we can plot the ray picture on top of Figure 5.17 by taking our reference ray to be the ray describing the $1/e^2$ point along the cavity mode (see Figure 5.19).

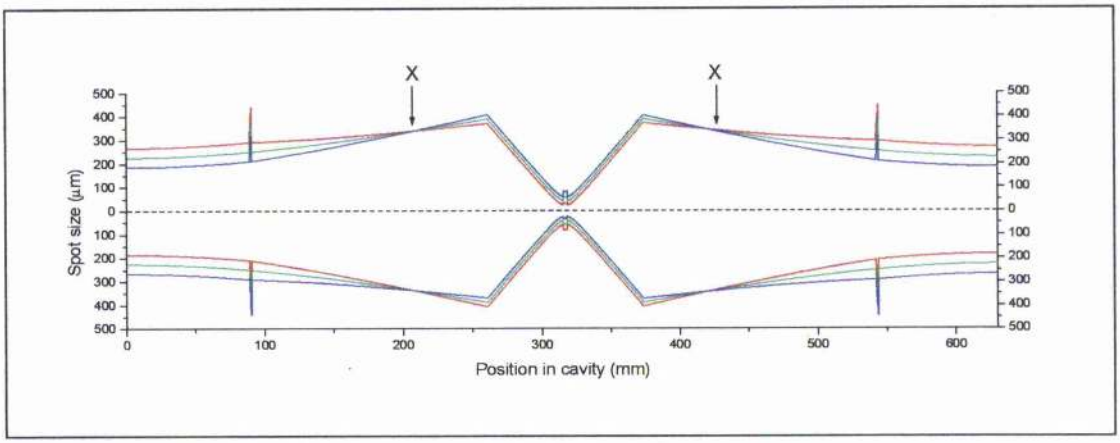

Figure 5.19 Tangential beam in the symmetric Aoshima-type cavity superimposed with the relative behaviour of two rays separated by 20 nm about a reference ray (green) at the $1/e^2$ point of the cavity mode, the rays cross at X.

It can be seen from Figure 5.18 that the rays in the space between the prisms and the end-mirrors are spatially dispersed but parallel and therefore do not contribute to the dispersion of the cavity. As suggested in reference 22 the rays between the folding mirrors, and therefore in the gain medium, are also spatially dispersed, which could explain the bandwidth limitation of the output pulses. The very slight angular dispersion visible in the folding section is due to the Brewster-angled gain medium, which if replaced with a plane cut crystal, would result in the rays becoming parallel. The conclusion of Aoshima[20] as to the origin of the dispersion in the cavity is therefore incorrect as the distance between the folding mirrors will not in general make a significant contribution to the dispersion in the cavity. It is clear from the diagram that the majority of the dispersion originates between the prisms and the folding mirrors as the rays in this element space have a large angular dispersion. Due to the relative angular and spatial displacement of the rays, the folding mirrors are acting as 'virtual' prisms at the ray crossing point X. This is interesting as one would not necessarily expect a mirror to contribute to the dispersion in this manner. The net effect is that the cavity behaves as if there are two pairs of oppositely oriented prisms in each cavity arm (see Figure 5.20).

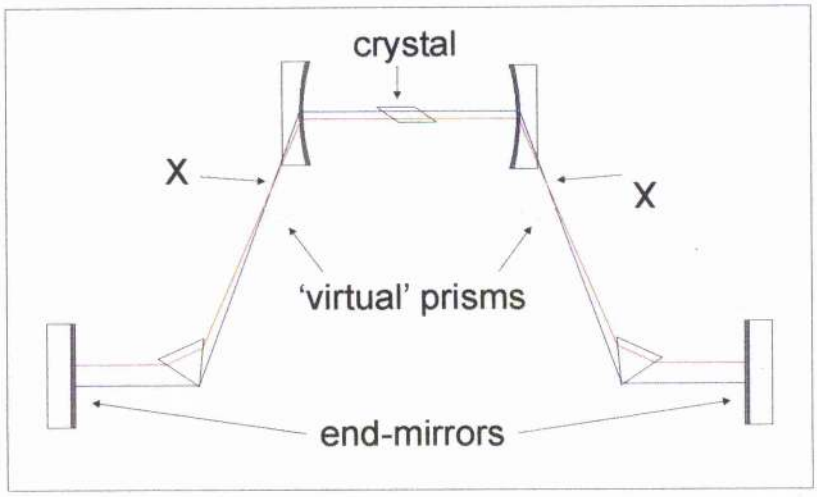

Figure 5.20 The behaviour of the ray crossing points X as 'virtual' prisms in the symmetric Aoshima-type cavity.

The delay between propagating pulses of differing frequencies in the model can be used to calculate a value for the quadratic phase or GVD of the cavity. The relative delay of a pulse from the reference pulse over a single round trip is given by

$$t_{out} = Gx_{in} + H\theta_{in} + If_{in}$$

Equation 5.9

By propagating several such pulses of different frequencies $f_1 \cdots f_5$ through the cavity an expression for the group velocity dispersion may be derived

$$GVD = \frac{\tau_1 - 8\tau_2 + 8\tau_4 - \tau_5}{24\pi\Delta f}$$

Equation 5.10

where Δf is the frequency separation of the pulses and τ_1, τ_2, τ_4 and τ_5 are the relative delays of the 4 pulses to the midband reference pulse $f_3 = 0, \tau_3 = 0$. The quadratic phase for the Aoshima-type cavity was calculated as -278 fs^2 less than a third of the value required for the shortest pulses[20].

The incorrect assumption of Aoshima[20] that the prism separation must be kept the same as in a standard z-fold cavity probably limited the ultimate pulse duration. Further investigation of this type of cavity must be made to determine the effect of the spatially dispersed beam in the gain medium, on the pulse duration.

The most crucial parameter for dispersion control in the Aoshima-type cavity is the prism/folding mirror separation and providing this is kept at a suitable distance the

contributions from the 'dead-space' from the prisms to the end-mirrors and space between the folding section may be ignored. This implies, as we have confirmed experimentally, the feasibility of highly asymmetric cavities of this type.

Modelling of the highly asymmetric Aoshima-type cavity

The highly asymmetric Aoshima-type cavity described in section 5.3 was modelled using the Kostenbauder matrix analysis presented in the previous section. The paths for two rays with wavelengths shifted up and down by 5 nm from an arbitrary reference ray at 869 nm (the central wavelength of the spectrum in Figure 5.7) were calculated. The relative spatial and angular relationship of the rays are plotted below in Figure 5.21. The rays are spatially dispersed at the output coupler (long arm) and undispersed at the A-FPSA (short arm). This is due to the fact that the prism in the short arm fortuitously lies at the position where the rays cross. The slight angular dispersion between the folding mirrors is again due to the Brewster-angled Cr:LiSAF crystal. Figure 5.22 shows the relative behaviour of two rays separated by 10 nm about a reference ray at the $1/e^2$ of the cavity beam.

The calculated value for the net quadratic phase was –86 fs^2 which could explain the broader pulses obtained from this cavity as this is not sufficient to balance the calculated SPM of 137 fs^2.

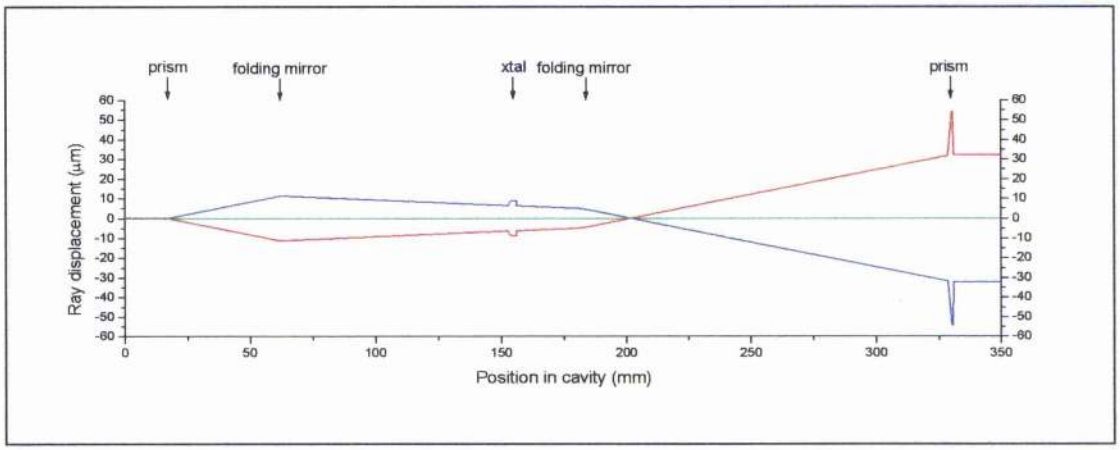

Figure 5.21 Relative paths traced by two rays separated by 10 nm, 864 nm (blue), and 874 nm (red) with respect to an arbitrary reference ray at 869 nm (green) in the highly asymmetric Aoshima-type cavity, the position of the cavity elements are indicated above.

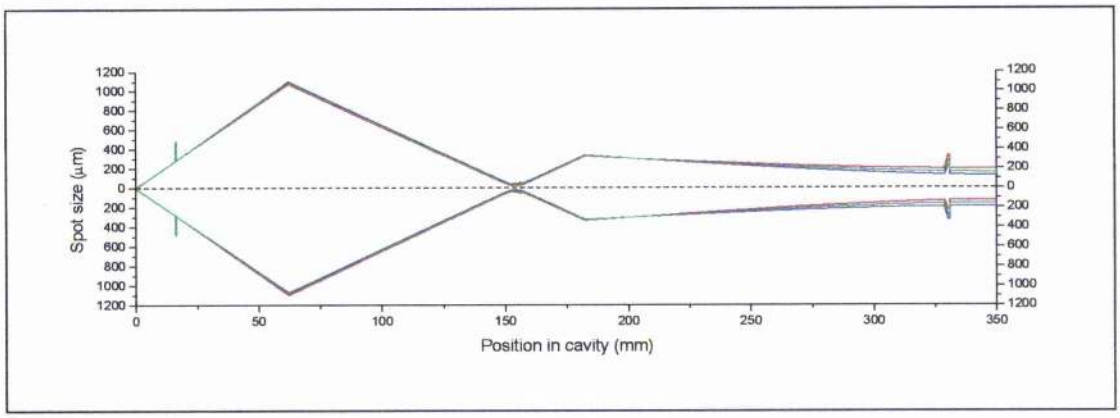

Figure 5.22 Tangential beam in the highly asymmetric Aoshima-type cavity superimposed with the relative behaviour of two rays separated by 10 nm about a reference ray (green) at the $1/e^2$ point of the cavity mode.

Modelling of the highly asymmetric Aoshima-type cavity with oppositely oriented prisms

As with the highly asymmetric Aoshima-type cavity with prism apices oriented in the same direction the cavity with the 'flipped' second prism was modelled using the Kostenbauder matrix analysis. The paths for two rays with wavelengths shifted up and down by 5 nm from an arbitrary reference ray at 868 nm (the central wavelength of the spectrum in Figure 5.16) were calculated. The relative spatial and angular relationship of the rays are plotted below in Figure 5.23. The rays are spatially dispersed at both the output coupler (long arm) and the A-FPSA (short arm). The effect of rotating the prism in the long arm causes the rays to cross in between the folding mirrors adding an opposite sign of angular dispersion in this section to the angular dispersion in the long arm. The calculated value for the net quadratic phase was -50 fs^2, which could explain the chirped pulses obtained from this cavity configuration.

Figure 5.24 shows the relative behaviour of two rays separated by 10 nm about a reference ray at the $1/e^2$ of the cavity beam.

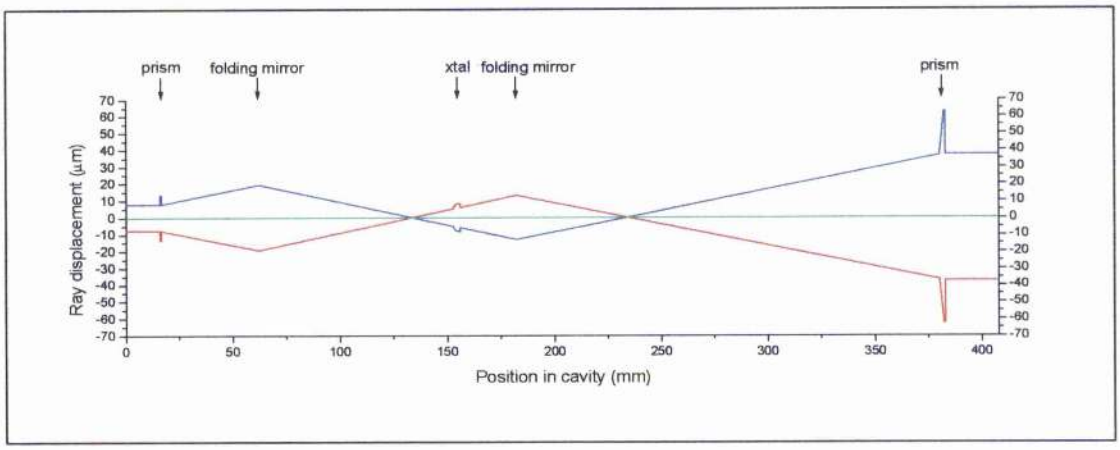

Figure 5.23 Relative paths traced by two rays separated by 10 nm, 863 nm (blue), and 873 nm (red) with respect to an arbitrary reference ray at 868 nm (green) in the highly asymmetric Aoshima-type cavity with oppositely oriented prisms, the position of the cavity elements are indicated above.

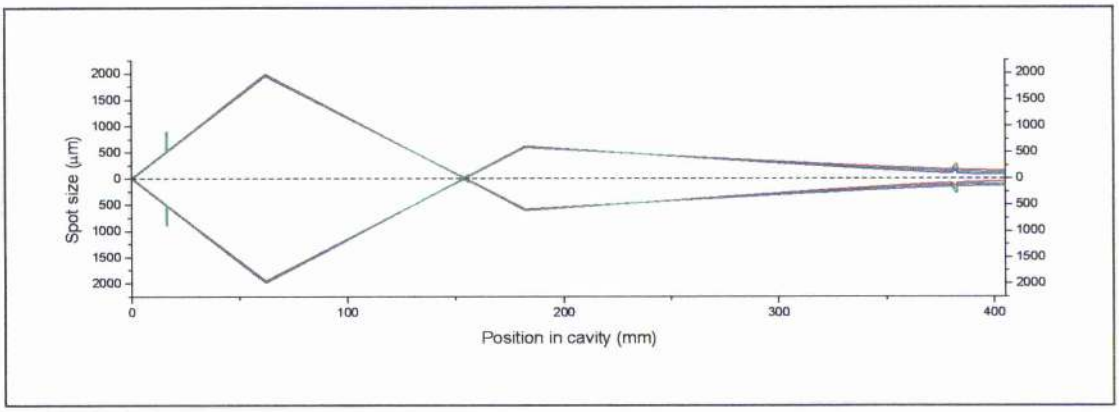

Figure 5.24 Tangential beam in the highly asymmetric Aoshima-type cavity with oppositely oriented prisms superimposed with the relative behaviour of two rays separated by 10 nm about a reference ray (green) at the $1/e^2$ point of the cavity mode.

5.5 A highly compact femtosecond laser with a single prism for dispersion compensation

An immediate conclusion from the modelling of the highly asymmetric Aoshima-type cavities presented in the previous section is that the prism in the short arm does not contribute a large amount of dispersion to the cavity due to the short distance from this prism to the folding mirror. This implies that this prism is not necessary to achieve an acceptable amount of negative dispersion, which is advantageous because of the problems in laser alignment encountered with this prism described earlier. Femtosecond

pulse operation from a dye ring laser with a single prism has already been reported[24] as well as in a Cr^{4+}:YAG laser[25] and in a diode pumped Nd:glass laser[26] for which a simple ray optic analysis was presented. A laser cavity in which a single prism is used is easier to align and lower loss due to a fewer number of cavity elements. For these reasons, a highly asymmetric compact laser cavity incorporating a single prism was investigated.

The laser cavity

The laser cavity was set up as in Figure 5.25. The Lak31 prism in the short arm was removed and the fold angle of the 75 mm ROC mirror set to 11°. The distance from this folding mirror to the Cr:LiSAF crystal was 95 mm and the length of the short arm was ~ 60 mm. The 50 mm ROC pump folding mirror and second Lak31 prism were initially separated by 125 mm and the space after the prism to the end-mirror was ~ 25 mm. Figure 5.26 and Figure 5.27 below show the paths for two rays with wavelengths shifted up and down by 5 nm from an reference ray at 860 nm and the relative behaviour of these rays about a reference ray at the $1/e^2$ of the cavity beam.

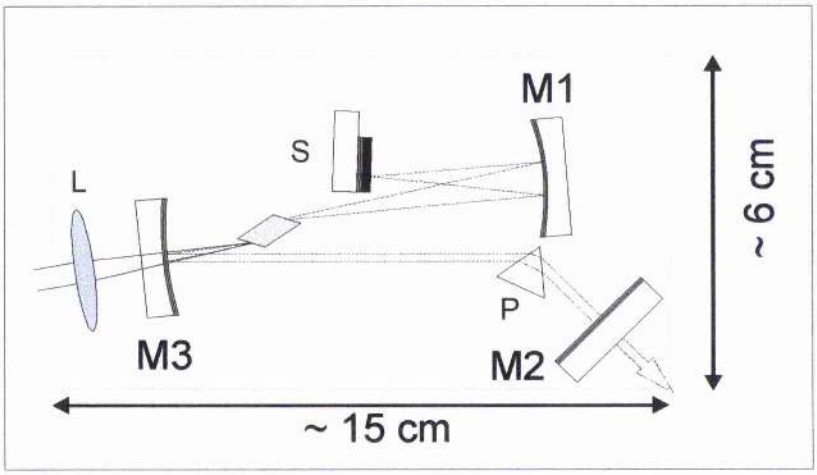

Figure 5.25 Schematic of the compact femtosecond laser with a single Lak31 prism for dispersion compensation, L 50 mm pump focus lens, M1 75 mm ROC folding mirror, M3 50 mm ROC folding mirror, M2 0.75% output-coupling mirror, S GaAs A-FPSA.

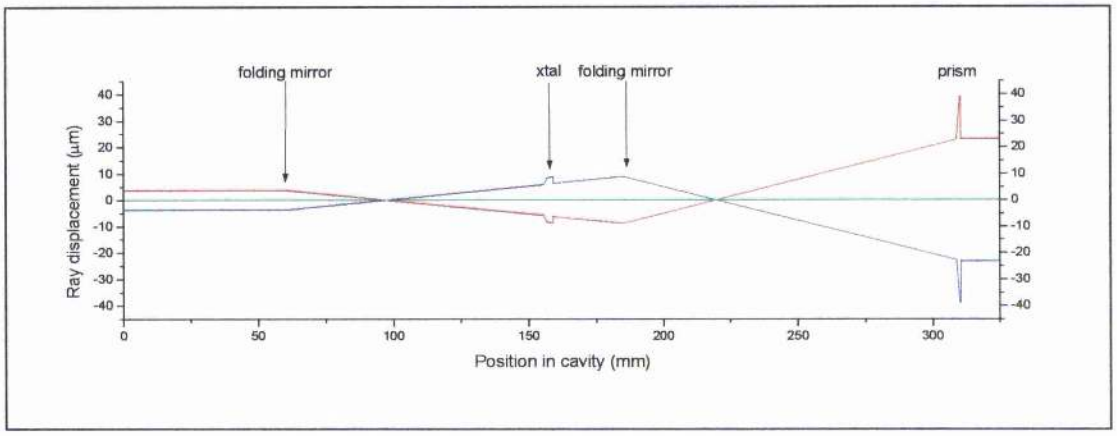

Figure 5.26 Relative paths traced by two rays separated by 10 nm, 855 nm (blue), and 865 nm (red) with respect to an arbitrary reference ray at 860 nm (green) in the highly asymmetric compact cavity with single prism, the position of the cavity elements are indicated above.

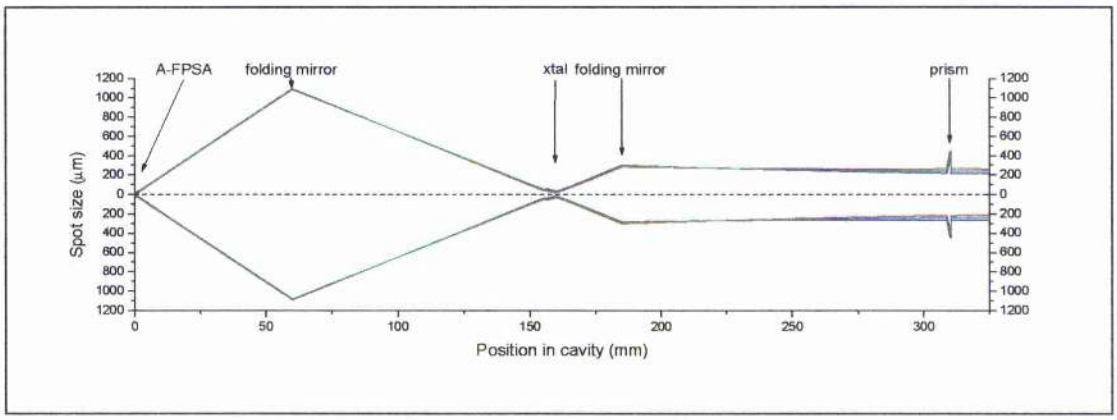

Figure 5.27 Tangential beam in the highly asymmetric compact cavity with single prism superimposed with the relative behaviour of two rays separated by 10 nm about a reference ray (green) at the $1/e^2$ point of the cavity mode.

The rays again cross in the folding section (although not as pronounced) suggesting that the cavity configuration is not optimum for maximising negative dispersion. Unfortunately, in the single prism cavity opposite alignment of the prism obviously has no effect.

Initial performance

The cw threshold was measured at 26 mW with the new 0.75% output-coupling mirror at 856 nm in place. CW output powers as high as 7 mW for 76 mW pump were recorded. The laser modelocked easily producing 250 fs chirped pulses with an output power of ~ 5 mW at a cavity frequency of 435 MHz.

Modelocked performance

The output pulse durations were optimised by careful alignment of the cavity elements and variation of the prism insertion. Stable pulses with durations as short as 160 fs with an average output power of 6.1 mW were produced over a period of many hours (see Figure 5.28). The GVD or quadratic phase of the cavity was calculated to be -157 fs^2 with ~ 2 mm of prism insertion. Unfortunately, spectral information was not available at the time these results were taken.

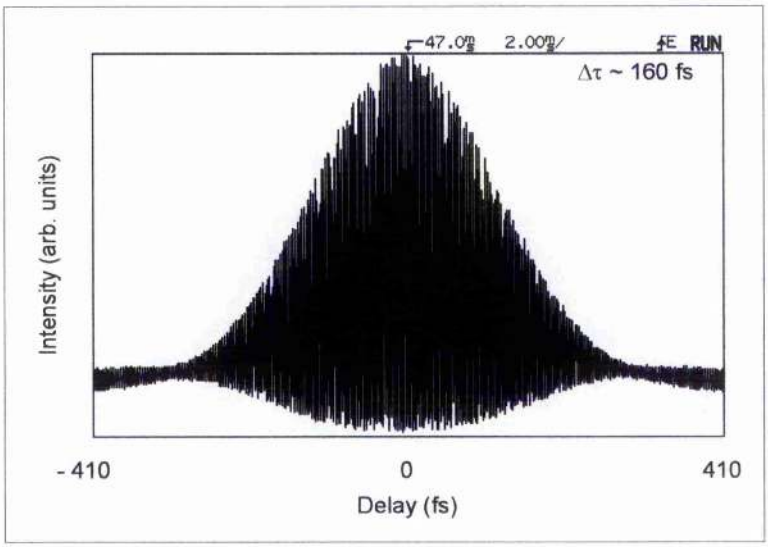

Figure 5.28 Interferometric autocorrelation of 160 fs pulses with a repetition frequency of 435 MHz and an average output power of 6.1 mW obtained from the compact single prism cavity for 76 mW pump.

The pump folding mirror prism separation was lengthened to 205 mm and the space after the prism to 70 mm. In this arrangement with about ~5 mm of prism insertion, the calculated quadratic phase was -253 fs^2 and the laser produced 133 fs pulses (see Figure 5.29). The repetition frequency was 315 MHz and the average output power was ~ 5 mW.

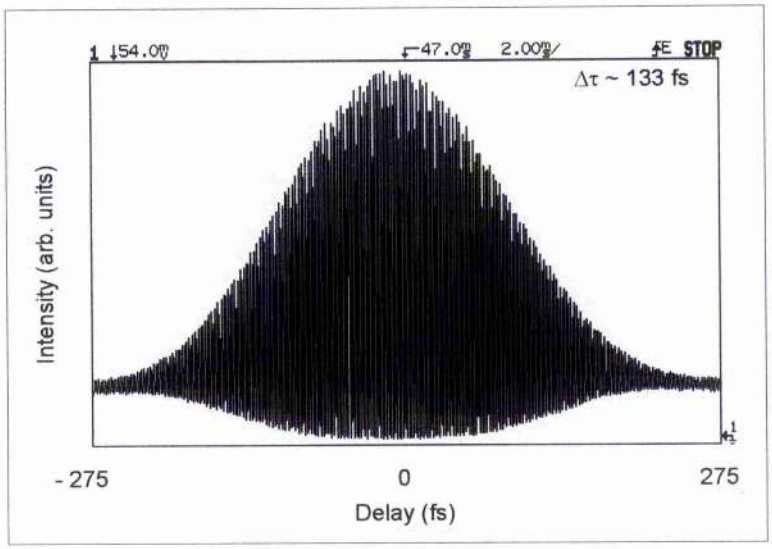

Figure 5.29 Interferometric autocorrelation of 133 fs pulses with a repetition frequency of 315 MHz and an average output power of 5 mW obtained from the compact single prism cavity for 76 mW pump.

One of the reasons proposed for the longer, chirped pulses obtained from the shorter cavity is the bandwidth limitation due to the spatially dispersed mode in the gain medium. This problem scales with cavity length as the size of the mode increases as the cavity length is reduced. Figure 5.30 below shows the spot size variation in the Cr:LiSAF crystal for the 435 MHz and 315 MHz single prism cavities. One possible solution of this problem would be to ensure the rays crossed inside the gain medium and hence not spatially dispersed.

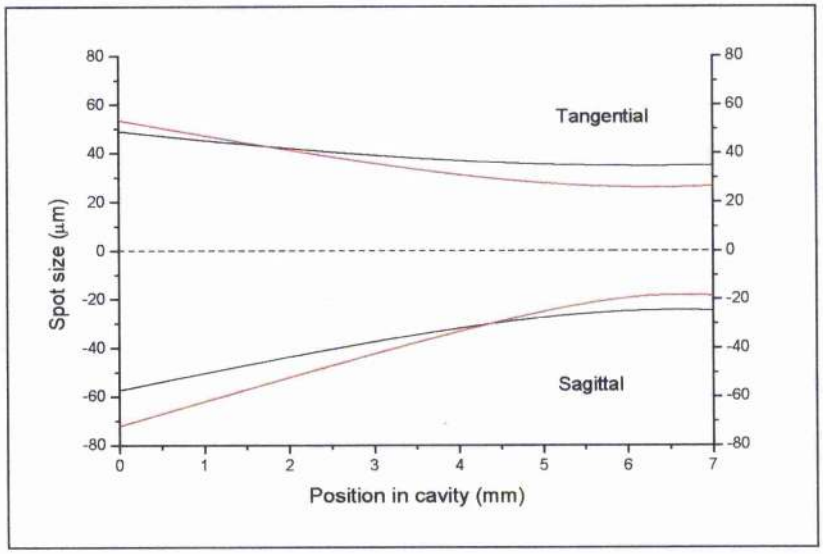

Figure 5.30 Cavity mode behaviour in the Cr:LiSAF crystal of the 435 MHz (black) and 315 MHz (red) compact single prism cavities of Figure 5.28 and Figure 5.29.

To fit the cavity within a smaller footprint, the Lak31 prism was replaced with an SF10 glass prism which exhibits a larger dispersion. The prism was placed 100 mm from the 50 mm ROC pump folding mirror with a space after the prism of 75 mm. In this configuration the calculated GVD was -368 fs^2 although the laser produced 330 fs pulses at a repetition frequency of ~ 400 MHz (see Figure 5.31). An output coupler (OC) could not be used in this configuration so the output power was limited to 1.1 mW. The footprint of the laser cavity was reduced to 15 × 6 cm and implemented using *Tiny Mounts*[27] and ½ inch (12.7 mm) optics on a small bread board on which a compact version of the pump laser diodes were included (see Figure 5.32 and Figure 5.33).

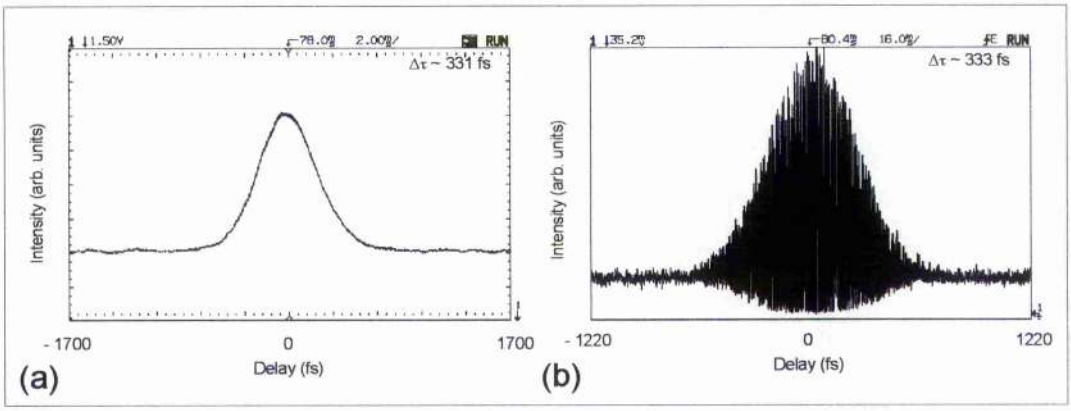

Figure 5.31 (a) Intensity and (b) Interferometric autocorrelation of ~330 fs pulses with a repetition frequency of ~400 MHz and an average output power of 1.1 mW obtained from the compact single prism cavity for 76 mW pump.

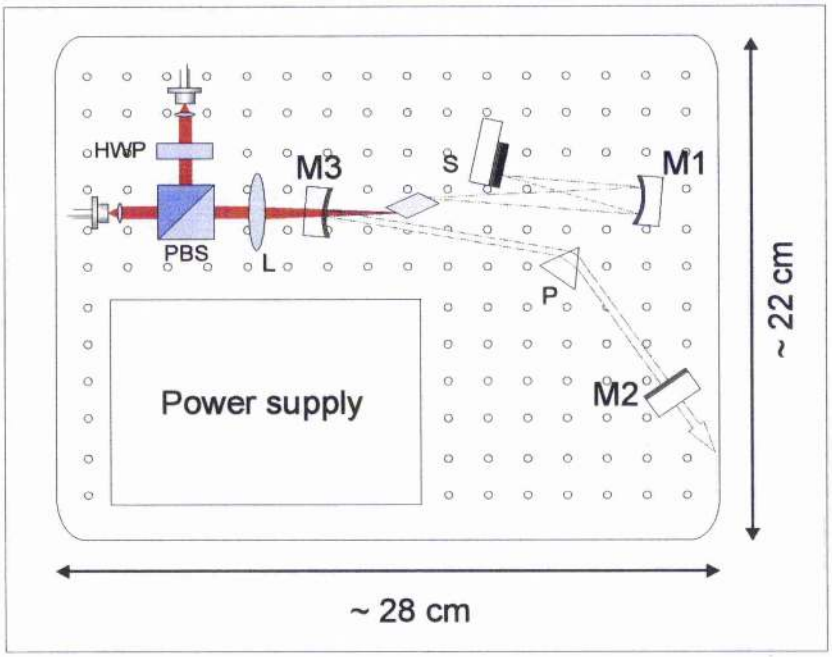

Figure 5.32 Schematic of the compact single prism femtosecond laser on a self contained breadboard, P – SF10 prism, L – 50 mm ROC pump focusing lens, PBS – polarising beam splitter cube, HWP – half-wave plate, S - A-FPSA.

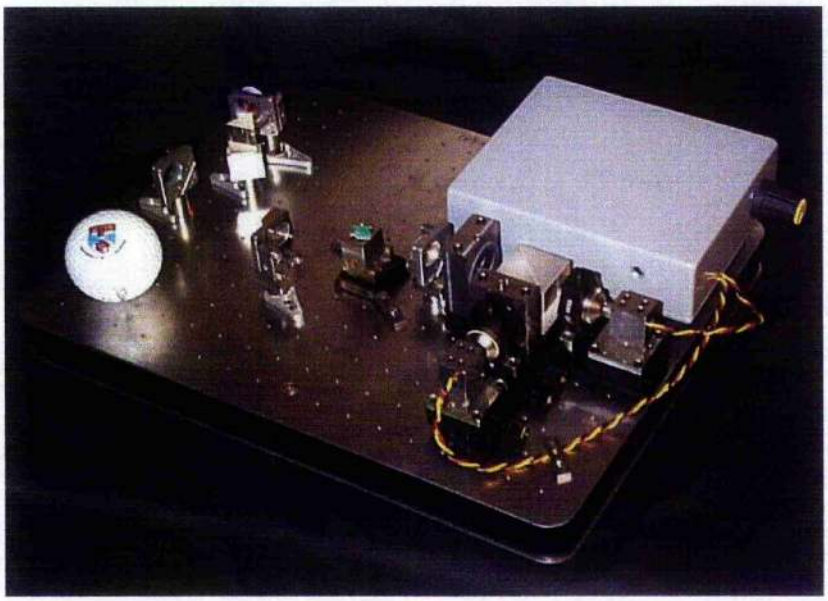

Figure 5.33 Photograph of the compact single prism femtosecond laser on a self contained breadboard, the battery power supply for the diodes is also included (as well as the infamous St. Andrews golf ball!).

5.6 Conclusions

In this chapter a number of highly compact femtosecond lasers have been demonstrated with footprints substantially smaller than the majority of commercially available short pulse sources. The lasers were based on a symmetric compact laser cavity design with a dispersion-compensating prism in each arm suggested by Aoshima *et al*[20]. Combining the compact design and the highly asymmetric lasers modelocked with a SESAM presented in the previous chapter 133 fs pulses were produced with cavity frequencies as high as 400 MHz. Average output powers were limited due to alignment issues in the compact cavities caused by the prism in the tightly focussing short arm. Dispersive ray-pulse matrix analysis was shown to describe the behaviour of the prism and lead to the conclusion only one prism was necessary. A compact laser with a single prism was then described which produced pulses as short as 160 fs were obtained with average output powers greater than 5 mW at repetition frequencies greater than 430 MHz. This represented an improvement in both repetition frequency and output power over the original compact cavity design obtained with over a magnitude less pump power. A version of this highly asymmetric single prism incorporating an SF10 prism was constructed on a tiny breadboard with a cavity configuration that produced ~ 300 fs pulses at an output power of 1.1 mW and a repetition frequency ~ 400 MHz.

With the demonstration of such simple, compact and portable femtosecond lasers, new applications may now be realised. Advances in diffraction limited AlGaInP laser diode sources will only improve the efficiency and output powers of short pulses of this type.

Endnotes

1 V. P. Yanovsky, A. Korytkin, F. W. Wise, A. Cassanho and H. P. Jenssen, *IEEE J. Sel. Topics Quantum Electron.* **2**, 465 (1996).

2 M. J. P. Dymott and A. I. Ferguson, *Appl. Phys.* **B 65**, 227 (1997).

3 R. Mellish, S. C. W. Hyde, N. P. Barry, R. Jones, P. M. W. French, J. R. Taylor, C. J. van der Poel and A. Valster, *Appl. Phys.* **B 65**, 221 (1997).

4 D. Kopf, K. J. Wiengarten, G. Zhang, M. Moser, M. A. Emanuel, R. J. Beach, J. A. Skidmore and U. Keller, *Appl. Phys.* **B 65**, 235 (1997).

5 S. Uemura and K. Torizuka, *Opt. Lett.* To Be Published.

6 V. P. Yanovsky, F. W. Wise, A. Cassanho and H. P. Jenssen, *Opt. Lett.* **20**, 1304 (1995).

7 M. Ramaswamy-Paye and J. G. Fujimoto, *Opt. Lett.* **19**, 1756 (1994).

8 B. E. Bouma and J. G. Fujimoto, *Opt. Lett.* **21**, 134 (1996).

9 V. L. Kalashnikov, V. P. Kaloosha, I. G. Poloyko and V. P. Mikhailov, *J. Opt. Soc. Am.* **B 14**, 965 (1997).

10 X. Guang Huang, F. Huang, W-K. Lee and M. R. Wang, *Opt. Commun.* **142**, 249 (1997).

11 X. Guang Huang and M. R. Wang, *Opt. Commun.* **158**, 322 (1998).

12 R. Mellish, S. V. Chernikov, P. M. W. French and R. Taylor, *Electron. Lett.* **34**, 552 (1998).

13 G. J. Valentine and W. Sibbett, *in Technical Digest of Conference on Lasers and Electro-optics (Optical Society of America, Washington D. C., 1998), paper* CtuM47.

14 G. J. Valentine, J-M. Hopkins, P. Loza-Alvarez, G. T. Kennedy, W. Sibbett, D. Burns and A. Valster, *Opt. Lett.* **22**, 1639 (1997).

15 G. J. Valentine, M. P. Critten, G. T. Kennedy, J-M. Hopkins, P. Loza-Alvarez and W. Sibbett, *in Technical Digest of Conference on Lasers and Electro-optics (Optical Society of America, Washington D. C., 1998), paper* CMI1.

16 S. Uemura and K. Miyazaki, *Opt. Commun.* **138**, 330 (1997).

17 J-M. Hopkins, G. J. Valentine, W. Sibbett, J. Aus der Au, F. Morier-Genoud, U. Keller and A. Valster, *Opt. Commun*, **154**, 54 (1998).

18 K. Gäbel, P. Rußbüldt, R. Lebert, P. Loosen, R. Poprawe, H. Heyer and A. Valster, *Opt. Commun.* **153**, 275 (1998).

19 D. Kopf, G. Zhang, R. Fluck, M. Moser and U. Keller, *Opt. Lett.* **21**, 486 (1995).

20 S. Aoshima, H. Itoh and Y. Tsuchiya, *IEEE J. Sel. Topics Quantum Electron.* **3**, 95 (1997).

21 G. J. Valentine, and W. Sibbett, *in Technical Digest of the Conference on Lasers and Electro-optics Europe (Optical Society of America, Washington D.C. 1998).* paper CtuM47.

22 A. G. Kostenbauder, *IEEE J. Quantum Electron.* **26**, 1148 (1990).

23 G. J. Valentine, *in Development of All-solid-state Modelocked Laser Sources at 1.55 μm,*, PhD thesis, University of St.Andrews, chapter 5, Appendix III.

[24] J. J. Fontarine, W. Dietel and J. C. Diels, *IEEE J. Quantum Electron.* **QE-19**, 467 (1983).

[25] Y. Chang, R. Maciejko, R. Leonelli and A. Spring Thorpe, *Appl. Phys. Lett.* **73**, 2098 (1998).

[26] D. Kopf, G. J. Spühler, K. J. Weingarten and U. Keller, *Appl. Optics*, **35**, 912 (1996).

27 New Focus, Inc. 2630, Walsh Ave. Santa Clara, CA 95051-0905, U.S.A.

Chapter 6: Concluding remarks

6.1 Summary and conclusions

The work described in this thesis was concerned with the design and operation of directly-diode-pumped, all-solid-state femtosecond laser sources having low pump thresholds. The laser systems were based on the Cr^{3+}:doped colquiriites, Cr:LiSAF and Cr:LiSGaF, and were optically pumped using AlInGaP laser diodes. By reducing intracavity parasitic losses and optimising laser resonator configurations for modelocked performance[1], cw and modelocking thresholds were reduced to a level that permitted efficient pumping with low-cost, low-power, narrow-stripe laser diodes. These laser diodes produced beams that were diffraction limited in both planes thereby allowing collimation and tight focussing of the pump beam with simple coupling optics. The use of these efficient low-power pump sources meant that no active or passive cooling of the gain medium was necessary. A number of laser systems using this novel pump source were designed and assessed, and these had progressively smaller footprints.

The noise properties of the low-threshold femtosecond lasers were investigated and found to be the best yet reported from free-running passively modelocked lasers without active stabilisation[2]. In chapter 4 the use of a semiconductor saturable absorber mirror improved the modelocking stability of the low-threshold lasers, producing pulses as short as 57 fs and average output powers as high as 9 mW for only 70 – 80 mW of incident pump power. This level of performance could be sustained for over fourteen hours using six AA-type batteries, highlighting the efficiency of the laser and permitting ultra-low noise operation[3]. The low noise operation has enabled the evaluation of a number of prototype streak camera systems and the best temporal resolution from a camera in synchroscan operation reported to date has been demonstrated.

A number of highly compact low-threshold lasers with novel dispersion compensation schemes were then presented in chapter 5. It was shown that by placing a prism on each side of the gain medium the necessary interprism separation could be distributed within the cavity and the cavity length significantly reduced. Dispersive ray analysis[4] of this cavity revealed that the major contribution to dispersion was the space between the

folding mirrors surrounding the gain medium and the prisms in each cavity arm and also that the distance between the folding mirrors did not significantly contribute to the net cavity dispersion. Finally a laser using a single prism in one cavity arm was shown to provide femtosecond pulse operation with cavity frequencies as high as ~450 MHz. This represented the most compact femtosecond laser geometry ever reported using standard low-insertion-loss 'off the shelf' optical components. Table 6-1 below summarises the most significant results obtained during the course of this project.

Laser	CW threshold	Pulse duration	Average output power	Pump power	Pump power required for sub-100 fs pulses	Rep. rate	page	comments
4-mirror Cr:LiSGaF	43 mW (22 mW)	87 fs	10 mW (1.5 mW)	150 mW	~ 100 mW	86 MHz	2-45	1.5 % OC (HR) Plane/Plane crystal
3-mirror Cr:LiSGaF	14 mW	65 fs	1 mW	130 mW	45 mW	172 MHz	3-11	HR mirrors Plane/Plane crystal
3-mirror Cr:LiSAF	8.5 mW	60 fs	1.5 mW	76 mW	30 mW	172 MHz	3-17	HR mirrors Brewster-angled crystal
Highly-asymmetric 4-mirror Cr:LiSAF	30 mW (15 mW)	57 fs	6.5 mW (1.3 - 1.5 mW)	76 mW	24 mW	~ 200 MHz	4-16	1.5 % OC (HR) A-FPSA Brewster-angled crystal
Compact asymmetric Aoshima-type Cr:LiSAF	~ 20 mW	115 fs	1.1 mW	76 mW	NA	407 MHz	5-11	HR mirrors A-FPSA Brewster-angled crystal
Compact Cr:LiSAF with single prism	26 mW (18 mW)	133 fs 160 fs	5 mW 6.1 mW	76 mW	NA	315 MHz 435 MHz	5-22	0.75 % OC (HR) A-FPSA Brewster-angled crystal

Table 6-1 Summary of performance obtained from the laser systems described in this thesis.

Although innovative and notable advances have been made into high power Cr:LiSAF and Cr:LiSGaF lasers capable of producing over 500 mW[5], the associated thermal and mechanical problems of these materials have meant that relatively involved pumping, cooling and cavity configurations be used, often employing specialised components. Recent advances in frequency-doubled diode-pumped-solid-state minilasers (DPSSL), for the purpose of pumping Ti:sapphire ultrashort pulse lasers, have meant that these sources can now be made reasonably compact and have reduced the requirement for high-power directly-diode pumped femtosecond lasers in the near-infrared. Spectra

Physics has recently launched a new frequency-doubled Nd:YVO_4 DPSSL[6] which gives over 10 W at 532 nm and measures only 35 × 15 × 10 cm. Time-Bandwidth Products Inc. have also recently developed a self-contained, sub-100 fs Ti:sapphire laser and DPSSL in a single unit measuring 63 × 37 × 19 cm giving over 200 mW average output power[7]. This is the largest power/footprint ratio for a short pulse laser of this type. For applications where limited tunability is required, advances in sub-ps fibre lasers[8] have also produced compact femtosecond pulse lasers with a greater degree of 'hands-off' reliability[9]. These groundbreaking developments, however, have led to systems that are still relatively expensive for the end users and some have a great degree of 'overkill' features for many of the applications and potential applications of ultrashort pulses.

The Cr^{3+}:doped colquiriites offer the most direct route to compact, tunable, low-noise and portable ultrashort pulse sources with moderate output powers for a fraction of the cost of many of the presently available commercial systems. The lasers described here offer attractive potential as versatile alternative femtosecond pulse sources for many low-power applications including stable, noise-free, seed pulses for regenerative amplification, or sensitive pump-probe-type experiments, jitter-free characterisation and calibration of pulse measurement systems and portable sources for specialist applications in the medical and imaging fields.

6.2 Future Work

The laser cavity designs and arrangements presented in this thesis are suitable for pumping with higher power diffraction-limited sources such as are already available in the form of master oscillator, power amplifiers[10] and high-power tapered diode lasers[11]. Recent advances in discrete semiconductor laser diodes[12] have heralded higher spatial quality and enhanced output power outputs directly from the diode chip. Using this type of diode, as a pump source, would allow the compactness of the systems described here to be retained. SDL Inc. have recently demonstrated over 300 mW in a diffraction-limited beam from an α-DFB laser at 670 nm[13]. Assuming a linear power scaling in the highly compact Cr:LiSAF lasers after the inclusion of appropriate air or thermoelectric cooling of the gain medium, output powers as high as 40 mW could be achieved with only one of these laser diodes as the pump source.

The demonstration of high powers (500 mW) from broad-area AlGaInP laser diodes with narrower stripe widths (50 μm) means that cavity designs of the type described could be readily optimised for close coupling and tight focussing of the pump beam. Future reduction in diode stripe widths and reduction of the radii of curvature of the cavity folding mirrors will further improve the efficiency of directly-diode-pumped femtosecond lasers.

Work at St. Andrews University is also commencing in the design of specific cavity configurations that optimise the pump beam, cavity mode overlap inside the gain crystal using broad area laser diodes and novel cavity component arrangements. In a preliminary Cr:LiSGaF laser arrangement cw output powers as high as 75 mW have been demonstrated for 600 mW of absorbed pump power from two 200 μm stripe laser diodes.

Pulse durations could also be further reduced by considering carefully the second-order and higher-order dispersions in the cavity. The resulting improvement in pulse peak power could then be used for more efficient intracavity second harmonic generation, and even third harmonic or sum-frequency generation, to produce a far-UV source around 260 – 280 nm. This spectral region is not generally accessible to ultrashort pulse lasers and is useful for photo-biological simulation of the UVA and UVB components of the solar spectrum.

By combining these shorter pulses with the hoped for increase in available output powers, there is also the possibility of developing a compact intracavity or extracavity pulsed optical parametric oscillators for the generation of tunable, low power pulses for a range of applications.

The increased portability of these versatile sources will suit many emerging applications where specialised equipment is required to be moved from one customer/patient/lab to another. Thus, whereas many of the applications have required that they be brought to the laser laboratory, in the future it is expected that the new generation of compact femtosecond lasers will be portable and available for convenient deployment at external sites or in specialist (i.e. photo-biological) environments.

Finally, the compact laser cavities could be applied directly in other wavelength regions using alternative directly diode pumpable solid state gain media such as Cr^{4+}:Forsterite[14] or the Ytterbium-doped oxaborates[15] and phosphate glasses[16]. These and other broadband gain materials will benefit from many of the observations and

design considerations described in this thesis as suitable laser diodes become available. For example work is presently underway at St. Andrews into the direct diode pumping of chromium doped zinc selenide (Cr^{2+}:ZnSe)[17] which is potentially tunable from 2150 to 2650 nm.

Endnotes

1 G. J. Valentine, M. P. Critten, G. T. Kennedy, J-M. Hopkins, P. Loza-Alvarez, and W. Sibbett in *Technical Digest of Conference on Lasers and Electro Optics*, (Optical Society of America, Washington, D. C. 1997), paper CMI1.

2 G. J. Valentine, J-M. Hopkins, P. Loza-Alvarez, G. T. Kennedy, W. Sibbett, D. Burns and A. Valster, *Opt. Lett.* **22**, 1639 (1997).

3 J-M. Hopkins, G. J. Valentine, W. Sibbett, J. Aus der Au, F. Morier-Genoud, U. Keller and A. Valster, *Optics Commun.* **154**, 54 (1998).

4 A. G. Kostenbauder, *IEEE J. Quantum Electron.* **26**, 1148 (1990).

5 D. Kopf, K. J. Weingarten, G. Zhang, M. Moser, M. A. Emanuel, R. J. Beach, J. A. Skidmore and U. Keller, *Appl. Phys.* **B 65**, 235 (1997).

6 Millenia Xs laser, Spectra-Physics, 1335 Terra Bella Avenue, Mountain View, CA, U.S.A.

7 Tiger 200, Time-Bandwidth Products Inc. Technoparkstrasse 1, Halle Zeppelin, 1. OG, CH-8005 Zurich, Switzerland.

8 G. Sucha, *Laser Focus World*, **34**, 121 (1998).

9 Femtolite 780 fibre laser, IMRA America Inc. 1044 Woodridge Avenue, Ann Arbor, MI 48105, U.S.A.

10 S. Tsuda, W. H. Knox and S. T. Cundiff, *Appl. Phys. Lett.* **69**, 1538 (1996).

11 A. Robertson, R. Knappe and R. Wallenstein, *Opt. Commun.* **147**, 294 (1998).

12 O. P. Kowalski, C. J. Hamilton, S. D. McDougall, B. Vögele, J. H. Marsh and A. C. Bryce, in *Technical Digest of Conference on Lasers and Electro Optics*, (Optical Society of America, Washington, D. C. 1998), paper CMJ4.

13 SDL Inc. 80 Rose Orchard Way, San Jose, CA 95134-1365, U.S.A.

14 X. Liu, L. J. Qian, F. Wise, Z. G. Zhang, T. Itatani, T. Sugaya, T. Nakagawa and K. Torizuka, Opt. Lett. 23, 129 (1998).

15 F. Mougel, K. Dardenne, G. Aka, A. KahnHarari and D. Vivien, J. Opt. Soc. Am. B 16, 164 (1999).

16 C. Honninger, F. Morier-Genoud, M. Moser, U. Keller, L. R. Brovelli and C. Harder, Opt. Lett. 23, 126 (1998).

17 R. H. Page, K. I. Schaffers, L. D. DeLoach, G. D. Wilke, F. D. Patel, J. B. Tassano, Jr. S. A. Payne, W. F. Krupke, K-T. Chen and A. Burger, IEEE J. Quantum Electron. QE-33, 609 (1997).

Appendix A – Summary of 4 × 4 element matrices for various optical components

Based on the discussion presented in:

A. G. Kostenbauder, *IEEE J. Quantum Electron.* **26**, 1148 (1990).

Free space propagation	Mirror
$\begin{bmatrix} 1 & L & 0 & 0 \\ 0 & 1 & 0 & 0 \\ 0 & 0 & 1 & 0 \\ 0 & 0 & 0 & 1 \end{bmatrix}$ where L is the propagation length	$\begin{bmatrix} 1 & 0 & 0 & 0 \\ \frac{-2}{ROC \cdot \cos\theta} & 1 & 0 & 0 \\ 0 & 0 & 1 & 0 \\ 0 & 0 & 0 & 1 \end{bmatrix}$ where ROC is the mirror radius of curvature and θ is the incidence half angle
Dispersive slab	**Lens**
$\begin{bmatrix} 1 & \frac{d}{n} & 0 & 0 \\ 0 & 1 & 0 & 0 \\ 0 & 0 & 1 & -\frac{\partial v_g}{\partial f}\frac{d}{v_g^2} \\ 0 & 0 & 0 & 1 \end{bmatrix}$ where d = thickness of the slab	$\begin{bmatrix} 1 & \frac{d}{n} & 0 & 0 \\ -\frac{1}{f} & 1 & 0 & 0 \\ 0 & 0 & 1 & -\frac{\partial v_g}{\partial f}\frac{d}{v_g^2} \\ 0 & 0 & 0 & 1 \end{bmatrix}$ where f = focal length of the lens d = thickness of the lens *note: this contains the approximation that the beam spot size << lens surface roc*
Brewster prism tip	**Brewster prism**
$\begin{bmatrix} 1 & 0 & 0 & 0 \\ 0 & 1 & 0 & -\frac{\partial n}{\partial f}\gamma \\ -\frac{\partial n}{\partial f}\frac{\gamma}{\lambda_0} & 0 & 1 & 0 \\ 0 & 0 & 0 & 1 \end{bmatrix}$ where $\gamma = \pm 1$ depending on the prism orientation	$\begin{bmatrix} 1 & \frac{d}{n^3} & 0 & -\frac{\partial n}{\partial f}\gamma\frac{d}{n^3} \\ 0 & 1 & 0 & -\frac{\partial n}{\partial f}\gamma \\ -\frac{\partial n}{\partial f}\frac{\gamma}{\lambda_0} & -\frac{\partial n}{\partial f}\gamma\frac{d}{n^3\lambda_0} & 1 & \left(\frac{\partial n}{\partial f}\right)^2\frac{d}{n^3\lambda_0} - \frac{\partial v_g}{\partial f}\frac{d}{v_g^2} \\ 0 & 0 & 0 & 1 \end{bmatrix}$ where $\gamma = \pm 1$ depending on the prism orientation d = thickness of the prism

Brewster slab

$$\begin{bmatrix} 1 & \frac{d}{n^3} & 0 & \frac{\partial n}{\partial f}\gamma\frac{d}{n^3} \\ 0 & 1 & 0 & 0 \\ 0 & -\frac{\partial n}{\partial f}\gamma\frac{d}{n^3\lambda_0} & 1 & -\left(\frac{\partial n}{\partial f}\right)^2\frac{d}{n^3\lambda_0}-\frac{\partial v_g}{\partial f}\frac{d}{v_g^{\,2}} \\ 0 & 0 & 0 & 1 \end{bmatrix}$$

where $\gamma = \pm 1$ depending on the slab orientation

General prism

$$\begin{bmatrix} m_\phi m_\varphi & \frac{dm_\phi}{nm_\varphi} & 0 & -\frac{\partial n}{\partial f}\gamma\frac{dm_\phi}{n}\tan\varphi \\ 0 & \frac{1}{m_\phi m_\varphi} & 0 & -\frac{\partial n}{\partial f}\gamma\frac{\tan\phi+\tan\varphi}{m_\phi} \\ -\frac{\partial n}{\partial f}\gamma\frac{m_\varphi(\tan\phi+\tan\varphi)}{\lambda_0} & -\frac{\partial n}{\partial f}\gamma\frac{d\tan\phi}{m_\varphi n\lambda_0} & 1 & \left(\frac{\partial n}{\partial f}\right)^2\frac{d\tan\phi\tan\varphi}{n\lambda_0}-\frac{\partial v_g}{\partial f}\frac{d}{v_g^{\,2}} \\ 0 & 0 & 0 & 1 \end{bmatrix}$$

where $\gamma = \pm 1$ depending on the prism orientation

φ = internal ray to entrance face normal angle

ϕ = internal ray to exit face normal angle

d = path length in glass

$$m_\phi = \frac{\sqrt{1-n^2\sin^2\phi}}{\cos\phi} \text{ and } m_\varphi = \frac{\cos\varphi}{\sqrt{1-n^2\sin^2\varphi}}$$

Appendix B – Programs contained on the accompanying CD ROM

Alfrey threshold prediction:

Borland Delphi 3

PAlfreyFast.exe - determines the threshold and slope efficiency of a longitudinally pumped solid state laser after A. J. Alfrey. *IEEE J. Quantum Electron.* **25**, 760 (1989).

cavity models:

Mathsoft MATHCAD 7

Fluence.mcd – Calculates the fluence on the SESAM in the short arm of the highly asymmetric cavity (Chapter 4)

Spot size calc.mcd – Calculates the spot size in the short arm of the highly asymmetric cavity (Chapter 4)

the following three algebra sheets show the symbolic working of the stability limits in a four-mirror resonator with equal and unequal radii of curvature mirrors and a three mirror resonator with unequal radii of curvature mirrors

stb limits equal R.mcd

stb limits unequal R.mcd

3-mirr stb limits unequal R.mcd

Dispersion and SPM:

Mathsoft MATHCAD 7

Spm-freq.mcd – Calculates the SPM in the frequency domain to approximate it with dispersion

Spm-time.mcd - Calculates the SPM in the time domain

Lemoff and Barty ver 3 (Borland Delphi 3) – Calculates 2nd and 3rd order material and geometric dispersion in a prism compensated ultrashort pulse laser and determines the optimum prism orientation/wavelength to minimise 2nd and 3rd order dispersion after the method described in B. E. Lemoff and C. P. J. Barty, *Opt. Lett.* **18**, 57 (1993).

Sadao Uemura.mcd – Calculates the material 2nd and 3rd order dispersion from the equations given in S. Uemura, *Jpn. J. Appl. Phys.* **37**, 133, (1998).

Kostenbauder:

Mathsoft MATHCAD 7

Kostenbauder simulation for Cr LiSAF.mcd (by G.J Valentine) Calculates the dispersion present in an Aoshima-type Cr:LiSAF laser cavity using dispersive ray analysis after A. G. Kostenbauder, *IEEE J. Quantum Electron.* **26**, 1148 (1990).

Magni_Cerullo:

Borland Delphi 3

Magni – Astig – Calculates a magni plot for a stable resonator after V. Magni, G. Cerullo, and S. De Silvestri, *Opt Commun.* **101**, 365 (1993).

Magni - Full 3-mirror pumped at apex after V. Magni, G. Cerullo, S. De Silvestri and A. Monguzzi, *J. Opt. Soc. Am.* **B 12**, 476 (1995).

Magni - Full 3-mirror pumped at retroreflektor after V. Magni, G. Cerullo, S. De Silvestri and A. Monguzzi, *J. Opt. Soc. Am.* **B 12**, 476 (1995).

Magni - Full 3-mirror semi-monolithic after V. Magni, G. Cerullo, S. De Silvestri and A. Monguzzi, *J. Opt. Soc. Am.* **B 12**, 476 (1995).

Magni - Full 4-mirror after V. Magni, G. Cerullo, S. De Silvestri and A. Monguzzi, *J. Opt. Soc. Am.* **B 12**, 476 (1995).

Magni - Simple for plane plane after V. Magni, G. Cerullo, and S. De Silvestri, *Opt. Commun.* **96**, 348 (1993).

Soft app Magni - Simple for plane plane after V. Magni, G. Cerullo, and S. De Silvestri, *Opt. Commun.* **96**, 348 (1993).

Pulses and autocorrelation:

Mathsoft MATHCAD 7

Autocorrelation worksheet.mcd – Calculates an Intensity and interferometric autocorrelation for a sech^2 pulse

Gaussian pulses w chirp.mcd – Calculates the pulse and spectral profile of a Gaussian pulse with or without linear frequency chirp

sech2 pulses w chirp.mcd– Calculates the pulse and spectral profile of a sech^2 pulse with or without linear frequency chirp

Publications

Journal publications

"Ultralow-pump-threshold, femtosecond Cr^{3+}:$LiSrAlF_6$ laser pumped by a single narrow-stripe AlGaInP laser diode"

G. J. Valentine, J-M. Hopkins, P. Loza-Alvarez, G. T. Kennedy, W. Sibbett, D. Burns and A. Valster, *Optics Letters*, Volume 22, Number 21, pp 1639 – 1641, 1997.

"Efficient, low-noise, SESAM-based femtosecond Cr^{3+}:$LiSrAlF_6$ laser"

J-M. Hopkins, G. J. Valentine, W. Sibbett, J. Aus der Au, F. Morier-Genoud, U. Keller and A. Valster, *Optics Communications*, Volume 154, pp 54 – 58, 1998.

Conference publications

"Novel resonator designs for low-threshold self-modelocking"

G. J. Valentine, M. P. Critten, G. T. Kennedy, J-M. Hopkins, P. Loza-Alvarez, and W. Sibbett in *Technical Digest of Conference on Lasers and Electro Optics*, (Optical Society of America, Washington, D. C. 1997), paper CMI1.

"Ultralow-threshold KLM Cr^{3+}:LiSAF laser pumped by a self-injection-locked AlGaInP diode laser"

P. Loza-Alvarez, J-M. Hopkins, G. J. Valentine, D. Burns and W. Sibbett in *Technical Digest of the Thirteenth UK Quantum Electronics Conference*, Cardiff, 1997, poster PVIII-1.

Cont...

"Femtosecond pulse generation from a Cr^{3+}:LiSAF laser pumped by a low-power, single-stripe, AlGaInP diode laser"

J-M. Hopkins, P. Loza-Alvarez, G. J. Valentine, M. P. Critten, D. Burns and W. Sibbett in *Technical Digest of the Thirteenth UK Quantum Electronics Conference,* Cardiff, 1997, poster PVIII-5.

"Efficient femtosecond Cr^{3+}:LiSAF laser powered by penlight batteries"

J-M. Hopkins, G. J. Valentine, W. Sibbett, J. Aus der Au and U. Keller in *Technical Digest of Conference on Lasers and Electro Optics,* (Optical Society of America, Washington, D. C. 1998), paper CThC2.

"Ultralow-noise battery operated, passively modelocked Cr^{3+}:LiSAF laser"

J-M. Hopkins, G. J. Valentine, W. Sibbett, J. Aus der Au, F. Morier-Genoud, U. Keller and A. Valster *in Technical Digest of Conference on Lasers and Electro Optics Europe,* (Optical Society of America, Washington, D. C. 1998), paper CWM2.

"Highly compact femtosecond Cr^{3+}:LiSAF laser with a simplified cavity geometry"

J-M. Hopkins, G. J. Valentine, W. Sibbett and U. Keller *in Technical Digest of Conference on Lasers and Electro Optics,* (Optical Society of America, Washington, D. C. 1999), paper CTuA4.

Ultralow-pump-threshold, femtosecond Cr^{3+}:$LiSrAlF_6$ laser pumped by a single narrow-stripe AlGaInP laser diode

G. J. Valentine, J.-M. Hopkins, P. Loza-Alvarez, G. T. Kennedy, and W. Sibbett

J. F. Allen Physics Research Laboratories, Department of Physics and Astronomy, University of St. Andrews, Fife KY15 9SS, Scotland, UK

D. Burns

Institute of Photonics, Wolfson Centre, University of Strathclyde, 106 Rottenrow, Glasgow G4 0NW, Strathclyde, Scotland, UK

A. Valster

Philips Optoelectronics-Research, Prof. Holstlaan, 4, 5656 AA Eindhoven, The Netherlands

Received June 25, 1997

We report what we believe to be the first demonstration of a Kerr-lens mode-locked Cr^{3+}:$LiSrAlF_6$ laser that is pumped by a single narrow-stripe AlGaInP laser diode with a diffraction-limited output beam. A novel low-loss three-mirror laser cavity design is described in which strong, localized Kerr lensing was exploited such that 75-fs-duration pulses were obtained for only 36 mW of incident pump power. This pump power was maintained for 18 h by just three AA batteries as the electrical power source. We have shown that mode locking can be sustained for pump powers as low as 22 mW. © 1997 Optical Society of America

Since the first demonstration of a direct AlGaInP laser-diode-pumped Kerr-lens mode-locked (KLM) Cr^{3+}:$LiSrAlF_6$ (Cr:LiSAF) laser,[1] it has been the most promising system for the development of a compact, cost-effective low-phase-noise source of tunable femtosecond pulses in the near IR. To date, most research has been concentrated on developing an all-solid-state replacement for the KLM Ti:sapphire laser based on pumping Cr^{+3}:LiSAF with high-power non-diffraction-limited broad-stripe laser diodes. Unfortunately, for optimum use of the non-diffraction-limited beams produced by these laser diodes, extended pump-optics schemes are required that detract from the aims of compactness and simplicity.

Recently a KLM Cr:LiSAF laser was reported in which a single 800-mW, 200-μm-wide stripe diode laser was used as the pump source for a novel, tight-focusing four-mirror resonator geometry.[2] This arrangement permitted pulses as short as 26 fs to be produced, but the total efficiency of this laser was rather low, probably owing to poor overlap of the laser mode with the non-diffraction-limited pump mode.

Narrow-stripe AlGaInP laser diodes (with stripe widths of <5 μm), which produce diffraction-limited output beams, offer the potential for the development of a highly compact, low-cost pump source for a KLM Cr:LiSAF laser. Unfortunately the low output powers that are currently available from such devices (~ 50 mW) are considerably lower than the pump thresholds that are normally required for KLM operation with standard four-mirror laser cavites.

In this Letter we report a novel, low-pump-threshold KLM laser[3] with a design that builds on previous low-threshold research.[4] This research has permitted, for the first time to our knowledge, the operation of a femtosecond laser with a single narrow-stripe diffraction-limited laser diode as the pump source.

The complete cavity and pumping geometry is illustrated in Fig. 1. We selected the three-mirror design, similar to the cavity described in Ref. 5, to address some of the key considerations for low cw threshold,[4] most notably a rod with a high pump absorption coefficient with the laser and pump modes focused on the pumped end of the rod. Figure 2(a) illustrates the difficulties associated with this in a standard Z or X cavity that is configured for a Brewster-angled gain medium. The beam can be focused on the rod end for just one plane (tangential), leading to a distributed focus through the crystal. In Ref. 4 a modified Z cavity was implemented by use of a plane–plane rod with cavity folding mirrors placed at near-normal incidence to eliminate astigmatic effects. With this configuration the two foci of the laser coincide in the pumped end of the rod, giving a very tight, highly localized beam waist

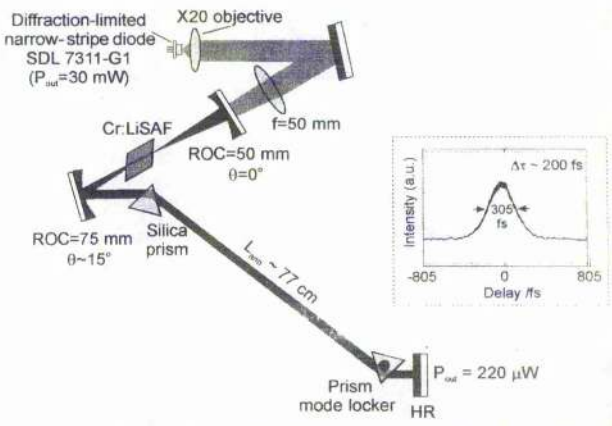

Fig. 1. Schematic of the low-threshold KLM Cr:LiSAF laser cavity pumped by a diffraction-limited SDL 30-mW laser diode. Inset: autocorrelation trace of 200-fs pulses obtained with this setup. ROC, radius of curvature.

0146-9592/97/211639-03$10.00/0

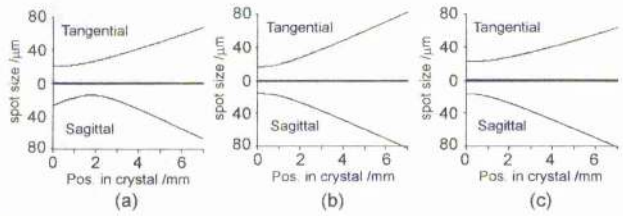

Fig. 2. Laser beams in Cr:LiSAF crystal in different resonator configurations: (a) Brewster-angled crystal in a standard Z cavity, showing distributed focus. (b) Plane–plane crystal in a standard Z cavity with tight focus on the end of the crystal. (c) Brewster-angled crystal in a three-mirror cavity, showing tight focus on end of crystal. Pos., position.

[Fig. 2(b)]. Unfortunately, even with high-quality antireflection coatings on the end faces of plane–plane rods, their use still leads to an increase in the round-trip parasitic losses. Using the three-mirror geometry shown in Fig. 1, and by pumping through the curved retroflecting end mirror, we found that the tangential and the sagittal foci coincide in the pumped end of a Brewster-angled rod, as indicated in Fig. 2(c). This coincidence is possible when the curved end mirror is placed at a distance from the pumped end of the rod equal to (for small beam waists) the mirror's radius of curvature (ROC). The pump laser beam was focused onto the rod face through the 5-cm ROC end mirror by a 5-cm focal-length lens. The 7.5-cm ROC folding mirror was angled to compensate completely for the astigmatism introduced by the Brewster angles, giving a circular beam from the high-reflecting (HR) plane end mirror. The HR-coated mirrors (LaserOptik GmbH) had reflectivities of 99.95% at the center wavelength of 840 nm and >99.9% from 800 to 870 nm.

The intracavity parasitic losses of the W cavity described in Ref. 4 were not minimized for a lowest cw threshold. Our three-mirror design has two fewer HR-mirror reflections per round trip than a standard Z cavity. In addition, a low-loss Infrasil fused-silica prism together with a fused-silica prism modulator provided negative intracavity group-velocity dispersion. The use of a prism mode locker permitted regenerative initiation to be implemented[6] without necessitating the inclusion of any additional intracavity elements. This cavity is thus well suited for the mode locking of lasers with media with low gain because the parasitic losses are minimal.

In addition to reducing the cw pump threshold, the tight, localized focus that is possible when the three-mirror design is used permits a strong Kerr lens to be induced for relatively low intracavity powers. The location of this lensing (at the rod end) is also the position at which it will have maximum effect on the laser mode throughout the cavity.

The total cavity length was ~85 cm, giving a pulse-repetition frequency of 180 MHz. The prism separation of 51.5 cm that was necessary for dispersion control prevented scaling the physical size of the cavity down to a more-compact design. More-dispersive material could be employed for second-order dispersion control, but for this laser, in contrast with the one described in Ref. 4, fused silica was the ideal material for minimal third-order dispersion. The gain medium was a 7-mm-long Brewster-angle-cut Cr:LiSAF slab with 1.5% Cr^{3+} doping.

A commercially obtained narrow-strip AlGaInP laser diode (SDL 7311-G1) that was p-polarization oriented (for optimal absorption in the Cr:LiSAF) was initially employed as the pump source. This laser diode was rated for 33-mW maximum output power at 680 nm but was driven at only 30 mW for our laser. The laser was directly pumped with the elliptical (~4:1) mode obtained from the laser diode, with no beam shaping or telescoping employed, giving the ultimate in simplicity for the pump geometry.

For KLM operation, the laser was first aligned for a low-cw threshold. Just 9.5 mW of power was required for cw threshold to be achieved for this low-loss cavity, which included group-velocity dispersion compensation and a mode-locking initiation device. Femtosecond operation could then be achieved routinely by careful adjustment of the folding mirror. With the maximum available pump power of 26 mW incident upon the pump focus lens, stable 200-fs-duration pulses were generated, resulting in 230 μW leaking through each HR mirror reflection (inset in Fig. 1). The incident pump power could be reduced to less than 22 mW before mode locking ceased.

Two prototype 50-mW 680-nm diffraction-limited narrow-stripe laser diodes (type CQL 806/50) developed by Philips Optoelectronics[7] were also used to pump the laser. These diodes, which were mounted orthogonally, were each operated at 42-mW output and polarization combined, giving 76 mW of power incident upon the pump focus lens. As before, no beam reshaping was used, and this resulted in a cross-shaped pump beam.

Stable, bandwidth-limited pulses of 60-fs duration were readily obtained (see Fig. 3) with 1.57-mW output beams that were available through each HR mirror. It should be possible to increase slightly the useful output power to >3.5 mW by replacement of the HR plane end mirror with an output coupler of slightly lower reflectivity ($R \sim 99.75\%$); however, mode-locked performance may be compromised.

Once stable femtosecond operation was accomplished with this arrangement, the regenerative-mode-locking

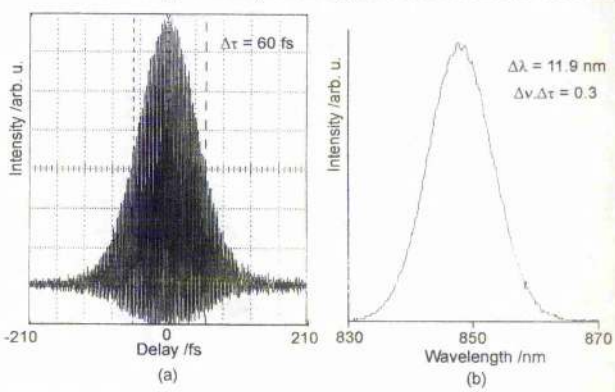

Fig. 3. Characterization of 60-fs pulses obtained with two Philips (CQL 806/50) narrow-stripe diodes as the pump source: (a) interferometric autocorrelation, (b) corresponding spectrum.

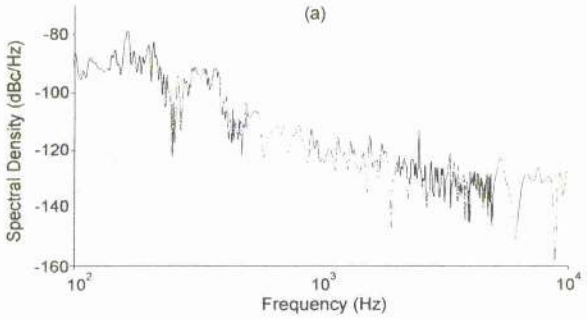

(b)

Frequency	Free-running low-threshold KLM Cr:LiSAF laser	Broad-area diode laser pumped KLM Cr:LiSGaF laser[9]	Free-running KLM Ar+-pumped Ti:sapphire laser[10]
50 - 1000 Hz	2200 fs	5000 fs	—
100 - 500 Hz	680 fs	1700 fs	3400 fs
500 -5000 Hz	73 fs	—	800 fs

Fig. 4. Phase-noise measurements on the low-threshold Cr:LiSAF laser pumped by two Philips 50-mW laser diodes: (a) single-sideband phase-noise spectrum, (b) comparison of timing jitter with a free-running laser-diode pumped Cr:LiSGAF and Ar^+-pumped Ti:sapphire lasers.

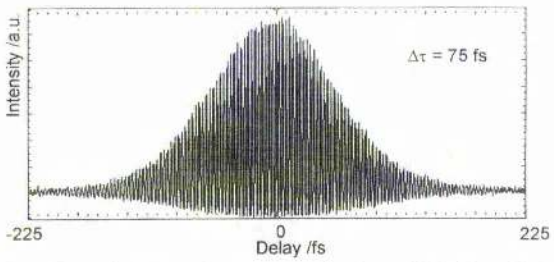

Fig. 5. Interferometric autocorrelation of 75-fs pulses obtained from Cr:LiSAF laser pumped by a single narrow-stripe Philips laser diode.

electronics could be switched off, at which stage the laser operated in a purely passively mode-locked manner. To assess the stability of the pulse train, we carried out a phase-noise measurement with the methodology described in Ref. 8. In our case a BPW28 broadband silicon photodiode was used in conjunction with a microwave spectrum analyzer to measure the spectra of the fundamental and the tenth harmonics of the laser cavity frequency. The single-sideband phase-noise spectrum is shown in Fig. 4(a). The phase noise is slightly lower than that of the low-noise broad-stripe laser-diode-pumped Cr:LiSGaF laser described in Ref. 9 and significantly better than the unstabilized Ti:sapphire laser of Ref. 10, as evidenced by a comparison of the rms timing jitter values in Fig. 4(b). Because the amplitude noise of the laser was lower than the detection limit of our measurement system, only a worst-case amplitude spectrum could be recorded. Less than 4% rms amplitude noise was measured on a second-harmonic-generated signal recorded over a 10-ms interval. This low-noise laser is currently being used in the evaluation of new synchroscan streak cameras operating in the subpicosecond regime.

Finally, the *s*-polarized laser was removed and the cavity dispersion optimized for pumping with one *p*-polarized Philips diode by introduction of more prism material into the cavity. Introducing more material compensates for the reduction in the total effective positive dispersion, as the lower intracavity power induces less self-phase modulation.[4] With only 36 mW of incident pump power, bandwidth-limited pulses as short as 75 fs at 730-μW output power were obtained (Fig. 5). To demonstrate the potential of this low-threshold laser system for low running costs and portability, we replaced the laser diode power supply with three AA penlight cells (Duracell MN1500) connected in series. An adjustable, low-dropout voltage regulator (LP2952) allowed the drive voltage to the Philips laser diode to be set to give the required 36 mW of incident pump power. This efficient power supply allowed constant output power from the narrow-stripe laser diode to be maintained for more than 18 h of operation before excessive battery discharge occurred.

We believe that this low-loss approach to laser cavity design should find application in achieving the aim of direct-diode pumping of other laser materials for Kerr-lens mode-locked operation when only limited pump power is available.

The authors thank Bill Sleat for technical assistance, the Optical Materials Research Centre of the University of Strathclyde for the loan of the Cr:LiSAF slab, and A. Valster of Philips Optoelectronics-Research for supplying the prototype laser diodes used. This research was supported by the UK Engineering and Physical Sciences Research Council (EPSRC). J-M. Hopkins acknowledges financial support through an EPSRC Defence Educaton and Research Agency studentship. P. Loza-Alvarez acknowledges funding from the National University of Mexico and a Chevening scholarship from the the British Council.

References

1. M. J. P. Dymott and A. I. Ferguson, Opt. Lett. **19,** 1988 (1994).
2. S. Uemura and K. Miyazaki, Opt. Commun. **138,** 330 (1997).
3. G. J. Valentine, M. P. Critten, G. T. Kennedy, J-M. Hopkins, P. Loza-Alvarez, and W. Sibbett, in *Conference on Lasers and Electro-Optics*, Vol. 11 of 1997 OSA Technical Digest Series (Optical Society of America, Washington, D.C., 1997), paper CMI1.
4. D. Burns, M. P. Critten, and W. Sibbett, Opt. Lett. **21,** 477 (1996).
5. B. E. Bouma and J. G. Fujimoto, Opt. Lett. **21,** 134 (1996).
6. D. E. Spence, J. M. Evans, W. E. Sleat, and W. Sibbett, Opt. Lett. **16,** 1762 (1991).
7. A. Valster, A. T. Meney, J. R. Downes, A. R. Adams, A. A. Brouwer, and A. J. Corbijn, in *Digest of the 15th International Semiconductor Laser Conference* (Institute of Electrical and Electronics Engineers, New York, 1996), p. 139.
8. D. von der Linde, Appl. Phys. B. **39,** 201 (1986).
9. V. P. Yanovsky, A. Korytin, F. W. Wise, A. Cassanho, and H. P. Jenssen, IEEE J. Sel. Topics Quantum Electron. **2,** 465 (1996).
10. D. E. Spence, J. M. Dudley, K. Lamb, W. E. Sleat, and W. Sibbett, Opt. Lett. **19,** 481 (1994).

Reprinted from

OPTICS COMMUNICATIONS

Optics Communications 154 (1998) 54–58

Efficient, low-noise, SESAM-based femtosecond Cr^{3+}:$LiSrAlF_6$ laser

J.-M. Hopkins [a], G.J. Valentine [a], W. Sibbett [a,*], J. Aus der Au [b], F. Morier-Genoud [b], U. Keller [b], A. Valster [c]

[a] *J.F. Allen Physics Research Laboratories, Department of Physics and Astronomy, University of St. Andrews, Fife KY16 9SS, Scotland, UK*
[b] *Ultrafast Laser Physics, Institute of Quantum Electronics, Swiss Federal Institute of Technology, ETH Hönggerberg-HTP, CH-8093 Zürich, Switzerland*
[c] *Philips Optoelectronics Research, Prof. Holstlaan 4, 5656 AA Eindhoven, The Netherlands*

Received 23 April 1998; accepted 2 June 1998

ELSEVIER

ELSEVIER

15 August 1998

Optics Communications 154 (1998) 54–58

OPTICS COMMUNICATIONS

Efficient, low-noise, SESAM-based femtosecond Cr^{3+}:$LiSrAlF_6$ laser

J.-M. Hopkins [a], G.J. Valentine [a], W. Sibbett [a,*], J. Aus der Au [b], F. Morier-Genoud [b], U. Keller [b], A. Valster [c]

[a] *J.F. Allen Physics Research Laboratories, Department of Physics and Astronomy, University of St. Andrews, Fife KY16 9SS, Scotland, UK*
[b] *Ultrafast Laser Physics, Institute of Quantum Electronics, Swiss Federal Institute of Technology, ETH Hönggerberg-HTP, CH-8093 Zürich, Switzerland*
[c] *Philips Optoelectronics Research, Prof. Holstlaan 4, 5656 AA Eindhoven, The Netherlands*

Received 23 April 1998; accepted 2 June 1998

Abstract

We report what we believe to be the first demonstration of a SESAM (semiconductor saturable absorber mirror)-based femtosecond Cr^{3+}:$LiSrAlF_6$ laser pumped by narrow-stripe AlGaInP laser diodes that have diffraction-limited output beams. A highly asymmetric, four-mirror laser cavity design is described for which 57 fs duration pulses at an average output power of 6.5 mW are obtained for only 72 mW of incident pump power. Pump powers of this order were maintained for over 14 h using just six 1.5 V AA batteries as the electrical power source. We have shown that mode-locking can be sustained for incident pump powers as low as 21.5 mW.

1. Introduction

In the research that is directed towards the development of compact all-solid-state femtosecond lasers, the impact of combining AlGaInP laser diodes with colquiriite gain media such as Cr:LiSAF has been very significant. It has led to the demonstration of extremely efficient sources of femtosecond pulses and although there now exist diode-pumped-solid-state (DPSS) lasers for pumping Ti:sapphire, directly diode-pumped femtosecond lasers have obvious advantages: not least of cost. Since the first report of such a system [1] there have been notable developments in mode-locked Cr:LiSAF lasers that incorporate semiconductor saturable absorbing mirrors (SESAM) [2], SESAMs that compensate for positive dispersion [3] and Kerr-lens mode-locked (KLM) versions [4]. The main thrust of these recent enhancements has been directed towards increasing the average output powers of the lasers such that up to 500 mW has already been reported [5]. There are, however, applications that do not require average output powers of this scale but for which stable and low-noise pulse sequences with average powers of the order of a few milliwatts would suffice. This low-power configuration has the additional advantages of simplicity and increased overall efficiency.

In this Letter we report a femtosecond Cr^{3+}:$LiSrAlF_6$ laser based on a highly asymmetric four-mirror geometry where the mode-locking is initiated and sustained using a SESAM incorporating a GaAs quantum well [3,5]. This cavity retains the low pump power requirements of a previously reported three-mirror KLM laser [6] allowing the use of diffraction-limited narrow stripe AlGaInP laser diodes (stripe widths 4–5 μm) to pump the laser. The inclusion of the SESAM permitted the use of a 1.5% output coupler in the cavity and an order of magnitude greater average output power to be obtained. This new

* Corresponding author. E-mail: jh3@st-and.ac.uk

0030-4018/98/$19.00
PII S0030-4018(98)00312-5

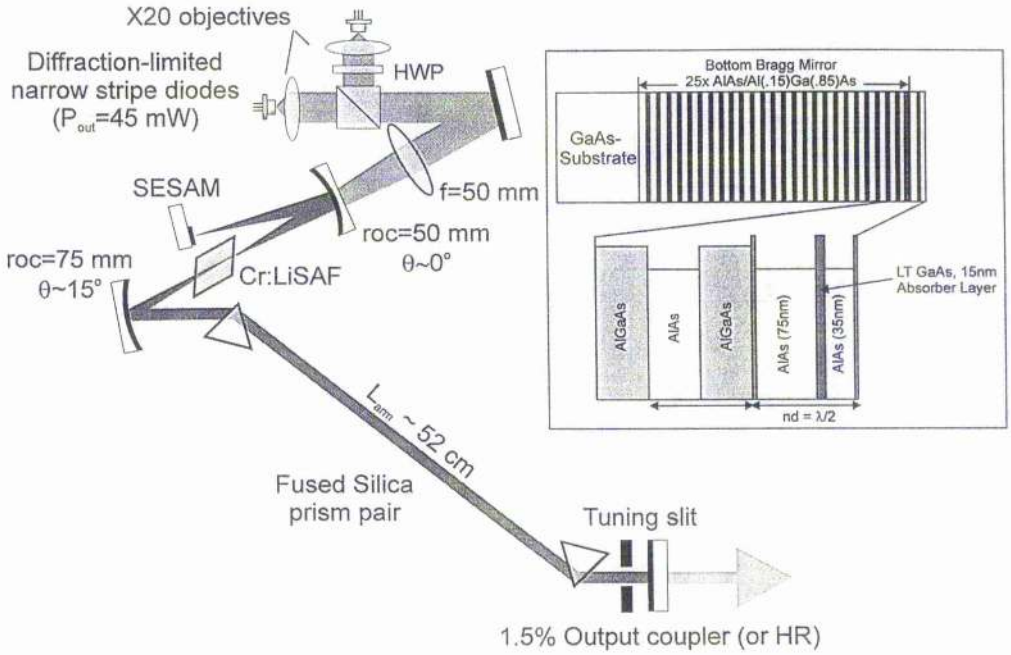

Fig. 1. Schematic of the low-threshold SESAM-mode-locked Cr:LiSAF laser cavity pumped by diffraction-limited Philips 50 mW laser diodes. (Inset: schematic of AlAs/GaAlAs SESAM.)

resonator configuration also provided an entirely self-starting femtosecond pulse operation.

2. Experiment

Fig. 1 shows a schematic of the complete cavity and pumping geometry used for the femtosecond Cr:LiSAF laser. A highly asymmetric four-mirror Z-cavity design is used in which the large angle ($\sim 30°$) between the long cavity arm and the folding section compensates entirely for the astigmatism introduced by the Brewster-angle cut gain medium (7 mm crystal of Cr^{3+}:$LiSrAlF_6$ with 1.5% Cr^{3+} doping). Provided that the angle between the folding section and the short cavity arm is small (close to zero), the pump and cavity modes may be tightly focused and made to coincide on the pumped crystal facet, thereby ensuring a low cw threshold. The highly asymmetric cavity design allows the cavity beam waist on the SESAM to be varied easily by adjusting the length of the short cavity arm (see Fig. 2). This enables the saturation of the SESAM to be optimised for variable intracavity powers. Initially the intracavity field was focused to a 22 μm spot radius on the SESAM by setting the short arm length to 54 mm.

The two curved folding mirrors had radii of curvature of 50 and 75 mm for the short and long cavity arms, respectively, and had high-reflectivity (HR) coatings centred around 850 nm (LaserOptik GmbH, $T = 0.05\%$). The plane end-mirror was either a HR coated mirror or a 1.5% transmitting output coupler. A slit placed in front of this end-mirror allowed the laser wavelength to be tuned to the bandgap of the SESAM around 860 nm. The total cavity length was approximately 1 m, giving a pulse repetition frequency of ~ 150 MHz. Intracavity dispersion compensation was provided by a pair of low insertion loss Infrasil fused-silica prisms separated by 51 cm. Fused silica was chosen initially to minimise the intracavity third-order dispersion originating from the prism pair.

The SESAM was a broadband low-finesse, antiresonant Fabry-Perot saturable absorber (A-FPSA) which has been described elsewhere [5,7]. The structure of the SESAM is shown in the inset of Fig. 1 and its characteristics are described comprehensively in Ref. [5]. It suffices to say

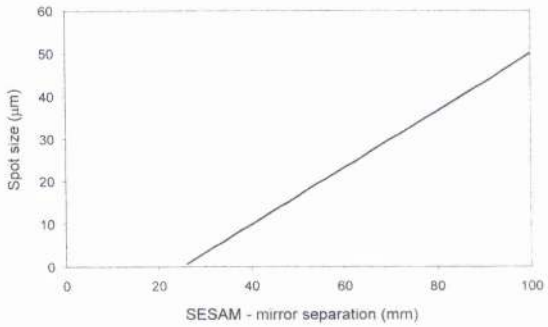

Fig. 2. Variation of intracavity focus on the SESAM with varying short cavity arm length.

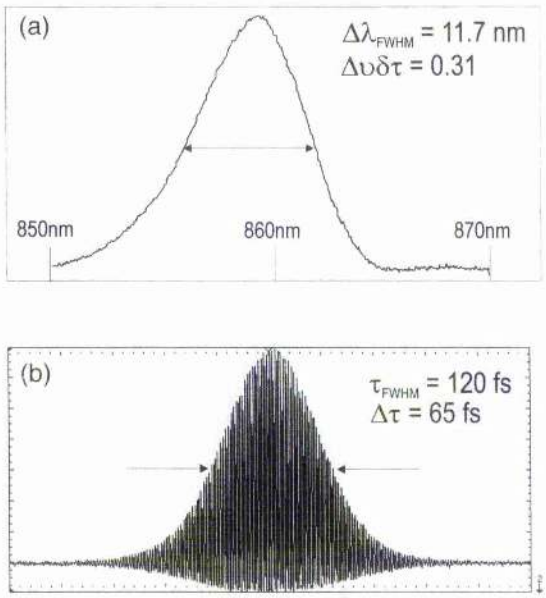

Fig. 3. Characterisation of 65 fs pulses obtained at a pump power of 72 mW (two Philips CQL 806/50 diodes): (a) interferometric autocorrelation and (b) corresponding spectrum.

here that this low-finesse Fabry-Perot is defined by the Fresnel reflectivity of the semiconductor–air interface at the top of the device ($R \approx 31\%$) and the MOCVD grown AlAs/AlGaAs Bragg mirror centred at 850 nm ($R > 99.5\%$). The SESAM was designed to give a relatively flat

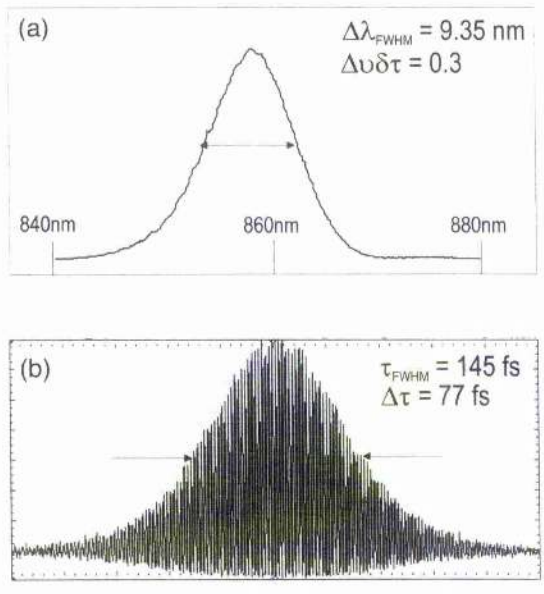

Fig. 4. Characterisation of 77 fs pulses obtained at a pump power of 35 mW (one Philips CQL 806/50 diode): (a) interferometric autocorrelation and (b) corresponding spectrum.

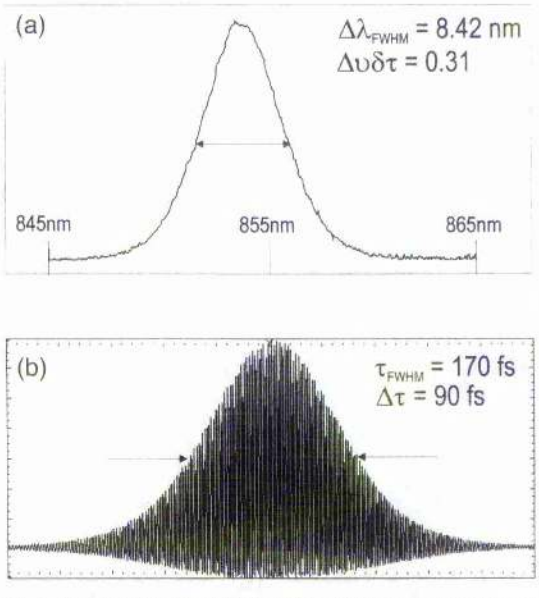

Fig. 5. Characterisation of 90 fs pulses obtained at a pump power level of 80 mW and an output coupling of 1.5%: (a) interferometric autocorrelation and (b) corresponding spectrum.

low-intensity (unsaturated) reflectivity of $98.5 \pm 0.7\%$ across a wavelength range of 50 nm. A 15 nm thick absorber quantum well is positioned within a half-wavelength, transparent AlAs spacer layer that satisfied the antiresonance condition of the F–P structure. The low-tem-

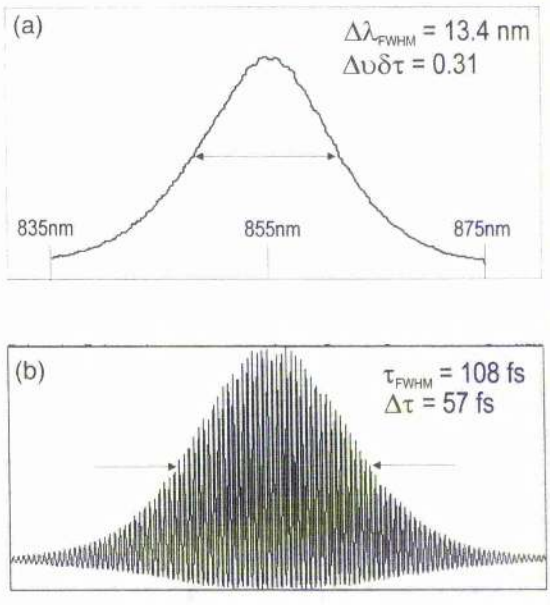

Fig. 6. Characterisation of 57 fs pulses obtained at a pump power level of 72 mW and an output coupling of 1.5%: (a) interferometric autocorrelation and (b) corresponding spectrum.

perature (400°C) MBE-grown GaAs quantum well had a bandgap that corresponded to an absorption centred at a wavelength of 860 nm. The SESAM used had a saturation fluence of 160 $\mu J/cm^2$ at 830 nm and was not significantly different at the preferred operating wavelength based around 860 nm. Its associated maximum reflectivity when saturated was 99.5% giving a modulation depth of $\sim 1.4\%$.

The two pump laser diodes were type-CQL 806/50 prototype narrow-stripe AlGaInP devices supplied by Philips Optoelectronics Research [8]. The diodes were specified to produce up to 50 mW at 680 nm from the diode facet in a 3:1 elliptical beam when collimated. The use of such diffraction-limited sources allows simple coupling optics to be employed and a more efficient pump/cavity mode overlap to be obtained. No reshaping of the elliptical mode was employed. The diode emissions were oriented parallel and collimated using standard $\times 20$ microscope objective lenses. The beams were then combined in a Glan–Thompson polarising cube using a half-wave plate to rotate the polarisation of one of the diodes. This pump light was subsequently focused into the gain medium using a 5 cm focal length spherical lens.

3. Results

The cw threshold of the laser was measured to be 20.4 mW with an HR end-mirror when pumped with a single diode having its *E*-field polarised parallel to the crystal *c*-axis (p-polarised). Absorption of Cr:LiSAF for p-polarised light is approximately twice that for s-polarised light at 670–680 nm. Tuning the laser for mode-locked operation while maintaining optimum GVD conditions, yielded a stable self-starting train of transform-limited 65 fs pulses from the HR end-mirror (see Fig. 3). An average output power of 920 μW was obtained from each of the cavity HR-mirrors for an incident pump power of 72 mW. With the cavity in this configuration the laser was pumped with a single narrow-stripe pump diode (p-polarised) giving a maximum available pump power of 35 mW incident on the crystal. At this lower pump power the laser pro-

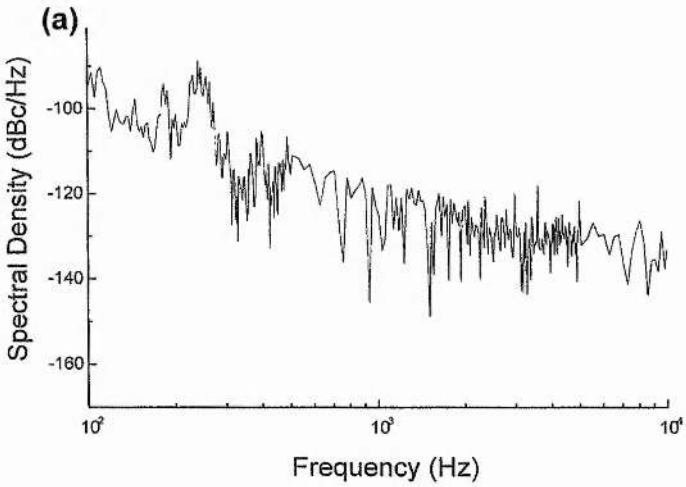

(b)

Frequency	Free-running Low-threshold Cr:LiSAF laser with SESAM	Free-running Low-threshold KLM Cr:LiSAF laser[6]	Free-running KLM Ar+-pumped Ti:Sapphire laser[10]	Actively-stabilised KLM Ar+-pumped Ti:Sapphire laser[10]
50-1000Hz	1 200 fs	2 200 fs	—	—
100-500Hz	302 fs	680 fs	3 400 fs	150 fs
500-5000Hz	73 fs	73 fs	800 fs	80 fs

Fig. 7. Phase-noise measurements on the battery-operated femtosecond Cr:LiSAF laser pumped by two laser diodes: (a) single-sideband phase-noise spectrum, (b) comparison of timing jitter with low-noise, KLM diode-pumped Cr:LiSAF and Ar^+-pumped Ti:sapphire lasers.

duced 77 fs pulses at an average output power of 460 μW (see Fig. 4) and mode-locked operation ceased only when the pump power was reduced below 21.5 mW. This value is close to the cw threshold of the laser and is an indication of the higher reflectivity available from the SESAM when saturated.

By replacing the mains electrical power supplies to the laser diodes by a battery pack containing six 1.5 V AA-type penlight batteries and a low drop-out voltage regulator circuit (LP2952), the diodes provided up to 80 mW of incident pump power. When the high-reflectivity plane mirror was replaced with a 1.5% output coupler, the laser exhibited a slope efficiency of 36% and produced transform-limited 90 fs pulses at an average output power of 9 mW (see Fig. 5). This performance represented an attractive overall electrical-to-optical efficiency of approximately 1%. Mode-locked laser operation could be sustained for over 14 h using these six batteries.

To further reduce pulse durations with the output coupler in place, the spot size on the SESAM was reduced to 13 μm to increase the incident energy fluence. This was achieved by reducing the SESAM folding mirror separation to 45 mm highlighting the suitability of the highly asymmetric cavity configuration for this purpose. The tuning slit was no longer necessary for mode-locked operation as a result of the increased cavity focussing and the cavity produced pulses as short as 70 fs at an output power of 6 mW for an incident pump power of 72 mW.

Using a complex matrix analysis of its multilayer structure the SESAM was found to contribute a minimal amount of group-velocity or second-order dispersion but a significant amount of positive third-order dispersion into the cavity [9]. For this reason the fused silica prisms were replaced with LaK31 prisms separated by 27 cm. This prism system provided a net negative third-order dispersion of a few hundred femtoseconds [3] that compensated for the dispersive effect of the SESAM [10]. In this configuration the laser produced 57 fs pulses at an average output power of 6.5 mW for an incident pump power of only 72 mW (see Fig. 6).

Using the methods described in Ref. [11], phase-noise measurements of the laser output were carried out. The laser beam was focused onto a BPW28 fast silicon-avalanche photodiode and the resulting signal displayed on a HP7000 microwave spectrum analyser system. The single sideband phase-noise spectrum is shown in Fig. 7a. Fig. 7b indicates the rms timing jitter for this laser as compared to a low-noise, KLM Cr:LiSAF laser pumped with narrow-stripe laser diodes [6], a free-running KLM Ti:sapphire laser [12] and an actively stabilised, cavity-referenced KLM Ti:sapphire laser which was coupled to a noise-eating system [12]. The noise figures compare favourably with these earlier system configurations, as the mode-locking mechanism was completely passive with no external noise reduction. A 'worst case' amplitude noise spectrum could only be recorded because the noise performance of this battery-operated laser was below the noise floor of our measurement system.

4. Conclusion

In summary, a compact, efficient, ultralow-noise femtosecond laser system that is pumped directly with narrow-stripe, diffraction-limited laser diodes has been demonstrated. Output powers as high as 9 mW and pulses as short as 57 fs have been obtained with a maximum available pump power of only 80 mW. The ability to use a small battery pack as an electrical power source in obtaining these results highlights the overall efficiency of the system. It follows that this low-threshold, self-starting type of laser cavity design could also be used in the direct diode pumping of other materials when either a limited pump power is available or a modest output power is acceptable.

Acknowledgements

The authors thank Dr. Bill Sleat for technical assistance, the Optical Materials Research Centre at the University of Strathclyde for the loan of the Cr:LiSAF crystal, and Philips Optoelectronics Research for supplying the prototype laser diodes used in this work. This research was supported by the UK Engineering and Physical Sciences Research Council (EPSRC) under the DTI/EPSRC LINK Photonics programme. J.-M.H. acknowledges financial support through an EPSRC/Defence Evaluation and Research Agency CASE studentship.

References

[1] R. Mellish, P.M.W. French, J.R. Taylor, P.J. Delfyett, L.T. Florez, Electron. Lett. 30 (1994) 223.
[2] D. Kopf, K.J. Weingarten, L.R. Brovelli, M. Kamp, U. Keller, Optics Lett. 19 (1994) 2143.
[3] D. Kopf, G. Zhang, R. Fluck, M. Moser, U. Keller, Optics Lett. 21 (1996) 486.
[4] S. Uemura, K. Miyazaki, Optics Comm. 138 (1997) 330.
[5] D. Kopf, K.J. Weingarten, G. Zhang, M. Moser, M.A. Emanuel, R.J. Beach, J.A. Skidmore, U. Keller, Appl. Phys. B. 65 (1997) 235.
[6] G.J. Valentine, J.-M. Hopkins, P. Loza-Alvarez, G.T. Kennedy, W. Sibbett, D. Burns, A. Valster, Optics Lett. 22 (1997) 1639.
[7] D. Kopf, A. Prasad, G. Zhang, M. Moser, U. Keller, Optics Lett. 22 (1997) 621.
[8] A. Valster, A.T. Meney, J.R. Downes, D.A. Faux, A.R. Adams, A.A. Brouwer, A.J. Corbijn, Sel. Topics Quantum. Electron. 3 (1997) 180.
[9] E.J.O. Williams, Ph.D. Thesis, The University of St. Andrews, Fife, UK, 1997.
[10] B.E. Lemoff, C.P.J. Barty, Optics Lett. 18 (1993) 57.
[11] D. Von der Linde, Appl. Phys. B. 39 (1986) 201.
[12] D.E. Spence, J.M. Dudley, K. Lamb, W. Sibbett, Optics Lett. 19 (1994) 481.

Acknowledgements

The maker and keeper of the road, I AM

Kirsty, soul-mate and team-mate

Mum, Dad and Rowan for everything else!

I am indebted to the following people for contributing to my enjoyment of the work I have undertaken and continue to undertake at St. Andrews:

Wilson for continued optimism and encouragement and for giving me the opportunity to be part of the W squad!

Matthew Critten for showing me the ropes and being very patient

David Burns for all the kit, chat and legacy of 'top science'

Gareth Valentine for experimental excellence, uncalculable contribution to this project and for knowing when to use words of one syllable and when to let me do it myself

Derryck Reid for knowledge of all things dispersive and answering persistent questions

St. Pablo Loza-Alvarez for being a most patient, tolerant and damn happy labmate and amigo!

Bill Sleat for friendship and his many insights into life on earth

Paul Faller for showing me how to do maths again

Kate McGowan for finding us a place to live

The W Squad old and new: Gordon, Karen, Zoe, Tom, David, Edik, Gregory, Ian and David

The A team: Alan, Dawn, Michael, Julia, Jonathan, and David

Steven White for waiting and for proof reading chapter 1, sorry it all got chopped!

Mr. Wilson for so many reasons that I miss

Jim, Dunx, Malx, Charlie, Graham, Natalie, Ian and mm-dave!

George, George, Jimmy, Andy, Willie and Ian for all the bits, bobs and thingmys

Morag, Mary, Leslie, Belinda and Anne for making the whole thing run

My mate Dave 'curry' Chambers..... and ZZtop!